SOME STUDIES ON ULTRASONIC JOINING OF THIN COPPER, ALUMINIUM AND PHOSPHOR BRONZE SHEETS

THESIS

SUBMITTED TO DELHI TECHNOLOGICAL UNIVERSITY

FOR THE AWARD OF THE DEGREE OF

DOCTOR OF PHILOSOPHY

IN

MECHANICAL ENGINEERING

By

BHARAT SANGA
(2K14/PhD/ME/03)

DEPARTMENT OF MECHANICAL ENGINEERING

DELHI TECHNOLOGICAL UNIVERSITY

DELHI-110042 (INDIA)

DECEMBER, 2022

SOME STUDIES ON ULTRASONIC JOINING OF THIN COPPER, ALUMINIUM AND PHOSPHOR BRONZE SHEETS

A Thesis submitted to the Delhi Technological University, Delhi in partial fulfillment of the requirement for the degree of

DOCTOR OF PHILOSOPHY

IN

MECHANICAL ENGINEERING

By

BHARAT SANGA

(2K14/PhD/ME/03)

Under the supervision of

Dr. REETA WATTAL
Professor
Department of Mechanical Engineering
Delhi Technological University

Dr. D. S. NAGESH
Professor
Department of Mechanical Engineering
Delhi Technological University

DEPARTMENT OF MECHANICAL ENGINEERING
DELHI TECHNOLOGICAL UNIVERSITY
DELHI-110042 (INDIA)
DECEMBER, 2022

DELHI TECHNOLOGICAL UNIVERSITY
BAWANA ROAD
DELHI-110042 (INDIA)

DECLARATION OF ORIGINALITY

I hereby declare that the research work presented in this thesis titled **"Some Studies on Ultrasonic Joining of Thin Copper, Aluminium and Phosphor Bronze Sheets"** is an original and authentic work carried out by me under the supervision of **Dr. Reeta Wattal and Dr. D. S. Nagesh**, Professor, Department of Mechanical Engineering, Delhi Technological University, Delhi. This thesis has been prepared in conformity with the rules and regulations of the Delhi Technological University, Delhi. The research work reported and the results presented in the thesis have not been submitted either in part or full to any other university or institute for the award of any other degree or diploma. As per my understanding, this thesis is free from any plagiarized contents.

BHARAT SANGA
2K14/PhD/ME/03
Research Scholar
Department of Mechanical Engineering
Delhi Technological University

Date:

Place: Delhi

DELHI TECHNOLOGICAL UNIVERSITY
BAWANA ROAD
DELHI-110042 (INDIA)

SUPERVISOR'S CERTIFICATE

This is to certify that the Ph.D. thesis entitled *"**Some Studies on Ultrasonic Joining of Thin Copper, Aluminium and Phosphor Bronze Sheets**"* being submitted by Mr. Bharat Sanga, Roll No. 2K14/PhD/ME/03 for the award of the degree of Doctor of Philosophy in Mechanical Engineering, to Delhi Technological University, Delhi, India, is a bonafide record of the original research work carried out by him under our guidance and supervision. The work presented in this thesis has not been submitted to any other university or institution for the award of any degree or diploma.

Dr. REETA WATTAL
Professor
Department of Mechanical Engineering
Delhi Technological University

Dr. D. S. NAGESH
Professor
Department of Mechanical Engineering
Delhi Technological University

Dedicated

To

My Mother

ACKNOWLEDGEMENTS

First and the foremost, I express my deep sense of gratitude to my supervisors Prof. Reeta Wattal and Prof. D. S. Nagesh for their encouragement, inspiring guidance, personal attention, constructive criticism, and valuable suggestions throughout the course of this research work.

I would like to convey my sincere gratitude to Prof. S. K. Garg, H.O.D., Department of Mechanical Engineering, DTU, Delhi for his valuable suggestions and motivation during this research work.

I would also like to sincerely acknowledge my gratitude to all faculty members of the Department of Mechanical Engineering, DTU for their wholehearted cooperation in my research work.

My appreciation and deep sense of gratitude to Dr. Pulak Mohan Pandey, Director, Bundelkhand Institute of Technology, Jhansi, UP, Dr. Sachin Maheshwari, Prof., Department of MPAE, NSUT, Delhi, Dr. Manas Mohan Mahapatra, Professor, Department of Mechanical Engineering, IIT, Bhubaneswar, Odisha and Dr. Arshad Noor Siddiquee, Professor, Department of Mechanical Engineering, Jamia Millia Islamia, Delhi for giving their valuable suggestions for the betterment of this work.

I sincerely thank the technical staff of the welding laboratory at DTU Mr. Vinay and Mr. Ashok and Mr. Jai Prakash at G. B. Pant Engineering College, Okhla for all the help received during the experimentation. I would also like to thank technical staff of central workshop and other laboratories of DTU, Mr. Pradeep Kumar, Mr. Lakhan, Mr. Rahul Mool, Mr. Amit, Mr. Tek Chand, and Mr. Om Prakash.

I am also thankful to the non-teaching staff of the Department of Mechanical Engineering, Central Library, Administration Department, and Academic Department for their timely help and cooperation.

I would also like to thank my fellow researchers, Ms. Deepanjali Nimkar and Mr.Anmol Bhatia, Dr. Pushp Baghel and my friends Dr. Jaji Varghese and Mr. Rakesh Verma, Dr. Avnish and Mr. Urfi for boosting my enthusiasm and extending help whenever I required.

I would also like to thank to all those who have helped me directly or indirectly during this research work.

Above all, I am deeply thankful and blessed to have such a wonderful family for their appreciation, patience, and motivation during this research work. A special thanks to my wife and children, who always supported me through the thick and thin.

Furthermore, I would like to express my sincere gratitude to my mother whose blessings are always with me. Last but not the least; I thank the ALMIGHTY for giving me strength during the course of this research work.

Bharat Sanga

ABSTRACT

The quest to produce cost-effective, efficient, and ergonomically designed products demands the use of assemblies fabricated with assorted materials. Because of the differences in their physical, chemical, and metallurgical properties, joining dissimilar metals has been a difficult task for the researchers. Ultrasonic metal welding has overcome some of these limitations due to its unique characteristics. A number of diversified applications, ranging from small components used in the electronics industry to aerospace and solar, are being fabricated by Ultrasonic Spot Metal Welding (USMW). USMW uses vibrational energy to produce heat at the interface of the faying surfaces. The sheets are subjected to combined normal and shear loading with the help of sonotrode assembly. These combined loads disperse the oxides and contaminants as well as remove the surface asperities so as to form pure metallic bonds in cold conditions without filler metal, flux, or shielding gas. It's an efficient, green process that takes very little processing time. Since USMW is designed to join dissimilar metals/materials, this study used both similar and dissimilar combinations of phosphor bronze (UNS C51100), copper (UNS C10300), and aluminum (Al 3003).

It was observed through the available literature that there is a need for the optimization of the process parameters along with the characterization of the weld joint in the case of USMW. With these goals in mind, experiments were carried out in both 'Time Control Mode' and 'Energy Control Mode' using different experimental designs. The Analysis of Variance (ANOVA) is utilized on the response parameters-tensile shear load and the weld area. Weld pressure is observed as the most significant parameter, followed by weld time, and vibration amplitude, in affecting the weld strength. A reasonably good correlation is observed between the tensile shear load and the weld area between all the combinations of the weld metals. The process parameters are optimized by coupling the regression model as a fitness function with

the simulated annealing optimization algorithm. Finally, the confirmatory experimental results substantiated the predicted results and validated the proposed methodology.

The modeling and simulation of the USMW process is carried out using FEM. The model is utilized for the study and prediction of the thermal profiles at the weld interface. The heat fluxes generated due to deformation and friction are calculated and assigned as boundary conditions during thermal simulation. The forecast of temperature is done under various welding conditions. The maximum temperature obtained by transient simulation at the weld interface is 368.8℃, 369.4℃ and 296.1℃ for PB-PB, PB-Cu, and PB-Al, respectively. The continuous reduction in the temperature is observed towards the extremes of the weld metal. The sonotrode and the anvil achieve a lower temperature in comparison to the weld interface. The effect of clamping force and bonding ratio on the interface temperature is observed to be positive. The weld interface is distinguished as the weld zone, TMAZ and HAZ. The model is validated with the maximum absolute errors within 5% for PB-PB joints, 6.26% for PB-Cu joints, and 5.68% for PB-Al joints between the observed and predicted temperature results. A correlation coefficient of 0.96, 0.87, and 0.86 is established between the simulated temperature result and the weld strength for PB-PB, PB-Cu, and PB-Al, respectively. Thus, it is clear that the interface temperature has a strong linear relationship with joint strength and is a major deciding factor for achieving strong joints.

The effect of the weld energy on interface temperature and weld strength is also explored. It is observed that the values of peak interface temperature and tensile-shear strength increase with the welding energy. The failure mode changes from interfacial to nugget pull-out at a considerably high energy level during the tensile-shear load test. There is a significant rise in the tensile-shear load initially, but a negligible change is observed in the last stage. The scanning electron microscopy (SEM) revealed that the joining line appears almost straight at a low energy level but fades away at a higher energy level. The bonding region ultimately

acquires the shape of a wavy, convoluted interface. Micro-bonding accompanied by interlocking is observed as the primary joining mechanism at high energy level. Hence, it can be concluded that joint strength in USMW was the combined result of the formation of micro-bonds and mechanical interlocking due to the swirling of metal at the interface.

The observations and the results of the current study reflect that different combinations of PB, Cu, and Al give very good responses to the ultrasonic spot metal welding in the given ranges of the parameters. Hence, this joining technique can be effectively used for the fabrication of thin components made of these metals. This study can provide useful inputs for the industries involved in the manufacturing of battery electrical vehicles, solar panels, small electrical and electronic products like relays, contacts, and heat sinks etc.

Keywords: USMW, Phosphor Bronze, Box-Behnken, RSM, SAO, Interface Temperature, Micro-bonding, FEA, SimScale.

CONTENTS

LIST OF FIGURES

LIST OF TABLES

NOMENCLATURE

List of Symbols

A_d	Area of Deformation Zone
A_s	Area of Sonotrode Tip
F_c	Clamping Force
f_{max}	Maximum Shear Stress
f_s	Shear Stress
F_w	Weld Force
H_d	Heat Flux due to Deformation
H_f	Heat Flux due to Friction
V_{avg}	Average Sonotrode Velocity
Y_t	Temperature-dependent Yield Stress
α_0	Coefficients of Constant
α_i	Coefficients of Linear Term
α_{ii}	Coefficients of Quadratic Term
α_{ij}	Coefficients of Interaction Term
μ_k	Dynamic Coefficient of Friction
H	Total Heat Flux
P	Power Dissipated
R^2	Coefficient of Determination
T_i	Weld Interface Temperature
V_a	Vibration Amplitude
V_f	Frequency of Vibrations
W_a	Weld area
W_e	Weld Energy
W_p	Weld Pressure
W_t	Weld Time

W_{Se}	Experimental Weld Strength/Tensile-Shear Load
W_{Sp}	Predicted Weld Strength
β	Bonding Ratio
σ_1 and σ_2	Principal Stresses
σ_N	Normal Stress due to pressure

List of Abbreviations

ANN	Artificial Neural Network
BBD	Box-Behnken Design
BEV	Battery Electric Vehicles
CCD	Central Composite Design
DAQ	Data Acquisition Module
DOE	Design of Experiments
DoF	Degrees-of-Freedom
ECM	Energy Control Mode
EDS	Energy Dispersive Spectroscopy
FEA	Finite Element Analysis
FEM	Finite Element Method
GA	Genetic Algorithm
HAZ	Heat Affected Zone
IMC	Inter-metallic Compounds
MS	Mean Sum of Squares
OA	Orthogonal Array
OFAT	One Factor At a Time
PB-Al	Phosphor Bronze-Aluminium
PB-Cu	Phosphor Bronze-Copper
PB-PB	Phosphor Bronze-Phosphor Bronze
RSM	Response Surface Methodology
SAO	Simulated Annealing Optimization

SEM	Scanning Electron Microscope
SoS	Sum of Squares
TCM	Time Control Mode
TMAZ	Thermo-mechanical Affected Zone
UC	Ultrasonic Consolidation
USW	Ultrasonic Welding
USMW	Ultrasonic Spot Metal Welding
UTM	Universal Testing Machine

CHAPTER 1

INTRODUCTION

1.1 Introduction

Ultrasound and infrasound are the ranges of frequencies beyond the upper and lower audible frequency band, respectively, as shown in Figure 1.1 (Sprawls Perry, 1995). Therefore, these frequencies are not responsive to the normal human ears. The frequency range of ultrasound is from 15 kHz to 200 kHz, whereas for infrasound it is from 0.1 Hz to 20 Hz. (Duck & Leighton, 2018, Pye & Langbauer, 1998). We need special instruments to detect these sounds. Both ultrasound and infrasound have numerous applications, but ultrasonic frequencies are being used in diverse areas of engineering and medical science, as shown in Figure 1.2 by wheel of acoustics (Simplifying Acoustics, Acoustic Bulletin, 2017).

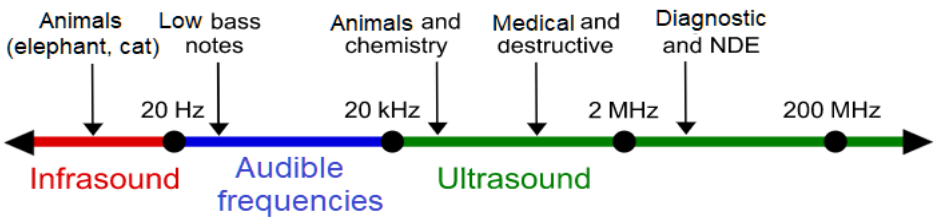

Figure 1.1: The range of sound waves frequencies (Sprawls Perry, 1995)

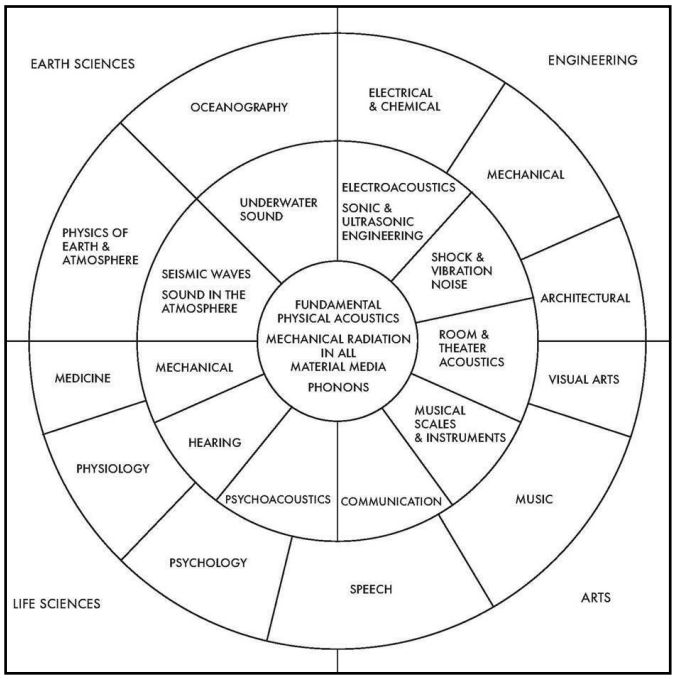

Figure 1.2: Wheel of acoustics (Simplifying Acoustics, Acoustic Bulletin, 2017)

A clear demarcation between low and high intensity ultrasound waves cannot be made, but the energy dissipated by the ultrasonic system divides its applications into two broad categories (Gallego & Graff, 2015; Harvey et al., 2014):

- Applications based on low-intensity, high-frequency vibrations
- Applications based on high-intensity, low-frequency vibrations

Low-intensity ultrasound uses an energy density of less than 1 W/cm^2 but the frequency range is more than 100 kHz. The main applications of low power ultrasound include non-destructive testing, ultrasonic processing of food, ultrasonic imaging and ultrasonic therapy in medical science; and ultrasonic mixing of cosmetics in a non-invasive manner. Despite the fact that high-intensity ultrasound applications have a high energy density, typically greater than 100 W/cm2 at low frequencies ranging from 20 to 100 kHz, they are capable of causing some changes in the material to which they are applied. The main applications are found in miscellaneous engineering fields where conventional manufacturing processes are assisted by high power ultrasonic vibrations, such as ultrasonic drilling (Debnath, 2014), ultrasonic-assisted milling (Kuo & Tsao, 2012), ultrasonic-assisted grinding (Li et al., 2018), ultrasonic peening (Malaki & Ding, 2015), ultrasonic-assisted powder metallurgy (Abedini et al., 2017), ultrasonic additive manufacturing (Bournias-Varotsis et al., 2018) and ultrasonic plastic and metal welding (Roopa Rani et al., 2015; Wu et al., 2015).

Ultrasonic Spot Metal Welding (USMW) was invented accidentally in Germany during World War II while attempting to use ultrasonic vibrations in the grain refinement of spot welding (Kumar et al., 2017). The first demonstration of ultrasonic welding (USW) was in the early 1950s and was limited to wire bonding, thin tube sealing, and thin foil joining (Matheny & Graff, 2014), but this technique has been continuously evolving since then and is being used for the joining of numerous metallic and non-metallic products. Presently, USMW has become an industrial technique that is used for joining two similar or dissimilar thin metal sheets or metal sheets to some non-metal substrate such as glass, ceramic, or polymers (AWS Handbook, 1997).

In USMW, a strong, defect-free joint is formed without melting the faying surfaces of the base materials by the local application of high-frequency ultrasonic vibration along with moderate external pressure (ASM Handbook, 1993). The capabilities of ultrasonic welding can be appreciated with the fact that a number of different difficult-to-weld dissimilar combinations of materials such as steel/aluminium, molybdenum/aluminium, brass/nickel,

metal/ceramic, metal/glass, and copper/aluminium can be welded using this technique (Hazlett T.H. et al., 1970). It is possible now to make joints among materials having different melting temperatures using USMW, giving more opportunities for novelty in design. USMW has been used to join a variety of metals and alloys, but the technique is best suited for making joints in softer metals such as aluminum, copper, silver, and gold (Soffar Hoba, 2016).

Due to its inherent features, USMW is one of the evolving techniques that have been gaining popularity in recent times. Furthermore, the newly developed materials demand more efficient production techniques. Conventional joining methods, such as spot welding and other fusion welding techniques are incapable of keeping up with the ever-changing and difficult design (Paul Kah, 2017). The issues related to the loss of critical mechanical, electrical, and microstructural properties encourage the use of newer techniques for joining dissimilar materials (Martinsen & Carlson, 2015). Recently, the quest to manufacture lightweight but stronger automobile vehicles is increasing incessantly. Simultaneously, alternative joining methods like USMW are being preferred owing to their reduced power requirements and absence of Heat Affected Zone (HAZ) unlike conventional methods such as resistance or laser welding (Chen, 2012).

1.2 Ultrasonic Spot Metal Welding (USMW) Equipments

Fundamentally, ultrasonic welding is used for fabricating two types of products: plastic and metallic products. Accordingly, the principles and designs of ultrasonic welding machines vary. In a plastic welding machine, the vibrational energy is transferred to the weld zone through longitudinal vibrations perpendicular to the joint. In this process, the mating parts' surfaces melt and subsequently join after cooling. While in the case of ultrasonic metal welding, the vibrations are produced laterally, parallel to the joint axis. No melting takes place and the joint is formed in cold conditions, i.e. solid-state bonding. The difference is shown diagrammatically in Figure 1.3.

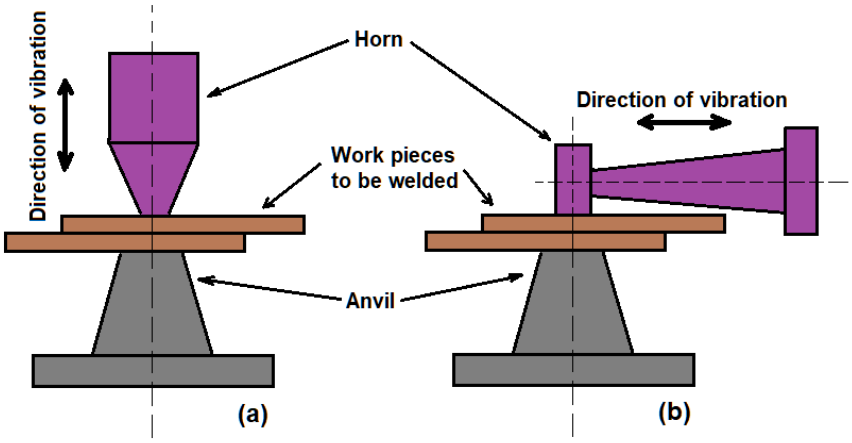

Figure 1.3: Schematic diagram showing the direction of vibration in (a) ultrasonic plastic welding (b) ultrasonic spot metal welding

Despite the difference in the basic working principle, both systems have six common basic parts (Gary F. Benedict, 1987). The schematic diagram of the USMW machine and sonotrode assembly is shown in Figures 1.4 (a) and (b), respectively.

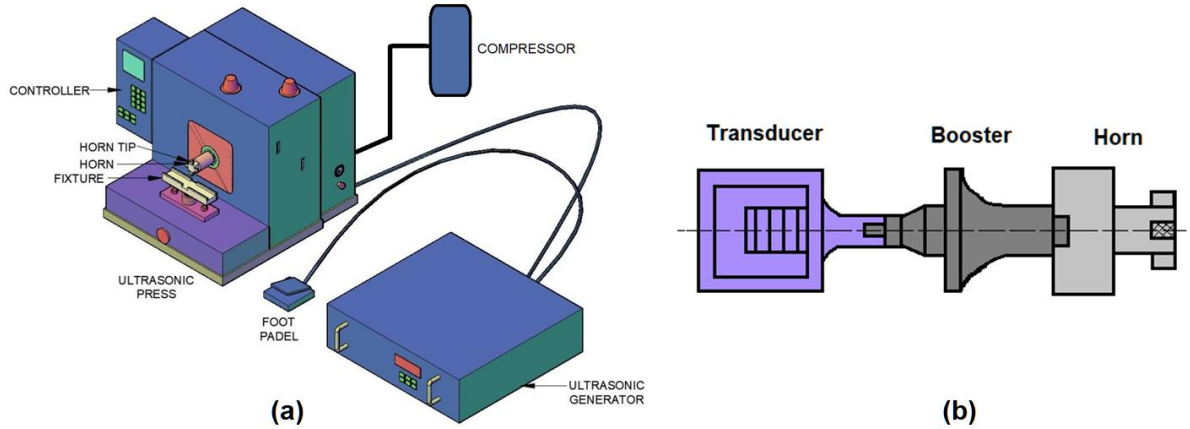

Figure 1.4: (a) Schematic diagram of ultrasonic metal welding machine set-up (b) Sonotrode assembly

- An *ultrasonic generator* changes the available low-frequency signals from the main supply to high-frequency electrical signals. The ultrasonic generators can generate frequencies in the range of 10 to 75 kHz. Generally, the lower frequencies are used for heavy-duty jobs such as welding of sheets and plates where power as high as 16 kW can be utilized, whereas higher frequencies are needed for low-power light-duty jobs like welding of wires, etc.
- A *transducer* converts high-frequency electricity into high-frequency sound waves (ultrasound). So, there is basically a conversion of electrical energy into mechanical energy. There are two types of transducers according to the application:

magnetostrictive and piezoelectric transducers. A magnetostrictive transducer has a stack of laminated nickel sheets. The electromagnetic effect is produced by wrapping the stack with a thick wire. There is a slight change in the length of the stack with every electrical pulse due to induced magnetism. On the other hand, the piezoelectric transducers are made from a piezoelectric material such as lead zirconate titanate. The piezoelectric materials respond to the electric current by changing their length (K. Graff, 1999).

- A *booster* enhances the output amplitude of the signals. The weak ultrasound signals produced by the transducer are amplified by the booster. The value of the 'gain' may be more than or less than one; accordingly, the booster increases or reduces the signals. The booster is placed between the transducer and the horn and serves as a major mounting location for the entire sonotrode assembly without affecting the 'gain'.
- A *horn* is used to focus the energy of the ultrasound vibrations on the weld metal**.** It is attached to the transducer through the booster with a threaded stud. The shape of the horn is important for getting more amplitude and less stress (Tao He et al., 2014). The end of the horn is provided with the projected tips having a knurling pattern on them. The weld materials come in direct contact with the tips; hence, the shape and size of the horn tips play a very important role in deciding the joint strength. It is the horn tip that exerts localized pressure and transports the ultrasonic energy at the weld area to deform the material underneath. The horn tip also acts as a tool and is consumed due to heavy wear and tear during usage. The replaceable horn tips are sometimes preferred due to the high cost of single unit ultrasonic horns, but they are seldom used in order to reduce the energy losses (Kim et al., 2019).
- An *anvil/fixture* holds the weld metal tightly between sonotrode and anvil with the help of air pressure supplied by a pneumatic system. Many times, the horn tip and anvil have similar serrations. The weld metal in contact with the anvil remains fixed while that in contact with the horn tip vibrates. Thus, a relative motion between both the weld metals starts, and frictional energy softens the metal.
- A *compressor* is used to produce air pressure. Weld pressure plays an important role in bond formation. The complete pneumatic circuit provides better control of the air pressure and can be varied in a wide range.

Ultrasonic metal welding has several versions, the most common being ultrasonic spot welding. Besides this, other popular versions, according to the applications, are ultrasonic

torsion, seam, ring, and line ultrasonic welding. The current study is focused on the study of ultrasonic spot welding due to the utilization of this joint in the electronic and automobile sectors. Two different types of configurations of ultrasonic welding equipment are used for making spot welds: lateral drive and wedge-reed machines.

1.2.1 Lateral Drive Ultrasonic Welding Machine

A lateral drive ultrasonic welding machine is shown in Figure 1.5 (a). In lateral drive ultrasonic welding equipment, the transducer, booster, and the horn are assembled together to build a rigid body. The alternating current mains supply available at 50-60 Hz is converted to a higher frequency electrical current by the ultrasonic generator. The transducer converts the electrical signals to ultrasonic vibrations, which are amplified by the booster and transferred to the surface of the workpieces through the horn. The increased amplitude is sufficient to produce the weld joints. The complete assembly of the transducer, booster, and horn is also called the 'stack'. The stack is mounted within the housing of the machine and a downward clamping force is exerted on it. As a result, the horn tip, also known as 'sonotrode tip' presses the upper part onto the lower part of the weld metal. The lower part rests on the anvil firmly due to surface knurling. The orientation of the stack is parallel to the direction of the ultrasonic vibration; therefore, it vibrates in the transverse direction. The horn tip at the end of the horn transfers the ultrasonic energy to the weldments through transverse vibrations (ASM Handbook, 1993).

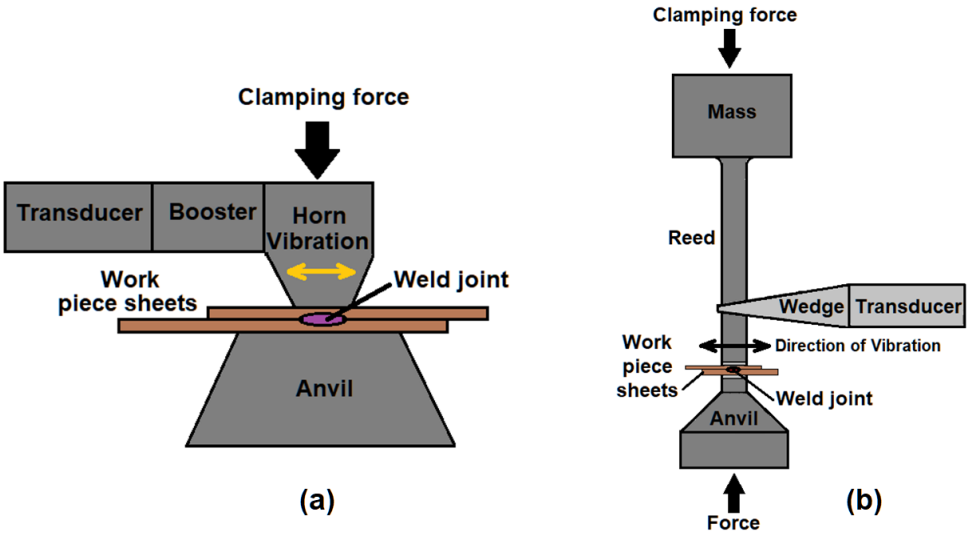

Figure 1.5: Ultrasonic welding machines (a) Lateral Drive type (b) Wedge Reed type

1.2.2 Wedge Reed Ultrasonic Welding Machine

The wedge-reed system also has all the essential parts for producing and transmitting ultrasonic vibrations to the workpiece. In this system, an ultrasonic transducer attached to a wedge-shaped booster drives the horn through a long rod known as a reed. The top of the reed has a mass attached to it which is axially compressed by the pneumatic pressure. The reed vibrates in the transverse plane at its end. The energy contained by the ultrasonic vibrations is transferred to the weld metal (Graff & Bloss, 2008).

The wedge is welded or brazed with the reed to reduce the losses. In some of the variations, the anvil is also made to vibrate to increase the relative motion in the lap surfaces. The wedge-reed system is capable of generating high energy values, so it can be used to join stronger alloy sheets. An illustrative diagram of the wedge-reed ultrasonic welding system is shown in Figure 1.5 (b).

The ultrasonic vibrations can be used to make joints in different applications using different versions of the basic USMW equipment. Some of the USMW versions are: ultrasonic wire bonding (P. Jeyaraj, 2018), ultrasonic seam welding (S. Elangovan et al., 2012), ultrasonic torsion welding (C. Born et al., 2003), and ultrasonic consolidation (H. Fujii et al., 2011).

Ultrasonic wire bonding is extensively used in the microelectronics and power electronics industries (K. Graff, 2005). The wire is placed on the substrate and pressed with the ultrasonic tool to make the connection. The process is very flexible and reliable. It can be easily automated for a number of applications with different wire lengths, heights, and directions. Similar to ultrasonic wire bonding is ultrasonic wire splicing, where a number of wires are joined together onto the substrate by applying pressure and ultrasonic vibrations. Like resistance seam welding, ultrasonic seam welding produces continuous joints without interruption in large metal sheets. The sonotrode is in the form of a disc and is supported by the bearings on both sides. Sometimes, the anvil is also shaped in the form of a roller. This version of ultrasonic welding is largely used in industries such as solar, textiles, and lather. Ultrasonic torsion welding, sometimes called ultrasonic ring welding, welds the metal sheets in the form of a circular ring. It has a pair of converter/booster combinations that produce torsional motion, as shown in Figure 1.6.

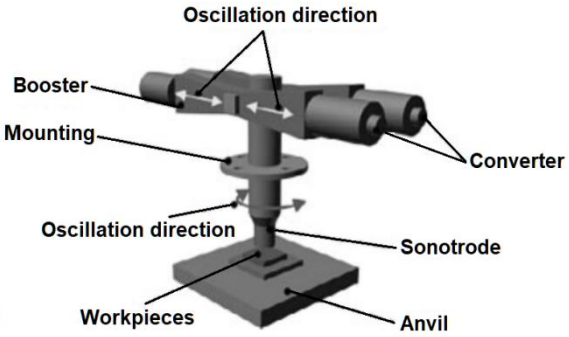

Figure 1.6: Ultrasonic torsion welding machine (Born C., 2003)

Lastly, ultrasonic consolidation (Janaki Ram et al., 2007) is the process of joining thin metallic foils layer by layer to make a thick part (Figure 1.7). The process can be easily mechanized to incorporate CNC machines so as to convert it to an additive or subtractive manufacturing system.

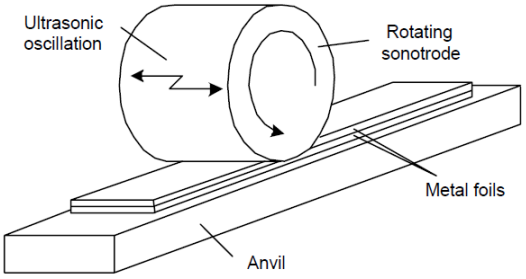

Figure 1.7: Schematic diagram of ultrasonic consolidation (Kong et al., 2003)

Ultrasonic welding has been in use for more than 60 years, but a lot of focus has been given to plastic welding. There are a number of unexplored areas in the case of USMW. Many metallic alloys are still to be investigated for their ultrasonic weldability. The acceptance of USMW as a common metal joining technique is possible only after a thorough understanding of its usability and the relationship of its parameters with the weld strength.

1.3 Principles of USMW

The USMW has been in use for many years with the same basic understanding, but its applications have grown in recent years with the development of new measurement techniques and softwares. The basic principles behind its joining mechanism are still being explored by joining new materials and their heterogeneous combinations.

During ultrasonic welding, the parts to be joined are pressed together. The sonotrode vibrates at an ultrasonic frequency in the range of 20 kHz to 40 kHz. The clamping force and the

vibrations of the sonotrode produce simultaneous normal and shear loading in the mating parts due to which the material under the sonotrode tip undergoes severe progressive shearing. Generally, the original material has layers of oxides and contaminants in the form of oil, grease, and rust. The surface condition of the metal also differs in terms of smoothness. The rough surfaces have a lot of peaks and valleys on them. These factors prohibit the metals from coming into intimate contact with each other, thus preventing the transfer of the atoms between them. The surface condition and the clamping force determine the level of contact between the metals.

The USMW works to remove these impediments. As soon as the sonotrode starts vibrating at ultrasonic frequency, keeping the top part pressed, the top part starts moving along with the vibrating sonotrode, whereas the bottom part remains fixed along with the stationary anvil. The first effect of the relative motion is to remove the surfacial oxide and other contaminants; secondly, the interfering surface asperities start to disappear. Simultaneously, the material undergoes plastic deformation and shearing. The relative motion between the mating parts results in excessive heat generation due to frictional forces, and the temperature at the interface rises instantaneously (Chang & Frisch, 1974). This is the time when nascent metal-to-metal contact starts occurring, which results in the formation of very tiny weld zones known as 'microwelds' at the interface. With the ongoing sonotrode pressure and vibrations, the area of the microwelds increases and spreads throughout the interface below the tip of the sonotrode (Shakil et al., 2014). Different stages during the joint formation in the USMW are shown in Figure 1.8.

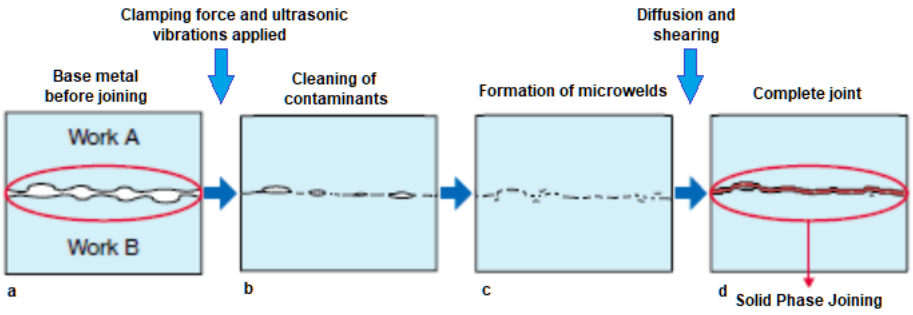

Figure 1.8: Different stages of joint formation during USMW

(http://www.avio.co.jp/english/products/assem/lineup/ultrasonic/welder/metal.html)

Various researches reveals that the maximum temperature reached at the weld interface is well below the melting temperature of the base metals. Hence, USMW is categorized to be a form of cold welding where the fusion of the base metals does not take place. But even then,

there is a significant rise in the temperature due to friction and plastic deformation of the weld metals in a very short span of time. As a result, the yield strength, which is affected by the temperature, is further reduced. The reduced yield strength accompanied by the normal and shear stresses promotes more deformation of the weld metal and the formation of more microwelds in a larger area.

The joining mechanism behind the USMW is quite complex. Researchers have been continuously working to explore it. The robustness and quality of the joint depend upon the machine parameters as well as material properties. The major parameters include weld time, weld pressure, vibration amplitude, and weld energy. The material hardness, surface smoothness, and thickness of joining parts are a few major material parameters. The control of parameters is very important to obtain a consistent weld quality. Improper control of machine parameters can result in weld defects and poor joints. Therefore, it is imperative to perform sufficient trial runs before finalizing the range of the parameters.

1.4 Parameters of USMW

A number of parameters affect the joint characteristics of USMW. The major parameters related to the machine are weld pressure or clamping force, vibration amplitude, frequency of vibrations, weld time or weld energy or power. Weld time, weld energy, and power represent the same parameter with different machine settings. Usually, USMW machines have the options of being operated in Time Control Mode (TCM) or Energy Control Mode (ECM). Other factors that affect the weld quality are specific to the weld specimen. The material hardness, the thickness of the workpiece, surface condition, as well as tool shape and size are some of the material parameters. Once the material-specific factors are fixed, there is a need to control the machine parameters. Therefore, understanding of the following major parameters is necessary:

1.4.1 Weld Pressure or Clamping Force

Weld pressure, or the clamping force, is produced by the pneumatic system attached to the USMW machines. The serrated sonotrode tip gets attached to the top sheet due to clamping force. At the same time, the faying surfaces of the mating parts to be joined come into close contact with each other due to the clamping force. It is critical to determine the correct clamping force because a lower value will prevent the top sheet from vibrating along with the sonotrode and a higher value will damage the overlapping surfaces and reduce relative motion between them, resulting in a lower value of friction generated heat. A few metals,

such as aluminium alloys, get stuck with the anvil and/or sonotrode tip at a higher value of the weld pressure (Li & Cao, 2019). The value of the clamping force depends upon the thickness of the workpieces and may vary from a very low value to a considerably higher value. Therefore, proper selection of the range of weld pressure is very necessary.

1.4.2 Weld Time, Weld Energy and Power

The weld time is determined according to the product properties. The thicker workpieces require more time to get the desired energy, whereas the thin workpieces need just a fraction of a second. Similarly, the hardness of the workpiece is also a deciding factor. Usually, weld-time ranges from 0.5 sec to 1.0 sec in most applications. Excessively higher weld time would result in poor weld quality with cracks and over burnt joint texture. A proper combination of power and weld time is essential to produce sound joints. High power with a small value of weld time would produce good joints, whereas, vice versa would result in poor joints **(**Brien, 2007).

The weld time, weld energy, and power are interconnected to each other. The energy to be dissipated to the weld is calculated by the controller of the machine according to the power rating and the weld time. So, if the welds are prepared in time control mode, then a certain amount of energy is dissipated to the weld until the time assigned for welding. On the other hand, if the machine is operated in energy control mode, then the specified amount of energy is transferred to the joint irrespective of the time duration. This way, either the weld time or the weld energy is specified while making a joint and their value is calculated accordingly at the run-time.

1.4.3 Vibration Amplitude

The vibration amplitude is a very important parameter that directly affects the ultrasonic power produced during the welding. The amplitude of the produced ultrasonic vibrations is magnified by the booster. Its value is determined according to the material characteristics, the design of the ultrasonic controller, and the power requirement. The thick and hard materials need a higher value of vibration amplitude to get the sufficient power needed for joint formation. The usual value of vibration amplitude ranges from 10 µm to 80 µm **(**Brien, 2007). In commercial ultrasonic welding machines, the vibration amplitude cannot be varied in a continuous manner. Rather, the machines have options for selection of three or four values of this parameter in terms of the percentage of the maximum amplitude at no-load

condition. The machine would use its full power to produce the joint if the amplitude was set to 100 percent.

1.4.4 Frequency of Vibrations

The ultrasonic frequency of the USMW machine depends upon the design of the ultrasonic transducer. The range of the ultrasonic frequency varies from 15 kHz to 300 kHz **(**Brien, 2007), but most of the high-power USMW machines are designed to operate at 20 kHz or 30 kHz. However, there is a slight deviation in the run-time frequency (± 2 to 3% deviation) for several reasons, such as the material used, ambient temperature, weld pressure, and welding load. Modern machines are equipped with advanced electronic circuitry to take care of this deviation. The current facility used for this research is designed to be operated at a vibration frequency of 20 kHz. Therefore, it is treated as a constant parameter.

1.5 Salient Features of USMW

Ultrasonic metal welding, being a solid-state joining method, has the following inherent features over other joining methods:

- The extremely fast processing time, including heating, joining, and cooling times, makes USMW a unique joining method. In most cases, the processing time is of the order of 1 second, making it possible for fast throughput and small changeover times (S. Kumar, 2017).
- One of the unique features of USMW is flexibility. A number of similar and dissimilar materials, including metal/non-metal combinations with varying thicknesses, can be welded. The process is especially suitable for joining very thin foils.
- Due to the involvement of minimal heat, while joining, the heat-affected zone is very small. Thus, material properties at the joint remain unaltered.
- The process does not require any spark, flame, flux, gas, or inert environment during welding, nor does it produce any gas, fumes, or smoke. This not only reduces the material costs but also helps in keeping the environment clean.
- A superior surface condition is not a prerequisite for USMW. Metallic surfaces with grease, dust, oxides and even coatings can be properly joined. However, clean surfaces give better joints.
- The whole process and the welding equipment are very safe as compared to other welding techniques. The heat produced is very small, localized, and targeted, making

the chances of damage to the equipment or the surroundings due to excessive heat to the minimal.

- The reliability of the process is of a high order due to the advanced electronic circuitry involved. After assembling and proper testing, the equipment can be automated with minimum human intervention to produce the parts incessantly. There is no need to hire skilled labour to operate the machine.

1.6 Limitations of USMW

Despite having several advantages over other welding methods, the USMW has many limitations due to which it is not profitable for many manufacturing industries. Some of the limitations are summarized below:

- It is limited to the lap joint with a flat surface only by the limitations of sheet thickness and hardness of the metal. It is found that aluminium sheets of up to 3 mm and other weldable metals of up to 1 mm can be joined successfully by USMW.
- The process cannot handle large sized components as the vibrational energy is not able to vibrate large sized components to produce sufficient heat.
- There is a tendency of sticking metals with the horn tip or the anvil (L. Rezenberg et al., 1973).
- The shape and structure of the components demand specific tooling, which increases the cost of the tooling.
- Very small particles are generated during the welding of terminals in PCBs, which increases the possibility of short-circuiting (David Guillon et al., 2018).
- The initial cost of the equipment in comparison to resistance spot welding and other welding equipment discourages potential buyers.
- The noise produced by ultrasonic vibrations poses a danger to the ears of the operators (Damongeot and Andre, 1988).

1.7 Applications of USMW

USMW finds its extensive applications in almost all the fields of engineering, including electrical, consumer electronics, and computer, automotive, aerospace, medical, packaging, and solar industries. Researchers have found that USMW can be efficiently used in both, water as well as in vacuum (Imai & Matsuoka, 2006). The USMW joints are not only found to be reasonably strong when compared to those made by other joining methods such as

resistance spot welding and GMAW, but they also consume less than 1/6th of the energy (Devine and Walsh).

The study of 'The Economics of Ultrasonics' revealed that USMW is cost-effective on all fronts, including energy, tooling, application, and other intangible costs (Austin Weber, 2003; Haddadi et al., 2012). However, when compared to other concurrent joining techniques such as riveting and crimping, soldering, laser, and resistance welding, the initial cost of the set-up is still higher, as shown in Table 1.1.

Table 1.1: Economic comparison of ultrasonic welding with other joining processes (Austin Weber, 2003)

Factor	Ultrasonic Welding	Resistance Welding	Crimping	Crimping and Soldering	Soldering
Investment Lifetime of tools	2	3	4	4	5
Required energy	3	2	3	3	3
Process time	4	1	5	2	3
Environmental Factors in production area	5	2	4	1	1
Flexibility of production *	5	3	2	2	5
Complexity of Welding parameters	4	2	3	3	5
Consumables	5	5	1	1	1
Quality assurance of the weld	5	3	2	2	1
Long term durability of the weld	5	3	2	4	3
Stability against vibration	4	3	2	3	3
Stability against bending **	5	1	5	5	5
Electric conductivity	5	4	3	3	3
5=Excellent; 1=Poor; * Time for tool change; required tools. ** Brittleness after heat built up.					

A brief summary of the numerous applications of USMW is given below:

i. **Applications in the fields of electrical, electronics, and computers:** USMW is capable of producing trustworthy, impervious joints in electrical switches, relays, and connectors where thin sheets of copper, phosphor bronze, and aluminium are joined. Fragile and delicate small micro-connections are suitably and conveniently made with

USMW as compared to other conventional joining methods. Junctions of wire harnesses, electric motor armatures, field coils, transformers, foil-wound capacitors, terminals of lithium-ion batteries, flash drives and computer disks, fuses and circuit breakers, ignition modules, starter motors, and photovoltaic panels are some of the examples where components are fabricated using USMW.

ii. **Applications in the fields of aerospace and automotive industries:** USMW is generally utilized in the aerospace industry when joining thin gauge sheets to other light-weight materials. Aluminum is a difficult–to-weld metal for conventional joining methods due to its high thermal conductivity. It is one of the easiest metals to weld with USMW because it is a softer metal and a solid-state weld is simple to achieve (Froes, 1994). Air ducts are typically welded with USMW. Even the entry door of the helicopter has been assembled using USMW. Many small electrical components, as well as large sized parts such as doors and panels, are also assembled using USMW in automobiles.

iii. **Applications in the fields of packaging and transportation:** The packaging industry is using USMW for the sealing of containers, tubes in thermal reactor, and HVAC, blister packs, and lighters. Dangerous materials such as explosives, fireworks, and other reactive chemicals require hermetic sealing but cannot be subjected to high temperatures. USMW, being a cold welding technique, is found to be very suitable for this purpose. Not only dangerous substances but also food items such as beverages, candy wrappers, and frozen foods are sealed using this technique.

iv. **Applications in the field of solar panels:** Excellent retention of post-weld thermal/electrical properties, improved quality, increased thermal efficiency, and reduced energy requirements are the major advantages with the USMW when used for the fabrication of solar panels. This technique has been well accepted as a cold welding technique for continuous welding of solar thermal components which keeps the basic property of the copper tube and the copper sheet unchanged. Without using any external solder or adhesive, the metallurgical bond between copper/aluminum sheets is achieved by ultrasonic technique. The resultant weld is continuous and there are no dry spots. Nowadays, thermal quilts and thermal blankets are also manufactured using USMW.

Some of the applications are shown in Figure 1.9.

Figure 1.9: Different applications of USMW
(https://www.sonobondultrasonics.com; https://brdason.en.alibaba.com/product)

1.8 The Need for Dissimilar Metal Joining

The need to join dissimilar metals and materials can be realized from the fact that an ordinary car is made of more than 10 different major materials, including steel, aluminium, copper, magnesium, plastics, and rubber (Fentahun et al., 2018). The need also calls for the evolution of new joining methods and their comparison (Martinsen et al., 2015). USMW is an emerging joining technique that can meet this challenge due to its inherent characteristics. In the present work, three different metals have been selected to explore their similar and dissimilar weldability. The materials have been selected according to their applications. Battery electric vehicles (BEV) are continuously evolving. The performance of BEV to a large extent depends upon its capability of producing and transmitting power. Their objectives can be met only by the successful joining of the dissimilar metals. Similarly, many electrical components need joints made of different conducting metals. The most demanding metals, being copper, aluminium, and phosphor bronze, have been selected for this research.

1.9 Organization of the Thesis

The presentation of the thesis is structured in the following sequence.

- **Chapter-1: Introduction** deals with the basic aspects of USMW, such as its background, principles, salient features, and applications. It also mentions the need for dissimilar metal joining.
- **Chapter-2: Literature Review** contains a literature review in respect of different aspects of USMW. The whole literature was broadly divided into four categories. Subsequently, the gaps in the existing research were identified. On the basis of the research gaps, the objectives of the present study were fixed.

- **Chapter-3: Methodology and Experimentation** describes the proposed methodology for the entire work. The details regarding the selection of material, parameters and their ranges, measurement of response parameters, experimental design, etc. have been included in this chapter. The chapter includes the details of the plan of investigation and the optimization technique used in this work. It also gives details of the modelling and simulation carried out for the weld joints. The experimental setup and other testing facilities that have been used during the measurement of response parameters were also discussed.
- **Chapter-4: Results and Discussion based on Response Surface Methodology** provides the results of the experiments conducted as per the Box-behnken design of RSM for all three combinations of materials. The adequacy of the regression model was checked and the influence of the parameters was found. The parameters were optimized using Simulated Annealing Optimization (SAO). The chapter also shows the results of the calculated weld area. Lastly, the experimental results were compared with the estimated results obtained from Response Surface Methodology (RSM) and SAO.
- **Chapter-5: Results and Discussion based on Thermal Modelling and Simulation** provide the results of the interfacial temperature measured experimentally and those obtained through simulation. The temperature prediction at different zones of the weld area was shown. The temperature and the size of the HAZ and Thermo-mechanical Affected Zone (TMAZ) were also estimated in this chapter. Lastly, the model was validated by comparing the experimentally measured interface temperature with the simulated results.
- **Chapter-6: Results and Discussion based on the Effect of Weld Energy** discussed the mechanical, thermal, and metallurgical effects of weld energy. Various findings of the relationship between weld energy and joint strength, as well as interface temperature, have been investigated. The chapter also gives details of the joint formation through SEM analysis.
- **Chapter-7: Conclusions** include the inferences obtained from the present study and also the future scope of this research.
- Appendices A1, and A2 include Coding for SAO algorithm and Calculation of Heat Flux respectively.

At the end of the thesis, the references used in the current work are listed.

CHAPTER 2

LITERATURE REVIEW

2.1 Introduction

Ultrasonic welding has been in use for many years to produce a number of products. Commonly used joining techniques such as resistance welding, micro-TIG welding, and laser welding pose electrical, thermal, metallurgical, and mechanical challenges to the joint characteristics (Abhishek Das et al., 2018). Incessant efforts are being made to evolve better techniques for thin sheet joining. Conventional joining methods are modified to suit the needs of heterogeneous tiny joints. Resistance micro-welding, laser droplet joining, duo-thermal soldering process, and precision miniaturized droplet deposition technique are some of the newly evolved techniques (B. Mo et al., 2011; M. Weigl, 2009; P. P. Conway et al., 2006; S. Consiglio, 2006). These techniques still need standardization due to diverse material characteristics. Therefore, the use of USMW as a metal joining process has been developed in the last few years, and now this technique is being used for a variety of applications in medical, automobile, aviation, microelectronics, and many other areas. It has become very convenient now to join thin sheets of copper and aluminium using USMW owing to its inherent advantages over some other joining techniques that have brought this technique to the shop floor. It is a friction oriented joining method that utilizes acoustic energy to plastically deform the metal and bring the nascent metal surfaces in close contact so as to form a strong metallic bond (Jhang et al., 2014). Although it may appeare fairly simple from the outside, the actual mechanism of joint formation in USW is quite complex (Dehoff and Babu, 2010). In fact, an accurate and well established theory related to the joint mechanism of USMW has yet to be developed.

2.2 Studies on Ultrasonic Spot Metal Welding

The studies conducted by different researchers relevant to the present work can be categorized and summarized as under:

- Characterization of the weld joint
- Effect of process parameters and their optimization
- Modelling and simulation of USMW

2.2.1 Characterization of the Weld Joint

Microstructural analysis has been an area of interest for researchers right from the early days of the invention in the field of USW. The bonding mechanism in USW has been the core interest for many researchers, but still, no common consensus on this issue has been reached. Different theories such as inter-atomic diffusion, recrystallization and recovery, melting at the interface, mechanical mixing/interlocking at the interface, and micro-welding have been proposed by the researchers. Okada et al. (1962), Daniels (1965), and Hazlett et al. (1970) conducted fundamental studies on the joining of similar and dissimilar combinations of pure metals such as Al, Cu, Zn, Ti, Be, Ag, and Ni, as well as alloys such as Brass and SS. The sheet thickness had been in the range of 0.06-0.5 mm. A common observation made by all the above researchers was that the temperature of the interface has reached above the recrystallization temperature and a recrystallization texture was also observed, but no Inter-Metallic Compound (IMC) or other phases were found to be present at the interface. However, no common observation was found regarding inter-atomic diffusion. Inter-atomic diffusion was observed between Cu and Ti by Okada (1962), but the technique used was X-ray micro-analysis. Later, Daniels (1965) confirmed that no melting or diffusion was observed in Cu to Ni welding. Hazlett's (1970) observations based on Scanning Electron Microscope (SEM) images supported the observations of Daniels (1965) to some extent. He concluded that "diffusion", which was supposed to be the main joining mechanism at the interface, was due to grain boundary rather than bulk diffusion. Mechanical mixing at the interface and the accompanying metal bonding at the nascent interface were found to be the main causes of joint formation.

H. Kreye (1977) investigated the joining phenomenon of Cu and Al alloy sheets joined by different solid state welding techniques, viz. ultrasonic welding, explosion, and friction welding. His findings differ from the results of Daniels (1965). It was observed that microstructural changes have occurred during ultrasonic welding, resulting in the formation of new grains along the interface, as shown in Figure 2.1. The bonding occurred predominantly by the melting of a very thin and narrow surface layer (thickness < 1 μm) for a very short time during ultrasonic welding. The small grain size of the particles and the cobalt particles taking more time in dissolution supported this theory. No IMC was observed due to rapid heat transfer from the bonding area to the surrounding atmosphere. The melting phenomenon was also observed by Bakavos and Pragnell (2010) and Chen et al. (2012).

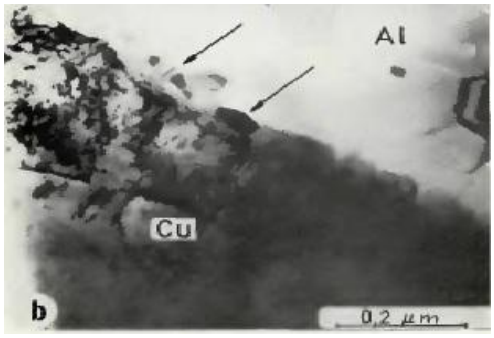

Figure 2.1: TEM micrograph of ultrasonically welded Cu /Al interface. Arrows show formation of new grains (H. Kreye, 1977)

Al-Sarraf et al. (2012) performed USW with different combinations of 0.1 mm and 0.5 mm sheets of Al and Cu and found that there was diffusion of Al on the Cu side. SEM images revealed that more Al was deposited on the Cu side as compared to less deposition of Cu on the Al side due to Cu being the softer metal of the two. But definitely, there was an interaction at the atomic level between the atoms of interacting surfaces during ultrasonic welding. This fact was proved by Watanabe et al. (2003). They used Auger Electron Spectroscopy (AES) to analyze the interface of ultrasonically joined 0.5 mm thick Al sheet with Alumina (Al_2O_3) and observed the formation of a chemical bond between the atoms of Al and oxygen of Al_2O_3.

Bakavos and Pragnell (2010) and Chen et al. (2012) studied the interfacial microstructural development in ultrasonic spot welding of 0.93 mm thick AA6111-T4 automotive sheet and contradicted the general concept that no Heat Affected Zone (HAZ) is present in the USW owing to the low-energy input. They have described the term 'Thermo-mechanically Affected Zone' (TMAZ) for the area covered between the sonotrode tip and anvil and 'HAZ' for the area outside the anvil. The same concept was also given by Shakil et al. (2014). TMAZ is shown in Figure 2.2. Another finding from this study was that natural aging in AA6111 alloy continued even after ultrasonic welding, as it would be in normal condition for conventional solution-treated sheets. This phenomenon was termed "Accelerated Natural Aging." This concept is also supported by Haddadi (2015).

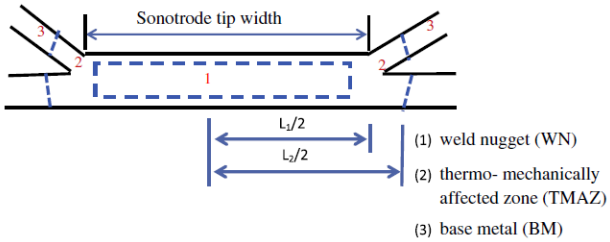

Figure 2.2: Weld zone classification (Shakil et al., 2014)

Recovery and recrystallization were also observed by Magin et al. (2014) during the ultrasonic torsion welding of aluminum and titanium sheets. It was confirmed that melting did not take place and the joint was formed well below the melting point in a solid state without the formation of any IMCs.

The works of Zhang et al. (2014, 2016) explored dissimilar ultrasonic welding with different thicknesses of Al and Ti alloys (AA6111/$TiAl_6V_4$ and AA2139/$TiAl_6V_4$). Almost similar results were obtained. No visible IMC layer was detected. It was observed that Al grains near the weld interface had been distinctly refined by the ultrasonic spot welding process, but there was no difference in the grains of $TiAl_6V_4$. Grain refinement was also observed by Prangnell et al. (2011) during USW of 1.0 mm thick Al 6111 sheet with automotive DC04 steel sheet. In a similar study on AA6061 and $TiAl_6V_4$, Zhu et al. (2012) discovered that diffusion occurred across the interface and that the thickness of the diffusion layer increased with increasing welding time. Frank Balle et al. (2015) also ultrasonically welded, 1.0 mm thick Al alloy AA7075 with $TiAl_6V_4$ and observed the initiation of micro-welds that spread along the joint interface, leading to the formation of solid state joints.

Contrary to the findings of Zhang et al. (2014, 2016), the presence of IMC was observed by Wang et al. (2015), during the ultrasonic joining of AA 5754 and $TiAl_6V_4$ alloy. They have made joints with and without putting aluminium interlayer. The weld coupons with the interlayer have shown more strength. Ultrasonic weldability of AA6111-T4 with bare and zinc coated steel of approximately 1 mm thickness was investigated by Haddadi and Abu-Farha (2015). Their investigation in reference to IMCs, also supported the findings of Wang et al. (2015). The growth of the Al-Fe intermetallic layer was seen spreading discontinuously along the interface. The presence of IMC was verified by the Energy Dispersive Spectroscopy (EDS) analysis. The formation of the Inter-metallic Compounds (IMC) was co-related to the fracture of the joint in the lap-shear test. The failure occurred due to cracking through the interface of the reaction layer and the steel sheet, where the brittle FeAl phase was formed, at sufficiently long weld times. Similar to Wang et al. (2015), Bakavos and Pragnell (2010), Shakil et al. (2014), and Chen et al. (2012) observed a significant HAZ/TMAZ.

The quality characteristics of dissimilar ultrasonic weld joint (Al/Cu) was defined by Shin-ichi Matsuoka and H. Imai (2009). The weld interface had no defects such as cracks or exfoliation. The presence of oxides or organic films was observed in incomplete welding

regions, but the interface of a good weld was free from such defects. The joint strength usually decreases due to the presence of IMCs around the weld interface. However, in the ultrasonic joint made between AA1050 and Cu by Fujii et al. (2014), the thickness of the reaction layer of the Al_2Cu IMC phase was found to be in the range of 40-100 nm, and it helped in increasing the joint strength, unlike normal IMC. He strongly advocated the recrystallization of grains at the interface. Recrystallization was attributed to the creation of large dislocation densities due to the deformation of the grains. Similar observations were made by the Fujii et al. (2016) again during USW of AA6061 and 304 SS steel sheets. The formation of Fe-Al IMC was attributed to pipe diffusion of Fe in Al around the interface due to excessive dislocation density at the interface owing to severe shear deformation during USW. The effects of excessive dislocation density were explained in detail by Gunduz et al. (2005).

Inclusion of an interlayer between the weld metals improves the strength of the ultrasonic joint, as proved by Balasundaram et al. (2014). They conducted welding experiments on Al and Cu alloys, with and without Zn inter-layer. When sheets were joined without an interlayer, SEM micrographs revealed a swirling interface with no IMCs present. However, when sheets were joined with a Zn interlayer, a flat and tight interface was obtained along with a discontinuous IMC layer of Al_2Cu, mostly on the Cu side due to the higher solubility of Al in Cu. Joint formation was attributed to micro-welds during the USW of AA 6061 and pure Cu reported by Zhao et al. (2013) at low energy input, but at higher energy input, deformation along with mechanical interlocking due to the formation of a swirl like pattern along the interface was found to be the main cause of joint formation. The Scanning Electron Microscope (SEM) micrographs revealed a swirling interface with the void when sheets were joined without interlayer. However, a flat and tight interface was obtained with Zn inter-layer. In a similar study by Zenglei et al. (2016), they joined Cu and Al sheets with an Al 2219 particle interlayer in between. The weld energy was varied within a range from 600 J to 1500 J. The lap shear tensile strength of the joint has increased continuously as weld energy increased, but hardness decreased on Al side. The Al particle interlayer had a significant effect on the mechanical properties.

Magnesium alloys are in high demand in aerospace and transportation sectors due to their light weight and high strength to weight ratio. Ultrasonic weldability of Mg alloys with other metals such as aluminium, HSLA etc. has been reported by some researchers (Panteli et al., 2012 and Patel et al. 2011, 2012, 2013). Thick layers of IMCs were clearly observed. The

thickness of the IMCs increased with increasing welding energy. The rapid growth rate of IMC layers was attributed to the enhanced dynamic diffusion. The enhanced dynamic diffusion was attributed to the diffusion-induced vacancies, a phenomena also observed by I. Gunduz et al. (2005) and supported by Fujii et al. (2014). Complete recrystallization of the microstructure and the grain size enlargement were observed with respect to the increased energy level. Melting at the interface between the IMC phase and the Mg alloy base at higher energy levels was also observed at some places. So it was suggested that the joint at the steel side was formed by a solid solution of Zn and Fe but strength decreased due to the formation of IMC at the interface when welded at high welding time without using insert material. Use of insert material improved the joint strength significantly since no IMCs were formed even at a higher welding time. Similar investigations were conducted on the interface microstructure of Mg alloy/Cu and mild steel/Al-Mg alloy combinations by Macwan and Chen (2015) and Watanabe et al. (2009), respectively. In both these cases, the joint strength has increased when the joint was made using insert material. However, the joint strength has decreased due to the formation of IMCs without using insert material.

A comprehensive study of the mechanisms and mechanics of USMW of aluminium sheet was done by De Vries (2004). It was established by him through experimentation that the temperature at the interface reaches up to 40-80% of the melting point of the base metal. That is why USMW is considered a solid-state welding technique. M. P. Satpathy et al. (2015) explored the welding interface during the USW of 0.3 mm thick sheets of Al alloy AA1100 and UNS C27000 Brass and categorized the joint as “under”, “good” and “over” on the basis of the condition of the interface. A good weld had a high density of micro-bonds and was free from gaps between sheets. Inter-atomic diffusion was observed as the main reason for joint formation.

2.2.2 Effects of Process Parameters and Their Optimization

The maximum utilization of a manufacturing process is possible only if the effects of all the process parameters are known and the process is optimized. This can be achieved only with an appropriate experimental design. Different USMW process parameters such as weld time, weld pressure, vibration amplitude, vibration frequency, welding energy, pre and post-burst time, surface condition, material hardness, etc. have been controlled by researchers to get defect free joints with maximum strength (Annoni and Carboni, 2011). A comparison of ultrasonic welding to other solid state joining methods reveals that deformation of metals and

energy consumption are lower in the case of USMW due to its very short welding time and lower peak interface temperature (370°C) (Magin and Balle, 2014; Vural, 2014). The research shows that USMW is far more efficient than other comparable joining processes such as friction stir welding, and resistance welding, as far as energy consumed and processing time is concerned (Bakavos and Pragnell, 2010). However, USMW is a cold welding technique, but it gives sufficiently good strength to the weld joints. In a study conducted by Kong et al. (2005), the thin foils of Al 6061 were joined by Ultrasonic Consolidation (UC) and the strength was found to be 7% greater than that of base metal. In another study conducted earlier by Kong et al. (2004), ultrasonic consolidation was performed on 100 μm thick Al 3003 foils. The authors tried to build a process window for the process parameters. The peel strength of the joints has increased across a wide range of parameters. The increased joint strength was attributed to the increased linear weld density. Different experimental designs have been used to perform the experimentation with USMW with the aim of finding out the effect of process parameters on the response parameters and optimizing the process parameters to get the maximum joint strength. Abhishek Das et al. (2018) used a 4-level full factorial design to join 1 mm Cu sheet with 0.3 mm multi-layer Al sheets. Such joints are used in the tabs of lithium-ion batteries. The effects of three process parameters, weld pressure, vibration amplitude and weld time, were investigated on the strength of the joint by testing tensile-shear and T-peel strengths. A third-order regression equation was developed to optimize the parameters, and a robust range was obtained using the Pareto front.

USMW is intrinsically suitable for joining dissimilar materials. A number of diversified material combinations have been successfully joined by USMW using different designs of experiments. Taguchi's method has been very conveniently and efficiently used by researchers. Typically, aluminum and copper based alloys are extensively chosen for manufacturing parts of Battery Electric Vehicles (BEV) such as electrical contacts, terminals, current collectors, and bus bars owing to their excellent strength and spectacular electrical and thermal properties (Yang and Cao, 2015). Ultrasonic joints in bi-metal (Cu-Al) using USMW were produced by Urfi et al. (2017). The experimentation was performed using Taguchi's L_9 Orthogonal Array (OA). Optimal parameter settings were obtained after finding the significant parameters. Weld pressure was observed as the most significant parameter, followed by weld amplitude and welding time. Similar work executed by Satpathy et al. (2014) included the optimization of the process parameters during the ultrasonic joining

of aluminium with brass using Taguchi's L_{16} OA. The S/N ratio has been improved using optimized parameter setting. Elangovan et al. (2011) used Taguchi's L_9 design to make a dissimilar Al-Al_2O_3 ultrasonic joint. The optimal range of the parameters has been found by using the S/N ratio to maximize the weld strength. The experimental weld strength was validated by the estimated strength. An ultrasonic joint between copper and nickel was made by Seo et al. (2015). Weld pressure and vibration amplitude have influenced the weld strength significantly. A maximum weld strength of 87.45 N was achieved at 0.25 sec weld time, 0.20 MPa weld pressure, and at 80% vibration amplitude.

The applications of USMW in the automobile sector are continuously increasing. USMW is amazingly suitable for joining aluminium sheets, which otherwise is a difficult-to-weld metal. The joint at the interface is formed under the influence of the weld energy. The weld energy, which is a product of the weld time and the power of the ultrasonic welding machine, can be regulated by controlling the weld time precisely. Ultrasonic welding can be performed on sheets of different thicknesses. However, the thickness of the upper sheet has a greater impact on weld joint quality than the thickness of the lower sheet because the upper sheet experiences more severe deformation during the process (Park et al., 2013). Zhang et al. (2014) explored the weldability of 2 mm thick Al 5754 automotive sheets by varying the weld energy in the range of 2250 J to 5800 J. It was accomplished by varying the weld time while holding the clamping force and vibration amplitude constant. The joint quality was determined by the tensile-shear load. It was established that the joint strength increased by increasing interface temperature and the failure mode changed from debonding at the interface to a partial nugget pull-out mode. The weld joints have shown significantly high strength at the interface temperature as high as 500 ℃, but the maximum temperature reached at the joint interface has never been in the melting range of the base metal. This fact has been established by many researchers (Yang et al., 2017; Elangovan et al., 2009). In a similar study, aluminium sheets used in automobiles were joined using USMW (Annoni and Carboni, 2011). ANOVA was employed to study the influence of the weld parameters and their interaction. It was observed that the amplitude had been the largest influencing parameter. However, the weld time and the pressure also affected the weld strength positively. All the interactions had a significant influence on the response parameter. The mechanical and metallurgical properties of ultrasonically joined Cu wires were investigated by Mohan Raj et al. (2016). RSM has been used to optimize the three process parameters, viz. weld pressure, weld time, and weld amplitude. The experimental weld strength has been

validated by FEM modelling. The joint characterization was done for the ultrasonically welded aluminium stranded wire on the copper terminals with different Ni platings by J. P. Bergmann (2017). Such a joint has applications in vehicle technology that is recently developing. The tensile-shear strength of the plated joint was compared with the plain Al/Cu joint, and it was found that the plated joints have more strength and less presence of IMCs. In a study conducted by Rezenberg et al. (1973), it was observed that the weld pressure or the clamping force is the most critical parameter as its lower value results in weaker joints, whereas the higher value leads to sticking of the weld metal with the sonotrode/anvil or the weld joints burning due to excessively high temperature rise. Research in the field of enhancing ultrasonic power to increase the thickness of the weld metals is in line. Different approaches have been used by researchers to obtain more power out of an existing system (Baboi and Grewell (2010). They have tried to use stepped amplitude during ultrasonic welding and compared the results with the normal amplitude value (fixed value). It was found that thicker sheets could be welded using stepped amplitude and there was an increase in the weld strength value.

The optimization of the parameters had been the prime concern for the researchers as they continuously looked for proper utilization of ultrasonic welding in manufacturing industrial products. Process optimization requires a continuous improvement towards goal oriented results using metaheuristic techniques. RSM coupled with some optimization technique has been employed by scientists to model the curved quadratic response surface due to continuous parametric variation. Elangovan et al. (2012) produced ultrasonic joints between 0.3 mm and 0.4 mm thick aluminum sheets. The Central Composite Design (CCD) was used to conduct the experiments with the aim of evaluating the significance of the process parameters. A second-order regression model was developed using RSM. Further, the welding parameters were optimized by coupling the regression model with a Genetic Algorithm (GA). The study gave excellent results. In a similar study, Anand et al. (2017) used CCD to evaluate the effects of pressure, inserting time, and holding time on the pull-out strength of the insert fitted with the ABS component using ultrasonic welding. A regression model developed using RSM was coupled with GA to optimize the process parameters. The pull-out strength increased with increasing pressure and holding time but decreased after a certain value of inserting time. The parametric study performed by Shin and Leon (2015) on A5052-H32 aluminium alloy revealed that the lower value of weld time and higher value of weld amplitude together produce sufficient temperature to make a sound joint. Shakil et al.

(2014) investigated the ultrasonically joined aluminium alloy AA 3003 and SS 304 steel. The joint area of the welded samples was classified into three distinguished zones, viz. weld nugget, TMAZ, and base metal. Bond formation was attributed to micro-bonding growth along the weld interface.

The effect of process parameters and their optimization has been done by many researchers, but very few have varied all the parameters simultaneously. Artificial Neural Network (ANN) has been demonstrated to be an effective tool to optimize the process parameters. Anand et al. (2018) have successfully optimized weld pressure, weld time and amplitude of vibration to get maximum weld strength in ultrasonic welding between copper sheets using ANN and multiple regression analysis. The results obtained from both the tools were compared and it was found that ANN was able to predict more precisely as compared to the regression model. Zhao et al. (2017) investigated the influence of vibration time, vibration amplitude, and clamping force on the ultrasonic joint between 1 mm Al 6061 and 1.5 mm A36 steel alloy using a full factorial design of experiment. Vibration time was observed as the significant parameter. Vibration amplitude and clamping force did not affect the joint strength significantly. However, all the parameters were found to affect significantly in combinations with each other. Optimization of parameters was done using an artificial neural network coupled with a genetic algorithm. It is imperative that strong ultrasonic joints can be achieved by the selection of appropriate values of the process parameters.

2.2.3 Modeling and Simulation of USMW

Modelling of the thermal field plays an important role in the prediction of the temperature profile at the weld interface. The response characteristics of the USW process can be forecast by simulating the model of the process, and the corresponding data can be optimally utilized by the industry. The stress analysis through modeling at the failed joint gives an insight into the molecular activities occurring at the joint. Carboni and Annoni (2011) prepared single and double spot joints in AA 6022 aluminium alloy using USMW. The fatigue behaviour of the joints based on experimental results was corroborated by the findings of finite element analysis. It was observed that the higher value of the stress intensity factor in the case of single spot joints in comparison to the double spot joint resulted in more run-outs and shorter life. The work carried out by Satpathy et al. (2018) includes the joining of dissimilar AA1100 and UNS10100. The work involved parametric optimization, microstructural evaluation, and numerical modelling. The thermo-mechanical analysis of the interface was done to predict

the TMAZ and HAZ. Heat fluxes due to plastic deformation and friction were precisely calculated and used as the boundary conditions during simulation. The thermal model helped in the estimation of the peak temperature at different zones of the welding site.

FEM-based models are simulated for estimating the mechanical and thermal impacts of operating conditions of ultrasonically welded joints. Zhong et al. (2019) performed experimental studies and created a model of the ultrasonic consolidation process of dissimilar Ti and Al alloys. It was observed through simulation that the highest temperature was obtained at the common surfaces of foil-sonotrode and foil-substrate. They also observed that the oscillator amplitude had more effect on the interfacial temperature than the consolidation pressure. Besides metals, modeling of thermo-plastics was performed using ANSYS software and the results were authenticated with the experimentally obtained data (Suresh et al., 2007). Zhang and Li (2009) during USW of Al foils simulated the coupled thermo-mechanical fields using a 3-D Finite Element Analysis (FEA) model to study the effects of heat generation and plastic deformation at the interface and concluded that it is only the severe, localized plastic deformation that is responsible for the bond formation.

A detailed study conducted by DeVries (2004) on different similar and dissimilar metal ultrasonic joints investigated the effect of significant process parameters, microstructural transformation, and evaluation of HAZ in the weld zone. Simulation of a 3-D thermo-mechanical CAD model was the primary objective of his work. The heat developed at the weld interface was estimated and the model was utilized to predict the interfacial temperature. Similar work was reported by Elangovan et al. (2009). The finite element based model was presented to simulate the actual working conditions of the ultrasonic welding to predict the temperature distribution at the weld interface as well as the stress distribution in the sonotrode and the joint. The simulated results were found to be in good agreement with those obtained experimentally. A 3-dimensional thermo-mechanical model of USMW was built by Chen and Zhang (2014) during the welding between Al and Cu. The aim of the study was to investigate the effect of acoustic softening on weld joints and heat generation. Acoustic softening was found to have a significant effect on joint formation, bringing metallic surfaces closer together, but had little effect on heat generation. Effects of ultrasonic vibrations on metals, particularly acoustic softening, were observed by Bertwin Langenecker (1966). He suggested that ultrasonic vibrations have a significant effect on the deformation of the weld material along with the heating effect due to friction. Plastic deformation has been

found to be a major factor in heat generation. Chen and Zhang (2015) constructed and simulated the 3-D model of USW of dissimilar automotive alloy and found that the temperature distribution was not uniform at the knurled surface of the sonotrode tip. The amount of heat produced due to plastic deformation was almost one-fourth of the total heat produced at the interface, and the highest temperature was located at the weld interface. Similar work conducted by Kim et al. (2011) included thermo-mechanical analysis of the FE model of ultrasonically welded AA5754 specimens. Experimentally obtained values of temperature and ultrasonic velocities were validated by simulated results. It has been proved that the heat generated due to friction and plastic deformation is the major cause of joint formation. Aluminum alloy AA 6011 was joined separately by magnesium alloy AZ31 and low carbon steel DC04 using USMW by Jedrasiak et al. (2014). The heat input during welding was evaluated using thermocouple data and some other evidence. The thermal histories were utilized to predict the thickness of the intermetallic compound. A 3-D finite element model of the thermal field was applied for temperature prediction at the weld interface. The same authors used finite element analysis to simulate heat generation in USW (Jedrasiak et al., 2018). A deformation model of a single cycle of oscillation was employed for calculating the heat generation rate sporadically. A continuous thermal model was capable of predicting the temperature field. Wire bonding has been a widely used application of USMW in microelectronics (Harman and Albers, 1977). Ding and Kim (2018) used 3-D FEM to model and simulate the bonding of Au wire with the bond pad made of Au, Ni, and Cu layers. The modelling was done with the aim of estimating the interface temperature and to evaluating the effect of bonding parameters on the temperature rise. It was observed that the bulk temperature did not exceed the melting temperature; hence, the solid state joining was established. A critical bond pad size was estimated so as to obtain the minimum bulk temperature rise.

2.3 Optimization using Simulated Annealing Optimization Algorithm

The response parameters achieve their best results at the optimized values of the process parameters. RSM provides promising results where multi-response optimization is required. But in the case of a 3-parameter design, it gives an optimal range of the process parameters where two parameters are varied at a time, while keeping the third parameter constant. So, different optimal ranges are obtained. Therefore, some metaheuristic optimization method is needed to achieve an optimal solution. RSM, coupled with some optimization techniques, is

employed by scientists to model the curved quadratic response surface to continuous parameters. Optimization of gas metal arc welding parameters was done using Box-Behnken Design (BBD) of RSM considering the desirability factor of the parameters by Srivastava and Garg (2017). The mathematical model was developed with the aim of maximizing the penetration and minimizing the width and height of the bead. The optimized results were validated with less than 2% error. Gupta et al. (2015) optimized the cutting parameters using the desirability factor of RSM and a Particle Swarm Optimization (PSO) technique. The estimated results obtained from both methods were compared with experimental results and were found to be in good agreement. The Taguchi L_9 orthogonal array design with gray relational analysis was employed by Sabdin et al. (2019) to optimize the process parameters in ColdArc welding of high strength steel plate. In a similar manner, a Gray Taguchi based approach was combined with RSM (GT-RSM) to optimize the plasma arc cutting process parameters by Adalarasam et al. (2015). The results had improved significantly using this approach.

Different optimization algorithms have been used by researchers. Simulated Annealing Optimization (SAO) is one of the popular optimization algorithms that gives promising results. Torabi and Kolahan (2018) implemented a central composite design combined with SAO to optimize the input parameters in pulsed laser welding of AISI 316L stainless steel thin sheets. The results obtained by both RSM and SAO were compared and found to be quite similar to each other. Moghaddam et al. (2019) used SAO to optimize the MIG welding input parameters such as current, frequency, welding speed, and gap. The experiment was conducted on a power plant pipe line. The estimated ultimate tensile strength was obtained with almost 2% error. The numerical model of heat transfer in gas metal arc welding was improved by optimizing the six unknown parameters using SAO by Bjelic et al. (2016). Beytolamani et al. (2018) used SAO in conjunction with the D-optimal design of RSM to optimize the EDM process parameters. The estimated results have been found to be in good agreement with the experimentally obtained results.

2.4 Research Gaps

The effects of in-process variables on the quality, mechanism of joint formation, effects of oxides and contaminants, tooling and part dimension, amount of heat generation and the extent of temperature at the interface are some of the aspects that need better understanding for implementing the USMW in mass production as a versatile joining technique. Hence,

there is a need to perform an organized research in this domain. It is evident from the available literature that many aspects of USMW have been explored, but still a lot of material combinations are available where analyses need to be performed to investigate the joining process. The following gaps are observed after conducting a literature survey:

Thin sheets of aluminum, copper, and phosphor bronze are invariably joined in a variety of applications, including battery contacts, LAN jacks, heat sink material, and new hyper fast connection solutions for computer processors, storage devices, and high-end servers. Electrical switches, relays, and circuit breakers; electrical spring contacts; solar panels; and BEV components are some of the applications where these metal combinations are used. Literature on ultrasonic joining of similar and dissimilar combinations of phosphor bronze with aluminium and copper is hardly found. The weld joint characterization of these combinations is an essential activity that needs to be explored.

Most of the work, explores the USMW process by varying only one parameter, either the weld pressure or the weld time (Allameh et al., 2005; K. Wang et al., 2017). The weld joint characterization was performed by varying weld energy by many researchers. But very few studies have been carried out where the effect of parameters was investigated by varying all the parameters simultaneously during ultrasonic welding. It is essential to choose a proper design of experiment to perform the experiments and then to analyze the obtained data statistically.

The strength of the weld joint, to a great extent, is the outcome of the weld area at the interface. Unlike resistance spot welding, a number of macro-bonds of different sizes are formed in USMW. It has been observed that the workpieces adhere to a relatively small portion of the interface in comparison to the area under the sonotrode tip, and it is very difficult to calculate the total area of the joint at the interface. Consequently, very few researchers have calculated and correlated it with the joint strength of ultrasonically welded joints.

The interface temperature is dependent on the material properties and the values of the process parameters. It is difficult to measure the temperature using theoretical approaches due to inadequate data of material properties at high temperatures. The measurement of the interfacial temperature and its validation by thermal modelling and simulation is an essential part of the study. It also gives an opportunity to evaluate not only the heat developed at the interface but also to assess the extent of the HAZ and TMAZ. Thermal modelling and

simulation of USMW of similar and dissimilar combinations of phosphor bronze is an important step to explore their ultrasonic weldability.

2.5 Research Objectives

The literature survey indicated that the information/data on USMW pertaining to the weldability of Phosphor Bronze in various applications is scanty. Therefore, there is a need to supplement the information. The existence of these gaps in the literature was used for deciding the objectives of the present research. The aims of this study will be to verify the results of some of the previous studies as well as overcome some of the issues encountered earlier. The study will have the following objectives associated with sheet metal combinations, particularly used in the electrical and electronics industries:

- To study the weld strength and weld quality of joined metal sheets of various thicknesses varying from 0.35 mm to 0.50 mm. and combinations (similar and dissimilar combinations of phosphor bronze, aluminium and copper).
- To study the relationship between response parameters and various process parameters such as clamping force, amplitude of vibration, and weld time.
- To calculate the weld area and correlate it with the weld strength.
- To explore the weld mechanism of USMW by studying the microstructure of the joint.
- To study the temperature profile of the interface.
- To identify the applications of ultrasonic welding joints in thin sheets.

2.6 Scope of the Present Study

The existing research gaps provide the scope to study the different aspects of ultrasonic weldability of similar and dissimilar combinations of phosphor bronze sheets with copper and aluminium. To apply USMW successfully for the production of thin and delicate parts in the electrical and electronics industry, it is necessary to carry out fundamental studies regarding the joining mechanism, definition of weld quality, analysis and optimization of the significant process parameters, and robust process design.

The main quality criterion for ultrasonically welded sheets is the tensile-shear load (Satpathy et al., 2018). It is required to be the maximum within the selected range of the parameters. Therefore, the present work focuses on the optimization of the parameters using some optimization algorithms based on the global maxima. The data thus obtained can be useful for academia and industry.

An insight into the weld interface to examine the changes occurring in such a short time gives a better understanding of the joining mechanism, variation in the temperature profile, and evolution of the microstructure. The measurement of the interfacial temperature using a thermocouple and SEM analysis of the weld interface assists in finding the effect of weld heat on the joint strength. The corroborative studies about the temperature profile and microstructural changes give support to the earlier theories.

The thermal modelling and simulation of the ultrasonic welding are required to be carried out to establish USMW as a cold welding technique. This exercise also helps in predicting the extent of HAZ/TMAZ. The validation of the experimental data with the simulated results is essential to justify the research.

CHAPTER 3

METHODOLOGY AND EXPERIMENTATION

3.1 Introduction

The objectives of the present work have been presented in the previous chapter. The methodology adopted to achieve those objectives is described here. The methodology mainly involves the selection of material, selection of process and response parameters, planning of suitable experimental design, and selection of a metaheuristic optimization technique. The approach was used to get the maximum weld strength by optimizing the weld parameters. The methodology also briefs the details regarding the thermal modelling of USMW with the aim of simulating the interface temperature using finite element analysis. Lastly, the need for the microstructural examination of the weld joint and the planning for the same are explained. The detailed methodology is described in the following sections:

3.2 Material Selection

Phosphor bronze, copper, and aluminium are extensively used in the electrical and electronics industries. The sheet metal coupons of size 100 mm x 25 mm were prepared as per the ASTM international code D1002-05 with a 25 mm overlap for making similar and dissimilar joints (ASTM International codes D1002-05, 2005). The ASTM code D1002-05 is the standard test method for finding the shear strength of a single lap joint made between adhesively bonded sheet metal specimens under tensile loading. The details of the selected materials are as given below:

A. Phosphor Bronze (PB) (UNS C51100), Nominal thickness: 0.36 mm
B. Copper (Cu) (UNS C10300), Nominal thickness: 0.45 mm
C. Aluminium (Al) (Al 3003-H12), Nominal thickness: 0.38 mm

Combinations: Different combinations of the selected materials (similar and dissimilar) were made. The placement of the strips in the overlapping position follows the sequence of the names.

(a) PB-PB (similar)
(b) PB-Cu (dissimilar)
(c) PB-Al (dissimilar)

The procured metal sheets were tested for their composition using spark atomic emission spectrometer. The composition of the material used is shown in Table 3.1.

Table 3.1: Chemical composition of the materials used for experimentation

Material	Element Composition (wt %age)								
	Cu	Al	Sn	P	Zn	Fe	Mn	Si	Rest
PB (UNS C51100)	95.18	-	4.09	0.21	0.13	0.08	-	-	0.31
Cu (UNS C10300)	99.76	-	-	0.004	-	-	-	-	0.24
Al (Al 3003 H12)	-	99.01	-	-	-	0.14	0.51	0.28	0.06

3.3 USMW Experimental Set-up

The microprocessor-controlled Ultrasonic Spot Metal Welding (USMW) Machine (Model: M-4000) attached with a Data Acquisition (DAQ) module manufactured by Roop Telesonic Ultrasonix Limited in technical collaboration with Telesonic, Switzerland was used for ultrasonic welding and measuring the real-time interface temperature during welding as shown in Figure 3.1.

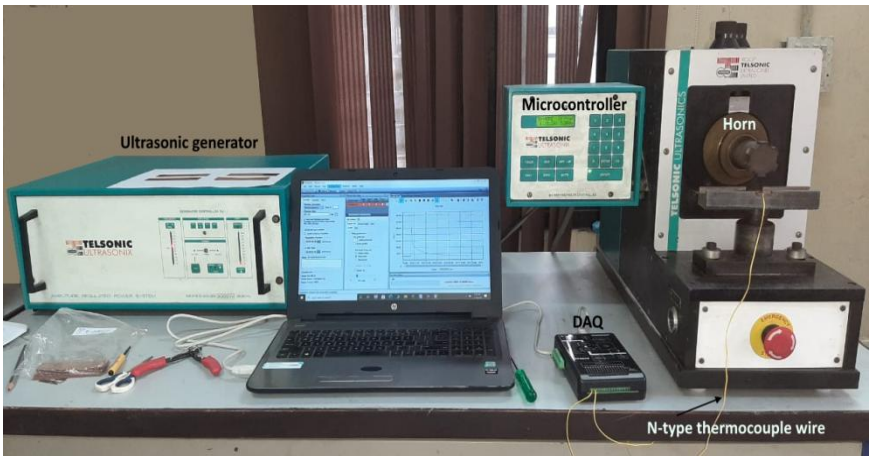

Figure 3.1: Ultrasonic Spot Metal Welding Set-up

It is a conventional ultrasonic metal welding machine with a working power of 3000 W at 20 kHz. The welding set-up was equipped with a calibrated pressure gauge and digital displays capable of showing the values of the process parameters such as welding time and energy to the third decimal place. The equipment is an assembly of the following units:

(i) The ultrasonic generator: The device that provides the electrical energy to power the ultrasonic transducers is known as the 'ultrasonic generator'. Basically, the ultrasonic generator converts electrical energy received from the power mains into electrical energy with the proper frequency, voltage, and amperage to power or drive the ultrasonic transducers. Low frequency electrical signals are converted into high frequency (ultrasonic frequency) electrical signals by an ultrasonic generator.

(ii) Welding press: The welding press houses the 'Horn' which is the main part of the system. A horn is an assembly of three parts, namely (a) Converter (b) Booster and (c) Sonotrode, connected to each other longitudinally. The converter transforms the electrical signals into mechanical vibrations, which are amplified by the booster and focused on the weld material through the sonotrode. The sonotrode was made of titanium alloy (Ti-6Al-4V). The sonotrode has four rectangular tips of different serrations attached at the end of it. The welding press is also comprised of a pneumatic system and an anvil. The pneumatic system exerts pressure on the components to be welded. It was operated with the help of dried compressed air supplied by a compressor. An anvil was also an inbuilt part of the welding press. It was made of high-quality, heat-treated tool steel and attached with a replaceable head having serrations. This arrangement ensured a tremendously rapid relative movement between the two contacting sheets. An alloy steel jig was also attached to the anvil to facilitate the placement of the weld coupons between the horn tip and the anvil.

(iii) Microprocessor controller: The microprocessor controller attached to the machine controls all the functions of the machine, such as mode selections, giving inputs to the timers and power settings, language selection, etc. The specifications of the USMW machine used in the current work are given in Table 3.2:

Table 3.2: Specifications of USMW machine

Make	M-4000 with MPS-3 / SG-22 Roop Telesonic Ultrasonix Limited, Gujrat, India
Stroke Length	25 mm max.
Maximum Pressure	10 bar Max.
Clamping Force	4000 N
Max. Current Input	10 A effective
Input Power	3 x 380/230 V, 50 Hz +20% -10%
Maximum output power	3000 W effectively
Working Frequency	20 kHz
Maximum Amplitude	35 µm ± 2%

3.3.1 Time Control Mode and Energy Control Mode

The ultrasonic welding set-up used for the experimentation has a sophisticated closed-loop control system. The USMW machine can be operated in two modes: Time Control Mode (TCM) and Energy Control Mode (ECM) as per the requirements. The present work involves both these modes. The ultrasound is active during the preselected welding time in TCM. The amount of energy that is produced during that time cannot be controlled. Whereas, in the case of ECM, the ultrasound remains active till the preset energy value is reached. The welding time/ultrasonic application time varies automatically during this mode to achieve the desired value of the weld energy. In a broad sense, the weld time and the weld energy are approximately interchangeable (Weld Energy = Power x Weld Time), but only one can be controlled precisely at a time. The focus of the study determines the mode to be used. As the current work investigates the effect of process parameters on the weld strength as well as that of weld energy on the mechanical, thermal, and microstructural characteristics of the ultrasonic joint, the weld samples were prepared in both modes.

3.4 Selection of Process and Response Parameters

The identification of the process parameters and their level is an important step in experimental planning. From the literature, it was found that among many parameters, the major process parameters affecting the weld strength are: weld time, weld pressure, vibration amplitude, and weld energy, whereas the main material parameters are: thickness of the workpiece, surface quality, hardness, and thermal conductivity (E. DeVries, 2004; M. C. Bloss, 2008). Besides these, the size of the sonotrode tip also affects the weld quality. The thicker material requires a high power ultrasonic generator with a larger tip size on the sonotrode. Weld time and weld energy are almost similar parameters and can be chosen as per need. The joint can be made by giving energy to the joint for some particular time period or by consuming some particular amount of weld energy irrespective of weld time. Weld time, weld pressure, vibration amplitude, and weld energy are the parameters that can be precisely controlled while welding. Considering these facts, the major parameters selected in the present work are weld time (W_t), vibration amplitude (V_a), and weld pressure (W_p) for the experimentation under TCM and weld energy (W_e) for the experimentation under ECM.

The quality and performance of the weld joint prepared by USMW were evaluated by some response parameters. A correlation has been established between these performance parameters. The important responses which have been studied during the research are:

- **Tensile-Shear Load (W_{Se}):** The strength of the joint should be sufficient to bear the design loads. The tensile-shear load that represents the experimental weld strength was measured using a computerized Universal Testing Machine (UTM) with the tensile load exerted parallel to the joint in the longitudinal direction.
- **Weld interface temperature (T_i):** The measurement of the weld interface temperature is important for the following reasons: (i) It gives information about the mode of joint formation at the interface (ii) The weld zone characterization is done on the basis of the peak interface temperature (iii) The relationship between the weld strength and the interface temperature aids in quality control during production. The real-time weld interface temperature was measured with the help of an N-type thermocouple wire placed at the middle of the overlapped portion of the weld coupons attached to a DAQ module interfaced with the QuickDAQ software.
- **Weld area (W_a):** The weld area is an important response parameter that ultimately dictates the weld strength. The joint in USMW is an accumulation of a number of weld nuggets at the weld interface which combine together to give strength to the joint. The total area of the weld joint at the interface depends upon the values of the parameters, the properties of the weld metal, and the shape and size of the serrations of the sonotrode tip. The actual weld area at the weld interface was measured using ImageJ software.

3.5 Design of Experiments

The Design of Experiments (DOE) is the set of experiments conducted efficiently in a planned manner with the aim of achieving valid and objective-oriented results from the obtained data. The experiments are performed according to the experimental design laid out in advance. A well-chosen experimental design improves the efficiency of the experimentation so that the maximum information can be extracted from the minimum efforts made for experimentation (R. Panneerselvam, 2012). The design of experiment is adopted to fulfill the following needs:

i. To discover the cause and effect connection between the factors affecting the process and the output of that process.
ii. To understand the effects of the interactions among the parameters.
iii. To evaluate the limits of the controllable parameters to optimize the performance.
iv. To reduce noise or the experimental error.
v. To improve the robustness of the design or the process.

The major experimental designs as per the number of parameters and their levels are:

- One Factor At a Time (OFAT) Design
- Factorial Design
- Response Surface Methodology (RSM) Design

3.5.1 One Factor At a Time (OFAT) Design

In this design type, only one factor is kept under investigation, keeping all other factors at a constant value. The main aim of the investigation is to verify if the effect of the factor is different at different levels of the factor (A. Nasma at el., 2018). Both qualitative and quantitative factors can be evaluated with this design. This design neither investigates the significant factors nor can it optimize a factor. But it can simply evaluate the effect of a factor on the response, keeping the values of other factors at mid-level, provided investigation of the interaction effects of the factors is not required. OFAT proves to be a useful design in some situations (Delgarm et al., 2018). This design has been used in the present work to investigate the effect of weld energy on the mechanical and metallurgical properties of the joint. The value of the weld energy was varied, keeping the values of other factors constant at their mid-levels. The experiments were conducted in the Energy Control Mode of the USMW machine.

3.5.2 Factorial Design

In factorial design, the investigation of more than one factor is done simultaneously. The factors may be both qualitative and/or quantitative in nature. The main objective of this design is to investigate the effect of significant process variables on the dependent variable and also to evaluate the effect of interaction on the response (Puertas and Luis, 2003). Some of the designs under this category can be used to predict the results. The advantage of factorial design over OFAT is that the individual and the combined effect of the parameters on the response can be studied simultaneously (Veronica, 1999). Factorial design can be divided into two broad categories: (i) full factorial design and (ii) fractional factorial design.

All possible combinations of all the factors are taken into consideration in a full factorial design. This design is used provided the time, money, or the number of samples does not pose any constraint. The most basic factorial design is a two-level factorial design. It consists of 2^k experimental runs. Here, all the combinations of ‘k’ factors are used at two levels. As the number of factors or levels increases, it becomes difficult to manage the experiments as

the number of runs increases geometrically. The need to increase the number of trials is usually accompanied by the requirement to evaluate the higher-order combinations of the factors. But such situations seldom occur and result in the wastage of resources. A better way to avoid this wastage is to use only a part of the full factorial design, thus reducing the number of trials. This evolves into a fractional factorial design.

The fractional factorial design is an efficient alternative to the issues discussed above. In this design, a subset of all possible combinations is selected for consideration. This systematic reduction allows for screening of a larger number of factors/levels with a minimum investment of resources (Youssef et al., 1994). However, there are some drawbacks. There is a possibility of misinterpretation of the results. Due to the elimination of some of the runs, the capability of the design to analyze all possible effects, particularly the combined effect of all the factors, is reduced. Secondly, this design is not capable of exploring the curvature of the response due to the absence of the quadratic terms (Montgomery, 2001). Some popularly used fractional factorial designs are: Placket-Burman factorial and Taguchi's orthogonal array factorial designs.

3.5.3 Response Surface Methodology (RSM)

When there is a curvature in the response surface, the linear model is not able to predict precisely. Response Surface Methodology (RSM) design is generally utilized after determining the important factors using screening and factorial design to explore the possible curvature in the response surface. It was invented by George E. P. Box and K. B. Wilson in 1951, and since then, this technique has been extensively used in many fields such as medicine, agriculture, science, and engineering. RSM is the most commonly used technique for the purpose of optimization of the process parameters (Neddermeijer et al., 2000). It is a combination of some statistical and mathematical techniques which are collectively termed RSM (Montgomery, 2001). The main objectives of using RSM are:

i. To predict the response by conducting a series of experiments as per the design over a specified range.
ii. To fit an empirical model to the data, acquired through experimentation as per the design.
iii. To optimize the input variables for maximizing or minimizing the response within the region of interest.

An RSM design is an extension of the factorial design where the squared terms are added to the relation of input and response variables. This way, the modelling of the curvature of the response becomes possible along with the estimation of the interaction effect of the parameters. RSM design is a very useful tool for optimizing and improving the process by making it more robust against external uncontrollable noise. The following steps are necessary to adopt RSM for experimentation (Onwubolu & Kumar, 2006; Gunaraj & Murugan, 1999):

a. Identification of the control parameters.
b. Fixing of upper and lower limits of the parameters.
c. Development of the experimental design matrix.
d. Conducting the experiments according to the design matrix.
e. Recording the values of the response parameters.
f. Development of the regression model polynomial and calculation of its coefficients.
g. Checking the adequacy of the regression model.
h. Representing the effect of process parameters on the response parameters in the form of a response surface.
i. Analysis of the results.

A second-order polynomial is the best representative of the input variables and the response. An optimal condition can be easily detected using a well-planned second-order response surface (Sarabia and Ortiz, 2009). But a second-order response surface needs at least three to five levels of the factors in the experimental design. A large number of experimental runs would be required if a full factorial design is utilized to obtain the response surface.

The second-order polynomial for three parameters, having linear terms, squared terms, products, and the intercept of the factors as shown in Equation 3.1 is essentially required to approximate the curvature of the true response surface.

$$y = \alpha_0 + \sum_{j=1}^{3} \alpha_j x_j \ + \sum_{j=1}^{3} \alpha_{jj} x_j^2 \ + \sum_{i=1}^{2} \sum_{j=1,i<j}^{3} \alpha_{ij} x_i x_j \qquad (3.1)$$

Where y is the response, x_j represents process parameters, and $\alpha_0, \alpha_i, \alpha_{ii}$ and α_{ij} are the coefficients of constant, linear, quadratic and interaction terms, respectively. In context to the current study, y represents tensile-shear load and x_j represent weld time, weld pressure and vibration amplitude.

As there are many interaction terms in the current study, this study employs a second-order polynomial due to its flexibility for taking a variety of functional forms and capability to

approximate the response surface. The two most popular and useful experimental designs under RSM are Central Composite Design and Box-Behnken Design. The current study uses the Box-Behnken design to fulfill some requirements of study.

3.5.3.1 Box-Behnken Design

It is generally needed to reduce the number of experiments without losing the important combinations while investigating the effects of the interactions and estimating the curvature. Box and Behnken devised a new experimental design for RSM in 1960 (Rao and Kumar, 2012), known as the Box-Behnken Design (Box and Draper, 1987). At least three levels of each independent factor are needed, which are equally placed and designated by -1, 0, +1. BBD does not have an embedded factorial or fractional factorial design. It is an independent design that can adequately fit a quadratic model. Among other characteristics, the BBD has a fully or nearly rotatable property. It means that the variance of the predicted value of the response variable is dependent on the distance of a point and not on the direction of the point from the centre. The parameter combinations are placed at the mid-point of the edges and the centre of the cubic workspace as shown in Figure 3.2. The workspace in terms of an inscribed sphere will be such that the surface of the sphere will be protruding through the faces of the cube and the mid-points of the edges will be tangential to the sphere surface. However, the BBD has no runs at the corner points, i.e. the extreme combinations of the parameters, but it has the capability to provide better prediction accuracy at the centre of the prediction space.

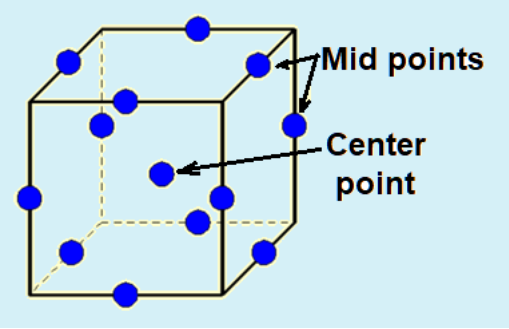

Figure 3.2: Box-Behnken design space

Three sets of factors each with four runs are formed in BBD for 3 factors. Each run of the set is constituted with one of the four combinations of the two factors at low and high levels and the third factor at mid-level. One run is added to include the central point where all the factors are at mid-level. This makes a total of 13 runs, but to increase the prediction possibility by reducing the pure error in the center of the design space, 2 or 4 additional centres are added further, thus making a total of 15 or 17 runs (George Box & Donald

Behnken, 1960). In the current study, four central points were added to the model to increase the prediction accuracy. Thus, there are 17 runs in the design matrix.

3.5.4 Selection of Experimental Design

The objectives of the present study involved determining the effect of the process parameters individually as well as in combination with each other and also investigating the effect of the weld energy on the weld interface. Both of these objectives require a lot of experimental work to be carried out with a specific experimental design. It is clear from the literature that the response has curvature. Therefore, BBD of RSM has been adopted for experimentation under time control mode. To investigate the effect of weld energy, it was planned to vary the weld energy value from the minimum to the maximum keeping other factors constant at the mid-level. So, the OFAT design has been adopted for experimentation under the energy control mode.

There are a few advantages a BBD has over a central composite design. Unlike CCD, all the design points of BBD are within the safe operating zone owing to the non-existence of the axial points. It reduces the chances of unachievable factor values while experimenting. It is also ensured while using BBD that all the factors will never be set at extreme values, which sometimes may prove beneficial in conditions where unsatisfactory results might come (Ferreira et al., 2007). Secondly, the BBD has fewer design points in comparison to CCD for the same number of factors; hence, a lesser number of runs. For a 3 factor with 3 levels, the required number of runs is 15 (taking 3 centre points) in BBD as compared to 20 in CCD.

3.6 Experimentation

The specimens used in this work are similar and dissimilar combinations of phosphor bronze (UNS C51100), copper (UNS C10300) and aluminium (Al 3003) sheets. The size and shape of the specimens are prepared according to the ASTM D 1005-05 standard (ASTM International Codes D1002-05, 2005). This standard describes the test method in the case of the tensile loading for metal-to-metal bonded test strips of standard size.

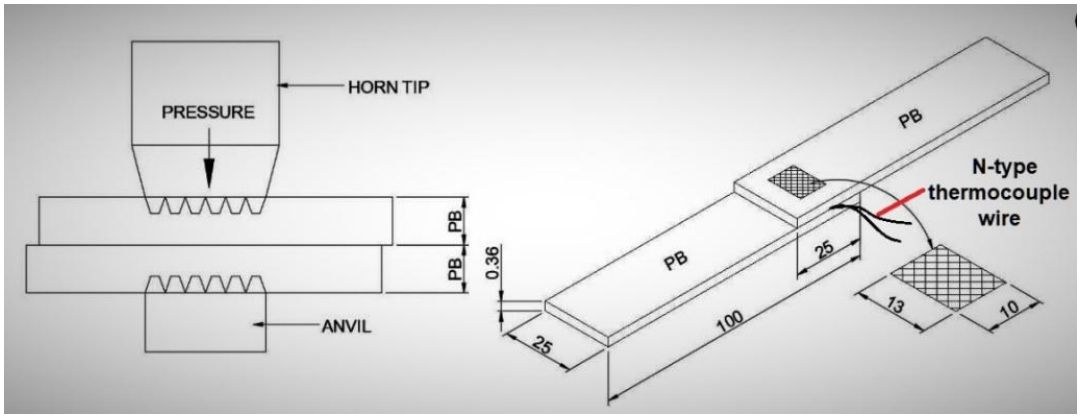

Figure 3.3: The size and shape of the weld specimen

The length and width of each strip were cut in 100 mm x 25 mm size with a 25 mm overlap as shown in Figure 3.3. The weld coupons were properly cleaned with acetone before placing them on the alloy steel jib fitted to the anvil to facilitate the placement of the weld coupons between the horn tip and the anvil.

3.6.1 Pilot experiments

A large number of pilot experiments were conducted to find out the maximum and minimum limits of weld parameters (W_t, W_p and V_a) with the following three combinations of materials:

- Phosphor Bronze/Phosphor Bronze (PB-PB) - Similar combination
- Phosphor Bronze/Copper (PB-Cu) - Dissimilar combination
- Phosphor Bronze/Aluminium (PB-Al) - Dissimilar combination

Two aspects were considered while selecting the range of the parameters for conducting the tests. Firstly, it was decided in a larger spectrum to cover the maximum number of applications and, secondly, samples having a visually good weld appearance, and further verified through tensile tests, were chosen for this purpose. The weld specimens, which were found very weak on the lower side or burnt on the higher side of the parameters helped in deciding the range of the parameters. Similarly, the range of the only parameter, i.e. weld energy (W_e) which was varied during experimentation under ECM while keeping other parameters constant, was also decided by carrying out a number of pilot runs.

Table 3.3: Levels of process parameters for joining PB-PB, PB-Cu, and PB-Al specimens under TCM

Metal Combination	Welding Time, W_t (Sec)			Weld Pressure, W_p (MPa)			Vibration Amplitude, V_a (µm)		
	-1	0	1	-1	0	1	-1	0	1
PB-PB	0.5	0.85	1.2	0.2	0.28	0.36	28	31.5	35
PB-Cu	0.6	0.8	1	0.14	0.22	0.3	28	31.5	35
PB-Al	0.2	0.45	0.7	0.2	0.27	0.34	24.5	28	31.5

Table 3.4: Range of process parameters for joining PB-PB, PB-Cu, and PB-Al specimens under ECM

Metal Combination	Weld Energy, W_e (J)		Step	Weld Pressure (Constant), W_p (MPa)	Vibration Amplitude (Constant), Va (µm)
PB-PB	200	2400	200	0.28	31.5
PB-Cu	600	3200	200	0.22	31.5
PB-Al	150	1450	100	0.27	28

The levels and the range of the parameters finally decided for different materials combinations under TCM and ECM are shown in Table 3.3 and Table 3.4, respectively.

3.6.2 Experimental Design Matrix

The experimental design matrices for experiments under TCM were developed as per the Box-Behnken design of RSM in the current work. Based upon the experimental design, selected parameters, and specified ranges of parameters, 17 runs were designed as shown in Tables 3.5, 3.6, and 3.7 for PB-PB, PB-Cu, and PB-Al, respectively. Lap joints were prepared in all the weld coupons of all the combinations. Six replicates were made in each experimental run, out of which, 3 replicates were used for measuring the tensile-shear load of the weld coupons by a computerized tensile testing machine, while another 3 replicates were utilized for the measurement of the run-time interface temperature using a thermocouple. In this way, a total of 102 weld coupons were prepared for each combination of the material.

Table 3.5: Experimental design matrix as per BBD for PB-PB under TCM

Run Order	Std. Order	Coded Values of Parameters			Actual Values of Parameters		
		W_t	W_p	V_a	W_t	W_p	V_a
		Weld Time (sec)	Weld Pressure (MPa)	Vibration Amplitude (µm)	Weld Time (sec)	Weld Pressure (MPa)	Vibration Amplitude (µm)
1	13	0	0	0	0.85	0.28	31.5
2	10	0	1	-1	0.85	0.36	28
3	14	0	0	0	0.85	0.28	31.5
4	5	-1	0	-1	0.5	0.28	28
5	9	0	-1	-1	0.85	0.2	28
6	1	-1	-1	0	0.5	0.2	31.5
7	6	1	0	-1	1.2	0.28	28
8	16	0	0	0	0.85	0.28	31.5
9	8	1	0	1	1.2	0.28	35
10	11	0	-1	1	0.85	0.2	35
11	4	1	1	0	1.2	0.36	31.5
12	12	0	1	1	0.85	0.36	35
13	17	0	0	0	0.85	0.28	31.5
14	7	-1	0	1	0.5	0.28	35
15	15	0	0	0	0.85	0.28	31.5
16	3	-1	1	0	0.5	0.36	31.5
17	2	1	-1	0	1.2	0.2	31.5

Table 3.6: Experimental design matrix as per BBD for PB-Cu under TCM

Run Order	Std. Order	Coded Values of Parameters			Actual Values of Parameters		
		W_t	W_p	V_a	W_t	W_p	V_a
		Weld Time (sec)	Weld Pressure (MPa)	Vibration Amplitude (µm)	Weld Time (sec)	Weld Pressure (MPa)	Vibration Amplitude (µm)
1	10	0	1	-1	0.8	0.3	28
2	11	0	-1	1	0.8	0.14	35
3	14	0	0	0	0.8	0.22	31.5
4	6	1	0	-1	1	0.22	28
5	12	0	1	1	0.8	0.3	35
6	16	0	0	0	0.8	0.22	31.5
7	4	1	1	0	1	0.3	31.5
8	15	0	0	0	0.8	0.22	31.5
9	5	-1	0	-1	0.6	0.22	28
10	3	-1	1	0	0.6	0.3	31.5
11	8	1	0	1	1	0.22	35
12	17	0	0	0	0.8	0.22	31.5
13	2	1	-1	0	1	0.14	31.5
14	7	-1	0	1	0.6	0.22	35
15	9	0	-1	-1	0.8	0.14	28
16	1	-1	-1	0	0.6	0.14	31.5
17	13	0	0	0	0.8	0.22	31.5

Table 3.7: Experimental design matrix as per BBD for PB-Al under TCM

Run Order	Std. Order	Coded Values of Parameters			Actual Values of Parameters		
		W_t	W_p	V_a	W_t	W_p	V_a
		Weld Time (sec)	Weld Pressure (MPa)	Vibration Amplitude (µm)	Weld Time (sec)	Weld Pressure (MPa)	Vibration Amplitude (µm)
1	2	1	-1	0	0.7	0.2	28.25
2	14	0	0	0	0.45	0.27	28.25
3	6	1	0	-1	0.7	0.27	24.5
4	10	0	1	-1	0.45	0.34	24.5
5	7	-1	0	1	0.2	0.27	31.5
6	15	0	0	0	0.45	0.27	28.25
7	13	0	0	0	0.45	0.27	28.25
8	1	-1	-1	0	0.2	0.2	28.25
9	17	0	0	0	0.45	0.27	28.25
10	8	1	0	1	0.7	0.27	31.5
11	9	0	-1	-1	0.45	0.2	24.5
12	16	0	0	0	0.45	0.27	28.25
13	3	-1	1	0	0.2	0.34	28.25
14	4	1	1	0	0.7	0.34	28.25
15	11	0	-1	1	0.45	0.2	31.5
16	12	0	1	1	0.45	0.34	31.5
17	5	-1	0	-1	0.2	0.27	24.5

The experiments were carried out as per the Run Sheet shown in Figure 3.4, prepared according to the design matrix.

RUN SHEET (PB/PB)- Based on trial runs conducted at GBPEC					
Run#1					
Weld Time (T)	**0.85**	**sec**	**Replicate#4 (R4)**		
Weld Pressure (P)	**2.8**	**bar**	Surface temp. taken by Th.Imager		°C
Amplitude (A)	**90**	**%**	Interface Temp. observed by TC		°C
			Surface temp. observed by TC		°C
Replicate#1 (R1)			Max. Power generated (Pmax)		%
Surface temp. taken by Th.Imager		°C	Energy used		Ws
Max. Power generated (Pmax)		%	Tensile Shear Strength (TSS)		N
Energy used		Ws	Weld Nugget Area (WNA)		mm2
Tensile Shear Strength (TSS)		N			
Weld Nugget Area (WNA)		mm2	**Replicate#5 (R5)**		
			Surface temp. taken by Th.Imager		°C
Replicate#2 (R2)			Interface Temp. observed by TC		°C
Surface temp. taken by Th.Imager		°C	Surface temp. observed by TC		°C
Max. Power generated (Pmax)		%	Max. Power generated (Pmax)		%
Energy used		Ws	Energy used		Ws
Tensile Shear Strength (TSS)		N	Tensile Shear Strength (TSS)		N
Weld Nugget Area (WNA)		mm2	Weld Nugget Area (WNA)		mm2
Replicate#3 (R3)			**Replicate#6 (R6)**		
Surface temp. taken by Th.Imager		°C	Surface temp. taken by Th.Imager		°C
Max. Power generated (Pmax)		%	Interface Temp. observed by TC		°C
Energy used		Ws	Surface temp. observed by TC		°C
Tensile Shear Strength (TSS)		N	Max. Power generated (Pmax)		%
Weld Nugget Area (WNA)		mm2	Energy used		Ws
			Tensile Shear Strength (TSS)		N
			Weld Nugget Area (WNA)		mm2

Figure 3.4: Run sheet for preparation of weld coupons

The experimental design matrix for ECM were developed by varying the energy value from the minimum value to the maximum value, keeping the values of other parameters constant at the mid level as chosen for the parameters under TCM. On the basis of pilot experiments conducted for all the combinations, the range of weld energy was divided into 12 parts for PB-PB and 14 parts for PB-Cu and PB-Al each.

The experimental design matrices of the weld coupons with PB-PB, PB-Cu, and PB-Al combinations prepared under ECM are shown in Table 3.8. At each run, seven replicates were prepared, three of which were used to measure the tensile-shear load, another three were used to measure the run-time interface temperature, and the last replicate was used to investigate the microstructure at the joint. Thus, 84 weld coupons were prepared for PB-PB and 98 weld coupons were prepared for PB-Cu and PB-Al each. In total, 280 weld coupons were prepared.

Table 3.8: Experimental design matrix as per OFAT design for conducting USMW experiments under ECM

PB-PB		**PB-Cu**		**PB-Al**	
Constant parameters		**Constant parameters**		**Constant parameters**	
Weld Pressure = 0.28 Mpa Vibration Amplitude = 31.5 µm		**Weld Pressure = 0.22 Mpa Vibration Amplitude = 31.5 µm**		**Weld Pressure = 0.27 Mpa Vibration Amplitude = 28 µm**	
Run No.	**Weld Energy, W_e (J)**	**Run No.**	**Weld Energy, W_e (J)**	**Run No.**	**Weld Energy, W_e (J)**
1	200	1	600	1	150
2	400	2	800	2	250
3	600	3	1000	3	350
4	800	4	1200	4	450
5	1000	5	1400	5	550
6	1200	6	1600	6	650
7	1400	7	1800	7	750
8	1600	8	2000	8	850
9	1800	9	2200	9	950
10	2000	10	2400	10	1050
11	2200	11	2600	11	1150
12	2400	12	2800	12	1250
		13	3000	13	1350
		14	3200	14	1450

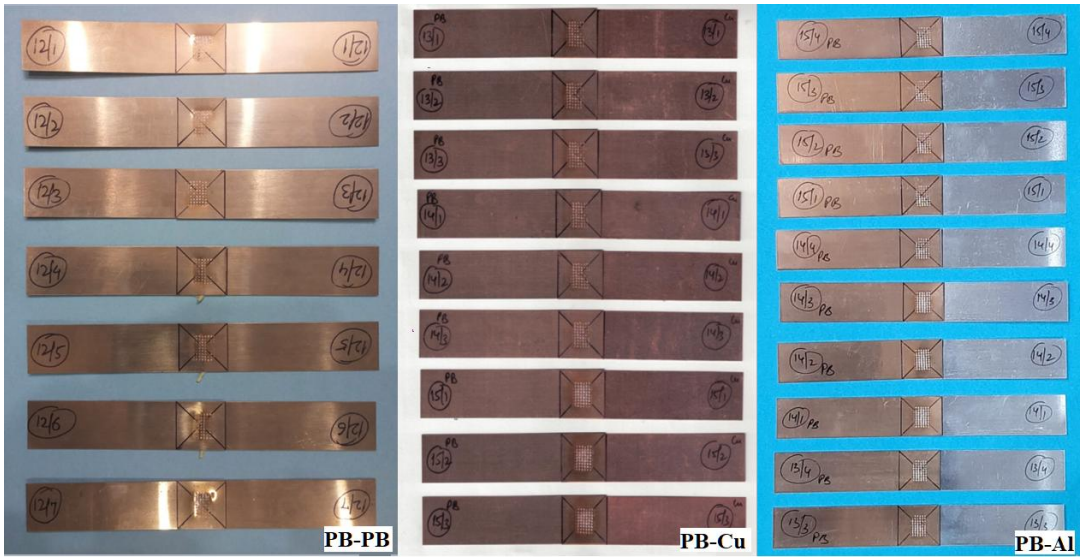

Figure 3.5: Ultrasonic welded actual specimens of PB-PB, PB-Cu and PB-Al

3.6.3 Conducting the Experiments

The experiments were conducted as per the design matrices developed for both TCM and ECM for all the three combinations of metals. All the weld coupons were properly cleaned with acetone and dried before welding. Figure 3.5 shows the actual weld specimens prepared with PB-PB, PB-Cu, and PB-Al, respectively.

3.7 Measurement of Response Parameters

The response parameters responsible for the performance of the weld joint were measured accurately. The weld interface temperature was measured during welding, and tensile-shear load and the weld interface area were measured after the weld joint formation.

3.7.1 Measurement of Tensile-Shear Load

The response parameter tensile-shear load, which represents the weld strength, was measured using a TINIUS OLSEN (Model: H50KS) computerized universal testing machine with constant crosshead speed at 1 mm/min. Due precautions were taken to keep the longitudinal axis of the weld coupons aligned with the axis of the tensile load exerted by the machine. Figure 3.6 (a) shows the UTM used in the current work.

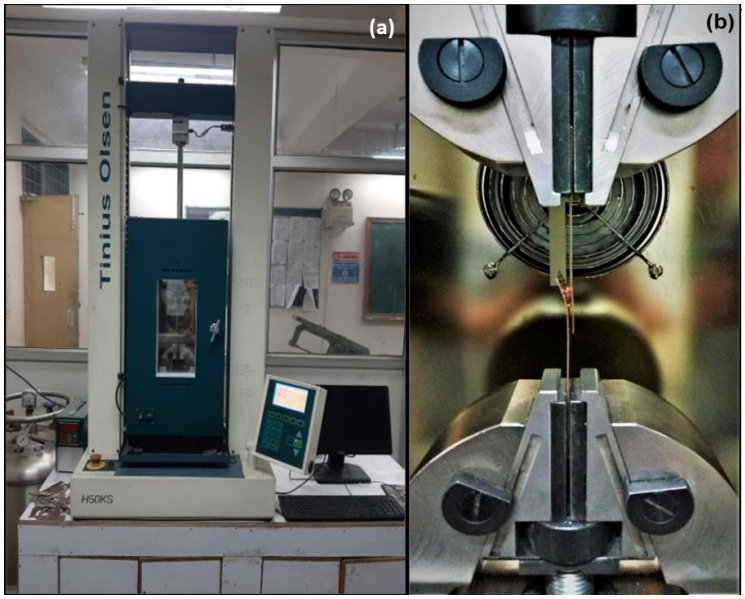

Figure 3.6: (a) Universal testing machine (b) Tensile-shear load testing of actual weld specimen

The machine is equipped with a number of load cells as low as 25 N up to 50 kN, a detachable gripper capable of gripping thin flat specimens (Figure 3.6 (b)) and DAQ system with the ability to acquire real-time load and deformation data at a rate of 1000 Hz accurately and precisely. The tensile-shear load values of all the welded specimens are collected and further analyzed.

3.7.2 Measurement of interface Temperature

The observed real-time interfacial temperature provides necessary information required to understand the joining mechanism and other microstructural activities that occurred due to the rise in temperature (Zhu et al., 2019). The interface temperature of the welded samples of PB-PB, PB-Cu, and PB-Al prepared under both TCM and ECM was measured in real-time using a DAQ module.

3.7.2.1 Data Acquisition Module

The temperature developed at the weld interface was measured in real-time by an 8 channel isolated thermocouple DAQ module (model DT9828) manufactured by Data Translation®, having a sampling rate of 600 Hz and an accuracy of 0.09°C. The module is equipped with cold junction compensation and open thermocouple detection circuits. Furthermore, the DAQ module was interfaced with the QuickDAQ software to process the interface temperature value. The QuickDAQ software has the functionality of converting the electrical signals

generated by the thermocouple to the temperature values and showing them in graphical form.

Precautions were taken while making the circuit. For example, the thermocouple wire was kept away from the electro-magnetic fields and the length of the wire was not taken very long as long wires are susceptible to unwanted noise. The hot junction was created by properly twisting the ends of the thermocouple wires for about 20 mm, and that end was attached to the lower weld coupon at the interface at the centrally marked point. To improve the consistency of the observations, best of three test samples were conidered as it was difficult to maintain the thermocouple exactly in the centre due to excessive vibrations of the sonotrode. The cold junction was attached to the terminal block of the DAQ module.

3.7.2.2 N-Type Thermocouple

The temperature measuring sensor used for this work was a 0.20 mm diameter sacrificial N-type (Nicrosil-Nisil) thermocouple wire which has a working range between -270°C and +1300°C. The N-type thermocouple has a very high sensitivity index (39µV/°C at 900°C) and thermo-electrical stability as compared to other thermocouples. The temperature values captured by the thermocouple are converted into electrical signals and are displayed digitally as well as graphically by the QuickDAQ software interfaced with the DAQ module. The whole system of temperature measurement and processing can be shown through the block diagram depicted in Figure 3.7. Figure 3.8 depicts the graphical representation of a temperature profile at the interface of one of the weld specimens.

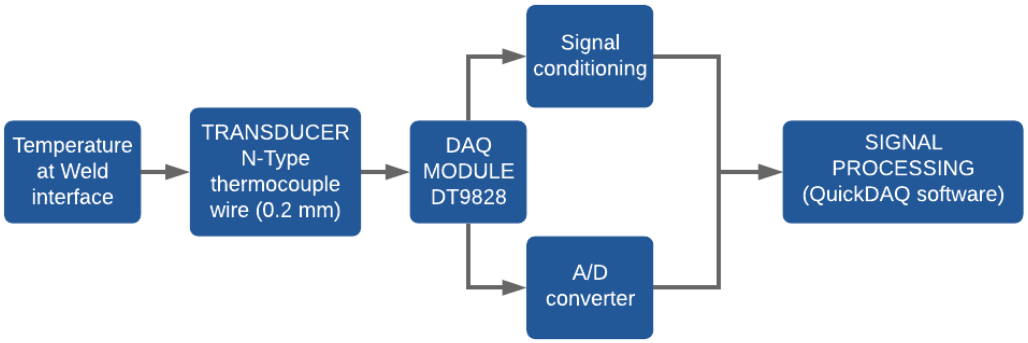

Figure 3.7: Block diagram of the DAQ system

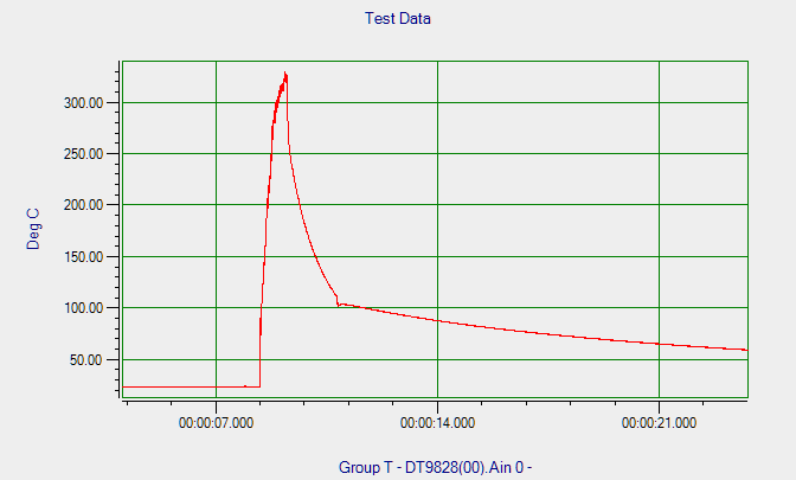

Figure 3.8: Temperature profile at the weld interface

3.7.3 Weld Area Measurement

The weld area at the interface is an important factor in deciding the efficacy of the welding process. The strength of the weld joint, to a great extent, is the outcome of the weld area at the interface. The fractured surfaces of the weld coupons were utilized to measure the actual weld area. The type of fracture was also observed in the weld coupons prepared under ECM to evaluate the effect of energy on the weld area and weld strength. Initially, the micro-welds start forming due to plastic deformation of the material under the sonotrode tip. The micro-welds accelerate, propagate, and combine quickly, converting into macro-welds or weld nuggets (Haddadi and Tsivoulas, 2016). Thus, the deformation zone expands continuously and, ideally, its maximum value may reach equal to the area of the sonotrode tip. But, teeth on the sonotrode tip penetrate up to a certain depth into the upper sheet depending upon the parameters' values; also, the presence of oxide at the interface restricts the formation of the micro-welds. Therefore, the deformation zone does not spread out over the whole area under the sonotrode tip.

Unlike resistance spot welding, a number of macro-bonds of different sizes and shapes are formed in USMW. Therefore, W_a is the aggregate of the areas of all the macro-bonds formed during the welding process. It has been observed that the workpieces adhere to a relatively small portion of the interface in comparison to the area under the sonotrode tip, and it is very difficult to calculate the actual area of the joint at the interface as the interface is not visible in many cases. Therefore, very few researchers have calculated and correlated it with the joint strength. Balle and Eifler (2012) used the nominal contact area of the sonotrode tip to calculate the joint strength. Similarly, the estimation of mean weld area was done by Satpathy

et al. (2015) by multiplying the area of a single weld spot with the number of knurling tips present at the horn tip.

In the present work, it was observed that PB-PB and PB-Al weld coupons prepared under TCM have got split at the interface during the tensile-shear load test, but in the case of PB-Cu, many weld coupons have got partial or no separation at the interface. It was also observed that the knurling patterns of the sonotrode tip and the anvil leave the teeth impressions at the top and bottom of the overlapped portion of the weld coupons. The impressions due to sonotrode tip have almost the same rectangular shape of size equal to 130 mm^2. However, the teeth impressions due to the anvil knurling pattern differ in weld coupons as shown in Figure 3.9. In PB-Cu weld coupons, it was observed that the weld area at the interface was close to the area of the bottom impressions (0.857926 times the area of the bottom impressions) as shown in Figure 3.10. The multiplying factor was deduced by establishing a relationship between the areas of the anvil knurling impressions at the bottom and the weld areas at the interface of a number of weld coupons prepared at different parameter combinations. Therefore, the weld area of PB-PB and PB-Al weld coupons was measured using teeth impressions at the interface, and that for PB-Cu was calculated on the basis of scanned and enlarged images of the knurling teeth impressions on the bottom side of the weld coupons.

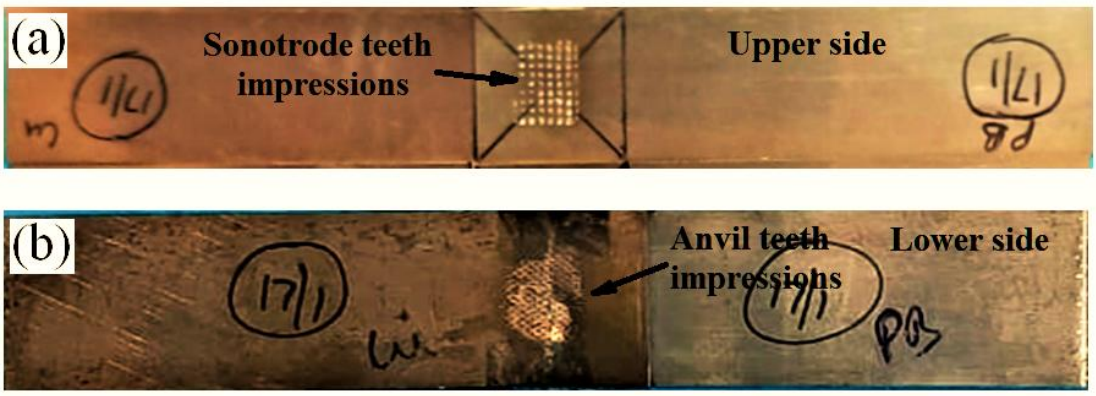

Figure 3.9: (a) Sonotrode teeth impressions on the upper side of the weld coupon (b) anvil teeth impressions on the lower side of the weld coupon

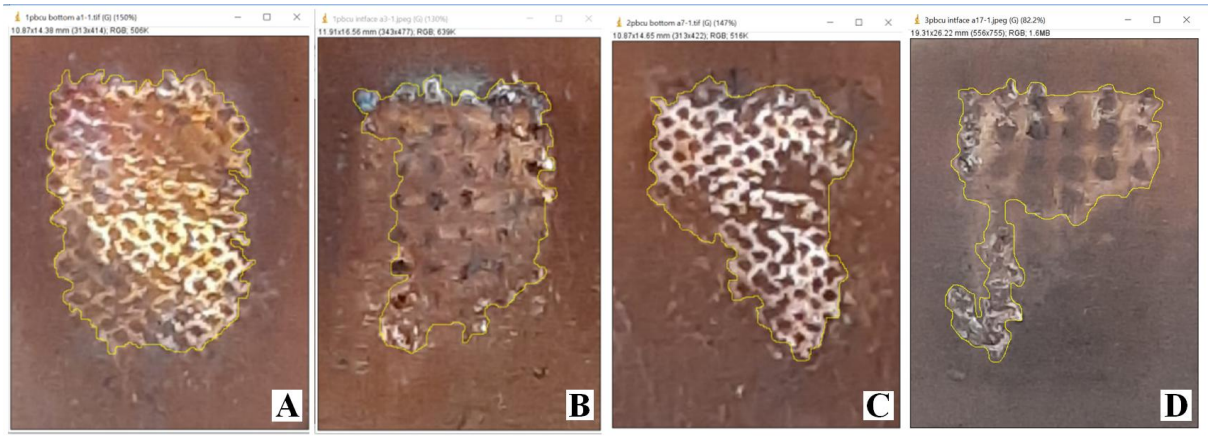

Figure 3.10: Impressions created by the anvil knurling pattern: (A) and (C) are the bottom side of the lower sheet (Cu); (B) and (D) are the corresponding impressions at the interface of the weld coupon

The teeth impressions on the magnified weld interface were summed up using ImageJ software (Version 1.52 a). The enlarged image of the weld area at the interface of a weld coupon separated during stretching and its corresponding threshold image is shown in Figure 3.11 (a) and (b). Such images were used to calculate the total area of all the macro-welds at the interface. The data collected was tabulated along with the corresponding tensile-shear load. A correlation coefficient was also calculated to find out the extent of the linear association between the two response-variables, experimental weld strength (W_{Se}) and weld area (W_a).

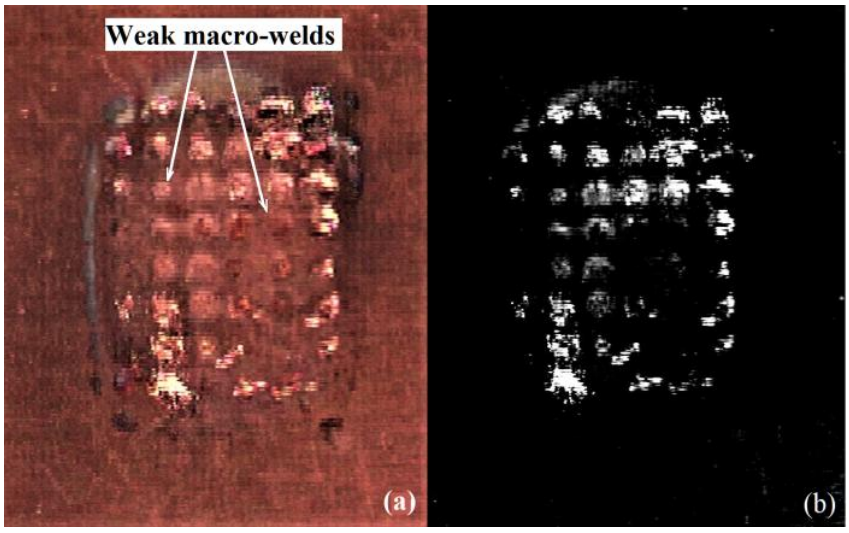

Figure 3.11: Enlarged view of weld interface (a) strong and weak macro-welds (b) the threshold image of the bonds used to calculate the area of the bonds

3.8 Recording of Responses

Similar and dissimilar metal ultrasonic joints have been prepared between PB-PB, PB-Cu, and PB-Al standard weld coupons under TCM and ECM. The response parameters, tensile-shear load and interface temperature, were recorded in both the modes. Besides these responses, the weld area was calculated for the weld coupons prepared under TCM.

3.8.1 Experimental Results under Time Control Mode

The Box-Behnken design was selected to prepare the weld coupons under TCM to study the influence of the process parameters on the response parameters. Every weld parameter was selected at 3 levels to conduct 17 randomized experiments, each of them having 6 replicates. For each combination, 51 weld coupons were prepared for conducting the tensile-shear test and calculating the weld area, while another 51 weld coupons were used for measuring interface temperature. The experimental results obtained with PB-PB, PB-Cu, and PB-Al combinations under TCM are shown in Table 3.9 to Table 3.14, respectively.

Table 3.9: Tensile-shear loads and interface temperatures under TCM for PB-PB

Run Order	Wt (sec)	Wp (MPa)	Va (μm)	W_{Se} (N)			Interface Temp. (°C)		
				Rep. 1	Rep. 2	Rep. 3	Rep. 1	Rep. 2	Rep. 3
1	1.2	0.28	28	1580	1610	1770	329.7	292.6	319.4
2	0.85	0.28	31.5	1775	1720	1850	301	327.1	315.1
3	0.85	0.36	28	1310	1220	1150	293.9	299.1	300
4	0.5	0.2	31.5	520	677	712	239.3	258.3	223.6
5	0.85	0.2	28	618	710	783	255.9	263.8	243.7
6	1.2	0.28	35	2300	2250	2370	345.6	335.2	340.6
7	0.5	0.28	35	1320	1270	1150	295.3	308.2	295.4
8	0.85	0.2	35	828	730	657	293.5	275.2	270.2
9	0.5	0.28	28	1400	1290	1311	290	294.9	283.5
10	0.85	0.36	35	2300	2470	2290	370.7	332.6	361
11	1.2	0.36	31.5	2500	2260	2490	370.5	330.8	346.8
12	0.85	0.28	31.5	1840	1880	1840	316.9	327.8	313.7
13	0.85	0.28	31.5	1856	1788	1766	322.8	329.1	298.7
14	0.5	0.36	31.5	1470	1410	1310	297.5	296.3	311
15	0.85	0.28	31.5	1840	1530	1630	318.9	315.7	304.1
16	1.2	0.2	31.5	1240	1120	1230	293.1	280.2	293.4
17	0.85	0.28	31.5	1824	1768	1806	312.5	304.8	313.7

Table 3.10: Tensile-shear loads and interface temperatures under TCM for PB-Cu

Run Order	Wt (sec)	Wp (MPa)	Va (μm)	W_{Se} (N)			Interface Temp. (°C)		
				Rep. 1	Rep. 2	Rep. 3	Rep. 1	Rep. 2	Rep. 3
1	0.8	0.3	28	1798	1857	1701	298.4	295.7	292.1
2	1	0.14	31.5	1288	1304	1444	269.8	280.3	305.1
3	0.6	0.3	31.5	1214	981	1141	250.1	313	243.5
4	0.6	0.22	28	781	735	810	261.3	232.4	266.4
5	1	0.22	35	1952	2135	1898	311.9	345.2	334.8
6	0.8	0.14	35	1264	1022	1343	265.7	274.6	263.2
7	0.8	0.22	31.5	1531	1701	1672	275.4	292.5	289.7
8	0.6	0.22	35	1002	933	1116	267.3	269.4	282.5
9	0.8	0.22	31.5	1600	1465	1787	268.7	253.6	264.7
10	1	0.22	28	1912	1726	1825	293.8	323.1	316.2
11	0.8	0.22	31.5	1817	1744	1543	282.4	315.4	292.4
12	0.8	0.22	31.5	1695	1774	1588	337.8	260.9	274.8
13	0.6	0.14	31.5	936	860	864	241.8	260.7	222.4
14	0.8	0.22	31.5	1610	1426	1528	294.7	314.4	299.4
15	0.8	0.14	28	1250	1087	1019	235.4	243.6	284.7
16	1	0.3	31.5	2255	1972	2162	377.1	341.7	366.5
17	0.8	0.3	35	1737	1895	2042	348.7	329.6	348.2

Table 3.11: Tensile-shear loads and interface temperatures under TCM for PB-Al

Run Order	Wt (sec)	Wp (MPa)	Va (μm)	W_{Se} (N)			Interface Temp. (°C)		
				Rep. 1	Rep. 2	Rep. 3	Rep. 1	Rep. 2	Rep. 3
1	0.7	0.2	28	1390	1460	1450	153.7	162.2	167.9
2	0.45	0.27	28	1430	1410	1278	196.9	203.4	212.1
3	0.7	0.27	24.5	1680	1465	1578	185.8	197.7	209.4
4	0.45	0.34	24.5	1590	1640	1698	267.4	307.4	287.4
5	0.2	0.27	31.5	1100	1020	1240	104.4	110.3	93.8
6	0.45	0.27	28	1580	1550	1530	187.2	213.5	201.7
7	0.45	0.27	28	1350	1440	1590	184.7	149.2	175.7
8	0.2	0.2	28	1010	920	889	95.3	98.2	103.7
9	0.45	0.27	28	1476	1450	1570	154.6	135.1	168.2
10	0.7	0.27	31.5	1320	1396	1470	168.9	150.7	173.1
11	0.45	0.2	24.5	1250	1270	1340	108.6	115.7	121.4
12	0.45	0.27	28	1430	1395	1520	162.7	168.2	159.7
13	0.2	0.34	28	1540	1601	1474	140.8	157.9	161.7
14	0.7	0.34	28	1778	1709	1732	266.7	291.9	322.7
15	0.45	0.2	31.5	1450	1401	1262	151.4	147.9	111.5
16	0.45	0.34	31.5	1810	1760	1860	272.6	287.8	265.7
17	0.2	0.27	24.5	1033	912	998	98.5	108.3	96.7

Table 3.12: Weld Area of PB-PB specimens under TCM

Run Order	Wt (sec)	Wp (MPa)	Va (µm)	Weld Area, Wa (mm2)		
				Rep. 1	Rep. 2	Rep. 3
1	1.20	0.28	28.0	59.91	48.47	63.72
2	0.85	0.28	31.5	65.13	65.46	62.8
3	0.85	0.36	28.0	47.97	49.73	62.7
4	0.50	0.20	31.5	55.77	56.57	51.7
5	0.85	0.20	28.0	32.87	31.31	34.67
6	1.20	0.28	35.0	72.52	76.76	78.09
7	0.50	0.28	35.0	49.74	44.52	51.91
8	0.85	0.20	35.0	58.53	59.48	59.81
9	0.50	0.28	28.0	39.57	36.22	46.59
10	0.85	0.36	35.0	86.78	98.81	68.21
11	1.20	0.36	31.5	84.49	78.25	63.28
12	0.85	0.28	31.5	72.72	76.44	68.98
13	0.85	0.28	31.5	71.47	69.91	66.26
14	0.50	0.36	31.5	51.96	54.15	46.7
15	0.85	0.28	31.5	58.88	54.85	61.34
16	1.20	0.20	31.5	36.82	31.43	32.26
17	0.85	0.28	31.5	68.02	76.29	67.81

Table 3.13: Weld Area of PB-Cu specimens under TCM

Run Order	Wt (sec)	Wp (MPa)	Va (µm)	Weld Area, Wa (mm2)		
				Rep. 1	Rep. 2	Rep. 3
1	0.8	0.30	28.0	64.27	75.28	69.69
2	1.0	0.14	31.5	70.57	64.72	67.66
3	0.6	0.30	31.5	49.05	59.66	57.59
4	0.6	0.22	28.0	51.87	50.89	56.02
5	1.0	0.22	35.0	108.86	107.24	99.85
6	0.8	0.14	35.0	53.90	50.52	42.99
7	0.8	0.22	31.5	97.12	93.05	89.14
8	0.6	0.22	35.0	52.40	56.48	55.95
9	0.8	0.22	31.5	83.40	86.69	93.02
10	1.0	0.22	28.0	78.99	72.09	74.65
11	0.8	0.22	31.5	85.59	89.67	95.84
12	0.8	0.22	31.5	74.26	69.19	73.25
13	0.6	0.14	31.5	47.69	54.28	49.15
14	0.8	0.22	31.5	76.16	75.42	80.06
15	0.8	0.14	28.0	78.21	74.85	75.95
16	1.0	0.30	31.5	109.69	118.56	102.26
17	0.8	0.30	35.0	103.17	112.79	105.20

Table 3.14: Weld Area of PB-Al specimens under TCM

Run Order	Wt (sec)	Wp (MPa)	Va (μm)	Weld Area, Wa (mm2)		
				Rep. 1	Rep. 2	Rep. 3
1	0.70	0.20	28.0	45.33	52.76	47.85
2	0.45	0.27	28.0	55.05	52.65	53.17
3	0.70	0.27	24.5	67.25	69.81	72.52
4	0.45	0.34	24.5	67.41	72.51	79.54
5	0.20	0.27	31.5	43.42	42.59	48.54
6	0.45	0.27	28.0	72.35	66.64	61.35
7	0.45	0.27	28.0	56.75	53.19	59.13
8	0.20	0.20	28.0	31.74	29.27	29.34
9	0.45	0.27	28.0	62.11	59.07	67.49
10	0.70	0.27	31.5	45.10	46.58	52.85
11	0.45	0.20	24.5	74.88	69.44	76.64
12	0.45	0.27	28.0	45.57	53.54	56.84
13	0.20	0.34	28.0	57.03	62.68	61.62
14	0.70	0.34	28.0	75.98	77.27	79.98
15	0.45	0.20	31.5	55.89	60.36	56.28
16	0.45	0.34	31.5	59.68	67.5.0	63.58
17	0.20	0.27	24.5	29.41	36.36	33.68

3.8.2 Experimental Results under Energy Control Mode

The weld coupons prepared under ECM were utilized to evaluate the effect of weld energy on weld joint strength, interface temperature, and microstructure for the ultrasonic joints made between PB-PB, PB-Cu, and PB-Al standard weld coupons as per OFAT experimental design. A total of 7 replicates were prepared for each run, out of which, 3 replicates were used for measuring the run-time interface temperature, another 3 were used for measuring tensile-shear strength, and 1 replicate was used for investigation of the microstructure at the joint. The weld coupons showing the maximum and minimum weld strengths in terms of tensile-shear load were used for the microstructural analysis. On the basis of pilot experiments conducted for all the combinations, the range of weld energy was divided into 12 parts for PB-PB and 14 parts for PB-Cu and PB-Al each. Thus, 84 weld coupons were prepared for PB-PB and 98 weld coupons were prepared for PB-Cu and PB-Al each. In total, 280 weld coupons were prepared. The experimental results under ECM are shown in Table 3.15 to Table 3.17 for PB-PB, PB-Cu, and PB-Al, respectively.

Table 3.15: Tensile-shear load and peak interface temperature for PB-PB under ECM (Constant Parameters: Weld Pressure = 0.28 MPa, Vibration Amplitude = 31.5 µm)

Run No.	Weld Energy, E (J)	Tensile-shear Load, W_{Se} (N)			Mean W_{Se}, (N)	Peak Interface Temp. (°C)
		Rep. 1	Rep. 2	Rep. 3		
1	200	433	405	456	431.33	197.5
2	400	425	475	503	467.67	201.2
3	600	603	595	542	580.00	234.9
4	800	860	854	838	850.67	255.4
5	1000	995	957	948	966.67	262.1
6	1200	1216	1226	1284	1242.00	293.4
7	1400	1487	1405	1396	1429.33	306.6
8	1600	1580	1666	1781	1675.67	313.2
9	1800	1958	1853	1902	1904.33	324.8
10	2000	2105	2215	2326	2215.33	329.7
11	2200	2304	2345	2295	2314.67	345.4
12	2400	2306	2340	2353	2333.00	368.6

Table 3.16: Tensile-shear load and peak interface temperature for PB-Cu under ECM (Constant Parameters: Weld Pressure = 0.22 MPa, Vibration Amplitude = 31.5 µm)

Run No.	Weld Energy, E (J)	Tensile-shear Load, W_{Se} (N)			Mean W_{Se}, (N)	Peak Interface Temp. (°C)
		Rep. 1	Rep. 2	Rep. 3		
1	600	775	752	618	715.00	231.2
2	800	895	835	828	852.67	234.5
3	1000	1160	1270	1240	1223.33	260.6
4	1200	1400	1410	1320	1376.67	281.0
5	1400	1470	1530	1493	1497.67	283.0
6	1600	1600	1580	1485	1555.00	291.0
7	1800	1725	1850	1530	1701.67	292.5
8	2000	1930	2075	1880	1961.67	311.0
9	2200	2300	2250	2290	2280.00	315.0
10	2400	2470	2490	2500	2486.67	329.2
11	2600	2568	2590	2734	2630.67	345.2
12	2800	2978	2944	2817	2913.00	347.5
13	3000	1801	1795	1694	1763.00	365.6
14	3200	1723	1809	1643	1725.00	377.8

Table 3.17: Tensile-shear load and peak interface temperature for PB-Al under ECM (Constant Parameters: Weld Pressure = 0.27 MPa, Vibration Amplitude = 28 µm)

Run No.	Weld Energy, E (J)	Tensile-shear Load, W_{Se} (N)			Mean W_{Se}, (N)	Peak Interface Temp. (°C)
		Rep. 1	Rep. 2	Rep. 3		
1	150	726	636	605	655.67	95.3
2	250	854	753	806	804.33	103.7
3	350	1162	1223	1096	1160.33	129.2
4	450	1122	1292	1175	1196.33	162.2
5	550	1372	1323	1184	1293.00	166.2
6	650	1441	1406	1531	1459.33	186.7
7	750	1543	1596	1517	1552.00	196.6
8	850	1615	1585	1604	1601.33	212.4
9	950	1745	1612	1719	1692.00	266.7
10	1050	1693	1725	1795	1737.67	291.9
11	1150	1723	1801	1866	1796.67	303.5
12	1250	1848	1821	1883	1850.67	305.4
13	1350	1943	1799	1876	1872.67	313.1
14	1450	1962	1828	1877	1889.00	322.7

3.9 Regression Model

The regression modelling is essentially carried out for the purposes of analysis, prediction, and optimization of the response variables using some statistical methods. Response surface methodology is the collection of mathematical and statistical methods that are used to determine the most influential variables, to analyze the effects of variables, and to optimize the variable with the aim of obtaining the best value of the response (Muhammet and Berkant, 2012). In the present study, the RSM was adopted to develop a second-order regression model. The model was used to predict the strength of the weld joint and to demonstrate the response of the process parameters in the form of a response surface using Design Expert 10.0.1 software. The regression model obtained from RSM was further utilized to estimate the optimum values of process parameters using a metaheuristic search procedure. For this, the model was embedded with the Simulated Annealing Optimization (SAO) algorithm using MATLAB v2016 software. A general second-order polynomial equation in three variables is specified by:

$$y = m_0 + m_1x_1 + m_2x_2 + m_3x_3 + m_{11}x_1^2 + m_{22}x_2^2 + m_{33}x_3^2 + m_{12}x_1x_2 + m_{23}x_2x_3 + m_{13}x_1x_3 \quad (3.2)$$

where, x_1, x_2 and x_3 are the independent variables and y is their estimated outcome. In the present case, y is the predicted weld strength and x_1, x_2, x_3 are W_t, W_p and V_a respectively; m_0, m_1, m_2, m_3, m_{11}, m_{22}, m_{33}, m_{12}, m_{23} and m_{13} are the coefficients. So, in terms of the actual weld parameters, the following regression model was developed to calculate the predicted weld strength (W_{Sp}) :

$$W_{Sp} = m_0 + m_1.W_t + m_2.W_p + m_3.V_a + m_{11}.W_t^2 + m_{22}.W_p^2 + m_{33}.V_a^2 + m_{12}.W_t.W_p + m_{23}.W_p.V_a + m_{13}.W_t.V_a \quad (3.3)$$

Design Expert 10.0.1 was employed to calculate the value of the coefficients m_0, m_1, m_2 etc. in the regression equations by giving the experimental values of the tensile-shear load as an input at 95% confidence level for all the three combinations of PB, Cu, and Al and are shown in Table 3.18.

Table 3.18: Coefficient obtained for regression equations for PB-PB, PB-Cu and PB-Al

Term	PB-PB			PB-Cu			PB-Al		
	Coeffi-cient	T-value	P-value	Coeffi-cient	T-value	P-value	Coeffi-cient	T-value	P-value
	Estimate	Estimate	Estimate	Estimate	Estimate	Estimate	Estimate	Estimate	Estimate
Constant	– 6735.23	36.55	0	-7252.01	36.55	0	-2739.62	36.55	0
Wt	– 3805.71	11.27	0.0001	7376.63	11.27	0.0001	7878.73	11.27	0.0001
Wp	484.65	17.94	< 0.0001	636.87	17.94	< 0.0001	-7045.2	17.94	< 0.0001
Va	446.58	6.58	0.0009	265.18	6.58	0.0009	193.25	6.58	0.0009
Wt - Wp	282.43	1.19	0.1593	8750	1.19	0.1593	-4642.86	1.19	0.1593
Wt - Va	142.04	4.22	0.015	-0.36	4.22	0.015	-110	4.22	0.015
Wp - Va	97.5	4.98	0.0023	13.39	4.98	0.0023	84.69	4.98	0.0023
W_t^2	– 243.41	-2.93	0.5755	-4491.25	-2.93	0.5755	-3052.4	-2.93	0.5755
W_p^2	– 565.08	-6.36	0.0008	-9945.31	-6.36	0.0008	17596.94	-6.36	0.0008
V_a^2	– 12.25	-3.25	0.0296	-3.83	-3.25	0.0296	-2.8	-3.25	0.0296

Based on the results shown in Tables 3.18, the final regression models in terms of actual factors have been developed to calculate the predicted weld strength (W_{Sp}) for PB-PB, PB-Cu and PB-Al joints and shown by Equations 3.4, 3.5, and 3.6 respectively:

For PB-PB ultrasonic welded joint:

$$[W_{Sp}]_{PB\text{-}PB} = -6735.23 - 3805.71 * W_t + 484.65 * W_p + 446.58 * V_a + 282.44 * W_t * W_p + 142.04 * W_t * V_a + 97.50 * W_p * V_a - 243.41 * W_t^2 - 565.08 * W_p^2 - 12.25 * V_a^2 \quad (3.4)$$

For PB-Cu ultrasonic welded joint:

$$[W_{Sp}]_{PB\text{-}Cu} = -7252.01 + 7376.62 * W_t + 636.87 * W_p + 265.18 * V_a + 8750.00 * W_t * W_p - 0.36 * W_t * V_a + 13.39 * W_p * V_a - 4491.25 * W_t^2 - 9945.31 * W_p^2 - 3.83 * V_a^2 \quad (3.5)$$

For PB-Al ultrasonic welded joint:

$$[W_{Sp}]_{PB\text{-}Al} = -2739.62 + 7878.73 * W_t - 7045.2 * W_p + 193.25 * V_a - 4642.86 * W_t * W_p - 110 * W_t * V_a + 84.69 * W_p * V_a - 3052.40 * W_t^2 + 17596.94 * W_p^2 - 2.8 * V_a^2 \quad (3.6)$$

3.9.1 Adequacy of the Regression Model

The adequacy of the regression model was checked by the Analysis of Variance (ANOVA) technique (Montgomary, 2001). Table 3.19 and Table 3.20 show the results of the ANOVA and the regression statistics of the model depicted by Equation 3.4 for the PB-PB combination. Similarly, Tables 3.21 to 3.24 are related to the ANOVA results and regression statistics of the models shown by Equations 3.5 and 3.6 for PB-Cu and PB-Al combinations, respectively.

As shown in ANOVA Tables 3.19, 3.21, and 3.23, the model F-values (55.28 for PB-PB, 27.07 for PB-Cu, and 24.05 for PB-Al) and P-values (< 0.05 for all combinations) at the desired confidence level (95%), imply that the models are significant for PB-PB, PB-Cu, and PB-Al. The regression statistics of the models shown in Tables 3.20, 3.22, and 3.24 also demonstrate the models' adequacy. The "Adj. R^2" values are high enough. It indicates that the response is affected significantly by all the terms in the respective Equations 3.4, 3.5 and 3.6.

Table 3.19: Results of the ANOVA analysis for the experimental data for PB-PB

Source	SoS ($x 10^3$)	DoF	MS ($x 10^3$)	F-Value	P-Value Prob>F	Inference
Model	4556.3	9	506.3	55.28	0.0002	Significant
W_t	1071.4	1	1071.4	116.99	0.0001	Significant
W_p	2041.9	1	2041.9	222.96	< 0.0001	Significant
V_a	460.2	1	460.2	50.25	0.0009	Significant
W_t - W_p	25	1	25	2.73	0.1593	Not significant
W_t - V_a	121.1	1	121.1	13.22	0.015	Significant
W_p - V_a	298.1	1	298.1	32.55	0.0023	Significant
W_t^2	3.3	1	3.3	0.36	0.5755	Not significant
W_p^2	482.9	1	482.9	52.73	0.0008	Significant
V_a^2	83.15	1	83.15	9.08	0.0296	Significant
Residual	45.8	5	9.2			Significant
Lack of Fit	28.1	3	9.4	1.05	0.5204	Not significant
Error	17.7	2	8.9	-	-	-
Total	4602.1	14	-	-	-	-

Table 3.20: Regression statistics of the model for PB-PB

S. No.	Model Statistic	P-value
1	Std. Dev.	95.69
2	Mean	1478.4
3	C.V. %	6.47
4	R^2	0.97
5	Adj. R^2	0.92
6	Pred. R^2	0.89
7	Adeq. Pre.	22.82

Table 3.21: Results of the ANOVA analysis for the experimental data for PB-Cu

Source	SoS ($x 10^2$)	DoF	MS ($x 10^2$)	F-Value	P-Value Prob>F	Inference
Model	24330	9	2704	27.07	0.0001	Significant
W_t	14170	1	14170	141.87	< 0.0001	Significant
W_p	6944	1	6944	69.52	< 0.0001	Significant
V_a	695.6	1	695.6	6.96	0.0335	Significant
W_t - W_p	784	1	784	7.85	0.0265	Significant
W_t - V_a	0.0025	1	0.0025	2.5×10^{-5}	0.9961	Not Significant
W_p - V_a	0.5625	1	0.5625	5.6×10^{-3}	0.9423	Not Significant
W_t^2	1191	1	1191	8.74	0.0212	Significant
W_p^2	318.14	1	318.14	2.33	0.1703	Not Significant
V_a^2	26.68	1	26.68	0.20	0.6714	Not Significant
Residual	699.2	7	99.88	-	-	Significant
Lack of Fit	512.12	3	170.71	3.65	0.1216	Not significant
Error	187.07	4	46.76	-	-	-
Total	25030.1	16		-	-	-

Table 3.22: Regression statistics of the model for PB-Cu

S. No.	Model Statistic	P-value
1	Std. Dev.	99.94
2	Mean	1475.24
3	C.V. %	6.77
4	R^2	0.82
5	Adj. R^2	0.81
6	Pred. R^2	0.86
7	Adeq. Pre.	18.67

Table 3.23: Results of the ANOVA analysis for the experimental data for PB-Al

Source	SoS ($x 10^2$)	DoF	MS ($x 10^2$)	F-Value	P-Value Prob>F	Inference
Model	8719.45	9	968.82	24.05	0.0002	Significant
W_t	3184.02	1	3184.02	79.04	< 0.0001	Significant
W_p	2941.44	1	2941.44	73.02	< 0.0001	Significant
V_a	96.60	1	96.60	2.40	0.1654	Not Significant
W_t - W_p	264.06	1	264.06	6.55	0.0375	Significant
W_t - V_a	370.56	1	370.56	9.20	0.0190	Significant
W_p - V_a	17.22	1	17.22	0.43	0.5341	Not Significant
W_t^2	1543.40	1	1543.40	38.25	0.0005	Significant
W_p^2	309.42	1	309.42	7.68	0.0276	Significant
V_a^2	50.91	1	50.91	1.26	0.2979	Not Significant
Residual	281.99	7	40.28			
Lack of Fit	160.48	3	53.49	1.76	0.2932	Not Significant
Error	121.50	4	30.37			
Total	900144.24	16				

Table 3.24: Regression statistics of the model for PB-Al

S. No.	Model Statistic	P-value
1	Std. Dev.	83.47
2	Mean	1410.5
3	C.V. %	4.5
4	R^2	0.88
5	Adj. R^2	0.86
6	Pred. R^2	0.88
7	Adeq. Pre.	17.32

The extent to which the model can be used to predict the response is explained by "Pred. R^2". A difference of less than 0.1 between the values of "Pred. R^2" and "Adj. R^2" indicates that the fitment of data in the model is very well. The value of "Adeq. Pre." greater than 4 is preferable as it shows the signal-to-noise ratio. The "Adeq. Pre." ratios of 22.82, 18.67 and 17.32 for PB-PB, PB-Cu and PB-Al respectively, indicate an adequate amount of signals. The insignificant "Lack of Fit" is also an indicator of the adequacy of the model. For PB-PB, the "Lack of Fit F-value" of 1.05 implies that the lack of fit is not significant relative to the pure

error. There is a 52.04% chance that "Lack of Fit F-value" of this size, could occur due to noise. Similarly, for PB-Cu and PB-Al, "Lack of Fit F-value" is 3.65 and 1.76. Both values imply that the lack of fit is insignificant in comparison to the pure error. Therefore, the regression statistics clearly indicate that the designed models can be efficiently used to predict the weld strength.

3.9.2 Comparison of Experimental and Predicted Results

The predicted tensile-shear load of the weld coupons was estimated with the established regression model. The experimental tensile-shear load and the predicted load were compared and tabulated in Table 3.25 to Table 3.27 for PB-PB, PB-Cu, and PB-Al respectively.

It is clear from Table 3.25 that the experimental and predicted values of the tensile-shear load are very close to each other. The absolute percent deviation is very small except for a few combinations of parameters as shown in Figure 3.12.

Table 3.25: Experimental and predicted tensile-shear loads for PB-PB

Run Order	Wt (sec)	Wp (MPa)	Va (µm)	Mean Exp. Load W_{Se} (N)	Pred. Load W_{Sp} (N)	Absolute % Deviation
1	1.2	0.28	28.0	1653.33	1539.50	6.89
2	0.85	0.28	31.5	1781.67	1767.27	0.81
3	0.85	0.36	28.0	1226.67	1248.91	1.81
4	0.50	0.2	31.5	636.33	584.71	8.11
5	0.85	0.2	28.0	703.67	784.50	11.49
6	1.20	0.28	35.0	2306.67	2274.60	1.39
7	0.50	0.28	35.0	1246.67	1287.26	3.26
8	0.85	0.2	35.0	738.33	717.18	2.87
9	0.50	0.28	28.0	1333.67	1156.58	3.28
10	0.85	0.36	35.0	2353.33	2367.18	0.59
11	1.20	0.36	31.5	2416.67	2326.05	3.75
12	0.85	0.28	31.5	1853.33	1767.27	4.64
13	0.85	0.28	31.5	1803.33	1767.27	2.00
14	0.50	0.36	31.5	1396.67	1436.96	2.88
15	0.85	0.28	31.5	1666.67	1767.27	6.04
16	1.20	0.2	31.5	1196.67	1157.47	3.28
17	0.85	0.28	31.5	1799.33	1767.27	1.78

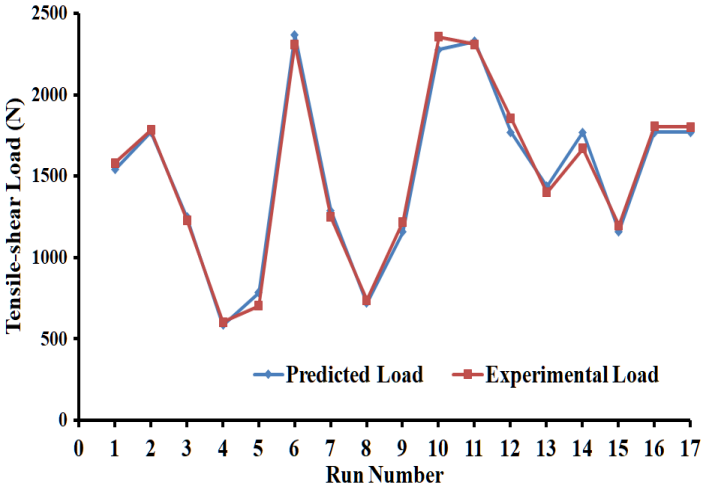

Figure 3.12: Graph between the predicted and experimental values of the tensile-shear load for PB-PB

Table 3.26: Experimental and predicted tensile-shear loads for PB-Cu

Run Order	Wt (sec)	Wp (MPa)	Va (μm)	Mean Exp. Load W_{Se} (N)	Pred. Load W_{Sp} (N)	Absolute % Deviation
1	0.8	0.30	28.0	1785.33	1698.87	4.84
2	1.0	0.14	31.5	1345.33	1354.75	0.70
3	0.6	0.30	31.5	1112.00	1102.25	0.88
4	0.6	0.22	28.0	775.33	870.87	12.32
5	1.0	0.22	35.0	1995.00	1899.12	4.81
6	0.8	0.14	35.0	1209.67	1296.12	7.15
7	0.8	0.22	31.5	1634.67	1612.00	1.39
8	0.6	0.22	35.0	1017.00	1057.87	4.02
9	0.8	0.22	31.5	1617.33	1611.80	0.34
10	1.0	0.22	28.0	1821.00	1713.12	5.92
11	0.8	0.22	31.5	1701.33	1611.80	5.26
12	0.8	0.22	31.5	1685.67	1611.80	4.38
13	0.6	0.14	31.5	886.66	793.00	10.56
14	0.8	0.22	31.5	1521.33	1611.80	5.95
15	0.8	0.14	28.0	1118.67	1117.12	0.14
16	1.0	0.30	31.5	2129.67	2224.00	4.43
17	0.8	0.30	35.0	1891.33	1893.47	0.11

Similarly, the estimated and predicted values of tensile-shear load and their absolute percent deviation for dissimilar PB-Cu and PB-Al combinations are shown in Table 3.26 and Table 3.27. It is evident from the results that both the values are very close to each other for both the combinations, as shown in Figure 3.13 and Figure 3.14 respectively. Therefore, it is proved that the model equations developed for predicting the weld strength for PB-PB, PB-Cu, and PB-Al can be efficiently utilized as the model is competent enough to predict the response.

Table 3.27: Experimental and predicted tensile-shear load for PB-Al

Run Order	Wt (sec)	Wp (MPa)	Va (μm)	Mean Exp. Load W_{Se} (N)	Pred. Load W_{Sp} (N)	Absolute % Deviation
1	0.70	0.20	28.0	1433.33	1460.25	1.88
2	0.45	0.27	28.0	1372.67	1475.80	7.51
3	0.70	0.27	24.5	1574.33	1509.86	4.10
4	0.45	0.34	24.5	1642.67	1644.11	0.09
5	0.20	0.27	31.5	1120.00	1182.25	5.56
6	0.45	0.27	28.0	1553.33	1475.80	4.99
7	0.45	0.27	28.0	1460.00	1475.80	1.08
8	0.20	0.20	28.0	939.667	898.75	4.35
9	0.45	0.27	28.0	1498.67	1475.80	1.53
10	0.70	0.27	31.5	1395.33	1388.75	0.47
11	0.45	0.20	24.5	1286.67	1308.49	1.70
12	0.45	0.27	28.0	1448.33	1475.80	1.90
13	0.20	0.34	28.0	1538.33	1444.75	6.08
14	0.70	0.34	28.0	1739.67	1681.25	3.36
15	0.45	0.20	31.5	1371.00	1350.00	1.53
16	0.45	0.34	31.5	1810.00	1775.00	1.93
17	0.20	0.27	24.5	981.00	889.74	9.30

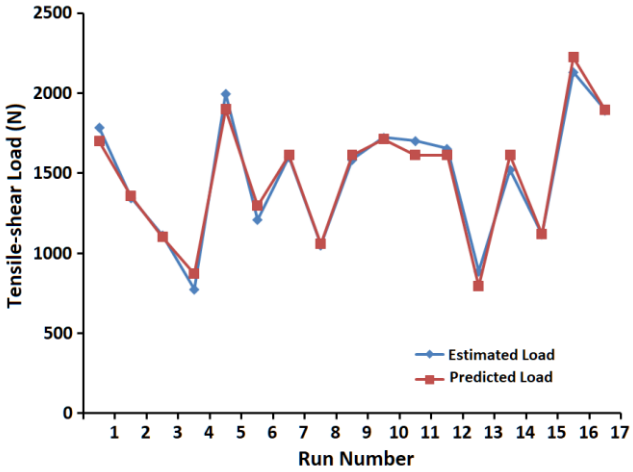

Figure 3.13: Graph between the predicted and the experimental values of the tensile-shear load for PB-Cu

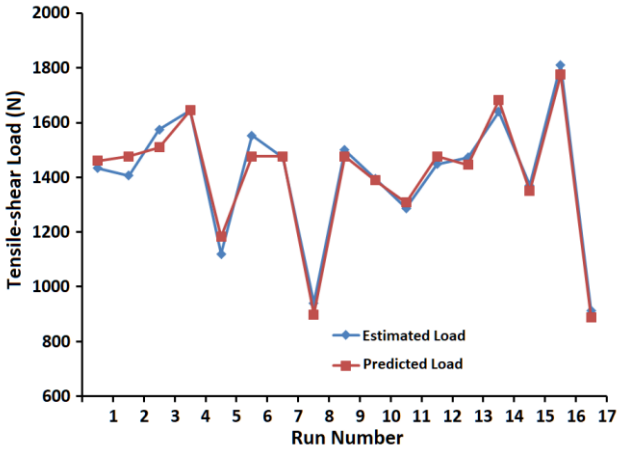

Figure 3.14: Graph between the predicted and the experimental values of the tensile-shear load for PB-Al

The coefficient of determination (R^2) was also calculated using the following equation (A. M. Brown, 2001):

$$R^2 = \sum \left(W_{Sp} - W_{Sa}\right)^2 / \sum (W_{Se} - W_{Sa})^2 \qquad (3.7)$$

where, W_{Sa} is the mean value of the experimental weld strength (W_{Se}) of weld coupons obtained by measuring the tensile-shear load on UTM. The value of R^2 calculated using the expression 3.7 is obtained as 0.97, 0.82, and 0.88 respectively, for PB-PB, PB-Cu, and PB-Al. The values of R^2 are sufficiently high and indicate a strong relationship between the experimental and predicted weld strength. Such a high value of the coefficient of determination indicates that the experimental as well as the predicted values of weld strength

are highly correlated. Hence, the weld strength of ultrasonically welded weld coupons for these metal combinations can be predicted without error using the regression equations**.**

3.9.3 Residual Plots

A residual is defined as the value obtained by the algebraic difference between the observed value and the estimated value of an independent variable. Hence, each data point of the variable has a residual. The residual plots are drawn between the residuals on the vertical axis and the value of the variable on the horizontal axis. The residual points are supposed to be dispersed randomly on both sides of the horizontal axis for the regression model to be appropriate (Martin et al., 2017). The residual pots are shown in Figure 3.15 to Figure 3.17 for PB-PB, PB-Cu, and PB-Al, respectively.

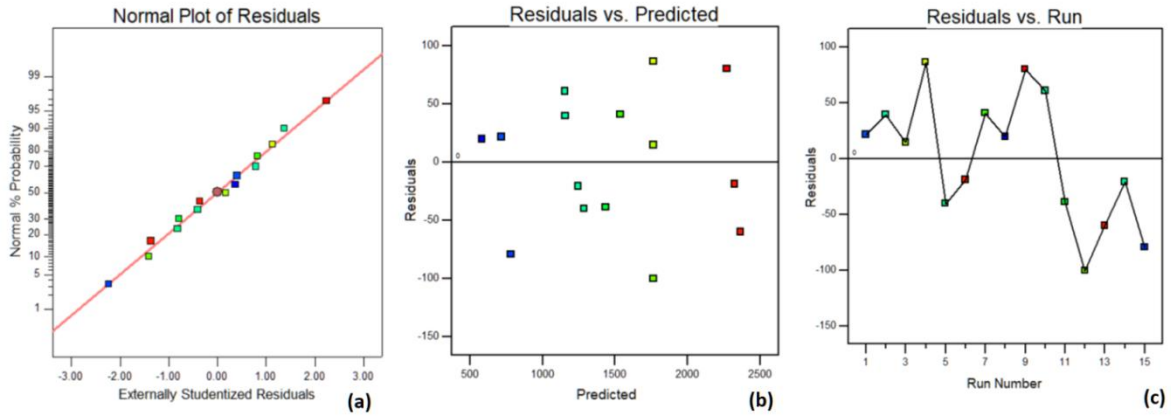

Figure 3.15: Residual plots drawn for PB-PB

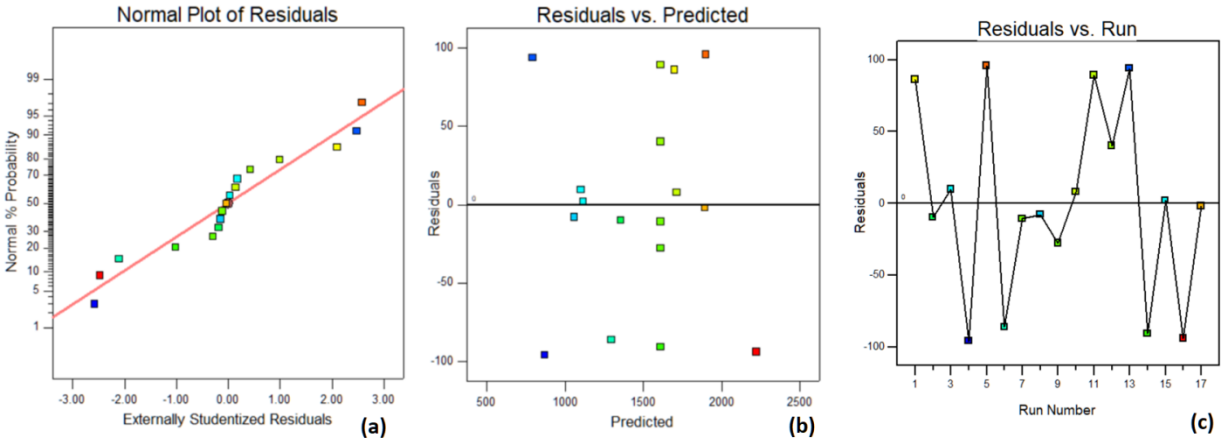

Figure 3.16: Residual plots drawn for PB-Cu

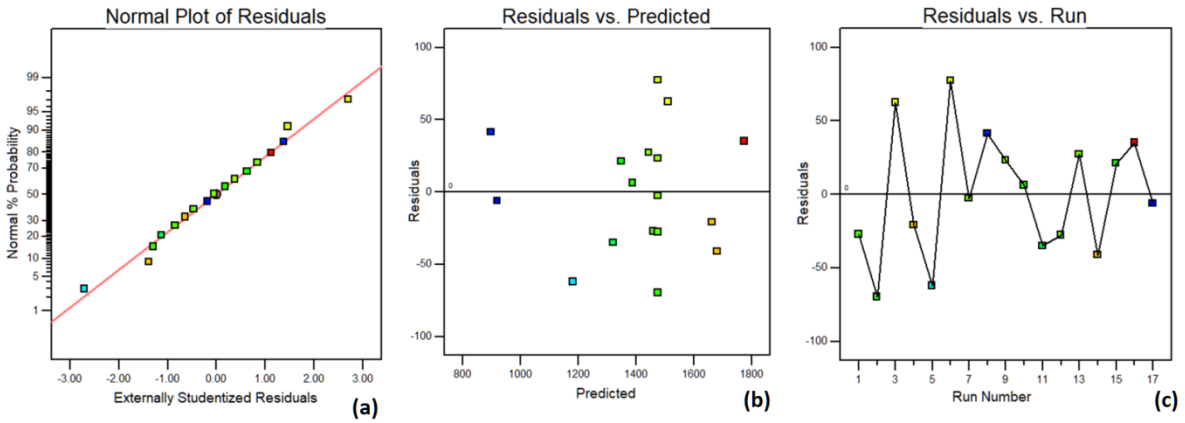

Figure 3.17: Residual plots drawn for PB-Al

It is clear from the normal plots of residuals shown in Figure 3.15 (a), Figure 3.16 (a) and Figure 3.17 (a) that the residual values are very close to the straight line showing the normal distribution of the errors. Figure 3.15 (b), Figure 3.16 (b), and Figure 3.17 (b) show that the residual values are dispersed randomly about the zero line on both sides. It shows that the variance of the errors is zero. In Figure 3.15 (c), Figure 3.16 (c), and Figure 3.17 (c) the dispersion of the residuals is shown on both sides of the zero line. All the points fall in the range of -100 and +100 randomly (H. S. Hasan, 2009).

3.10 Optimization of the Process Parameters

RSM gives many useful information but different optimal areas are obtained due to consideration of only two parameters at a time. Therefore, an optimization technique is essential to reach to an accurate optimal solution. The regression model obtained from RSM was further utilized to estimate the optimum values of process parameters using a metaheuristic search procedure. For this, the model was embedded with the Simulated Annealing Optimization algorithm using MATLAB v2016 software. SAO algorithm applied in this work gives the optimal values of all the three process parameters.

3.10.1 Simulated Annealing Optimization Algorithm

Simulated Annealing Optimization is a metaheuristic optimization technique developed by Kirkpatrick et al. in 1983 (S. Kirkpatrick, 1983) on the pattern of the annealing process where the metal is initially heated to a higher temperature and then cooled down to a lower temperature in a controlled manner to improve the properties by optimizing the grain structure of the material. This algorithm optimizes a problem by approximating a global

optimum in a larger search space.

3.10.2 Terminology for Simulated Annealing Optimization

Ingber Lester (2012) defined the important terms of SAO as follows:

a. Objective function (ΔE): It is the function that is required to be optimized. The algorithm attempts to reach the global minimum of the objective function.
b. Temperature (T′): Temperature is an important parameter in SAO. It takes some value as the 'initial temperature' in the beginning. Afterwards, it decides the gap between the next and the current trial point.
c. Rate of cooling: This criterion decides the next value of the temperature after selecting the best point so far. By default, the rate of cooling is such that the next temperature is 95% of the previous temperature. A better optimal solution is obtained with a lower rate of temperature fall but with a longer run time.
d. Acceptance function: It becomes the criterion to decide whether the new trial point is acceptable or not, depending upon its quality with respect to the current point. If the new point is better than the current, it is accepted and made the next point. But even if it is not better than the current point, the algorithm can still assign it the new next point based on the result of the acceptance function, which gives a probability value within an acceptable range.
e. Annealing parameter: This parameter is a substitute for the iteration number. To increase the temperature value, the annealing parameter is set at a value that is lower than the most recent iteration.
f. Re-annealing: This step is the reverse of annealing. The temperature decreases continuously during the annealing process, whereas during re-annealing, the algorithm increases the temperature once the algorithm finds some local optimal solution and starts searching for the optimal solution at a higher temperature. This way, the algorithm protects itself from getting trapped in a local minimum.

Imitating the annealing process, the SAO starts with a higher value of T′ and reaches to the next point of temperature randomly. The difference in estimation of the values of the objective function (E) at both points is calculated; if the value at the new point is better, the new point is chosen; if it is inferior, the SAO algorithm chooses this new point based on the Boltzmann probability distribution criterion to expand the search space and avoid the local

optimized value. The value of T′ is reduced according to some specified rate of cooling after selecting a new point. Achieving a global optimum is similar to reaching the minimum energy state at the end. If the rate of cooling from temperature T′ is controlled precisely, the algorithm, after N number of iterations executed at every temperature, finally reaches either a satisfactorily small value of T′ or a very minor variation in the function value is observed (Sathiya et al., 2006). Figure 3.18 shows a flow chart for the SAO process.

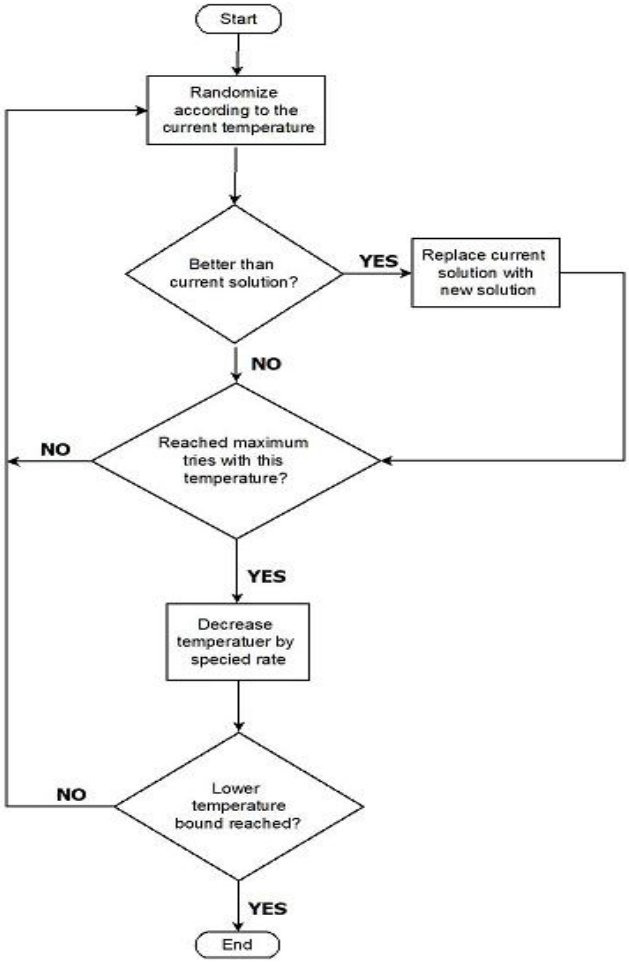

Figure 3.18: Flow chart for the simulated annealing algorithm

In the current work, the optimization problem is of maximization of the weld strength; therefore, the negative of the objective function was used in order to convert a minimization problem into a maximization problem. The objective function is a multivariable function of three parameters, namely W_t, W_p, and V_a. The standard mathematical format of the maximizing function, under the following constraints, has been given below for different combinations of materials:

(i) Find: W_t, W_p, V_a to maximize: Y (W_t, W_p, V_a) for PB-PB joint,

Subject to: $0.5 \text{ sec} \leq W_t \leq 1.2 \text{ sec}$

$0.20 \text{ MPa} \leq W_p \leq 0.36 \text{ MPa}$

$28 \text{ μm} \leq V_a \leq 35 \text{ μm}$

(ii) Find: W_t, W_p, V_a to maximize: Y (W_t, W_p, V_a) for PB-Cu joint,

Subject to: $0.6 \text{ sec} \leq W_t \leq 1.0 \text{ sec}$

$0.14 \text{ MPa} \leq W_p \leq 0.30 \text{ MPa}$

$28 \text{ μm} \leq V_a \leq 35 \text{ μm}$

(iii) Find: W_t, W_p, V_a to maximize: Y (W_t, W_p, V_a) for PB-Al joint,

Subject to: $0.2 \text{ sec} \leq W_t \leq 0.7 \text{ sec}$

$0.20 \text{ MPa} \leq W_p \leq 0.34 \text{ MPa}$

$24.5 \text{ μm} \leq V_a \leq 31.5 \text{ μm}$

where, Y = Weld strength and W_t, W_p, V_a are as defined earlier.

The optimization procedure was performed using the SAO function ***simulannealbnd*** of the MATLAB optimization toolbox. The initial value of temperature T′ was set at 400 for all three parameters. The scheme used for the rate of cooling was such that the temperature at a given state is 0.95 times the temperature at the previous state. To prevent the algorithm from being trapped in a local minimum, the re-annealing temperature was set at 50. This scheme may achieve a slow cooling at the beginning, but it increases as the targeted values come nearer. The code written for the simulation is shown in Appendix A-1.

3.11 Finite Element Analysis

Finite element analysis is the study and analysis of systems using the Finite Element Method (FEM). FEM is the technique to solve complex problems related to structural analysis, heat transfer, fluid flow, etc. where the larger problem is subdivided into smaller and simpler components called ‘finite elements’. The process of dividing a larger system into smaller elements or units which are interconnected either at the ends/nodes or at the edges or at the surfaces with a few other elements in the vicinity is known as ‘discretization’. The discretization is implemented in the form of a ‘mesh’. The approximate values of the

solutions are obtained for the discrete elements at the ‘nodes’, which are assembled to predict the solution for the entire system (M. Kuczmann, 2015).

3.11.1 Weld Zone Classification

The mechanism of joint formation in USMW makes it a complicated joining process due to the application of remarkably high-frequency vibrations to a small region for a very short period. The heat produced at the joining surfaces is not sufficient to melt the metal but is ample enough to reduce the yield strength of the base metal and, hence, produce a strong joint in the cold condition. The zone where deformation of the weld metal takes place and the formation of the micro-welds starts is known as the ‘deformation zone’. The effects of heat and stress are observed in this zone. This zone is surrounded by the ‘friction zone’, whose size is slightly larger than the deformation zone due to the vibrating sonotrode. Although the weld metal gets deformed in this zone, the formation of micro-welds does not take place due to insufficient heat generation. This zone is known as the thermo-mechanically affected zone. The deformation of metal and the friction between the faying surfaces are the primary factors of heat generation in the ‘deformation zone’ and the ‘friction zone’ respectively. Lastly, the heat affected zone is found adjacent to TMAZ, which is characterized by heat only (Chang and Frisch, 1974; DeVries, 2004; Shakil et al., 2014). Figure 3.19 shows the different zones of the affected area.

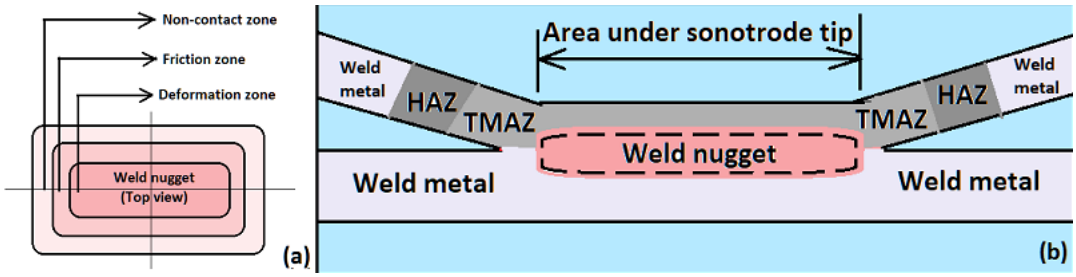

Figure 3.19: (a) Weld nugget divided into three zones: deformation zone, friction zone and non-contact zone (b) schematic view of the weld nugget, TMAZ and HAZ

This work involves the well-approximated estimation of the heat generation due to deformation of the metal and friction between the mating surfaces. Based on these estimations, a thermal model has been prepared and utilized to calculate the size of the weld zone, TMAZ and HAZ.

3.11.2 CAD Model of USMW

Modelling of the thermal field plays an important role in the prediction of the temperature profile at the weld interface. The response characteristics of the ultrasonic welding process can be forecast and the corresponding data can be utilized optimally by the industry. A 3-D Finite Element (FE) model of USMW was developed using Onshape, a cloud based CAD software. All the components of the FE model were presumed equivalent to the actual physically assembled USMW process in their orientation and physical attributes. The anvil, a stationary part of the ultrasonic metal welding machine, was made fixed in the FE model also by restricting all of its degrees of freedom. The CAD model equipped with the material properties, boundary conditions, and meshing was used to predict the temperature at different zones of the interface.

3.11.3 Heat Flux Calculation

The deformation of the metal and the friction between the faying surfaces are the primary factors of heat generation in the 'deformation zone' and the 'friction zone' respectively. The total heat flux 'H' is the sum of the heat flux due to deformation (H_d) of the material and the heat flux due to friction (H_f) between the contacting surfaces. The power dissipated (P) in the deformation zone produces heat flux at the interface, which is a function of the average sonotrode velocity (V_{avg}), temperature-dependent yield stress (Y_t), clamping force (F_c) and, the area of the deformation zone (A_d); whereas, the heat flux due to friction (H_f) between the mating surfaces of workpieces depends upon the dynamic coefficient of friction between the surfaces (μ_k), the clamping force (F_c), and the average sonotrode velocity (V_{avg}). The value of clamping force (F_c) was measured by a force sensor installed with the USMW experimental set-up. The display on the machine gives the values of the clamping force corresponding to the weld pressure in set-up mode. Based on that data, the Clamping Force Vs Weld Pressure graph was drawn (shown in Figure A2.1, Appendix A-2). The value of the dynamic coefficient of friction between the surfaces (μ_k) for all the combinations was obtained experimentally and is described in Appendix A-2.

The size of the deformation zone (A_d) increases continuously and may reach up to the size of the sonotrode tip (A_s) conforming to the perfect bonding. But practically, 100% bonding does not take place between the overlapping surfaces. The extent of bonding depends upon many factors, such as the penetration of the sonotrode teeth, the surface quality of the mating

surfaces, and the heat generated at the interface. A factor 'β' called 'bonding ratio' which is the ratio of the actual weld area (W_a) to the area of the sonotrode tip (A_s), may be defined. This term signifies the coverage of the area under the sonotrode tip that is transformed into a weld joint. Its value is an indicator of the effectiveness of the process. The ideal value of 'β' should be 1 when the whole of the area under the sonotrode tip is engrossed with the micro-welds, but due to the presence of oxide, asperities, and other contaminants, some portion remains unbounded and the value of 'β' is obtained below 1.

Table 3.28: Heat flux calculation for PB-PB

Run No.	F_c	W_t	V_a	W_a	$\beta = W_a / A_s$	$V_{avg} = 4 * V_a * V_f$	$H_d = (\beta/2) * V_{avg} * (((Y_t)^2) - ((F_c/A_s))^2)^{1/2}$	$H_f = \mu_k * F_c * V_{avg} / A_s$	$H = H_d + H_f$
	(N)	(sec)	(μm)	(mm^2)		(m/sec)	(kW/m^2)	(kW/m^2)	(kW/m^2)
Run 1	1650	1.20	28.0	57.4	0.44	2.24	145241.38	7846.89	153088.28
Run 2	1650	0.85	31.5	64.5	0.50	2.52	185677.90	8827.75	194505.66
Run 3	2200	0.85	28.0	50.1	0.39	2.24	128643.80	10462.52	139106.32
Run 4	1100	0.50	31.5	54.7	0.42	2.52	156049.77	5885.17	161934.94
Run 5	1100	0.85	28.0	33.0	0.25	2.24	82566.02	5231.26	87797.28
Run 6	1650	1.20	35.0	75.7	0.58	2.80	239318.19	9808.62	249126.80
Run 7	1650	0.50	35.0	48.7	0.37	2.80	152668.50	9808.62	162477.12
Run 8	1100	0.85	35.0	59.3	0.46	2.80	189901.83	6539.08	196440.91
Run 9	1650	0.50	28.0	40.8	0.31	2.24	102329.16	7846.89	110176.05
Run 10	2200	0.85	35.0	84.6	0.65	2.80	268007.92	13078.15	281086.07
Run 11	2200	1.20	31.5	75.3	0.58	2.52	215230.97	11770.34	227001.31
Run 12	1650	0.85	31.5	72.7	0.56	2.52	207959.25	8827.75	216787.01
Run 13	1650	0.85	31.5	69.2	0.53	2.52	196818.58	8827.75	205646.33
Run 14	2200	0.50	31.5	50.9	0.39	2.52	144724.27	11770.34	156494.61
Run 15	1650	0.85	31.5	58.4	0.45	2.52	167110.12	8827.75	175937.87
Run 16	1100	1.20	31.5	33.5	0.26	2.52	96602.24	5885.17	102487.41
Run 17	1650	0.85	31.5	70.7	0.54	2.52	200532.14	8827.75	209359.89

The heat flux at the interface was calculated for all the three combinations of materials, viz. PB-PB, PB-Cu, and PB-Al as shown in Table 3.28 to 3.30. During the thermal modeling, the heat flux produced due to the deformation of metal under the sonotrode tip was applied as a boundary condition at the interfaces between the sonotrode tip and the upper weld sheet, whereas heat flux produced due to friction was applied between the overlapped portion of the upper and lower weld sheet.

Table 3.29: Heat flux calculation for PB-Cu

Run No.	F_c	W_t	V_a	W_a	$\beta = W_a / A_s$	$V_{avg}=4*V_a*V_f$	$H_d=(\beta/2)*V_{avg}*(((Y_t)^2)-((F_c/A_s))^2)^{1/2}$	$H_f = \mu_k*F_c*V_{avg} / A_s$	$H = H_d+H_f$
	(N)	(sec)	(µm)	(mm^2)		(m/sec)	(kW/m^2)	(kW/m^2)	(kW/m^2)
Run 1	1800	0.8	28.0	76.41	0.59	2.24	194721.16	8870.40	203591.60
Run 2	700	1.0	31.5	67.65	0.52	2.52	193251.81	3880.80	197132.60
Run 3	1800	0.6	31.5	55.43	0.43	2.52	159654.85	9979.20	169634.05
Run 4	1200	0.6	28.0	52.93	0.41	2.24	135397.67	5913.60	141311.27
Run 5	1200	1.0	35.0	105.32	0.81	2.8	334366.19	7392.00	341758.19
Run 6	700	0.8	35.0	49.21	0.38	2.8	156913.85	4312.00	161225.85
Run 7	1200	0.8	31.5	93.08	0.72	2.52	267492.95	6652.80	274145.75
Run 8	1200	0.6	35.0	54.94	0.42	2.8	173375.06	7392.00	180767.06
Run 9	1200	0.8	31.5	87.7	0.67	2.52	248917.05	6652.80	255569.85
Run 10	1200	1.0	28.0	75.25	0.58	2.24	191538.16	5913.60	197451.76
Run 11	1200	0.8	31.5	90.37	0.70	2.52	260062.59	6652.80	266715.39
Run 12	1200	0.8	31.5	72.23	0.56	2.52	208050.07	6652.80	214702.87
Run 13	700	0.6	31.5	50.39	0.39	2.52	144938.85	3880.80	148819.65
Run 14	1200	0.8	31.5	77.21	0.59	2.52	219195.62	6652.80	225848.41
Run 15	700	0.8	28.0	59.66	0.46	2.24	151958.68	3449.60	155408.28
Run 16	1800	1.0	31.5	110.16	0.85	2.52	315596.79	9979.20	325575.99
Run 17	1800	0.8	35.0	107.05	0.82	2.8	338286.76	11088.00	349374.76

Table 3.30: Heat flux calculation for PB-Al

Run No.	F_c	W_t	V_a	W_a	$\beta = W_a / A_s$	$V_{avg}=4*V_a*V_f$	$H_d=(\beta/2)*V_{avg}*(((Y_t)^2)-((F_c/A_s))^2)^{1/2}$	$H_f = \mu_k*F_c*V_{avg} / A_s$	$H = H_d+H_f$
	(N)	(sec)	(µm)	(mm^2)		(m/sec)	(kW/m^2)	(kW/m^2)	(kW/m^2)
Run 1	1100	0.70	28.0	48.65	0.37	2.24	122197.70	6292.68	128490.38
Run 2	1575	0.45	28.0	53.62	0.41	2.24	135349.71	9009.97	144359.68
Run 3	1575	0.70	24.5	69.86	0.54	1.96	155982.29	7883.72	163866.01
Run 4	2150	0.45	24.5	73.15	0.56	1.96	161641.38	10761.91	172403.29
Run 5	1575	0.20	31.5	44.85	0.35	2.52	129985.24	10136.22	140121.46
Run 6	1575	0.45	28.0	66.78	0.51	2.24	168361.83	9009.97	177371.80
Run 7	1575	0.45	28.0	56.36	0.43	2.24	141952.14	9009.97	150962.10
Run 8	1100	0.20	28.0	30.12	0.23	2.24	75960.73	6292.68	82253.41
Run 9	1575	0.45	28.0	62.89	0.48	2.24	158458.20	9009.97	167468.17
Run 10	1575	0.70	31.5	48.18	0.37	2.52	137412.97	10136.22	147549.18
Run 11	1100	0.45	24.5	73.65	0.57	1.96	141600.71	5506.09	147106.81
Run 12	1575	0.45	28.0	51.98	0.40	2.24	132048.50	9009.97	141058.47
Run 13	2150	0.20	28.0	60.44	0.46	2.24	151744.97	12299.32	164044.29
Run 14	2150	0.70	28.0	77.74	0.60	2.24	197928.22	12299.32	210227.54
Run 15	1100	0.45	31.5	57.51	0.44	2.52	163480.71	7079.26	170559.97
Run 16	2150	0.45	31.5	63.59	0.49	2.52	181846.55	13836.74	195683.30
Run 17	1575	0.20	24.5	33.15	0.26	1.96	75102.58	7883.72	82986.31

3.11.4 Assumptions for Thermal Modelling

The following assumptions were made for the execution of the thermal modelling and simulation work:

i. The simulation was executed in a transient condition, taking a time step of 0.1 sec.

ii. The complete assembly of the sonotrode was not included in the model, as the thermal conductivity of the sonotrode material is very low as compared to the weld metal, and

the process time in USMW is very small. Hence, only the sonotrode tip was included in the analysis.

iii. The clamping force plays an important role in the formation of the weld joint in USMW. So, it becomes imperative to give due consideration to its effect on different contact areas in the FE model. The contacting parts must have a large thermal contact conductance, being highly conductive soft metals with clean and flat faying surfaces. Pressure as well as vibratory motion also contributes to enhancing its value (L. S. Fletcher, 1988). So, the value of thermal contact conductance was taken as 10^4 W/m^2°C for the weld interface and the interface between the sonotrode tip and the upper weld coupon based on the study conducted by Jedrasiak et al. (2014); and also on the data provided by the web portal, www.engineersedge.com.

iv. Ideally, for thin sheets, the area of deformation (A_d) can be considered equal to the sonotrode area (A_s) since the entire area beneath the sonotrode tip gets deformed. Hence, $A_d = A_s$ is assumed at the end of welding. The deformed area, which is not exactly equal to the sonotrode tip area, is taken care of by 'β', the bonding ratio, which signifies the extent of the area under the sonotrode tip that is transformed into a weld joint.

v. The loss of vibrational energy due to overhung of the weld coupon beyond the overlap is not taken into consideration (Bongsu Kang, 2014).

vi. The heat flux due to friction is produced at three interfaces viz. the sonotrode and the upper sheet, the upper and the lower sheets and the lower sheet and the anvil. But the heat flux due to friction is applied only at the interface between two sheets as the values of the heat flux at the other two interfaces are comparatively smaller. The portion of the weld metal below the sonotrode tip undergoes severe deformation, therefore, heat flux due to deformation is assumed as the main source of heat in this area.

vii. The heat flux values calculated according to the Equations a2.6 and a2.7 (Appendix A-2) were applied to interfaces only rather than to the entire assembly. It was done in accordance with the work of Jedrasiak et al. (2016), who established that in the case of thin metallic deforming sheets, the heat fluxes applied separately to the interface and the bulk do not significantly affect the temperature distribution at the interface.

viii. The upper surface of the sonotrode tip and the bottom surface of the anvil were kept at a fixed temperature of 30°C assuming there would be no heat flux across these surfaces in this short weld time.

ix. The outer surfaces of the model which were exposed to the air and not in contact with the sonotrode or the anvil were assigned with natural convection, having a convective heat transfer coefficient of 5 $Wm^{-2}°C^{-1}$ (Elangovan et al., 2009).

x. The ambient temperature was taken as 30°C and the whole model was set at this initial temperature.

3.11.5 Boundary Conditions

SimScale offers four types of boundary conditions for thermal modelling: fixed temperature value, surface heat flux, convective heat flux and volume heat flux. The four surfaces of the model were kept at a fixed temperature of 30°C; the top surface of the sonotrode tip, the bottom of the anvil, and the extreme ends of the weld strips. The heat flux due to deformation was fed to the bottom of the sonotrode tip, whereas heat flux due to friction was fed to the bottom of the overlapped portion of the upper sheet as surface heat fluxes. The values of these heat fluxes have been calculated for each run. The convective heat flux was considered for all the exposed surfaces with a convective heat transfer coefficient as 5 $Wm^{-2}°C^{-1}$. Lastly, the volume heat flux was not considered in the present case as there was no other source of heat in the system.

3.11.6 Modelling and Simulation of CAD Model

The CAD models of the ultrasonic welded joint between PB-PB, PB-Cu and PB-Al sheets were prepared and simulated for thermal analysis using SimScale Workbench 2.0 software (SimScale GmBH). SimScale Workbench is an open source cloud based CAE computing environment providing up to 96 core of computing capability for simulation (M. Winters, 2013).

It is very essential to choose the proper meshing type, element type, material properties, boundary conditions, and geometry of the model during FE analysis (Kremer et al., 1981). Figure 3.20 depicts the geometry, mesh, and working boundary conditions of the FE model of USMW. One of the most important aspects that must be taken into account to achieve simulation accuracy is creating a high-quality mesh. SnappyHexMesh, a mesh generator that produces meshes iteratively based on the model's geometry, is used for meshing on SimScale. Tet-dominant algorithms are frequently utilized in 3D models where robustness is more crucial. Necessary measures must be taken before the mesh is finalized. Geometries must be reliable and impenetrable. There shouldn't be any unusual characteristics like intersections or protruding outcrops. It must be enclosed and defect-free in order to have a clean geometry.

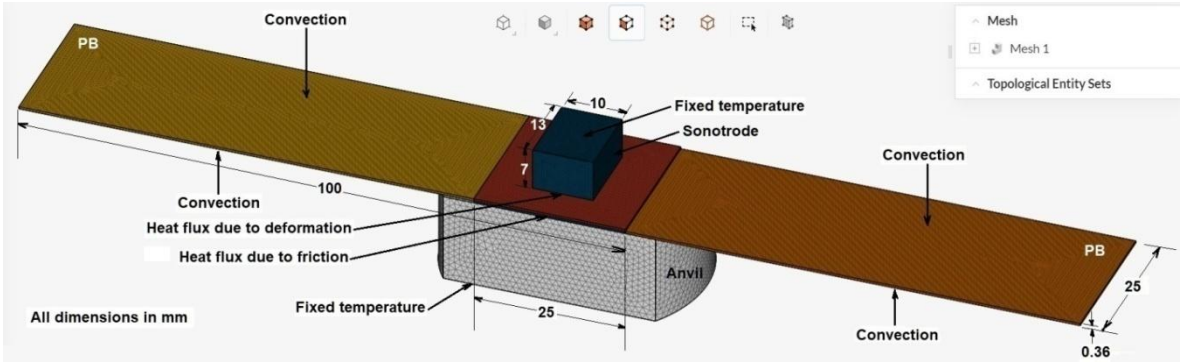

Figure 3.20: A 3D FE model of USMW showing geometry, meshing and boundary conditions

In addition to these broad guidelines, a mesh convergence study must be carried out to produce the best mesh design. A proper mesh convergence study provides a precise and efficient mesh design. It particularly becomes vital to achieve a balance between computing time and accuracy in the case of large and complicated meshes. A general mesh must be built for the problem scenario, a simulation must be run, and data must be collected, according to a mesh convergence study. After that, the procedure is repeated while the mesh fineness is gradually increased. The procedures are repeated with progressively finer mesh until the results produced deviate to a range of less than 1% to 5% depending on criteria. Considering all the above factors, the meshing of the model was kept to the finest with tetrahedral mesh elements graded from coarse to fine and the finest mesh at the central part. This meshing scheme was adopted to improve the computational accuracy of the analysis and to reduce the hourglass effect (Jedrasiak et al., 2015). Despite all efforts, it is almost impossible to achieve ideal values of the mesh quality parameters within the given constraints (Egorova et al., 2007). The main mesh quality parameters obtained are given the Table 3.31:

Table 3.31: Values of Mesh Quality Parameters

Mesh Quality Parameter	Value	Ideal Value
Aspect Ratio	2.4	Max value < 5
Skewness	Max. Value = 0.58, Average = 0.19	Max value < 0.95, Average < 0.33
Non-orthogonality	Max. Value = 66.80, Average = 22.39	Between 0 (ideal) and 90 (worst)
Volume Ratio	1.19	Near to 1 (ideal)
TriMaxAngle	80.09	Between 60 (ideal) and 180 (worst)
TriMinAngle	32.88	Between 0 (ideal) and 60 (worst)
TetEdgeRatio	18.4	<< 100

The CAD model, actually a replica of the USW process, was comprised of three parts connected closely with each other: the weld metals, the anvil, and the sonotrode. Accordingly, the model was associated with three types of materials: (i) the weld materials: phosphor bronze, copper and aluminium, (ii) the sonotrode material: Ti alloy and (iii) the anvil material: tool steel.

The physical, mechanical and thermal properties of these materials such as melting point, Young's modulus, yield strength, Poisson's ratio, thermal conductivity etc. were included in the model (J. Chaskalovic, 2008) and are shown in Table 3.32.

Table 3.32: Assignment of material properties to the CAD model

Property	Unit	Weld Material			Sonotrode Material – Ti alloy	Anvil Material – Tool Steel
		Phosphor Bronze	Copper	Aluminium		
		UNS C51100	UNS C10300	Al 3003-H12	Ti-6Al–4V	
Density	Kg/m^3	8860	8940	2730	4430	7670
Young's modulus	GPa	110	115	68.9	113.8	205
Yield Strength	MPa	295	205	124	880	-
Poisson's ratio	-	0.34	0.31	0.33	0.34	0.3
Thermal conductivity	W/m°C	84	386	163	6.7	20
Specific heat	J/kg°C	380	385	893	526.3	460

3.12 Weld Energy Effect

Many studies have been conducted to correlate the parameters with the microstructural evolution in the immediate vicinity of the weld interface (H. S. Shin & M. De Leon, 2015; Kido et al., 2010; Kim et al., 2011). In the present work, the weld coupons prepared under ECM were used to investigate the effects of welding energy on the mechanical, thermal, and microstructural characteristics of the weld joint to meet the objectives of the research.

3.12.1 Optical and Scanning Electron Microscopy

The metallurgical samples were prepared to examine weld attributes under a metallurgical microscope and Scanning Electron Microscope. The cutting of the welded samples was done parallel to the vibration direction across the centre of the overlap, passing through the row of indentation marks of the sonotrode tip as shown in Figure 3.21. The sectioning was done on a wire EDM machine so as to keep the residual stresses to a minimum. The sample preparation was accomplished as per the standard procedures of cold mounting in the epoxy resin, grinding, polishing, and etching.

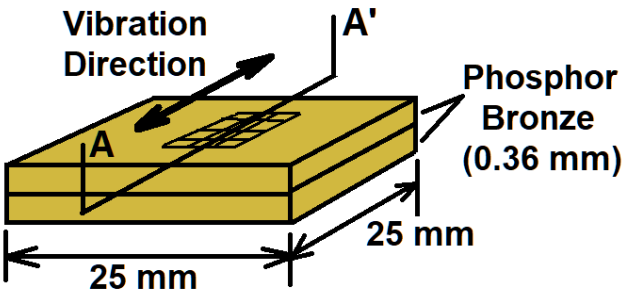

Figure 3.21: Sectioned view of the weld specimen used for microscopy

Initial microstructural examination of the weld interface of the selected specimens was done by images captured at different resolutions by optical microscope. Further analysis of the weld interface was done by SEM images of the weld samples using a ZEISS scanning electron microscope (Figure 3.22).

Figure 3.22: Scanning Electron Microscope

3.12.2 Weld Interface Characterization

The study of microstructural characterization of the weld interface was performed with the following aims:

- Investigation of the effect of weld energy on peak interface temperature and tensile-shear strength of the joint.
- Observing the changes in the failure mode of the weld coupons with varying energy levels

- Re-establishing the bonding mechanism.
- Assessment of TMAZ and HAZ

3.13 Summary

The detailed planning of the research has been discussed in this chapter. Different combinations of thin sheets of PB, Cu and Al alloys have been chosen for making lap joints by the Ultrasonic Spot Metal Welding set-up as per the Box-Behnken design of RSM under TCM and OFAT under ECM. The quality characterization is done by measuring the tensile-shear load, real-time interface temperature, and the interface area. The details of the equipment used, methods adopted, and software used for measuring the response parameters are briefed in this chapter. The following chapters provide the analysis of the results obtained.

CHAPTER 4

RESULTS AND DISCUSSION BASED ON EXPERIMENTATION USING RESPONSE SURFACE METHODOLOGY

4.1 Introduction

This chapter presents the results and discussion on the study of ultrasonic joints formed between PB-PB, PB-Cu and PB-Al under time control mode using the response surface method. The analysis of the results has been done on the basis of experimental and theoretical values. The values of the experimental tensile-shear loads were fed into the Design Expert software to calculate the coefficient of the regression equations developed during this work. The regression equations were further utilized for the optimization of the parameters. The detailed methodology of the work has been discussed in the previous chapter.

4.1.1 ANOVA Analysis

The ANOVA analysis was performed to evaluate the significance of the individual parameters and their interactions on the response parameter for all the three combinations of the weld metals (Montgomary, 2001). The results of ANOVA analysis for PB-PB, PB-Cu, and PB-Al are shown in Table 3.19, 3.21, and 3.23 in Section 3.9.1.

The ANOVA analysis of PB-PB (Table 3.19, Section 3.9.1) shows that the terms W_t, W_p, V_a, $(W_p)^2$, $(V_a)^2$ and interactions W_t-V_a, W_p-V_a are the significant terms. The term $(W_t)^2$ along with the interaction term W_t-W_p, have F-values greater than 0.05; hence these terms are not considered significant. The ANOVA results for the PB-Cu shown in Tables 3.21 (Section 3.9.1) indicate that the terms W_t, W_p, V_a, $(W_t)^2$ and interaction W_t-W_p are significant terms. The terms $(W_p)^2$, $(V_a)^2$ and interactions W_t-V_a and W_p-V_a have F-values greater than 0.1; so these terms are not considered significant. In the same manner, the ANOVA analysis of the PB-Al model (Tables 3.23, Section 3.9.1) depicts W_t, W_p, $(W_t)^2$, $(W_p)^2$ along with the interactions W_t-W_p, W_t-V_a as significant terms.

4.1.2 Main Effect and Interaction Effect Plots

According to the ANOVA table for PB-PB, the F-values of W_t, W_p and V_a are 116.99, 222.96 and 50.25 respectively ($\alpha = 0.05$). All the F-values exceed the critical value of $F_{0.95;1,5} = 6.607$. It indicates that all the parameters affect the tensile-shear load significantly, with W_p being the

most significant parameter, followed by W_t and V_a. (Gunaraj and Murugan, 1999). This is in agreement with the results of the main effect plots shown in Figure 4.1.

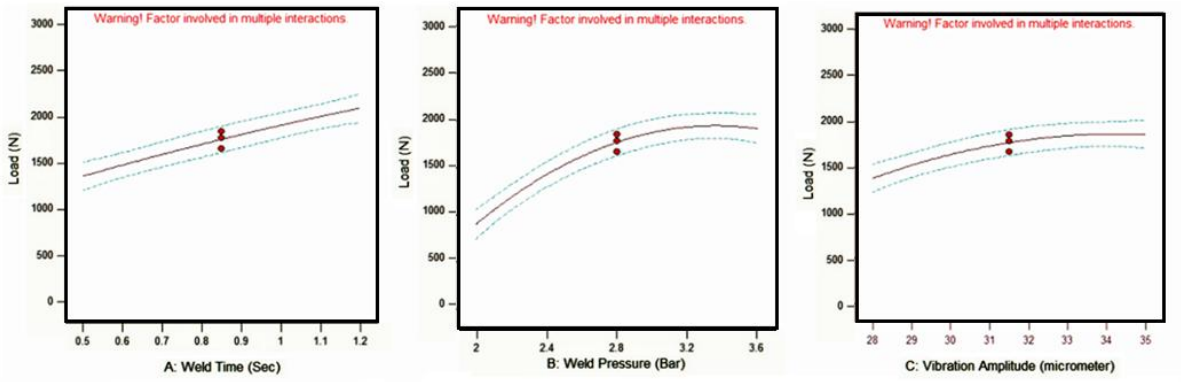

Figure 4.1: Main effect plots for PB-PB

Further, the F-value of interaction term W_p-V_a is 32.55, which is quite higher than the critical value of $F_{0.95;1,2}$ = 18.513; however, the F-value of interaction term W_t-V_a is 13.22, which is near to the critical value, and that of W_t-W_p interaction is quite less than the critical value. So, it can be concluded that the interaction between W_p-V_a, significantly affects weld strength. The interaction between W_t-V_a, also affects the weld strength to some extent due to the F-value being close to the critical value, but the weld strength is not affected much by the interaction W_t-W_p. The above facts were also clear from the interaction plots shown in Figure 4.2.

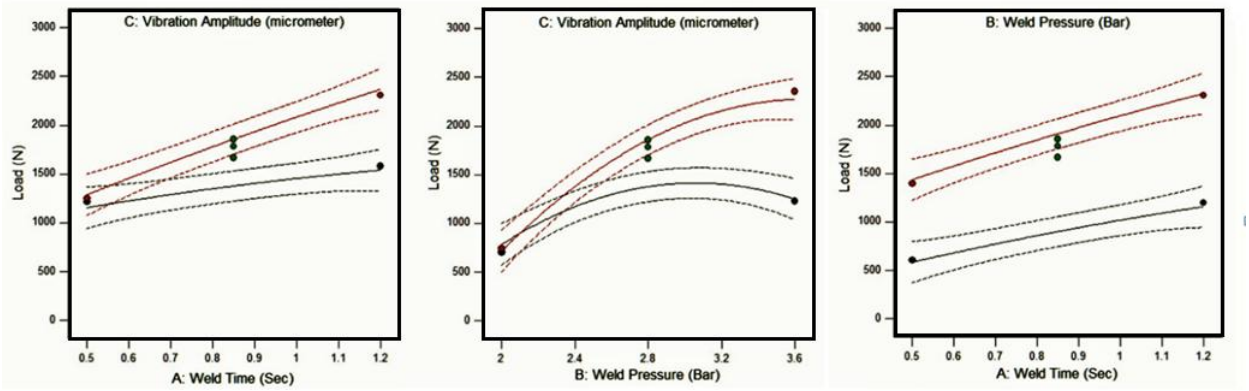

Figure 4.2: Interaction effect plots for PB-PB

The percent contribution of the significant terms associated with the regression model in case of PB-PB is shown in Figure 4.3. It is evident from the graph that effect of individual terms is more than that of their interactions.

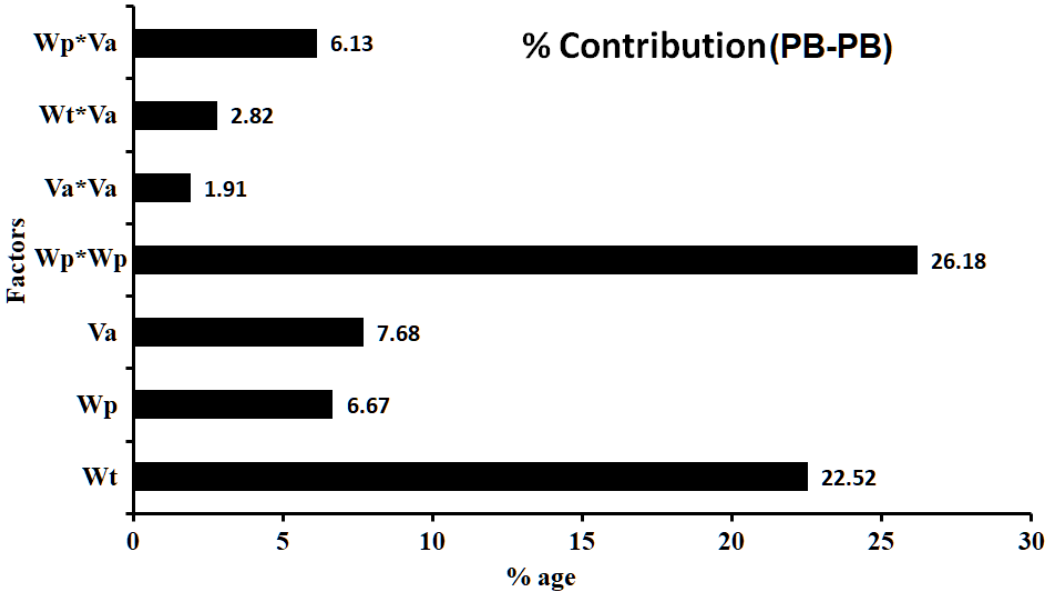

Figure 4.3: Percent contribution of significant terms for PB-PB

The significant parameters and their interactions for the ultrasonic welding of PB-Cu and PB-Al were also chosen on the basis of ANOVA analysis. It is visible from Table 3.21 (Section 3.9.1) that for PB-Cu, the F-values of W_t, W_p and V_a are 141.87, 69.52 and 6.96, respectively, for α=0.05. The F-values of W_t and W_p exceed the critical value of $F_{0.95;1,7}$ = 5.591 with a considerable difference, but the difference is very small in the case of V_a. It indicates that the weld strength was significantly affected by W_t and W_p but hardly affected by V_a. This is in agreement with the results of the main effect plots shown in Figure 4.4, drawn for PB-Cu joints.

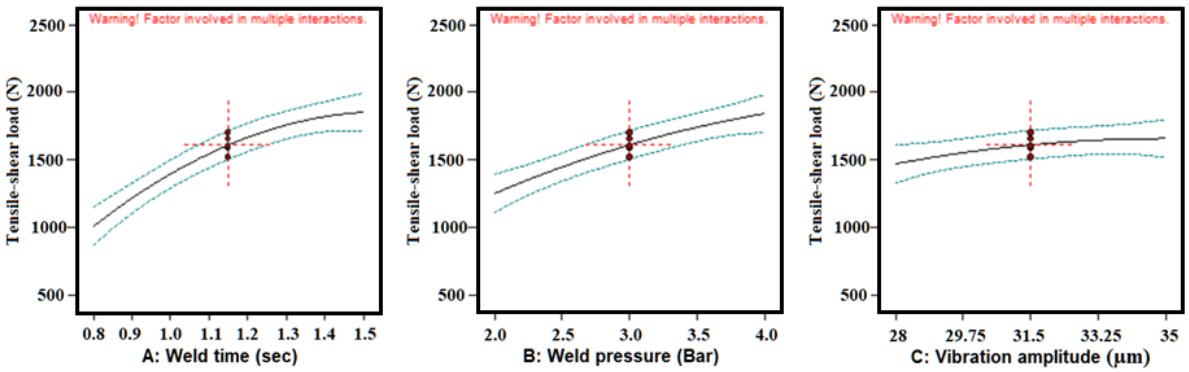

Figure 4.4: Main effect plots for PB-Cu

Further, the F-value of interaction term W_t-W_p is 7.85, which is slightly higher than the critical value of $F_{0.95;1,4}$ = 6.708; however, the F-values of interaction terms W_t-V_a and W_p-V_a are very small as compared to the critical F-value. So, it can be concluded that the interaction term W_t-W_p affects the weld strength. But the weld strength is not affected by the interactions W_t-V_a

and W_p-V_a. The above facts are also clear from the interaction plots shown in Figure 4.5, drawn for PB-Cu joints.

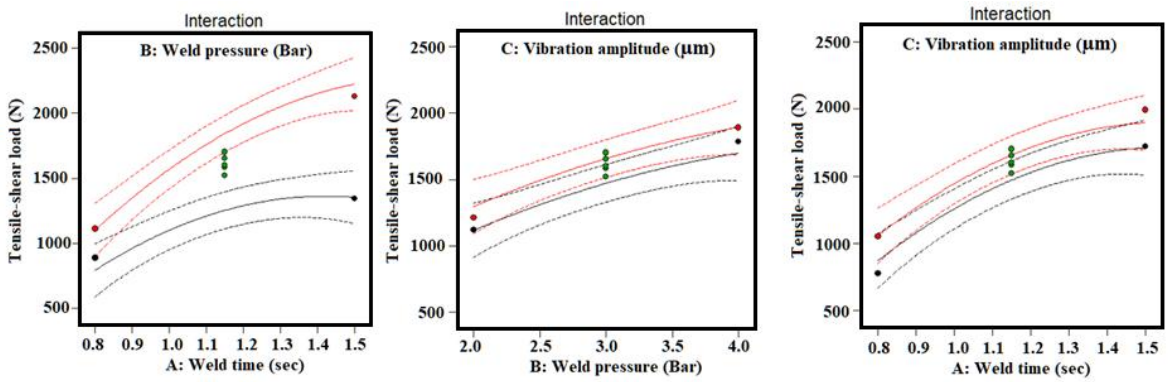

Figure 4.5: Interaction effect plots for PB-Cu

In a similar pattern, the ANOVA analysis for PB-Al joints was also performed. ANOVA Table 3.23 in Section 3.9.1 shows that W_t and W_p are the significant parameters as the F-values for W_t and W_p considerably exceed the critical value of $F_{0.95;1,7} = 5.591$. Similarly, the critical value of $F_{0.95;1,4} = 6.708$ is less than the F-value for the W_t-V_a interaction (= 9.20) and almost equal to the F-value for the W_t-W_p interaction (= 6.55), last interaction (W_p-V_a) has its F-value quite lower than this (=0.43). Hence, the interaction term W_t-V_a is the most significant, followed by the interaction W_t-W_p. The interaction term W_p-V_a does not affect the response parameter in the case of ultrasonic welding of PB-Al. This is in agreement with the results of the main effect plots and interaction plots shown in Figure 4.6 and Figure 4.7, respectively, drawn for PB-Al joints.

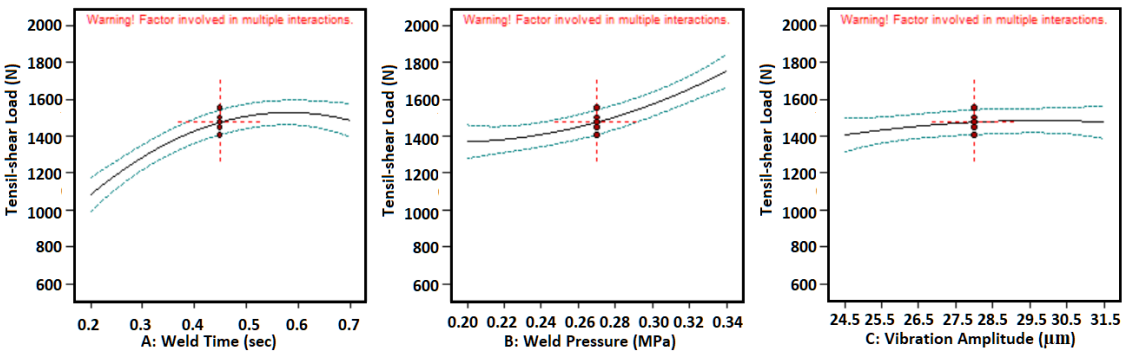

Figure 4.6: Main effect plots for PB-Al

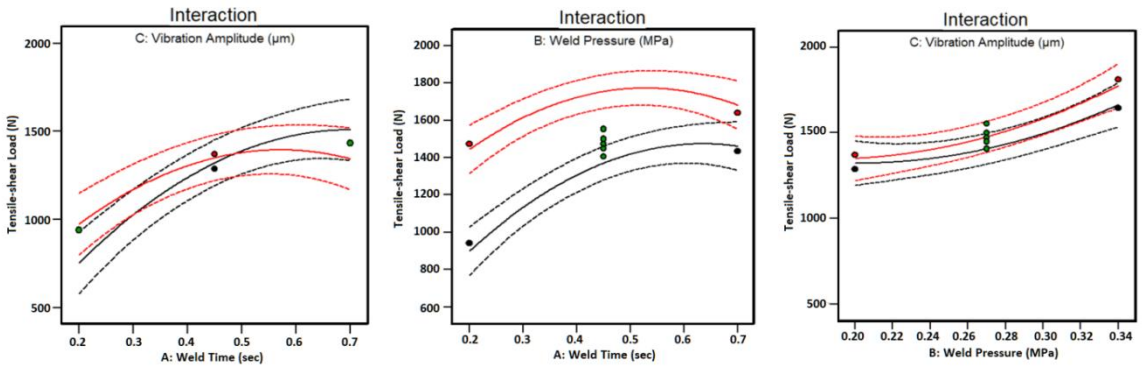

Figure 4.7: Interaction effect plots for PB-Al

The percent contribution of the significant terms associated with the regression models in case of PB-Cu and PB-Al are shown in Figure 4.8, and 4.9 respectively.

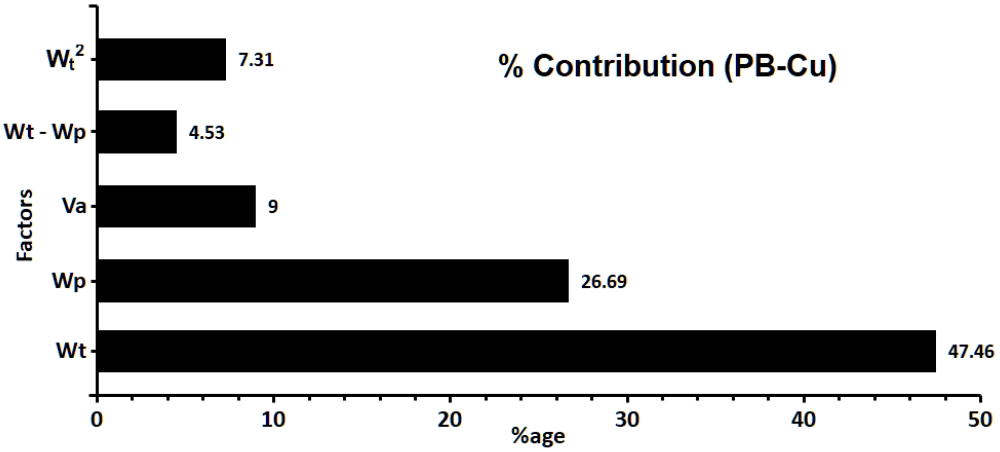

Figure 4.8: Percent contribution of significant terms for PB-Cu

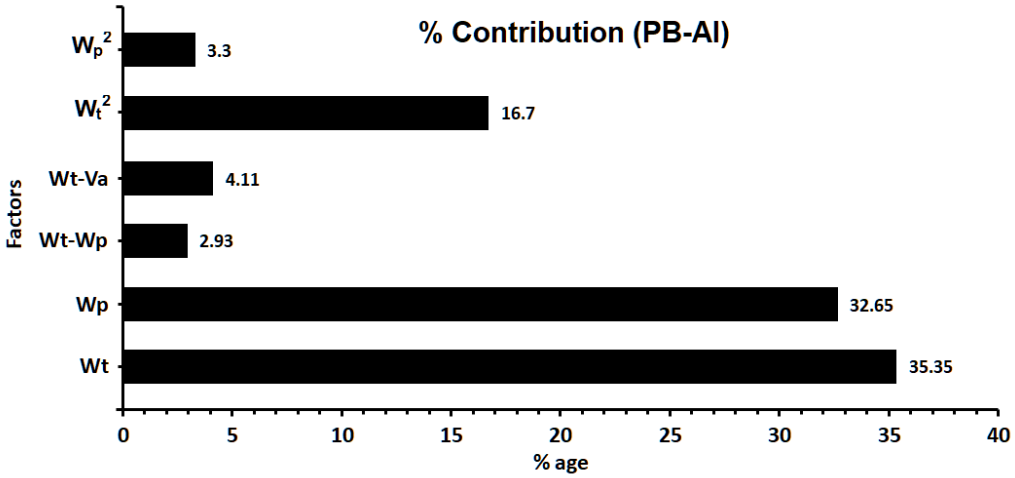

Figure 4.9: Percent contribution of significant terms for PB-Al

It is evident from the graphs that effect of individual terms on weld strength is greater than that of their interactions. A similar observation was made by Zhao et al. (2017) during the ultrasonic

welding of dissimilar magnesium and titanium alloys. They investigated the influence of parameters, and the clamping force was observed as the most significant parameter. But in another study by Zhao et al. (2017), the weld strength of the ultrasonically welded dissimilar joint between aluminium and steel was most significantly affected by the interaction of vibration time and vibration amplitude rather than individual parameters.

The possible cause of such differences lies in the fact that different metal combinations have different joining mechanisms. It is observed that weld pressure or the clamping force becomes important when a joint is made between two similar or dissimilar metals, which have a possibility to make metallurgical bonds with each other. The removal of the surface asperities due to higher pressure brings the faying surfaces closer to each other. On the other hand, some combinations were found to have solid state diffusion due to plastic deformation as their joining mechanism. Vibration amplitude is observed to be the most influential parameter in such cases, as observed by Annoni and Carboni (2011) since the material gets more interaction area to complete the bonding at the interface.

4.1.3 Response Surface Analysis

The interaction effects of different combinations of weld parameters W_p, W_t and V_a in the form of response surfaces and contour plots are shown in Figure 4.10 to Figure 4.18 for all three combinations of the weld metals. It was observed that all the response surfaces have a convex shape. The prediction of the optimal area between the two parameters was made with the help of these graphs. It is necessary to keep the third parameter constant to analyze any two factors simultaneously.

Figure 4.10 shows the interaction effect of W_p-W_t on the tensile-shear load for PB-PB. It is clear that the load is increasing steadily with increasing values of W_p and W_t. The optimal range for the weld strength > 2000 N shown in the corresponding contour plot is for W_t > 0.9 sec. and W_p > 2.7 bar (0.27 MPa) for PB-PB.

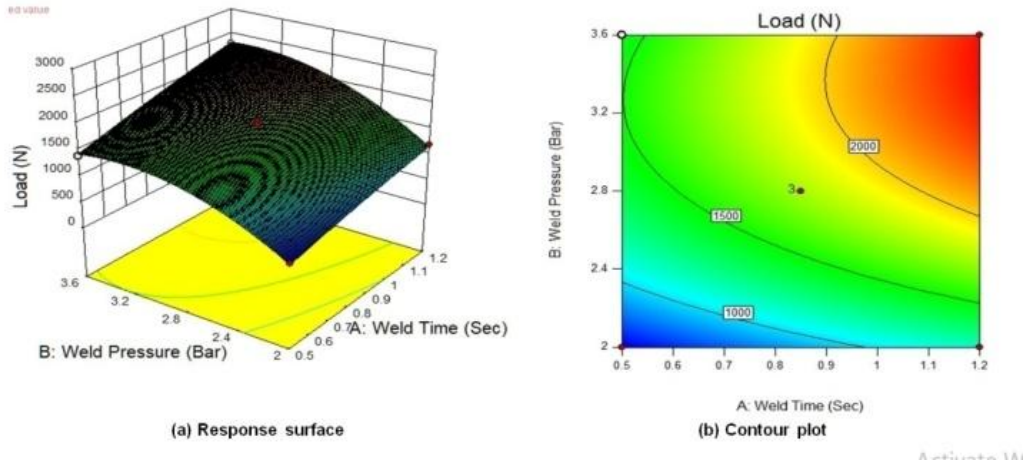

Figure 4.10: Response surface and contour plot showing the effects of weld pressure and weld time on tensile-shear load for PB-PB

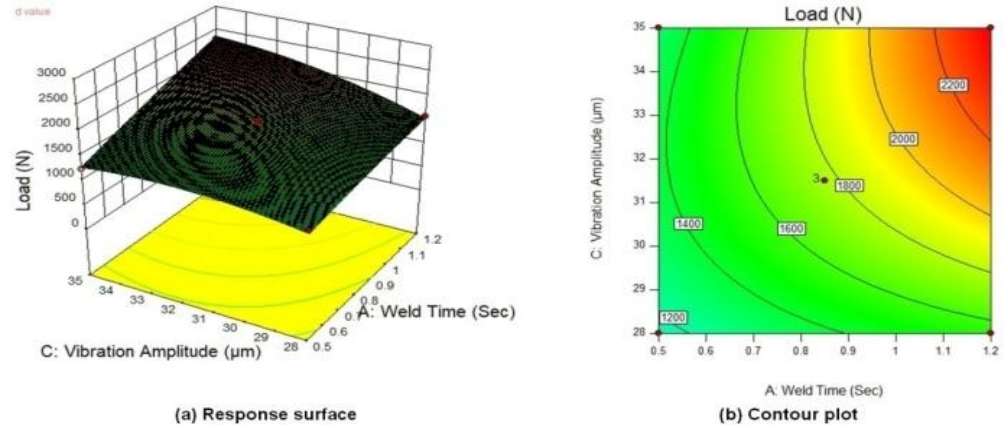

Figure 4.11: Response surface and contour plot showing the effects of weld time and vibration amplitude on tensile-shear load for PB-PB

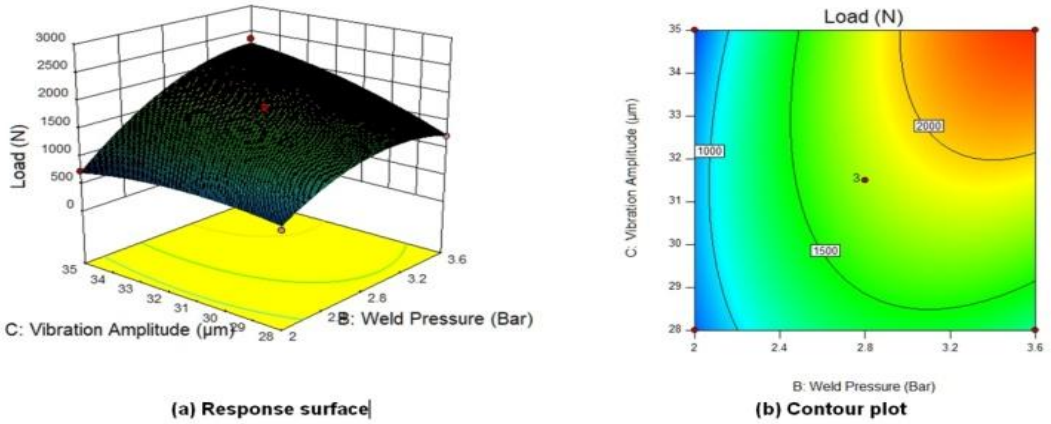

Figure 4.12: Response surface and contour plot showing the effects of weld pressure and vibration amplitude on tensile-shear load for PB-PB

Figure 4.11 depicts the interaction between V_a-W_t and their combined effect on tensile-shear load. The shape of the response surface is upward with a slight curvature towards the varying parameters' upper bound. The optimal range of the weld strength for more than 2200 N is shown

in the corresponding contour plot for V_a > 32 µm and W_t > 1.1 sec. As the value of V_a increases, the interface area of the two mating surfaces increases. The availability of a larger area for welding for a longer duration of time promotes more elastic-plastic deformation and diffusion across the interface. There is a tendency for more dispersion of the oxide and other contaminants when vibration amplitude is increased. All these factors result in the formation of an increased number of microbonds and give better weld strength.

The third response surface and contour plot shown in Figure 4.12 were drawn to demonstrate the interaction effect of V_a-W_p on tensile-shear load for PB-PB. The tensile-shear load is continuously increasing with increasing values of both the varying parameters, and the highest value of the load is obtained at the highest values of V_a and W_p. However, the effect of the W_p is seen more in comparison to V_a. The optimal range of weld strength > 2000 N was achieved for W_p > 3 bar (0.3 MPa) and V_a > 32 µm.

The interaction effects of the process parameters W_p, W_t and V_a in the form of response surfaces and contour plots for PB-Cu are shown in Figures 4.13, 4.14, and 4.15. All the response surfaces have convex shapes. Figure 4.13 shows the interaction effect of W_p-W_t on the tensile-shear load. It is clear that the tensile-shear load is increasing steadily with increasing values of W_p and W_t. The optimal range for the weld strength > 2000 N shown in corresponding contour plot is for W_t > 0.86 sec. and W_p > 0.25 MPa.

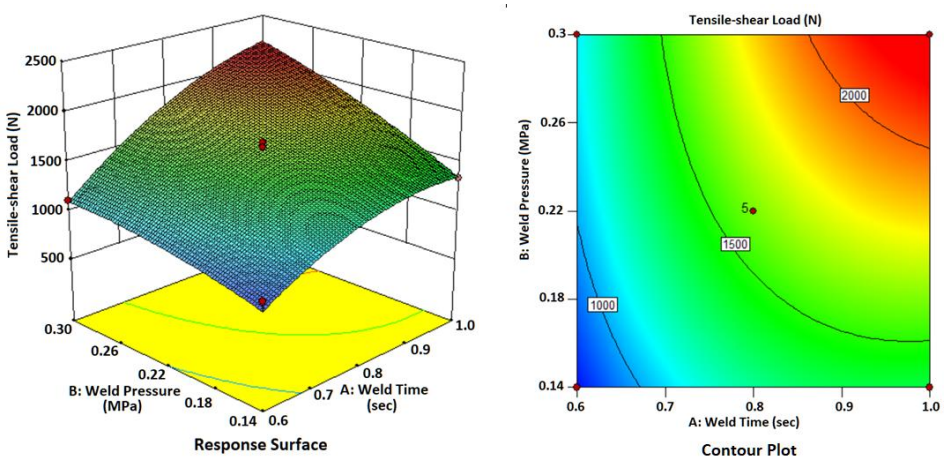

Figure 4.13: Response surface and contour plot showing the effects of weld pressure and weld time on weld strength for PB-Cu

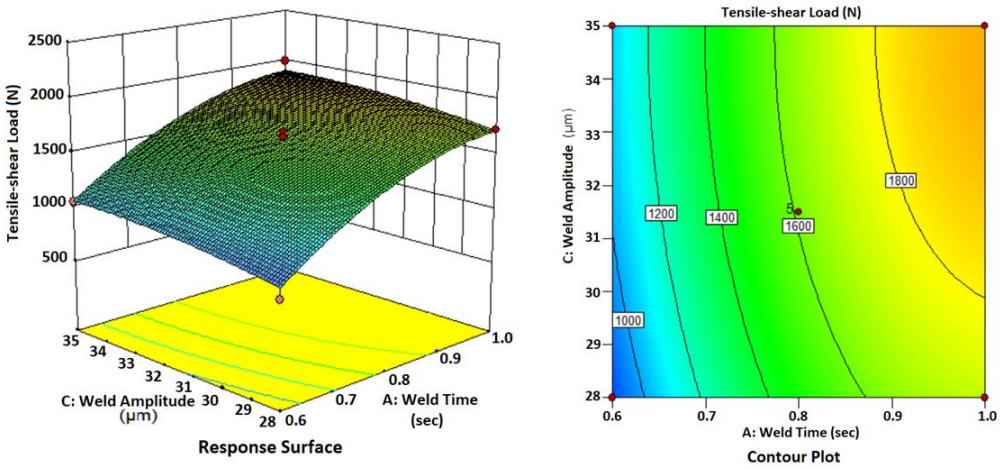

Figure 4.14: Response surface and contour plot showing the effects of weld time and vibration amplitude on tensile-shear load for PB-Cu

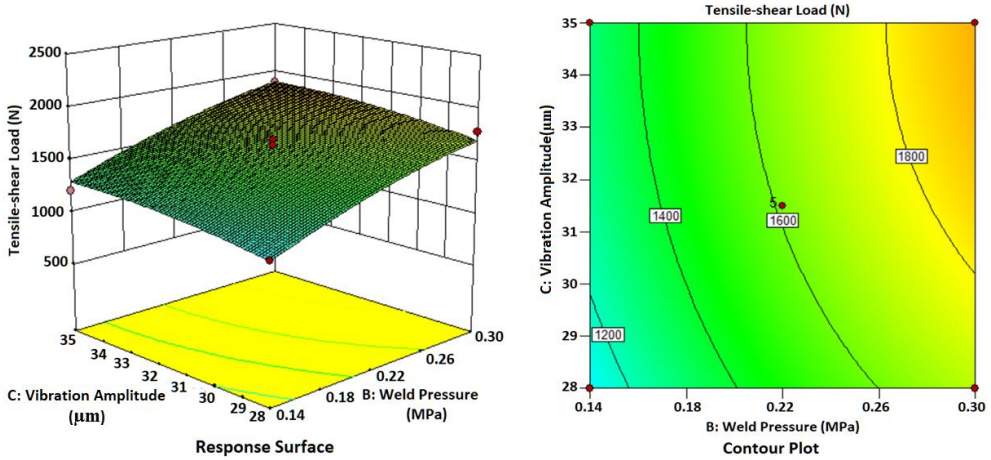

Figure 4.15: Response surface and contour plot showing the effects of weld pressure and vibration amplitude on tensile-shear load for PB-Cu

Figure 4.14 and 4.15 depict the response surfaces for interactions V_a-W_t and V_a-W_p for PB-Cu having a maximum contour line of 1800 N. Moreover, it is also clear from the graphs showing percent contribution of the significant terms in Figure 4.4 and the interaction effect plots for PB-Cu in Figure 4.5 that the interactions of parameters in case of PB-Cu are not significantly affecting the response parameter, hence they may be ignored.

Following the same pattern, the interaction effects of process parameters W_p, W_t and V_a in the form of response surfaces and contour plots for dissimilar PB-Al joints are shown in Figures 4.16, 4.17, and 4.18. The response surfaces have a mix of both convex and concave shapes. Figure 4.16 shows the interaction effect of W_p-W_t on the tensile-shear load. It is clear that the tensile-shear load is increasing steadily with increasing values of W_p and W_t. The optimal value of the parameters has a specific range, which provides numerous combinations. The optimal

range for the weld strength > 1600 N shown in the corresponding contour plot is 0.30 sec < W_t < 0.7 sec. and W_p > 0.30 MPa.

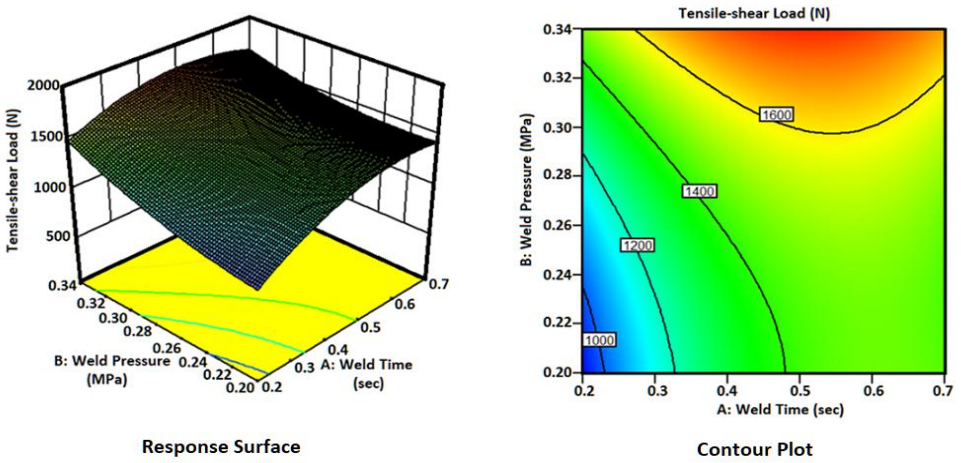

Figure 4.16: Response surface and contour plot showing the effects of weld pressure and weld time on the tensile-shear load for PB-Al

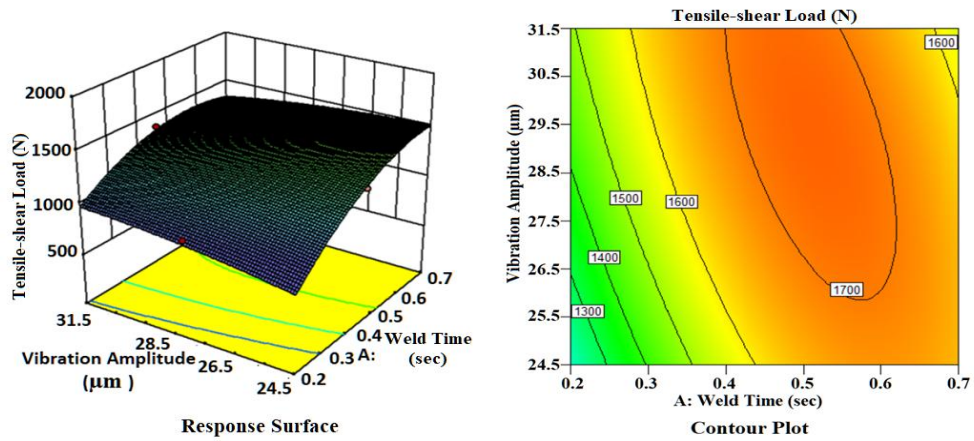

Figure 4.17: Response surface and contour plot showing the effects of weld time and vibration amplitude on tensile-shear load for PB-Al

Figure 4.17 depicts the effect of the interaction term V_a-W_t on the tensile-shear load. The optimal range of the weld strength > 1700 N shown in corresponding contour plot is V_a > 26.5 µm and 0.45 > W_t < 0.62 sec. Different combinations of V_a and W_t within these ranges will provide an optimum result.

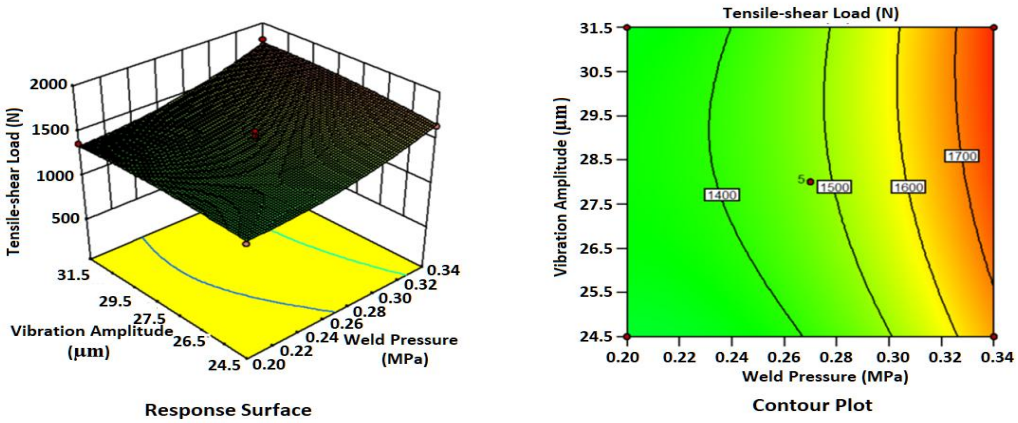

Figure 4.18: Response surface and contour plot showing the effects of weld pressure and vibration amplitude on tensile-shear load for PB-Al

The third response surface and contour plot shown in Figure 4.18 are drawn to demonstrate the interaction effect of V_a-W_p on tensile-shear load. The load is continuously increasing with rising values of both the varying parameters. However, the effect of the W_p is seen more in comparison to V_a. The optimal range of weld strength > 1700 N is achieved for V_a > 25.5 µm and W_p > 0.33 MPa.

When the weld time is increased, the process gets more time to dislocate the contaminants and more metallic surfaces come into contact. Longer weld times combined with higher weld pressure values (W_t-W_p interaction) result in better material mixing and increased penetration. A thicker diffusion layer results in a stronger joint and, as a result, higher load values are obtained. The interaction of W_t-V_a results in a larger area available for welding for a longer period of time. It increases the number of microbonds formed and thus improves weld strength. On the other hand, as weld pressure increases, more surface asperities at the interface come into contact, and a higher value of vibration amplitude increases the area of the faying surface (W_p-V_a interaction). These conditions increase the possibility of producing a greater number of micro-welds, which increases weld strength.

4.2 Optimization of Process Parameters using Simulated Annealing Optimization Algorithm

The regression model obtained from RSM was further utilized to estimate the optimum values of process parameters using a metaheuristic search procedure. For this, the model was embedded with the simulated annealing optimization algorithm using MATLAB v2016 software. Different combinations of welding conditions were tried to obtain the optimal results. The maximum weld strength is achieved when the best combinations of welding conditions are obtained after

conducting a number of trials with different settings of weld parameters as per the coding for fitness function shown in Appendix A1.

The results of the optimization are shown in Figure 4.19 for PB-PB. The value of the objective function at the optimized parameters is shown as negative in the convergence plot. This is due to the fact that the SAO algorithm works to find the global minima, but in the present case, the need is to find the global maxima. Therefore, the negative of the objective function was used in order to convert a minimization problem into a maximization problem. For PB-PB, the maximum value of the load was found to be 2674.44 N at {X(i) = 0.958, 0.36, 28}, i.e. at W_t = 0.958 sec, W_p = 0.36 MPa and V_a = 28 µm as shown by the convergence plot.

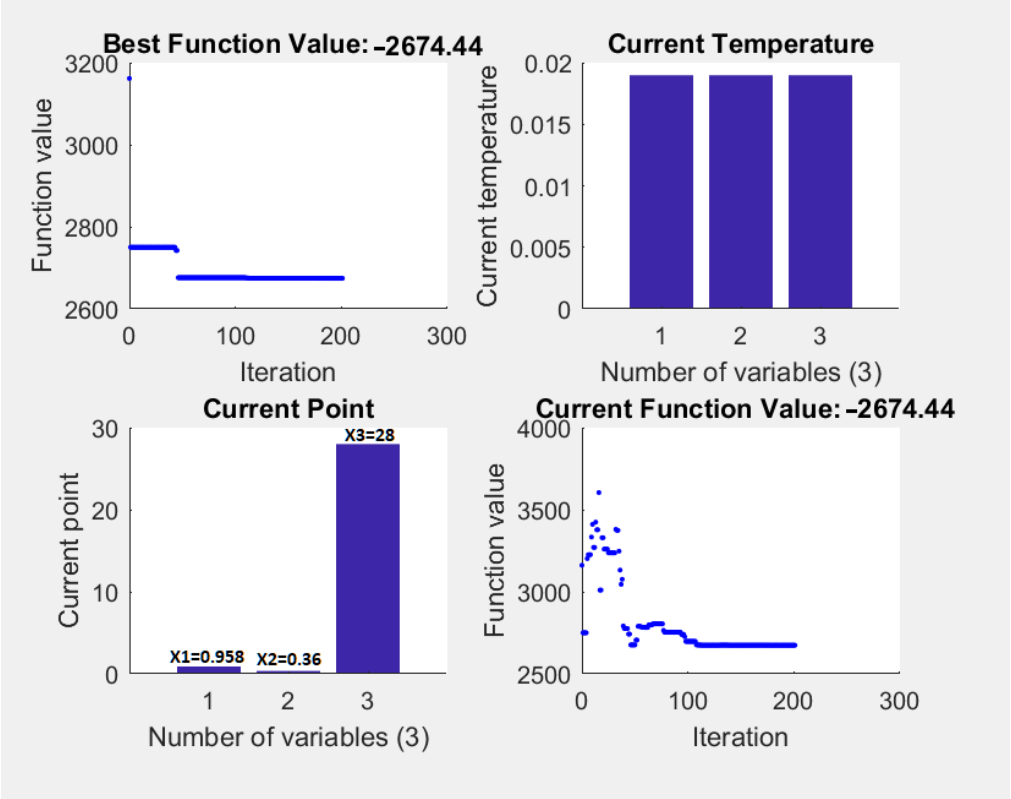

Figure 4.19: Optimization results using simulated annealing in case of PB-PB joints

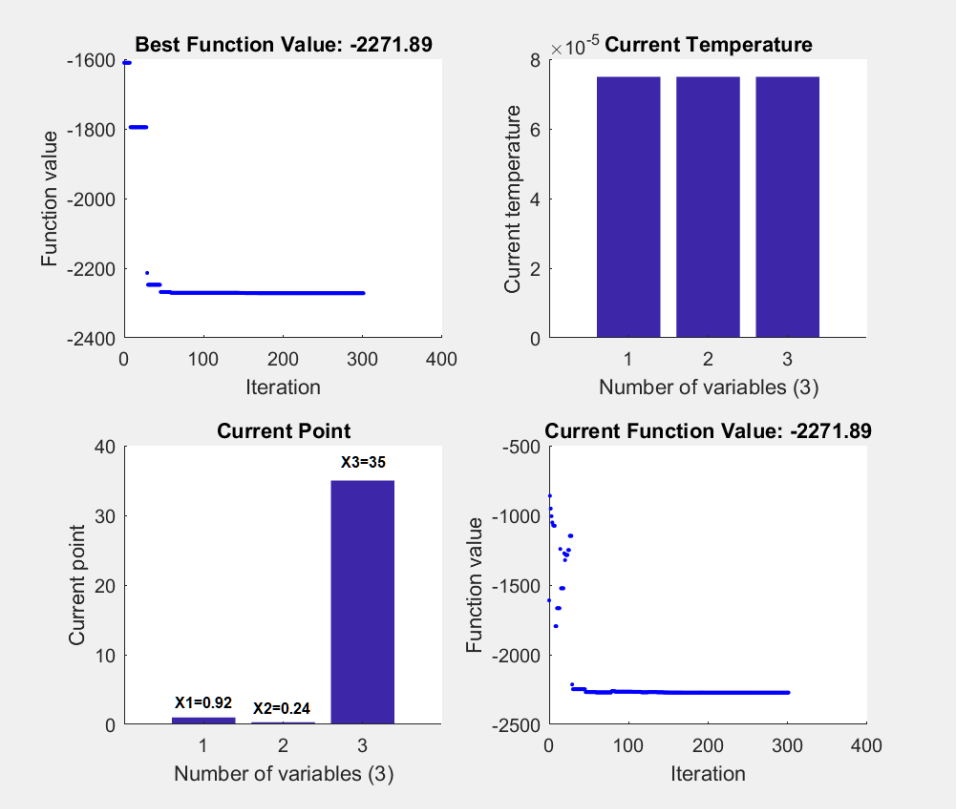

Figure 4.20: Optimization results using simulated annealing in case of PB-Cu joints

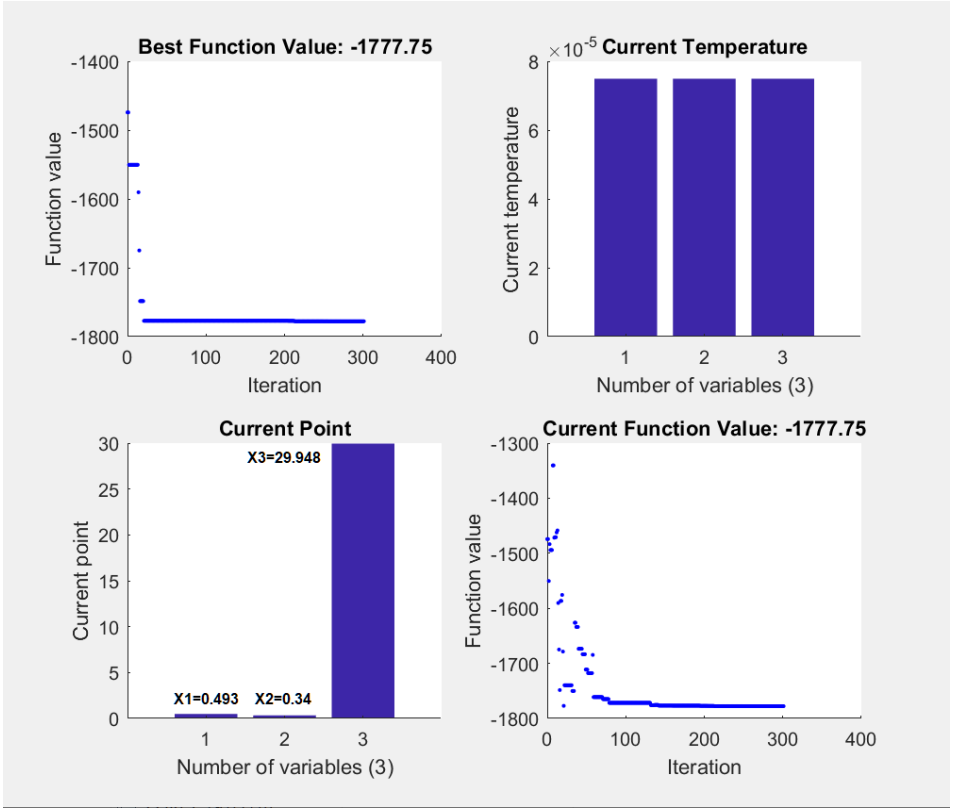

Figure 4.21: Optimization results using simulated annealing in case of PB-Al joints

Similarly, the results of the optimization for PB-Cu and PB-Al are shown in Figure 4.20 and Figure 4.21 respectively. The maximum value of the load for PB-Cu was found to be 2271.89 N at {X(i) = 0.92, 0.24, 35}, i.e. at W_t = 0.92 sec, W_p = 0.24 MPa and V_a = 35 µm whereas that for PB-Al, it was 1777.75 N at {X(i) = 0.493, 0.34, 29.948}, i.e. at W_t = 0.493 sec, W_p = 0.34 MPa and V_a = 29.948 µm as shown by the convergence plots for best function value in Figures 4.20 and 4.21.

4.2.1 Validation of the Optimization Technique

The optimized values of the weld parameters were used for validation of the technique. For this purpose, the confirmatory tests were performed at the optimized values of the parameters. The selection of the parameters and their range is considered appropriate if the result of the confirmatory test falls within the defined confidence level of the true mean. There may be misinterpretation of the significant factors and their interactions if the mean value of the confirmatory results does not fall within the confidence level (Stefan and Mats, 2017).

To validate the test results, three weld coupons were prepared at the optimized values of the parameters for all the combinations, i.e. PB-PB, PB-Cu, and PB-Al. The optimized solutions given by SAO for all three combinations were within the range of the parameters. It is also important to check the feasibility of the optimized solutions. It was observed that the optimized values of the parameters obtained by the SAO algorithm for PB-PB and PB-Cu, were well within the range as well as feasible as per the USMW machine settings. But in the case of PB-Al, the fixing of vibration amplitude at 29.948 µm was not possible as the USMW machine used for the experimentation could be fixed only at four possible values, i.e. 24.5, 28, 31.5, and 35 µm. So, the next possible value near to 29.948 µm i.e. 31.5 µm was selected. The reason for this modification was one of the findings of the ANOVA analysis for PB-Al: V_a was not a significant parameter. A minor change in the value of V_a would not affect the result.
The optimized data for all the material combinations and the corresponding tensile-shear load of the confirmatory tests has been tabulated in Table 4.1. Table 4.2 shows the comparison of the tensile-shear load predicted by RSM and SAO with the experimental data at the similar parameter setting. Figure 4.22 depicts this comparison graphically. It is clear from the related data that the estimated values of the tensile-shear load in case of PB-PB and PB-Cu are more than the experimental value. However, in case of PB-Al, the experimental value is slightly more than the estimated values. Secondly, the SAO estimate and corresponding confirmatory test result in case of PB-PB are exceptionally higher than the corresponding values of experimentally

measured load and RSM estimate. This exception is not observed in other cases i.e. PB-Cu and PB-Al. The possible cause of this difference may be due to some measurement error.

Table 4.1: Confirmatory test results

Material Combination	Wt (sec)	Wp (Mpa)	Va (µm)	Tensile-shear load (N)			Mean tensile-shear load (N)
				Trial 1	Trial 2	Trial 3	
PB-PB	0.958	0.36	28	2622.7	2798.3	2655.6	2692.2
PB-Cu	0.92	0.24	35	2305.8	2325.2	2136.1	2255.7
PB-Al	0.493	0.34	31.5	1795.3	1911.7	1802.4	1836.47

Table 4.2: Comparison of tensile-shear load under different testing criteria

Combi-nation	Tensile-shear Load Criteria	Wt (sec)	Wp (Mpa)	Va (µm)	Mean Tensile-shear Load (N)	Absolute Deviation (%)
PB-PB	Experimental Load	0.85	0.36	35	2353.33	-
	RSM Estimate	0.85	0.36	35	2367.18	0.59
	SAO Estimate	0.958	0.36	28	2674.44	13.64
	Confirmatory test results	0.958	0.36	28	2692.2	14.4
PB-Cu	Experimental Load	1	0.3	31.5	2129.67	-
	RSM Estimate	1	0.3	31.5	2224	4.43
	SAO Estimate	0.92	0.24	35	2271.89	6.68
	Confirmatory test results	0.92	0.24	35	2255.7	5.92
PB-Al	Experimental Load	0.45	0.34	31.5	1810	-
	RSM Estimate	0.45	0.34	31.5	1775	1.93
	SAO Estimate	0.493	0.34	29.948	1777.75	1.78
	Confirmatory test results	0.493	0.34	31.5	1836.47	1.46

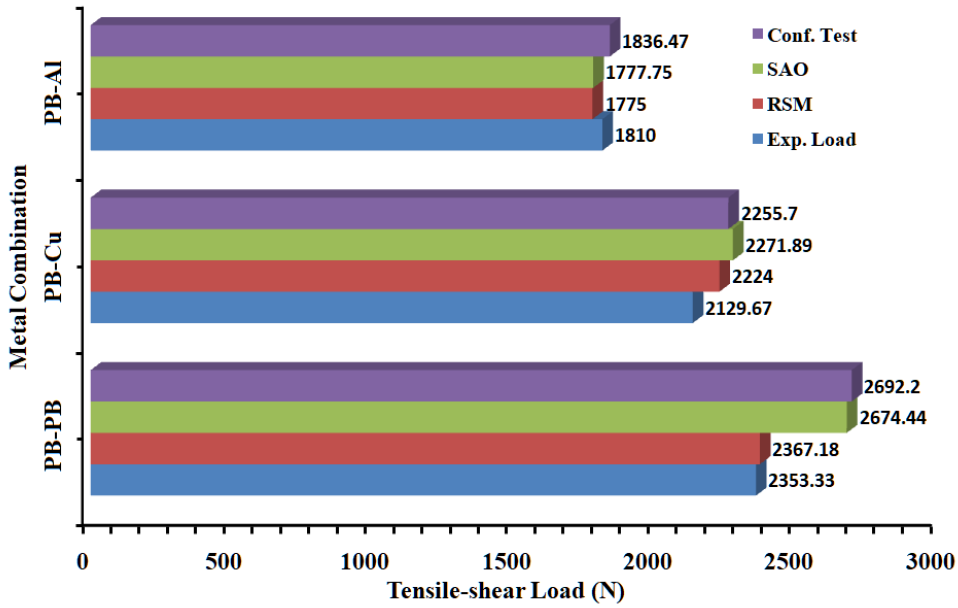

Figure 4.22: Comparison of estimated and experimental tensile-shear load for PB-PB, PB-Cu, and PB-Al

4.3 Relation between Weld Strength and Weld Area

The data related to the weld area collected for PB-PB, PB-Cu, and PB-Al weld coupons along with the corresponding weld strength are shown in Table 4.3 to Table 4.5. The values of the correlation coefficients calculated to find out the extent of the linear association between the two response variables were 0.79, 0.87, and 0.81, respectively, for PB-PB, PB-Cu, and PB-Al. These values show a sufficiently strong correlation between the mean weld area and the weld strength, as shown in Figures 4.23, 4.24, and 4.25. It signifies that the weld area may be considered to be an indicator of weld strength.

It was observed that the tensile-shear load increased with increasing weld area, but the maximum weld area does not correspond to the maximum value of tensile-shear load always. Similarly, some weld coupons show a comparatively larger area but their corresponding tensile-shear load is relatively lower. It indicates that some of the spots, however, appeared to be the result of the broken bonds, but actually, the bonds were not formed at those points. Formation of microbonds is governed by one of the joining mechanisms in USMW proposed by different researchers under different theories such as adhesion, diffusion, melting, and interlocking (Sanga et al., 2018).

Table 4.3: Calculation of interface area for PB-PB

Run Order	Wt (sec)	Wp (MPa)	Va (µm)	Mean W_a (mm^2)	Mean W_{Se} (N)
1	1.20	0.28	28.0	57.37	1653.33
2	0.85	0.28	31.5	64.46	1781.67
3	0.85	0.36	28.0	50.14	1226.67
4	0.50	0.20	31.5	54.68	636.33
5	0.85	0.20	28.0	32.95	703.67
6	1.20	0.28	35.0	75.69	2306.67
7	0.50	0.28	35.0	48.72	1246.67
8	0.85	0.20	35.0	59.27	738.33
9	0.50	0.28	28.0	40.79	1333.67
10	0.85	0.36	35.0	84.60	2353.33
11	1.20	0.36	31.5	75.34	2416.67
12	0.85	0.28	31.5	72.72	1853.33
13	0.85	0.28	31.5	69.21	1803.33
14	0.50	0.36	31.5	50.94	1396.67
15	0.85	0.28	31.5	58.38	1666.67
16	1.20	0.20	31.5	33.50	1196.67
17	0.85	0.28	31.5	70.70	1799.33

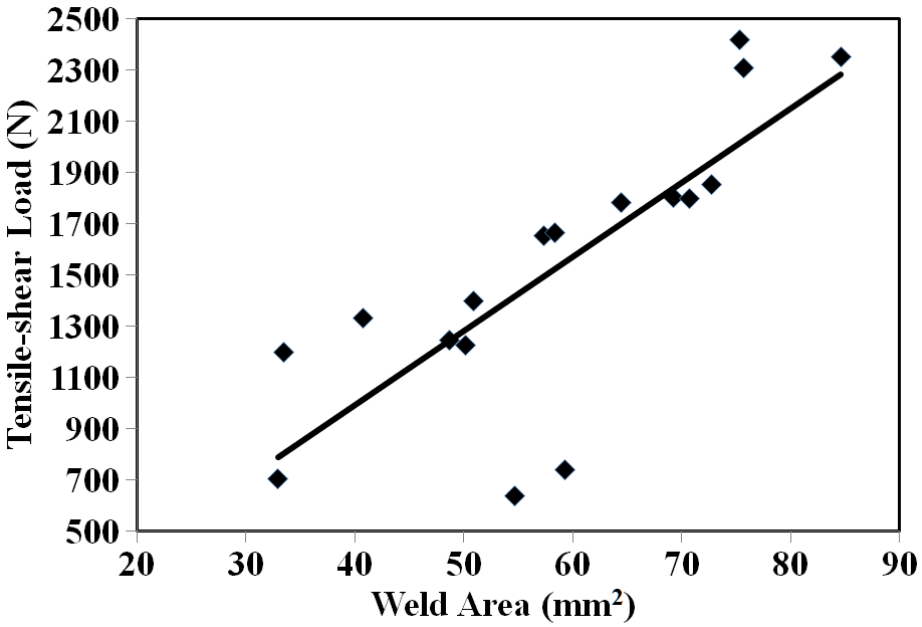

Figure 4.23: Correlation plot between weld area and tensile-shear load for PB-PB joint

Table 4.4: Calculation of interface area for PB-Cu

Run Order	W_t (sec)	W_p (Mpa)	V_a (µm)	Mean W_a (mm2)	Mean W_{Se} (N)
1	0.8	0.30	28.0	69.75	1785.33
2	1.0	0.14	31.5	67.65	1345.33
3	0.6	0.30	31.5	55.43	1112.00
4	0.6	0.22	28.0	52.93	775.33
5	1.0	0.22	35.0	105.32	1995.00
6	0.8	0.14	35.0	49.13	1209.67
7	0.8	0.22	31.5	93.08	1634.67
8	0.6	0.22	35.0	54.94	1017.00
9	0.8	0.22	31.5	87.7	1617.33
10	1.0	0.22	28.0	75.25	1821.00
11	0.8	0.22	31.5	90.37	1701.33
12	0.8	0.22	31.5	72.23	1685.67
13	0.6	0.14	31.5	50.37	886.67
14	0.8	0.22	31.5	77.21	1521.33
15	0.8	0.14	28.0	76.33	1118.67
16	1.0	0.30	31.5	110.16	2129.67
17	0.8	0.30	35.0	107.05	1891.33

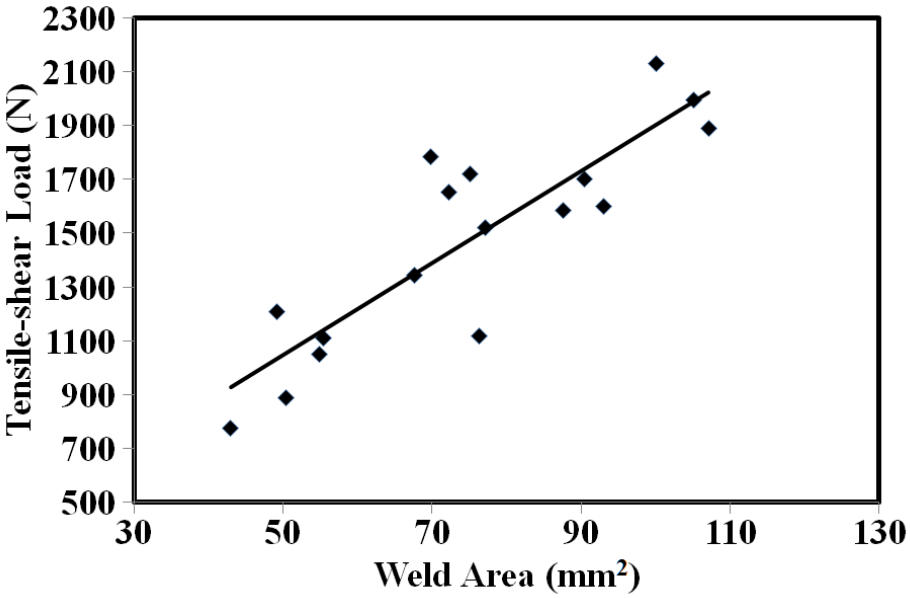

Figure 4.24: Correlation plot between weld area and tensile-shear load for PB-Cu joint

Table 4.5: Calculation of interface area for PB-Al

Run Order	Wt (sec)	Wp (MPa)	Va (μm)	Mean W_a (mm^2)	Mean W_{Se} (N)
1	0.70	0.20	28.0	48.65	1433.33
2	0.45	0.27	28.0	53.62	1372.67
3	0.70	0.27	24.5	69.86	1574.33
4	0.45	0.34	24.5	73.15	1642.67
5	0.20	0.27	31.5	44.85	1120.00
6	0.45	0.27	28.0	66.78	1553.33
7	0.45	0.27	28.0	56.36	1460.00
8	0.20	0.20	28.0	30.12	939.67
9	0.45	0.27	28.0	62.89	1498.67
10	0.70	0.27	31.5	48.18	1395.33
11	0.45	0.20	24.5	73.65	1286.67
12	0.45	0.27	28.0	51.98	1448.33
13	0.20	0.34	28.0	60.44	1538.33
14	0.70	0.34	28.0	**77.74**	1739.67
15	0.45	0.20	31.5	57.51	1371.00
16	0.45	0.34	31.5	63.59	**1810.00**
17	0.20	0.27	24.5	33.15	981.00

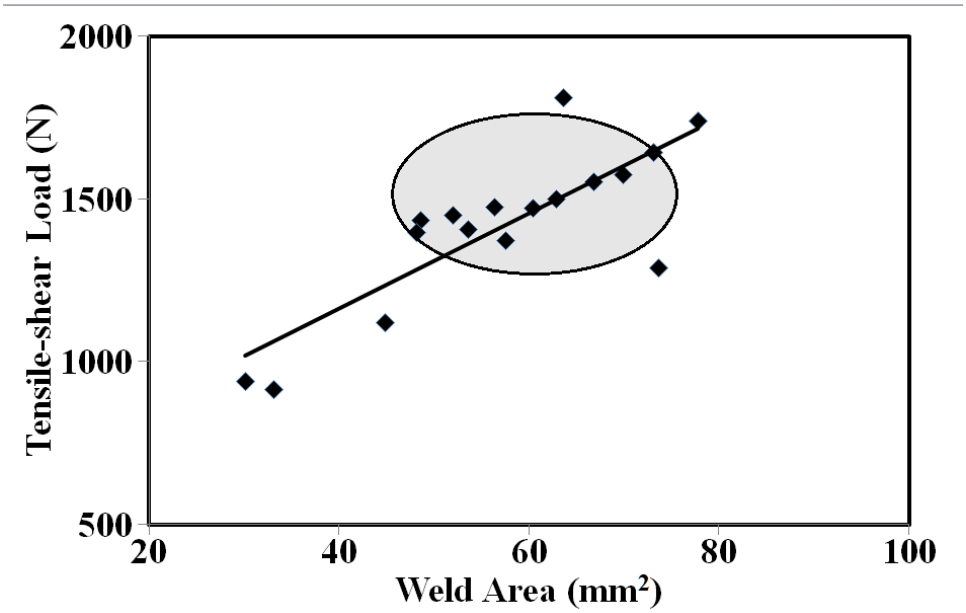

Figure 4.25: Correlation plot between weld area and tensile-shear load for PB-Al joint.

Local microbonds are formed initially around the teeth of the sonotrode tip due to continuous shear oscillations. Subsequently, the material starts flowing in a convoluted wave-like form and the microbonds propagate along the weld interface. The microbonds develop till the layers of the material keep slipping, which results in increased plastic deformation. But enhanced material

flow at the interface makes the material thinner and softer. As a result, weaker bonds break and do not contribute to the strength of the joint (Lee et al., 2013; Shakil et al., 2014; Zhang et al., 2014). On the other hand, properly built-up bonds become stronger as cooling of the joint starts at the end of the welding process. Therefore, the net area of the completely built-up microbonds only contributes to the weld strength of the joint. This explanation is also supported by the enlarged view of the interface area in Figure 3.11 in Section 3.7.3, where many weak bonds are visible at the macroscopic level. These weak bonds add up to form the cumulative weld area but do not actually contribute to the weld strength.

It was also observed that the weld area of about 65% of the weld coupons of PB-Al falls within a certain range, as shown in Figure 4.21 by the gray colour oval. They fall between 48.18 mm^2 and 73.15 mm^2 of weld area and 1371 N and 1642.67 N of tensile-shear load. Such a pattern was not shown by PB-PB and PB-Cu weld coupons. It could be because aluminium loses its yield strength abruptly at temperatures as low as 150 °C (Pattrick Summers, 2015). There is a rise in the temperature at the joint, due to stretching of the weld joint during the tensile-shear test. The aluminium alloys have sufficient resistance for deformation before a certain temperature, but after that plastic deformation increases significantly and failure occurs.

The estimation of weld area is essential for the calculation of heat flux at the interface. The calculation is further used in the FE analysis of the weld interface to evaluate the extent and effects of HAZ and TMAZ covered in Chapter 5.

4.4 Summary

The results of tensile-shear load measurement for ultrasonically welded specimens of PB-PB, PB-Cu and PB-Al have been found satisfactorily good within the range of the process parameters. No visual defects have been observed in the weld joints. The maximum tensile-shear load for PB-PB, PB-Cu, and PB-Al joints was 2353.33 N, 2129.67 N, and 1810 N, respectively. The significant parameters and interactions were chosen based on ANOVA analysis. A quadratic regression model was developed to calculate the estimated weld strength. The experimental and estimated weld strengths calculated by the regression model were found to be in good agreement with each other. Response surfaces and contour plots were drawn to get the optimal range. The regression equation was embedded with the SAO algorithm to obtain the optimized values of the process parameters. The results of the confirmatory tests conducted using optimized parameters were found to be close to the experimental values. The weld area of all the weld specimens was calculated using ImageJ software. Its correlation with tensile-shear load was also established.

CHAPTER-5

RESULTS AND DISCUSSION BASED ON THERMAL MODELLING AND SIMULATION

5.1 Introduction

The results related to the response surface methodology and optimization of the parameters of the ultrasonically welded PB-PB, PB-Cu, and PB-Al joints have been analyzed in Chapter 4. The interface temperature measured during welding was essential to be validated through simulation of the thermal model of the ultrasonic welding process using the finite element method. Modelling of the thermal field plays an important role in the prediction of the temperature profile at the weld interface. The response characteristics of the USMW process can be forecast and the corresponding data can be utilized optimally by the industry. This chapter is focused on the analysis of the simulation results of the 3-D Finite Element (FE) model of the ultrasonically welded joints of thin sheets of the selected materials. The CAD model was used to conduct a close inspection of the thermal phenomenon that led to the joining process and to assess its impact. This work involved the following objectives:

- To develop a CAD model and analyze it using an FEA technique to predict the temperature at different zones of the interface.
- To establish a correlation between the interface temperature and the strength of the joint.
- To calculate the heat flux at the weld interface.
- To assess the expansion of the HAZ and TMAZ.

5.2 Finite Element Modelling and Simulation

The simulation was performed on the CAD models of ultrasonically welded PB-PB, PB-Cu, and PB-Al sheets. The run-time interface temperature was measured during welding. Due precautions were taken during the temperature measurement. Despite that, some results were found inconsistent due to extremely fast processing time, the possibility of thermocouple deformation and vibration at the point of measurement. The effect of tremendous vibrations on the temperature profile was visible in the enlarged view, where the temperature values were fluctuating in the range of 10-15°C within a period of about 0.011 seconds as shown in Figure 5.1 for PB-PB joint. A similar pattern of thermal profiles was observed in PB-Cu and PB-Al

joints also. Therefore, the measurements were repeated until reliable results were obtained and only those temperature profiles were accepted that had similar heating and cooling histories without any abnormal fall or quick rise.

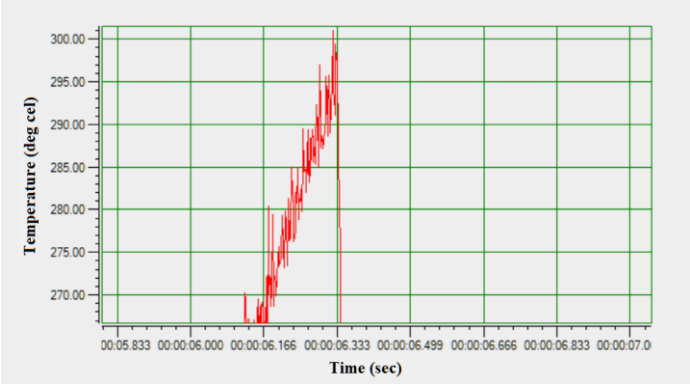

Figure 5.1: Fluctuation of temperature during ultrasonic welding of PB-PB

The CAD model equipped with boundary conditions, material properties, and appropriate meshing was simulated using SimScale cloud based software. Heat flux calculated in Chapter 3 was fed as a boundary condition.

5.2.1 Comparison of Experimental and Simulated Temperature Profiles

(A) PB-PB

The prediction results and the experimentally observed values of the interface temperature for the PB-PB combination were tabulated in Table 5.1. The first simulation trial was performed at run number 5, which had the smallest value of bonding ratio ($\beta = 0.25$) with clamping force of 1100 N, sonotrode vibration amplitude of 28.0 µm and, weld time of 0.85 sec. The values of two process parameters, the clamping force and the sonotrode vibration amplitude, were assigned at a low level in that run. The heat flux values H_d and H_f were 82.56 x 10^6 W/m^2 and 5.23 x 10^6 W/m^2 respectively. The simulation trial performed with these heat flux inputs produced a temperature of 244.2 ℃. The value of the peak average interface temperature obtained by the thermocouple at the same parameter settings was 254.5 ℃. With these parameter settings, the tensile-shear load was obtained as 703.67 N. The values of the interface temperature and the load are towards the lowest side at the low level of parameters and bonding ratio. The corresponding results from real-time observation and simulation are shown in Figure 5.2. The temperature distribution is shown along the longitudinal section (x-axis) of the assembly.

Table 5.1: Experimental and simulation temperature data for PB-PB

Run No.	Clamping Force, F_c (N)	Weld Time, W_t (sec)	Vibration Amplitude, V_a (μm)	Weld Area, W_a (mm^2)	Bonding ratio (β)	Exp. Interface Temp.* (°C)	Simulated Interface Temp. (°C)	Tensile-shear load* (N)
1	1650	1.20	28.0	57.37	0.44	313.9	323.0	1653.33
2	1650	0.85	31.5	64.46	0.50	314.4	329.4	1781.67
3	2200	0.85	28.0	50.14	0.39	297.7	287.6	1226.67
4	1100	0.50	31.5	54.68	0.42	240.4	245.2	636.33
5	**1100**	**0.85**	**28.0**	**32.95**	**0.25**	**254.5**	**244.2**	**703.67**
6	1650	1.20	35.0	75.69	0.58	340.5	328.6	2306.67
7	1650	0.50	35.0	48.72	0.37	299.6	294.3	1246.67
8	1100	0.85	35.0	59.27	0.46	279.6	285.7	738.33
9	1650	0.50	28.0	40.79	0.31	289.5	284.3	1333.67
10	**2200**	**0.85**	**35.0**	**84.60**	**0.65**	**354.7**	**368.8**	**2353.33**
11	2200	1.20	31.5	75.34	0.58	349.4	360.0	2416.67
12	1650	0.85	31.5	72.72	0.56	319.5	313.9	1853.33
13	1650	0.85	31.5	69.21	0.53	316.9	304.8	1803.33
14	2200	0.50	31.5	50.94	0.39	301.6	287.5	1396.67
15	**1650**	**0.85**	**31.5**	**58.38**	**0.45**	**312.9**	**313.9**	**1666.67**
16	1100	1.20	31.5	33.50	0.26	288.9	288.1	1196.67
17	1650	0.85	31.5	70.70	0.54	310.33	304.4	1799.33

* The mean of three experimental replicates

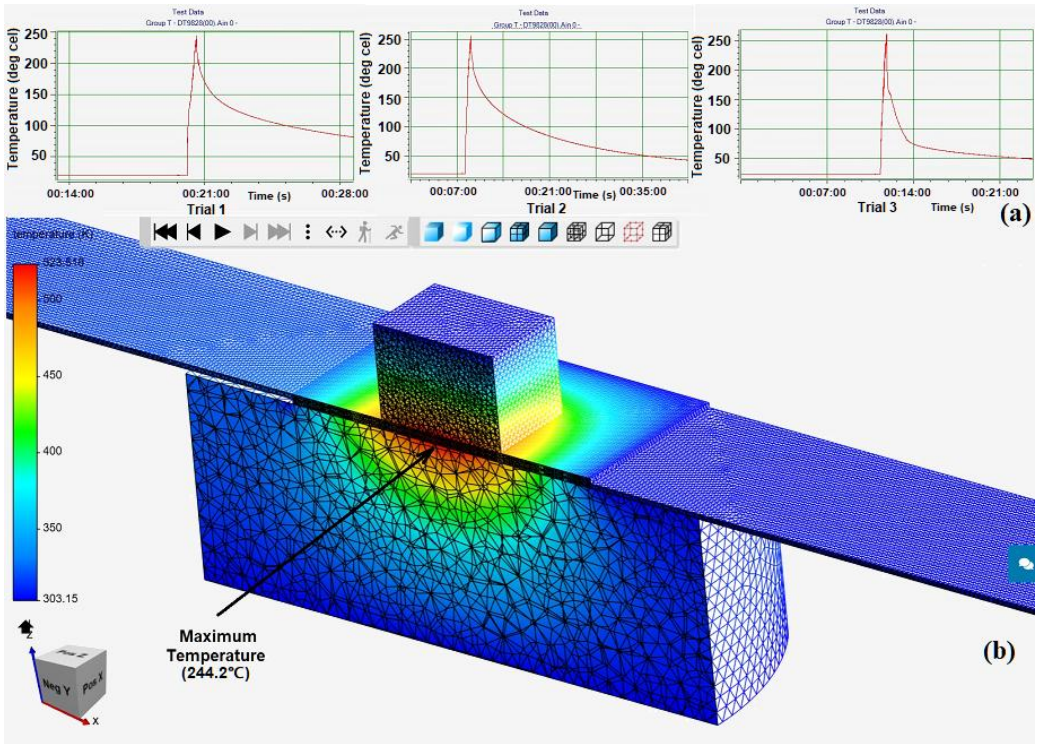

Figure 5.2: Temperature profile of run 5 for PB-PB (a) Experimental results (b) Simulation result

The second simulation trial was performed at run number 15, which had almost the middle value of bonding ratio ($\beta = 0.45$) with clamping force of 1650 N, sonotrode vibration amplitude of 31.5 µm, and weld time of 0.85 sec. The values of all the process parameters were also assigned at the middle level in that run. The heat flux values H_d and H_f were 167.11 x 10^6 W/m^2 and 8.82 x 10^6 W/m^2 respectively. The simulation trial performed at these inputs generated a temperature of 313.9°C. The value of the peak average interface temperature obtained by the thermocouple at the same parameter settings was 312.9°C. The tensile-shear load obtained at this parameter setting was 1666.67 N. The values of interface temperature and load value are higher than those of the previous simulation run. The corresponding results from real-time observation and simulation are shown in Figure 5.3. The temperature distribution is shown along the longitudinal section of the assembly.

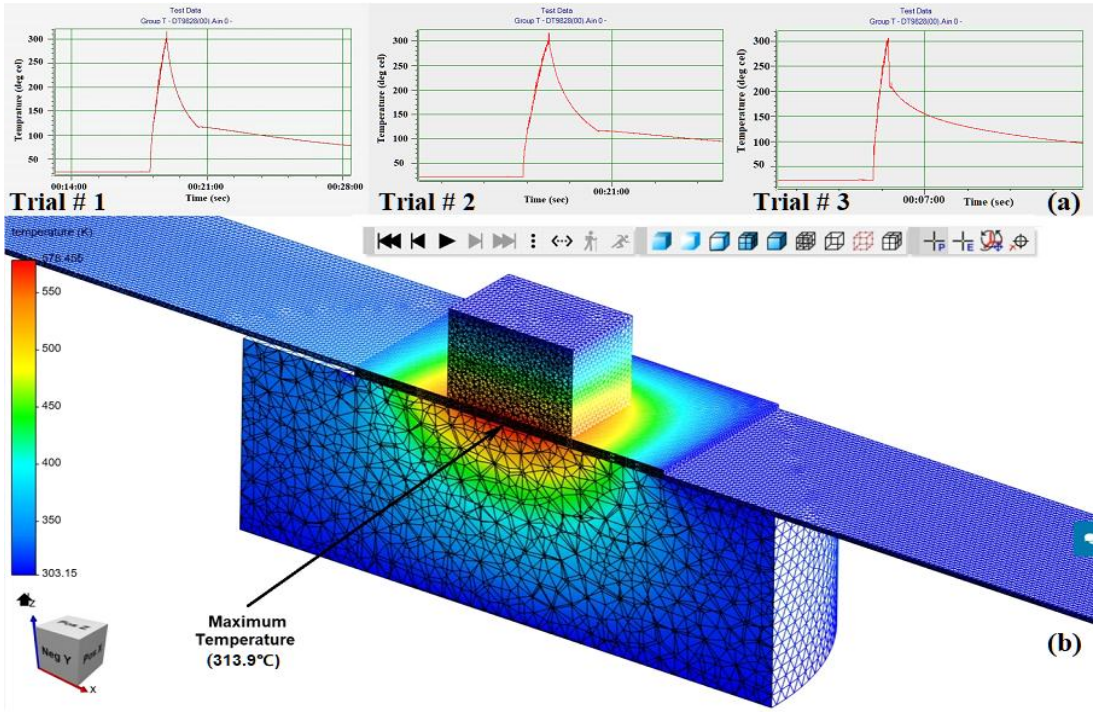

Figure 5.3: Temperature profile of run 15 for PB-PB (a) Experimental results (b) Simulation result

The third simulation trial was performed at run number 10, which had the highest value of bonding ratio ($\beta = 0.65$) with clamping force of 2200 N, sonotrode vibration amplitude of 35.0 µm, and weld time of 0.85 sec. The values of two process parameters, the clamping force and sonotrode vibration amplitude were also assigned at a high level in that run. The heat flux values H_d and H_f were 268.01 x 10^6 W/m^2 and 13.08 x 10^6 W/m^2 respectively. The simulation trial performed with those inputs produced a temperature of 368.8°C. The value of the peak average interface temperature obtained by the thermocouple at the same parameter settings was 354.7°C.

The tensile-shear load obtained at that parameter setting was 2353.33 N. The values of interface temperature and load were the highest at the high level of parameters and bonding ratio. Figure 5.4 shows the corresponding real-time and simulation results.

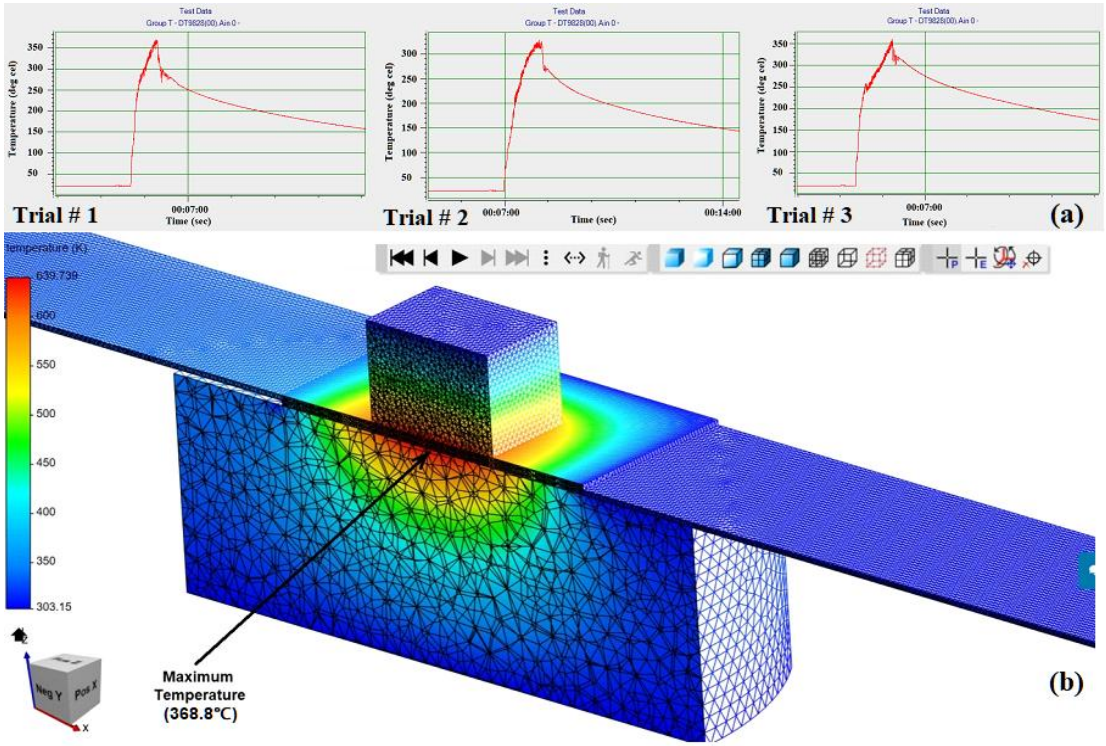

Figure 5.4: Temperature profile of run 10 for PB-PB (a) Experimental results (b) Simulation result

Further, it was observed from the simulated results that the values of interface temperature as well as tensile-shear load increased with the increased clamping force while keeping the vibration amplitude and weld time constant. Run 5 and Run 3 were simulated at a low level of vibration amplitude (28.0 µm) while keeping the weld time constant at 0.85 sec. The simulated results of interface temperature and the value of tensile-shear load increased from 244.2℃ to 287.6℃ and from 703.67 N to 1226.67 N, respectively, when the clamping force was increased from 1100 N to 2200 N during these runs. Run 4 and Run 14 were simulated at the middle level of sonotrode vibration amplitude (= 31.5 µm) and the fixed value of weld time at 0.5 sec. The interface temperature and the tensile-shear load increased from 245.2℃ to 287.5℃ and from 603 N to 1396.67 N, respectively, when the clamping force was increased from 1100 N to 2200 N. Similarly, a high level of vibration amplitude (35.0 µm) and a fixed value of weld time of 0.85 sec. were used for simulating runs 8 and 10. The interface temperature increased from 285.7℃ to 368.8℃, while the tensile-shear load increased from 738.33 N to 2553.33 N when the clamping force was increased from 1100 N to 2200 N.

(B) PB-Cu

The prediction results and the experimentally observed values of the interface temperature for the PB-Cu combination are tabulated in Table 5.2.

Table 5.2: Experimental and simulation temperature data for PB-Cu

Run No.	Clamping Force, F_c (N)	Weld Time, W_t (sec)	Vibration Amplitude, V_a (μm)	Weld Area, W_a (mm^2)	Bonding ratio (β)	Exp. Interface Temp. * (°C)	Simulated Interface Temp. (°C)	Tensile-shear load* (N)
1	1800	0.8	28.0	76.41	0.59	295.40	307.5	1785.33
2	700	1.0	31.5	67.65	0.52	285.07	297.2	1345.33
3	1800	0.6	31.5	55.43	0.43	268.87	281.8	1112.00
4	1200	0.6	28.0	52.93	0.41	253.37	264.9	775.33
5	1200	1.0	35.0	105.32	0.81	330.63	348.5	1995.00
6	700	0.8	35.0	49.21	0.38	267.83	278.6	1209.67
7	1200	0.8	31.5	93.08	0.72	285.87	299.4	1634.67
8	1200	0.6	35.0	54.94	0.42	273.07	283.8	1017.00
9	1200	0.8	31.5	87.7	0.67	262.33	266.1	1617.33
10	1200	1.0	28.0	75.25	0.58	311.03	321.4	1821.00
11	1200	0.8	31.5	90.37	0.70	296.73	307.6	1701.33
12	1200	0.8	31.5	72.23	0.56	291.17	296.5	1685.67
13	**700**	**0.6**	**31.5**	**50.39**	**0.39**	**241.63**	**256.1**	**886.67**
14	**1200**	**0.8**	**31.5**	**77.21**	**0.59**	**302.83**	**319.2**	**1521.33**
15	700	0.8	28.0	59.66	0.46	254.57	265.3	1118.67
16	**1800**	**1.0**	**31.5**	**110.16**	**0.85**	**361.77**	**369.4**	**2129.67**
17	1800	0.8	35.0	107.05	0.82	342.17	349.7	1891.33

* The mean of three experimental trials.

The first simulation trial was performed at run number 13, which had the lowest value of simulated interface temperature and almost the minimum value of bonding ratio ($\beta = 0.39$). The values of process parameters are: clamping force = 700 N, vibration amplitude = 31.5 μm and, weld time = 0.60 sec. The values of two process parameters, the weld time and clamping force, were assigned at a low level in this run. The heat flux values H_d and H_f were 144.93 x 10^6 W/m^2 and 3.88 x 10^6 W/m^2 respectively. The simulation trial performed with these inputs generated the temperature value of 256.1°C. The value of the peak average interface temperature obtained by the thermocouple was 241.63°C and the tensile-shear load was 886.67 N at the same parameter settings. The values of interface temperature and load are towards the lowest side at the low level of parameters and bonding ratio. The corresponding results from real-time observation and

simulation are shown in Figure 5.5. The temperature distribution is shown along the longitudinal section (x-axis) of the assembly.

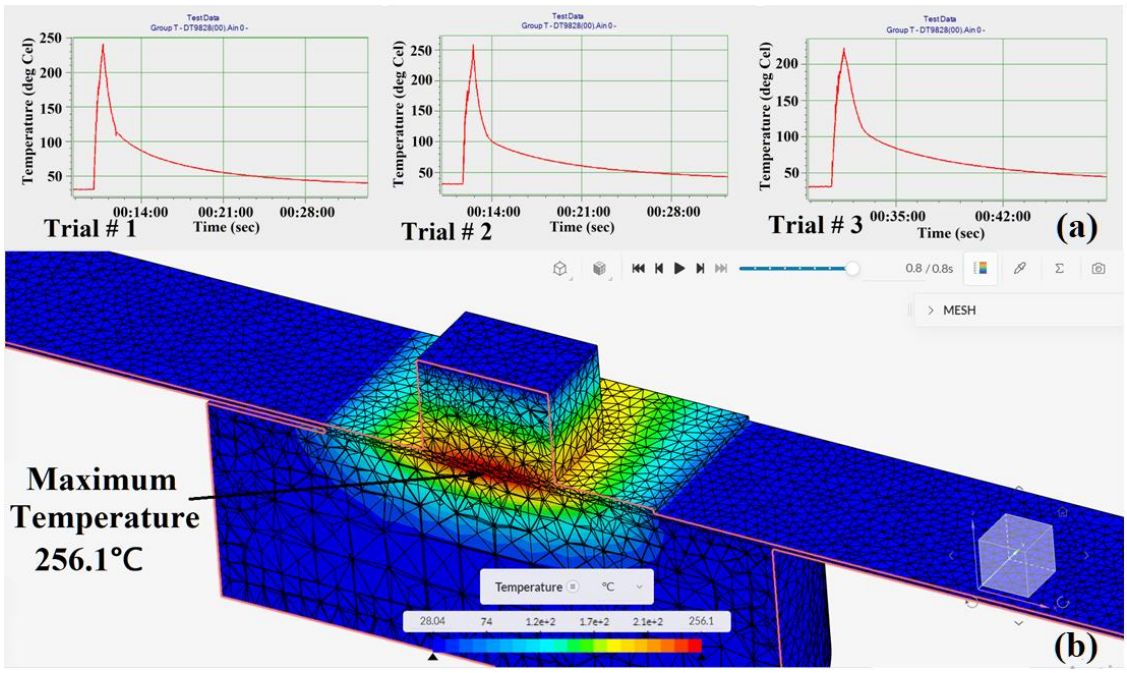

Figure 5.5: Temperature profile of run 13 for PB-Cu (a) Experimental results (b) Simulation result

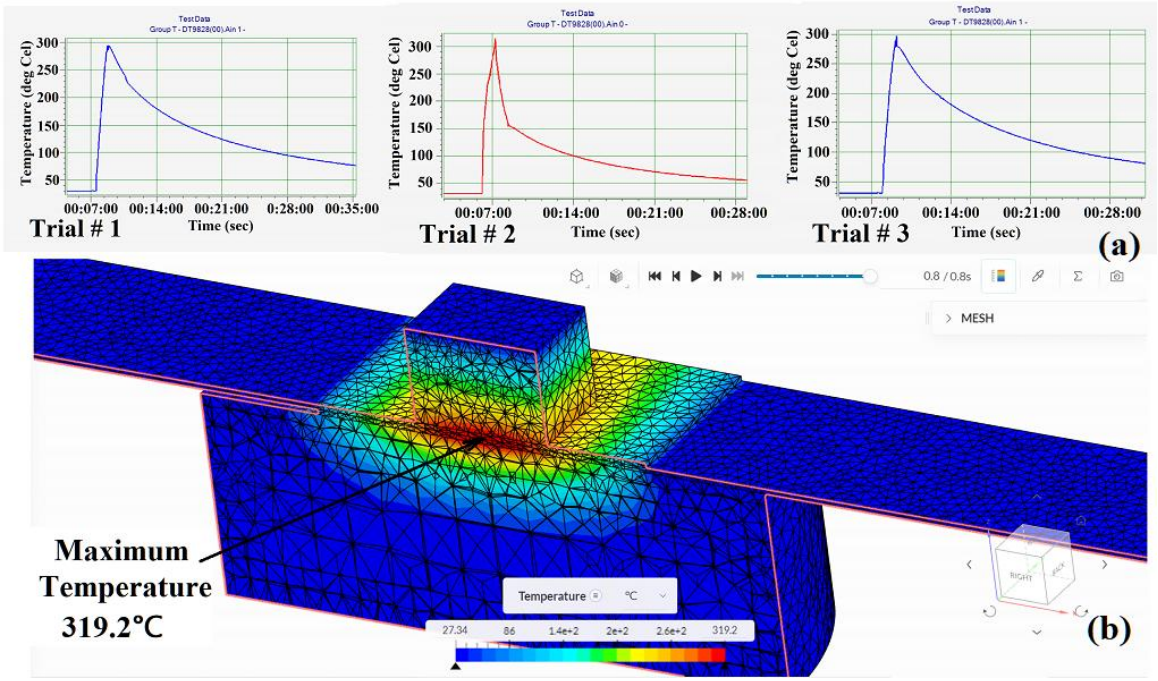

Figure 5.6: Temperature profile of run 14 for PB-Cu (a) Experimental results (b) Simulation result

The second simulation trial was performed at run number 14, which has a moderate value of bonding ratio ($\beta = 0.59$) with clamping force of 1200 N, vibration amplitude of 31.5 µm, and

weld time of 0.80 sec. The values of all the process parameters were assigned at the middle level in that run. The heat flux values H_d and H_f were 219.19 x 10^6 W/m^2 and 6.65 x 10^6 W/m^2 respectively. The simulation trial performed at these inputs produced a temperature of 319.2℃. The value of the peak average interface temperature obtained by the thermocouple at the same parameter settings was 302.33℃. The tensile-shear load obtained at this parameter setting was 1521.33 N. The values of interface temperature and load value are higher than those in the previous simulation run. The corresponding results from real-time observation and simulation are shown in Figure 5.6. The temperature distribution is shown along the longitudinal section of the assembly.

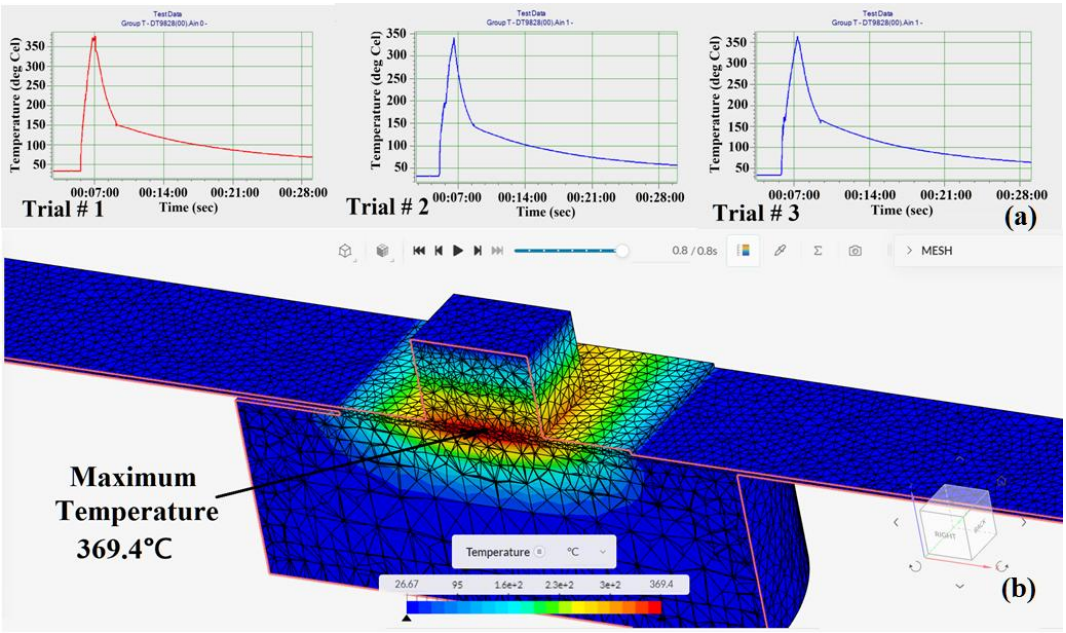

Figure 5.7: Temperature profile of run 16 for PB-Cu (a) Experimental results (b) Simulation result

The third simulation trial was performed at run number 16, which has the highest value of bonding ratio (β = 0.85) with clamping force of 1800 N, sonotrode vibration amplitude of 31.5 µm, and weld time of 1.0 sec. The values of two process parameters, the clamping force and weld time, were assigned at a high level in that run. The heat flux values H_d and H_f were 315.59 x 10^6 W/m^2 and 9.98 x 10^6 W/m^2 respectively. The simulation trial performed with those inputs generated a temperature of 369.4℃. The value of the peak average interface temperature obtained by the thermocouple at the same parameter settings was 361.33℃. The tensile-shear load obtained at that parameter setting was 2129.67 N. The values of interface temperature and load are the highest at the high level of parameters and bonding ratio. The corresponding results from real-time observation and simulation are shown in Figure 5.7. The temperature distribution is shown along the longitudinal section of the assembly.

Further, it was observed from the simulated results that the values of interface temperature as well as tensile-shear load increased with the increased clamping force while keeping the other parameters constant. Run 15 and Run 1 were simulated at the same values of vibration amplitude (= 28.0 µm) and weld time (= 0.80 sec) while vibration amplitude is at a low level. The simulated results of interface temperature and the value of tensile-shear load increased from 265.3℃ to 307.5℃ and from 1118.67 N to 1785.33 N respectively, when the clamping force was increased from 700 N to 1800 N. Run 13 and run 3 were simulated at the middle level of vibration amplitude at 31.5 µm and at a fixed value of weld time of 0.6 sec. The interface temperature and the tensile-shear load increased from 256.1℃ to 281.8℃ and from 886.67 N to 1112 N, respectively, when the clamping force was increased from 700 N to 1800 N. Similarly, a high level of vibration amplitude (= 35.0 µm) and a fixed value of weld time of 0.80 sec. were used for simulating runs 6 and 17. The interface temperature increased from 278.6℃ to 349.7℃, while the tensile-shear load was increased from 1209.67 N to 1891.33 N when the clamping force was increased from 700 N to 1800 N.

(C) PB-Al

The prediction results and the experimentally observed values of the interface temperature for the PB-Al combination are tabulated in Table 5.3. The first simulation trial was performed at run number 8, which had the least value of bonding ratio ($\beta = 0.23$). The values of process parameters are: clamping force = 1100 N; weld time = 0.20 sec; and vibration amplitude = 28.0 µm. The values of two process parameters, the weld time and clamping force, were assigned at a low level in that run. The heat flux values H_d and H_f were 75.96 x 10^6 W/m^2 and 6.29 x 10^6 W/m^2 respectively. The simulation trial performed with these inputs produced a value for the mean temperature of 102℃ which is the lowest value obtained. The value of the average peak interface temperature obtained by the thermocouple was 99.07 ℃ and the tensile-shear load was 939.67 N at the same parameter settings. The values of interface temperature and load are towards the lowest side at the low level of parameters and bonding ratio. The corresponding results from real-time observation and simulation are shown in Figure 5.8.

Table 5.3: Experimental and simulation temperature data for PB-Al

Run No.	Clamping Force, F_c (N)	Weld Time, W_t (sec)	Vibration Amplitude, V_a (μm)	Weld Area, W_a (mm^2)	Bonding ratio (β)	Exp. Interface Temp. * (°C)	Simulated Interface Temp. (°C)	Tensile-shear load* (N)
1	1100	0.70	28.0	48.65	0.37	161.27	167.1	1433.33
2	**1575**	**0.45**	**28.0**	**53.62**	**0.41**	**204.13**	**210.3**	**1372.67**
3	1575	0.70	24.5	69.86	0.54	197.63	205.1	1574.33
4	2150	0.45	24.5	73.15	0.56	287.4	293.8	1642.67
5	1575	0.20	31.5	44.85	0.35	102.83	110.9	1120.00
6	1575	0.45	28.0	66.78	0.51	200.8	204.2	1553.33
7	1575	0.45	28.0	56.36	0.43	169.87	165.9	1460.00
8	**1100**	**0.20**	**28.0**	**30.12**	**0.23**	**99.07**	**102.0**	**939.67**
9	1575	0.45	28.0	62.89	0.48	152.63	153.8	1498.67
10	1575	0.70	31.5	48.18	0.37	164.23	160.8	1395.33
11	1100	0.45	24.5	73.65	0.57	115.23	121.0	1286.67
12	1575	0.45	28.0	51.98	0.40	163.53	164.6	1448.33
13	2150	0.20	28.0	60.44	0.46	153.47	161.7	1538.33
14	**2150**	**0.70**	**28.0**	**77.74**	**0.60**	**293.77**	**296.1**	**1739.67**
15	1100	0.45	31.5	57.51	0.44	136.93	134.0	1371.00
16	2150	0.45	31.5	63.59	0.49	275.37	285.8	1810.00
17	1575	0.20	24.5	33.15	0.26	101.17	106.2	981.00

* The mean of three experimental trials.

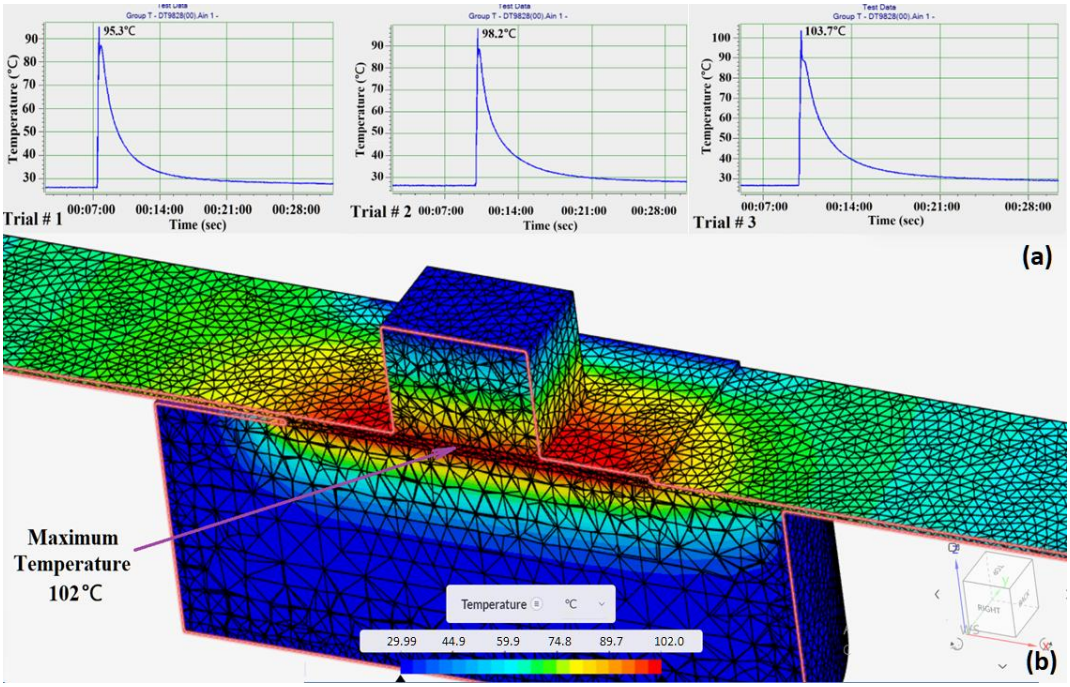

Figure 5.8: Temperature profile of run 8 for PB-Al (a) Experimental results (b) Simulation result

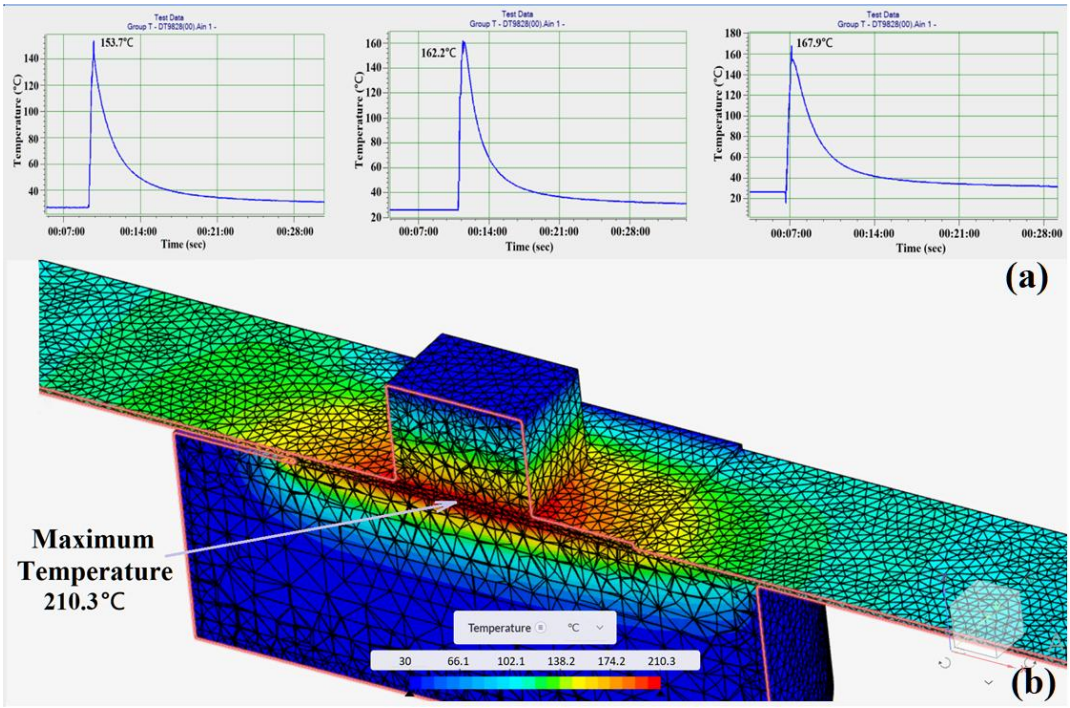

Figure 5.9: Temperature profile of run 2 for PB-Al (a) Experimental results (b) Simulation result

The second simulation trial was performed at run number 2 which had the middle value of bonding ratio ($\beta = 0.41$) with clamping force = 1575 N, weld time = 0.45 sec and vibration amplitude of 28 µm. The values of all the process parameters were assigned at the middle level in that run. The heat flux values H_d and H_f were 135.35 x 10^6 W/m^2 and 9.01 x 10^6 W/m^2 respectively. The simulation trial performed at these inputs produced a temperature of 210.3℃. The value of the peak average interface temperature obtained by the thermocouple at the same parameter settings was 204.13℃. The tensile-shear load obtained at this parameter setting was 1406 N. The values of interface temperature and load value are higher than those in the previous simulation run. The corresponding results from real-time observation and simulation are shown in Figure 5.9.

The third simulation trial was performed at run number 14, which has the highest value of bonding ratio ($\beta = 0.60$) with clamping force of 2150 N, weld time of 0.7 sec, and sonotrode vibration amplitude of 28 µm. The values of two process parameters, the clamping force and weld time, were assigned at a high level in that run. The heat flux values H_d and H_f were 197.93 x 10^6 W/m^2 and 12.29 x 10^6 W/m^2 respectively. The simulation trial performed with those inputs generated a temperature of 296.1℃. The value of the peak average interface temperature obtained by the thermocouple at the same parameter settings was 293.77℃. The tensile-shear load obtained at that parameter setting was 1740 N. The values of interface

temperature and load are the highest at the high level of parameters and bonding ratio. The corresponding results from real-time observation and simulation are shown in Figure 5.10.

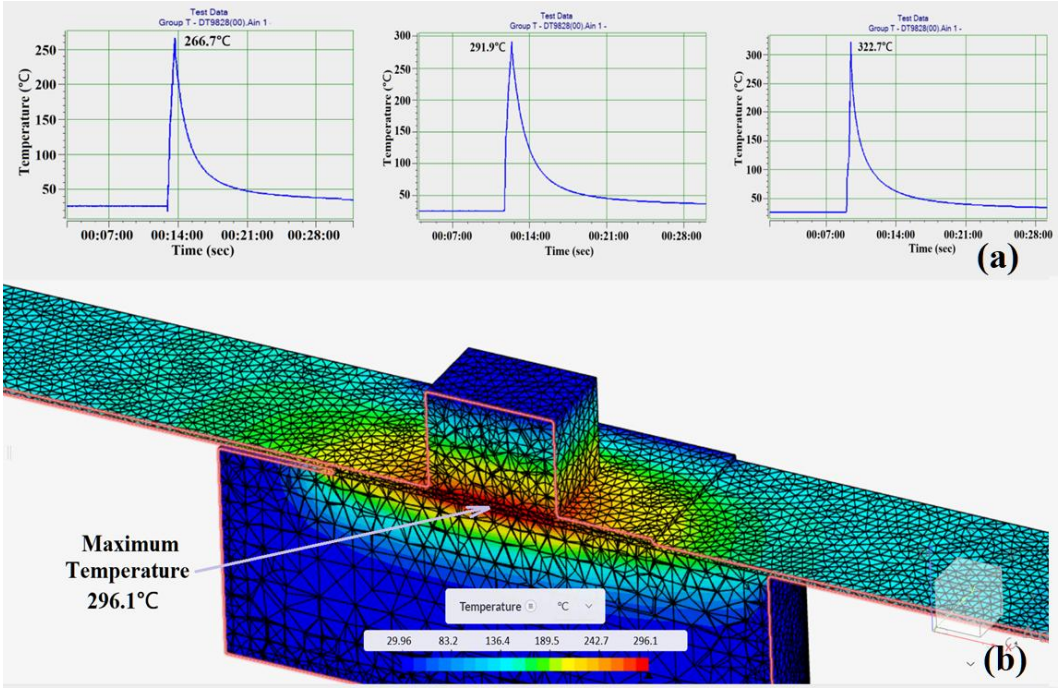

Figure 5.10: Temperature profile of run 14 for PB-Al (a) Experimental results (b) Simulation result

In the case of PB-Al joints also, it was observed from the simulated results that the values of interface temperature as well as tensile-shear load increased with the increased clamping force while keeping the other parameters constant. Run 11 and Run 4 were simulated at the same values of vibration amplitude (= 24.5 µm) and weld time (= 0.45 sec), while vibration amplitude was at a low level. The simulated results of interface temperature and the value of tensile-shear load increased from 121℃ to 293.8℃ and 1286.67 N to 1642.67 N respectively, when the clamping force was increased from 1100 N to 2150 N. Run 8 and run 13 were simulated at the middle level of vibration amplitude at 28.0 µm and at a fixed value of weld time of 0.2 sec. The interface temperature and the tensile-shear load increased from 102℃ to 161.7℃ and from 939.67 N to 1471.67 N, respectively, when the clamping force was increased from 1100 N to 2150 N. Similarly, a high level of vibration amplitude (= 31.5 µm) and a fixed value of weld time of 0.45 sec. were used for simulating runs 15 and 16. The interface temperature increased from 134℃ to 285.8℃, while the tensile-shear load was increased from 1371 N to 1810 N when the clamping force was increased from 1100 N to 2150 N.

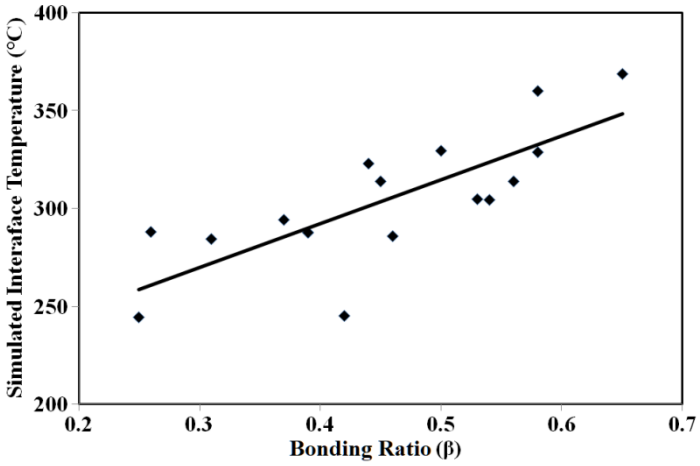

Figure 5.11: Effect of bonding ratio on simulated results of interface temperature for PB-PB

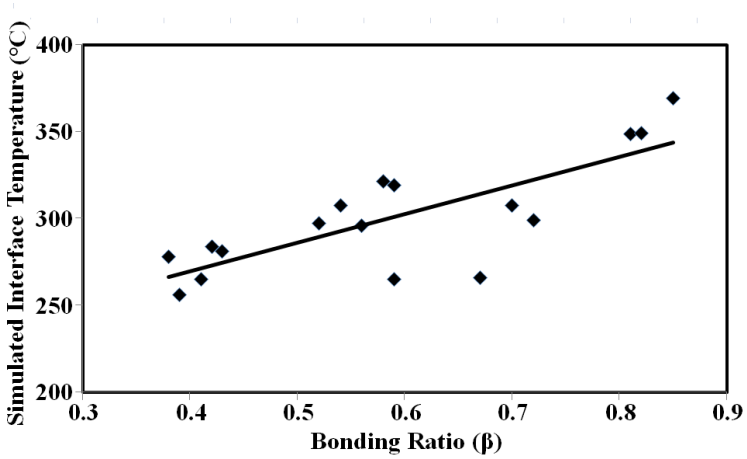

Figure 5.12: Effect of bonding ratio on simulated results of interface temperature for PB-Cu

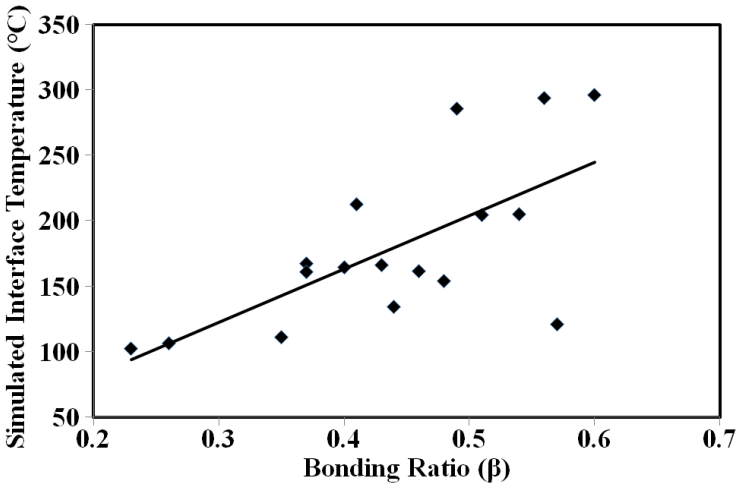

Figure 5.13: Effect of bonding ratio on simulated results of interface temperature for PB-Al

It is also evident from the observation that the interface temperature increases with the increasing value of the bonding ratio in all the three cases, i.e. PB-PB, PB-Cu, and PB-Al, as shown in Figure 5.11 to 5.13, respectively.

The bonding ratio represents the part of the area under the sonotrode tip that gets converted into the actual weld area. If the value of the bonding ratio is on the higher side, it implies that more deformable area has been available for the heat flux for deformation. The simultaneous action of ultrasonic vibration and clamping force produces a parallel relative motion in the contacting surfaces. The higher value of clamping force brings the contacting surfaces into close contact with each other, thereby, providing more area for action. As a result, heat generation at the overlapped areas increases, which reduces the resistive strength of the oxide and other contaminants against the progressive plastic deformation as well as shearing of the surface asperities. Ultimately, the nascent metallic surfaces start forming micro-welds. The experimental results also corroborate the simulated results.

5.2.2 Prediction of Temperature Profiles in Weld Zones

The thermal analysis of the USW process can be utilized to predict the temperature at different zones in the weld interface as well as in different parts of the assembly, such as the sonotrode and anvil. In the case of PB-PB joints, run number 10, having the highest temperature value and joint strength, has been used for prediction analysis.

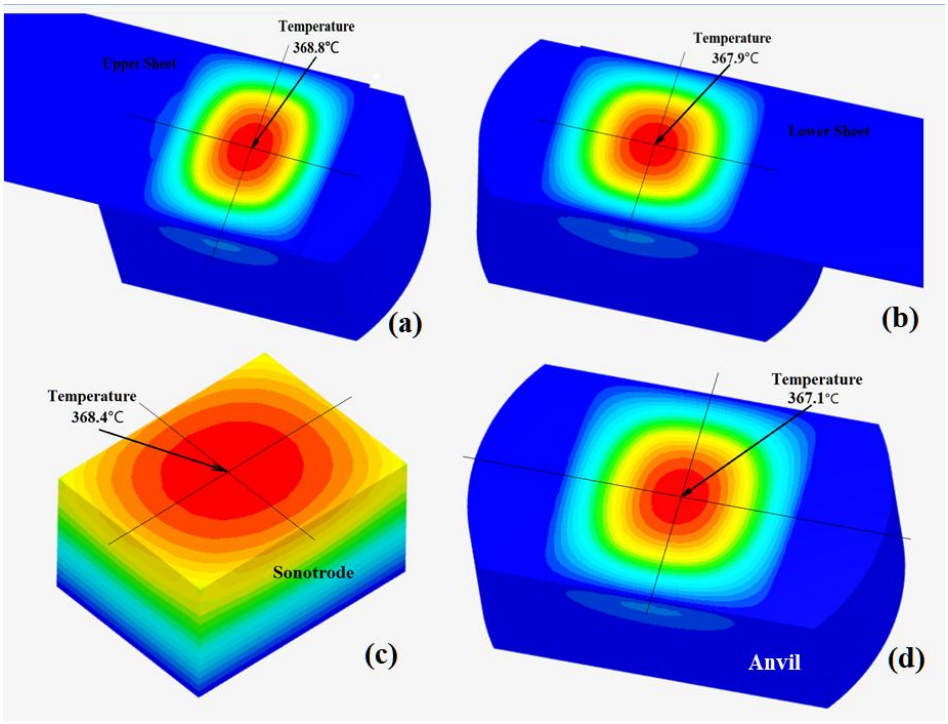

Figure 5.14: Temperature contour profile in (a) upper sheet (b) lower sheet (c) sonotrode tip and (d) anvil for PB-PB joints

Figure 5.14 shows the uniformly distributed temperature zones in the phosphor bronze upper and lower sheets, sonotrode tip, and anvil.

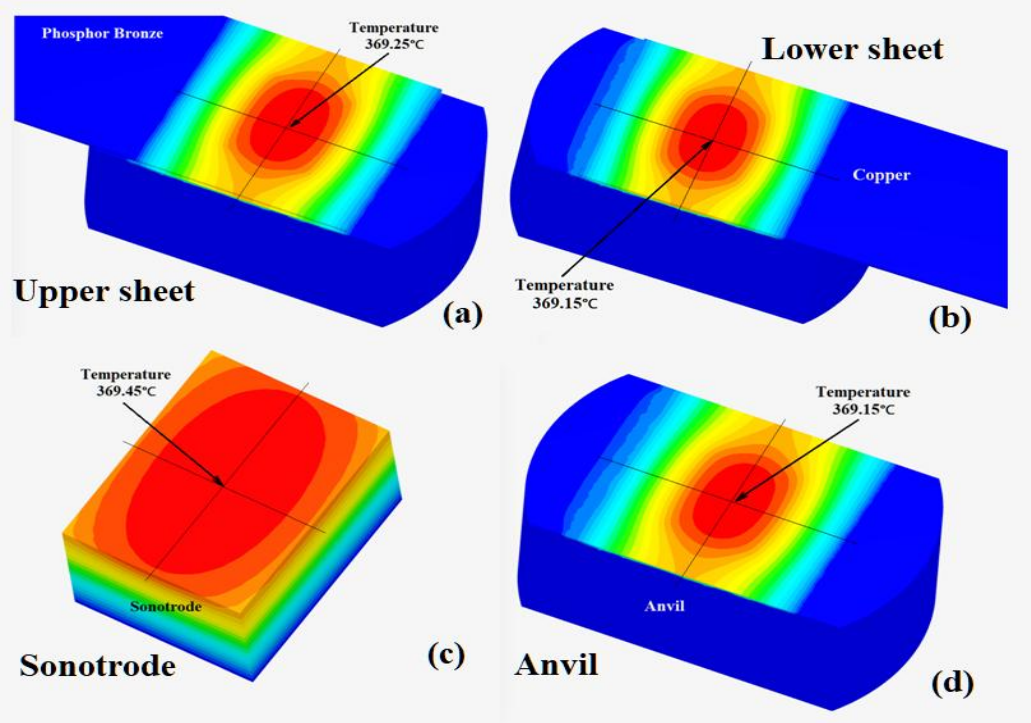

Figure 5.15: Temperature contour profile in (a) upper sheet (b) lower sheet (c) sonotrode tip and (d) anvil for PB-Cu joints

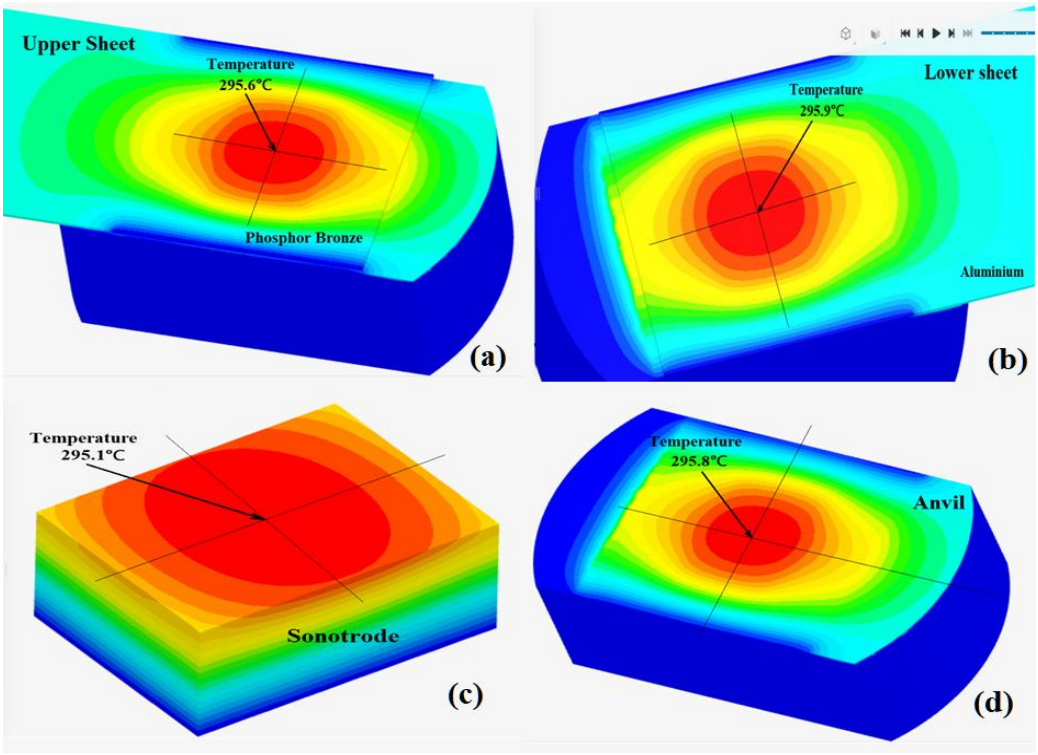

Figure 5.16: Temperature contour profile in (a) upper sheet (b) lower sheet (c) sonotrode tip and (d) anvil for PB-Al joints

Similarly, Figure 5.15 and Figure 5.16 show the temperature zones in different parts of the weld joint assembly, including the work pieces and the tooling for PB-Cu and PB-Al, respectively. In the case of PB-Cu and PB-Al joints, run numbers 16 and 14 have been selected for analysis as these runs give the maximum value of interface temperature and tensile-shear load.

The temperatures at the centres of the zones are shown in Figures 5.14 to 5.16. The red colour zones indicated the highest temperature near the weld zone which gradually changed to blue colour away from it indicating the lowest temperature zone. The value of the peak temperature in this zone is 368.8℃ for PB-PB, 369.2℃ for PB-Cu, and 295.6℃ for PB-Al. These temperatures are high enough to mobilize the considerable interface activities. Besides, significant plastic deformation having taken place, the oxides layer also gets burst and pure metallic adhesion takes place (Bakavos and Pregnell, 2010). The highest temperature is experienced by the area under the sonotrode tip as indicated by the above figures. Therefore, the top part and the interface of both the sheets go through severe plastic deformation, and the material starts yielding. The surrounding areas, however, are not susceptible to much yielding, as is evident from the blue colour of the weld metal sheets. The temperatures towards the extremes of sonotrode and anvil are very low as compared to the weld zone due to their low thermal conductivity as well as low thermal contact conductance relative to the weld material at contacting surfaces. But the surfaces of the sonotrode and the anvil which come into contact with the parent metal get instantaneous heat, and the temperature at the centre of these surfaces reaches very close to the interface temperature instantly.

5.2.3 Estimation of Heat Affected Zone and Thermo-Mechanical Affected Zone

The temperature predictions using thermal simulation corroborate the existence of TMAZ and HAZ in the vicinity of the weld zone. The temperatures at the weld zone were observed at the end of the weld cycle to explore further thermal activities at the weld interfaces of PB-PB, PB-Cu, and PB-Al combinations. Figure 5.17 to Figure 5.19 show the variation of the temperature at the weld interface starting from the centre line below the sonotrode tip and in its surroundings for PB-PB, PB-Cu, and PB-Al weld coupons having the highest bonding ratio respectively.

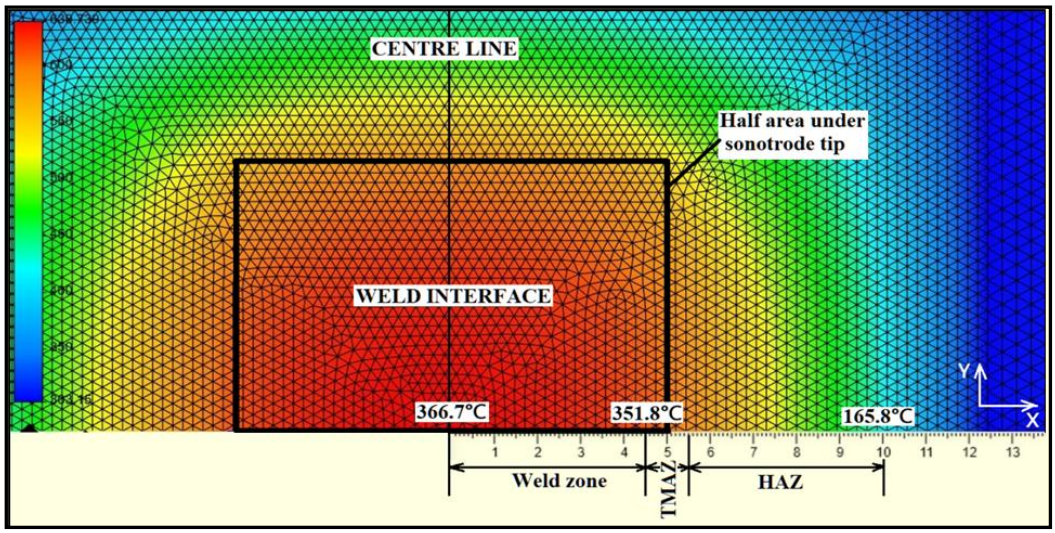

Figure 5.17: Temperature variations at the weld interface along X axis for the PB-PB joint

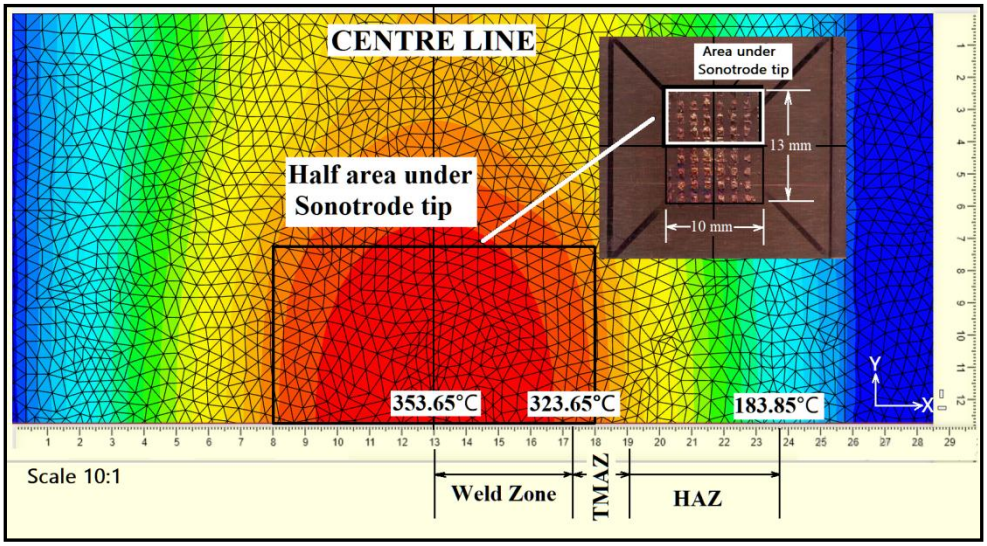

Figure 5.18: Temperature variations at the weld interface along X axis for the PB-Cu joint

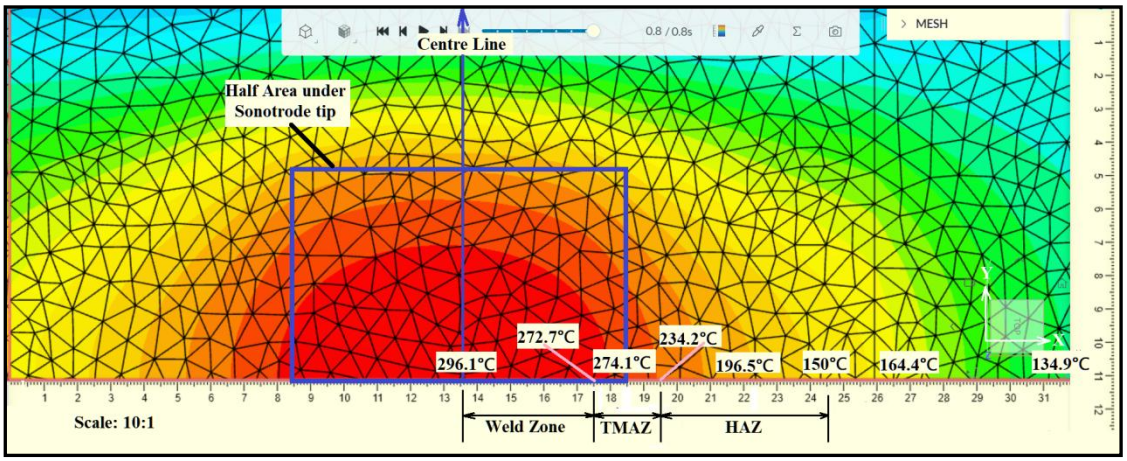

Figure 5.19: Temperature variations at the weld interface along X axis for the PB-Al joint

There was a continuous variation in the colour of the interface both in X and Y directions, ranging from the hottest (red colour) to the coolest (blue colour) temperature. The central part had the maximum temperature where the effects of clamping force and ultrasonic vibrations were concentrated. The interface in this region underwent severe plastic deformation and heat generation due to friction, so it had the highest temperature. In this region, the oxide layer breaks and asperities decrease, bringing nascent metals into close contact and initiating micro-bonding.

Plotting the interface temperature along the X-axis with respect to the distance from the centre, as shown in Figures 5.20, 5.21, and 5.22 revealed more information related to the HAZs and TMAZs for all the three combinations.

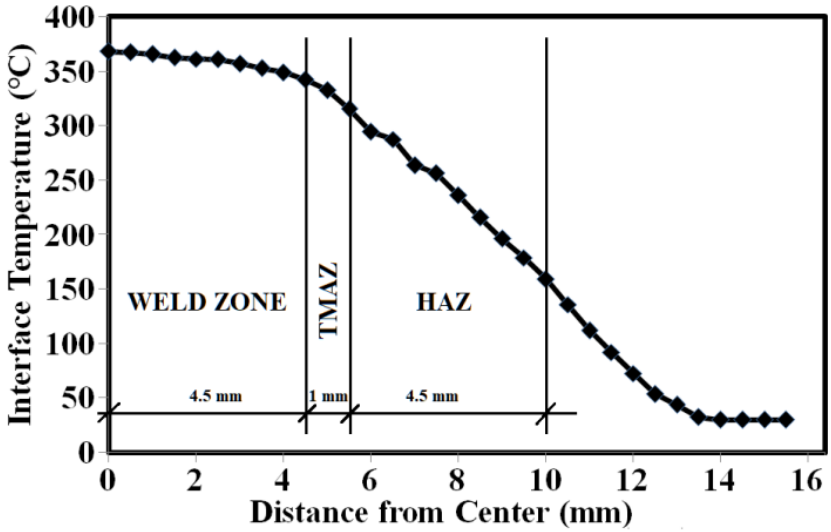

Figure 5.20: Different zones in the weld interface for the PB-PB joints

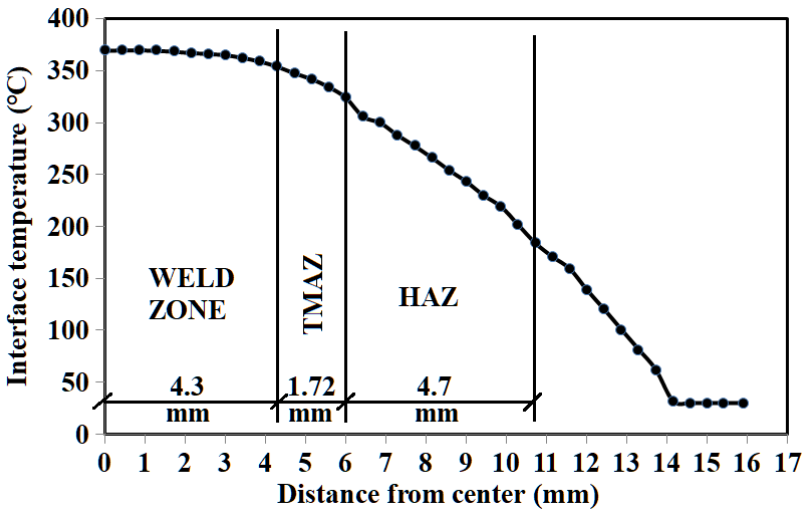

Figure 5.21: Different zones in the weld interface for the PB-Cu joints

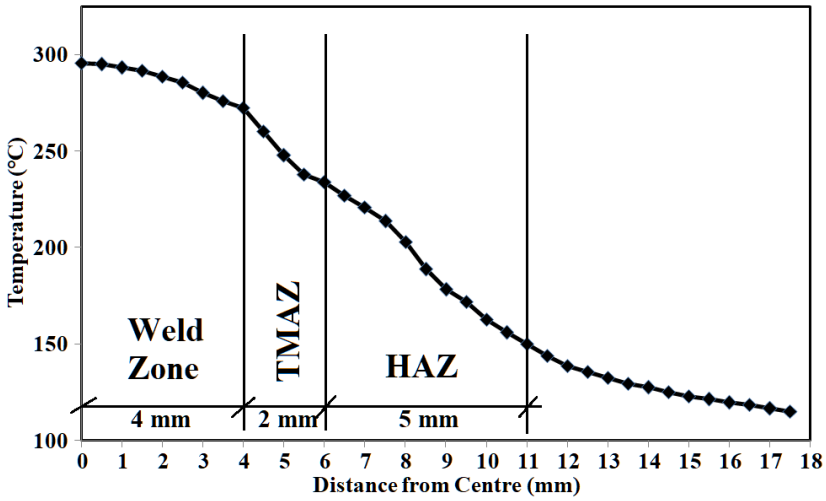

Figure 5.22: Different zones in the weld interface for the PB-Al joints

It was observed that the maximum interface temperature at the end of the weld cycle was almost constant up to a certain distance along the X-axis. It started decreasing at a certain distance from the centre. It was the area that experienced severe plastic deformation. The micro-bonding initiated in this region. This area is known as the 'deformation zone' or 'weld zone.' There was a sharp fall in the temperature afterward. This zone also experienced metal softening due to plastic deformation and frictional heat. This is called the 'friction zone' and may be considered as TMAZ. It spreads beyond the boundary of the sonotrode tip. The recrystallization temperature is usually 0.3 to 0.6 times the melting temperature (Bhargava et al., 2017). The temperature in TMAZ was within this range.

Afterwards, there was a continuous fall in the interface temperature for a sufficiently longer distance. This is the 'non-contact zone' where no bonding takes place, but some microstructural changes may be observed due to heat. This may be treated as HAZ.

The spans of the 'deformation zone', the 'friction zone', TMAZ, and HAZ along the X axis, for all the three combinations have been shown in Figure 5.20, 5.21, and 5.22 respectively. The summary of the interface temperature and distance along the X axis applicable for different zones in the three combinations is briefed in Table 5.4.

Table 5.4: Summary of the interface temperature and distance along X axis measured for different zones for PB-PB, PB-Cu, and PB-Al

Weld Joint combi-nation	Temp. at the Centre (°C)	Temp. at the end of Defor-mation zone (°C)	Temp. at the end of Friction zone (°C)	Temp. at the end of HAZ (°C)	Distance of Defor-mation zone from Centre line along X axis (mm)	Distance of Friction zone from Centre line along X axis (mm)	Distance of Non-contact zone from Centre line along X axis (mm)	Length of Defor-mation Zone along X axis (mm)	Length of TMAZ along X axis (mm)	Length of HAZ along X axis (mm)
PB-PB	367.9	342.8	318.0	163.7	4.5	5.5	10.0	4.5	1.0	4.5
PB-Cu	353.6	323.6	279.1	183.8	4.3	6.0	10.7	4.3	1.7	4.7
PB-Al	296.1	272.7	234.2	150.0	4.0	6.0	11.0	4.0	2.0	5.0

Similarly, the thermal profile of the sonotrode at the end of weld time in an upward direction has been shown in Figure 5.23 (a), Figure 5.24 (a), and Figure 5.25 (a) for the three weld combinations.

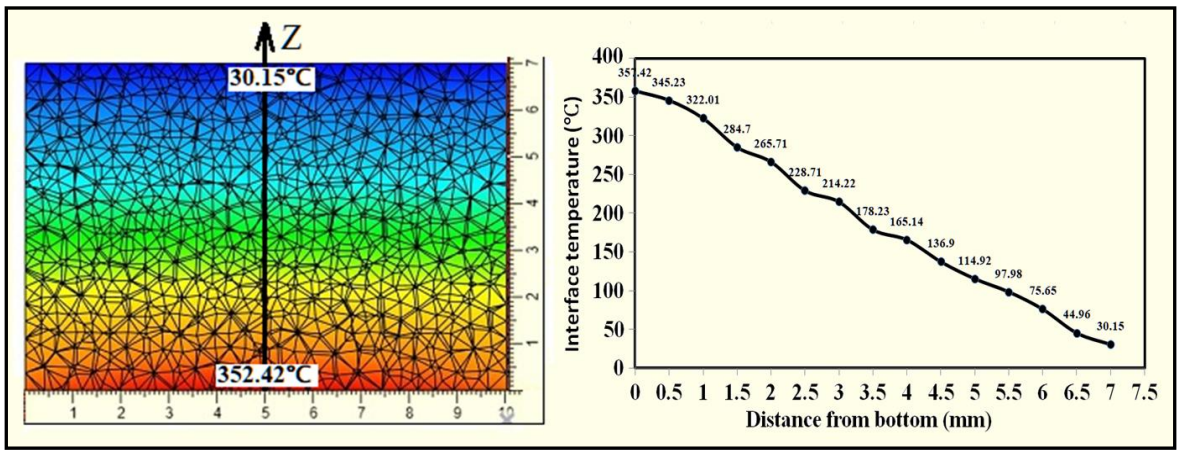

Figure 5.23: Temperature profile for sonotrode – PB-PB joint (a) simulated temperature variation along Z axis (b) Plot between sonotrode temperature and distance along Z axis

The colour distribution corresponding to the temperature varied from the hottest (red colour) at the bottom to the coolest (blue colour) at the top within a height of 7 mm. It was obvious that the span of TMAZ was nil and HAZ was spread in a very small area in comparison to the weld metal. The very low thermal conductivity of sonotrode material and exposure of all the surfaces except one to the atmospheric air were responsible for this effect.

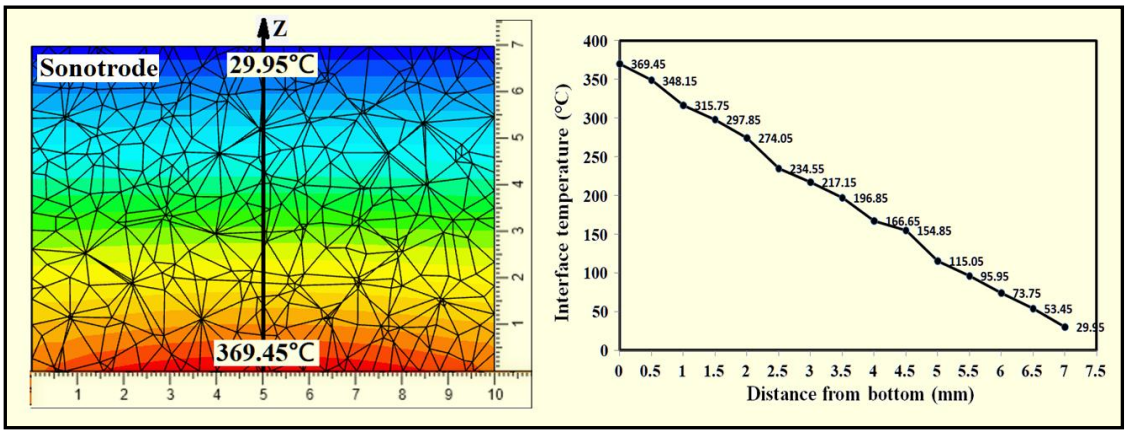

Figure 5.24: Temperature profile for sonotrode – PB-Cu joint (a) simulated temperature variation along Z axis (b) Plot between sonotrode temperature and distance along Z axis

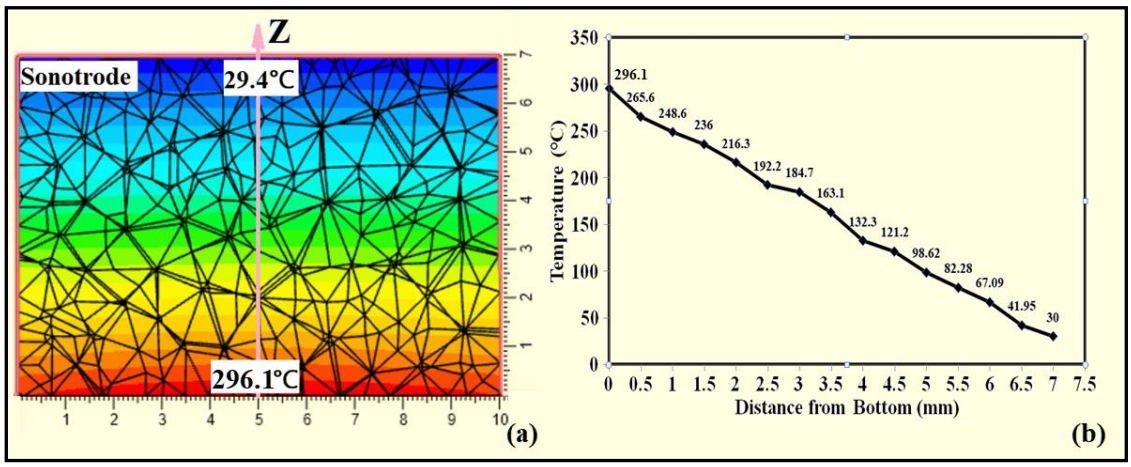

Figure 5.25: Temperature profile for sonotrode – PB-Al joint (a) simulated temperature variation along Z axis (b) Plot between sonotrode temperature and distance along Z axis

The temperature variation of the sonotrode tip along the Y-axis has been plotted in Figure 5.23 (b), 5.24 (b), and 5.25 (b) for the three weld combinations. The temperature consistently decreased while moving upward from the bottom of the sonotrode with a temperature gradient of 46°C/mm for PB-PB joints, 48.5°C/mm for PB-Cu joints, and 38°C/mm for PB-Al joints.

5.3 Validation of Finite Element Model

A model is considered efficient if it gives comparable results. The temperature values measured by the thermocouple and those obtained by the simulation were compared. Both the results were in good agreement with each other, with the maximum absolute errors within 5% for PB-PB joints, 6.26% for PB-Cu joints, and 5.68% for PB-Al joints. The relation between interface temperature and the tensile-shear load was also established. Experimental and simulated interface temperature values were plotted with the corresponding tensile-shear load as shown in

Figures 5.26, 5.27, and 5.28 for PB-PB, PB-Cu, and PB-Al respectively to prove the strong relationship between them. It is clear that the developed FEA model can be efficiently utilized to predict the interface temperature and the boundary conditions presumed in the model may be treated as valid.

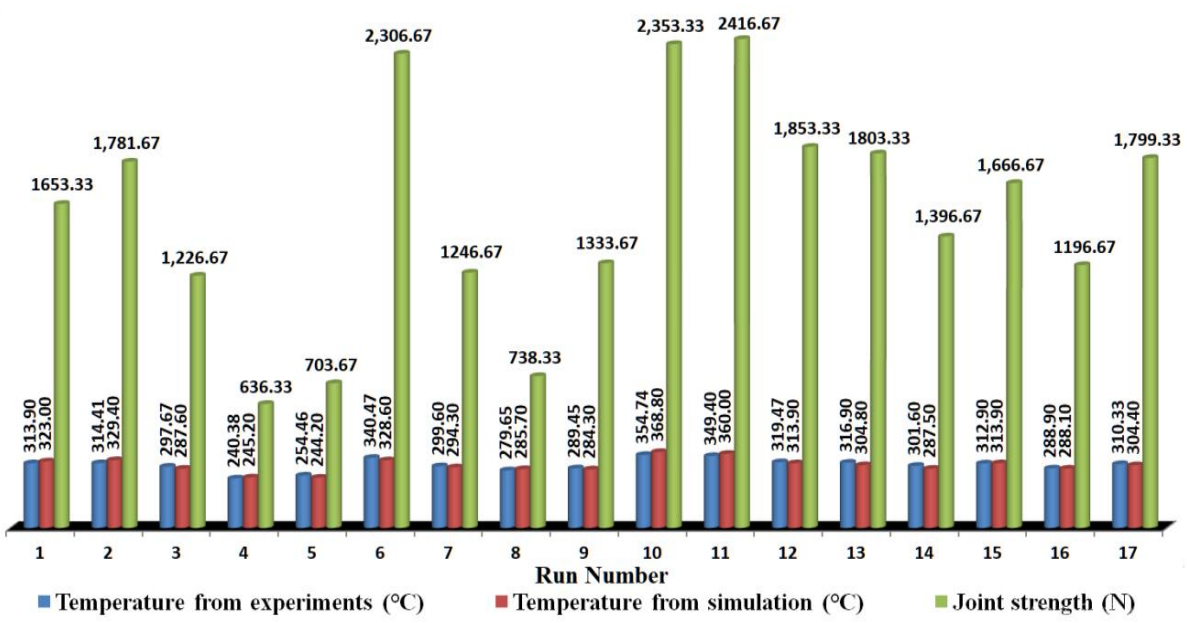

Figure 5.26: Comparison of interface temperatures with tensile-shear load for PB-PB joint

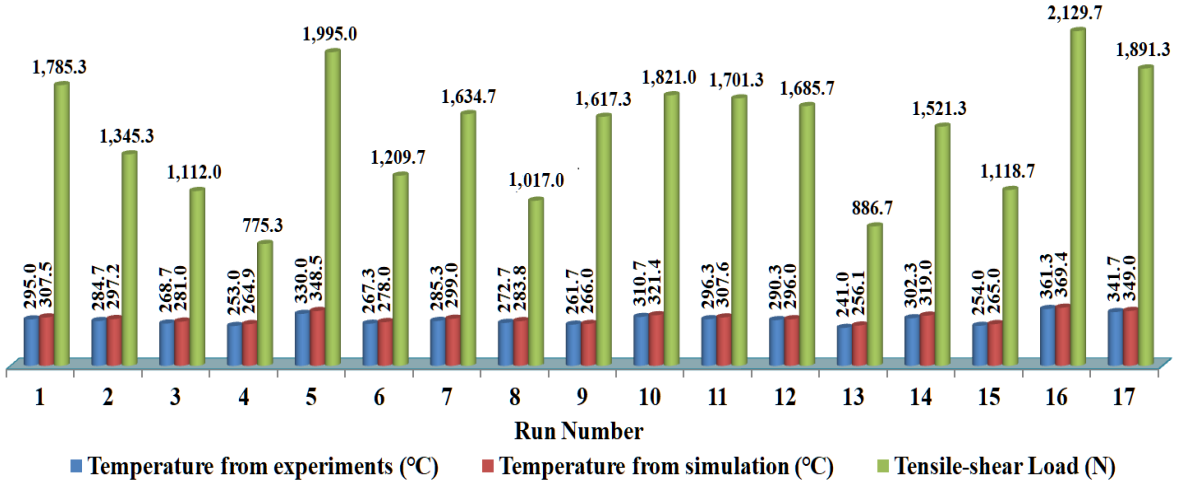

Figure 5.27: Comparison of interface temperatures with tensile-shear load for PB-Cu joint

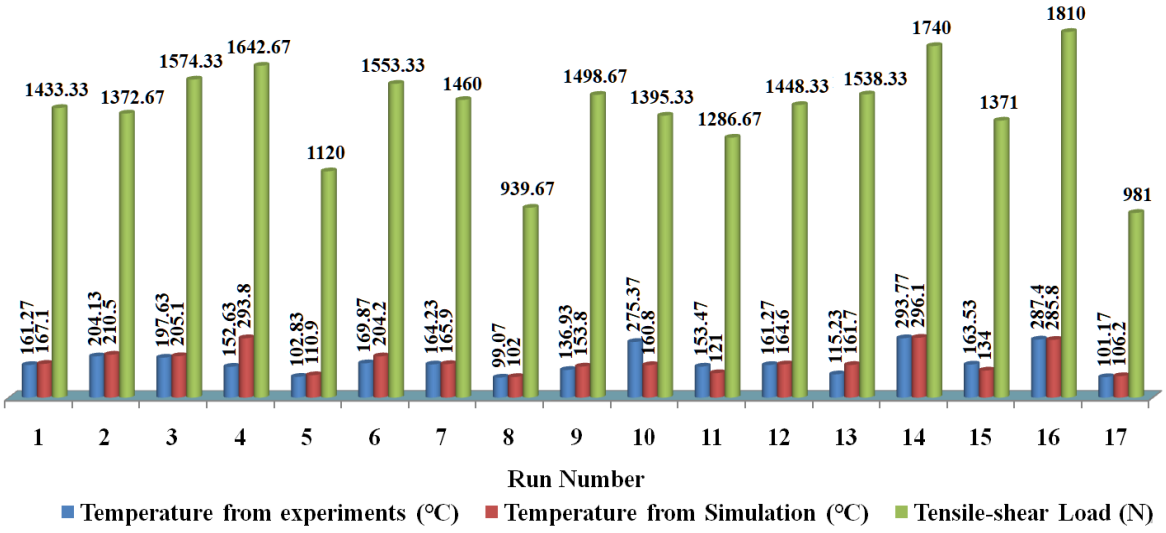

Figure 5.28: Comparison of interface temperatures with tensile-shear load for PB-Al joint

The linear association between the interface temperature obtained by simulation and the tensile-shear load was established by calculating the correlation coefficient for all three combinations of materials. The values of the correlation coefficient for PB-PB, PB-Cu, and PB-Al were 0.96, 0.87, and 0.86. These values prove a sufficiently strong correlation between the temperature developed at the interface and the weld strength. It signifies that the interface temperature may be considered to be an indicator of weld strength, and its value plays an important role in achieving stronger joints.

5.4 Summary

The thermal models of USMW of PB-PB, PB-Cu, and PB-Al joints were simulated to predict the peak interface temperature. The temperature profiles in different parts of the model were elaborated. An assessment of the expansion of the weld zone, HAZ and TMAZ has been done using the simulated temperature profiles. The interface temperature values obtained experimentally were validated by the values obtained from simulation, with the value of the correlation coefficient equal to 0.9.

CHAPTER-6

RESULTS AND DISCUSSION BASED ON THE EFFECTS OF WELD ENERGY

6.1 Introduction

The analysis related to the thermal and microstructural properties corroborates the experimental results. The present work investigated the effects of weld energy on the mechanical, thermal, and microstructural characteristics of the weld joint prepared under Energy Control Mode to meet some of the objectives. Tensile-shear load and the interface temperatures of the weld coupons were recorded. Tables 3.15, 3.16, and 3.17 in section 3.8.2 show the data obtained for the three metal combinations PB-PB, PB-Cu, and PB-Al, respectively. These tables show the tensile-shear load and the peak interface temperature.

6.2 Effect of Weld Energy on Interface Temperature

The weld interface temperature was measured by a 0.2 mm diameter N-type thermocouple wire placed at the middle of the overlapped portion of the weld coupons. Different researchers have used different methods to measure the actual temperature at the weld interface during USMW, such as placing thermocouples at the interface (Sooriyamoorthy et al., 2010; J. Yang et al., 2017), using infrared camera (Jedrasiak et al., 2015), co-relating interface temperature with the diffusivity of base metals (Hu et al., 2014) and through thermo-electromotive force between the joined surfaces (Tsujino et al., 1998). In all the cases, the observed base metals were not pre-heated, and a significant difference in the observed temperature at the weld interface has been found, but it was well below the melting temperature of the base metals.

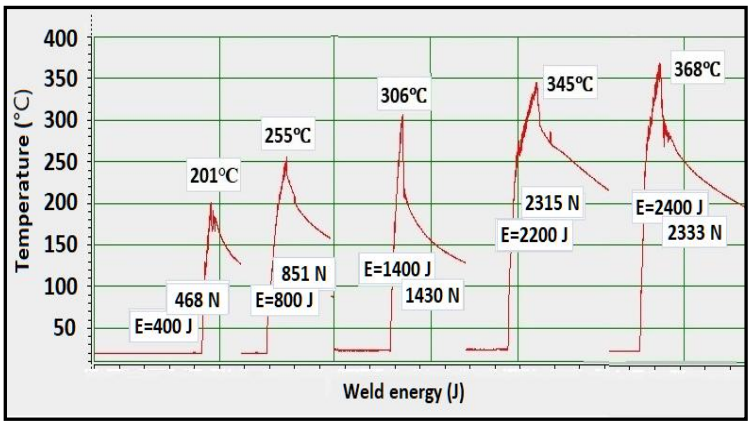

Figure 6.1: Temperature profiles showing increment in peak interface temperature and tensile-shear load with increment in weld energy for PB-PB joints

Figure 6.1 shows the thermal profiles of the weld coupons' peak interface temperatures at different energy levels along with the values of tensile-shear load for PB-PB. A similar pattern was shown by PB-Cu and PB-Al also, as shown in Figure 6.2 (a) and (b) for PB-Cu and PB-Al joints captured at the highest value of the weld energy. The variation of maximum interfacial temperatures with varying weld energy is shown in Figure 6.3 for PB-PB, PB-Cu, and PB-Al metal combinations. It was clear from the figures that the peak value of the interface temperature has increased continuously with the increasing weld energy for all the metal combinations.

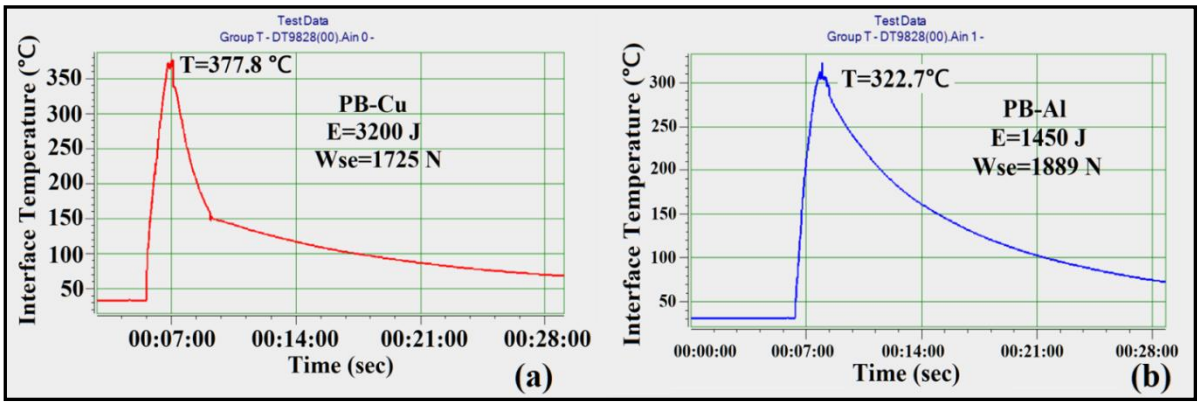

Figure 6.2: Temperature profiles showing peak interface temperature and tensile-shear load at highest weld energy (a) for PB-Cu joint (b) for PB-Al joint

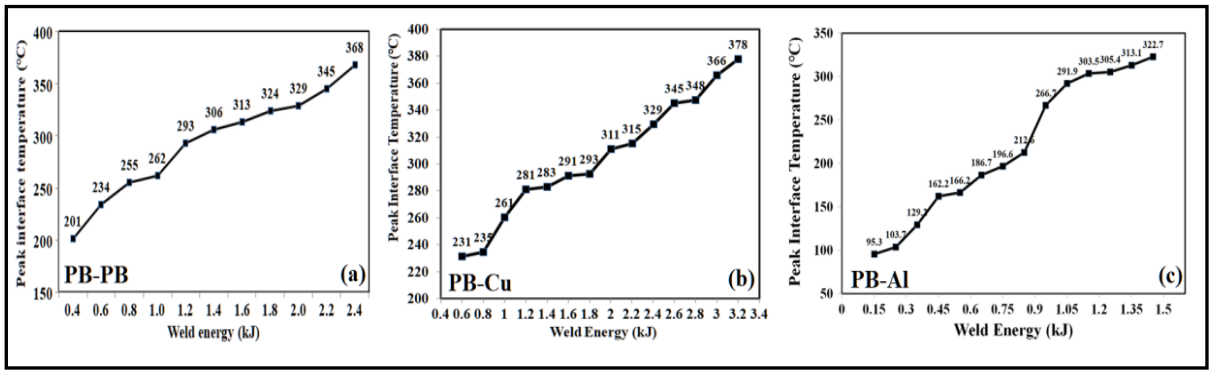

Figure 6.3: Peak interface temperature as a function of weld energy for PB-PB, PB-Cu, and PB-Al joints

The curves in Figure 6.1 show that the temperature increased instantly from room temperature to the maximum value in a very short span equal to the weld time and then rapidly derceased in the next few seconds. Afterwards, for the rest of the period, the cooling took a gentle slope and on an average, 2.5 minutes spent to reach the ambient temperature. In the case of PB-PB joints, the maximum interface temperature of 368℃ was achieved at a maximum energy value of 2400 J. Increasing the weld energy further, however, gave higher values of interface temperature but also caused the weld specimen to stick with the sonotrode tip. Therefore, sound joint could not

be achieved with higher energy values. However, the maximum interface temperature was in the range of 1/3rd of the melting temperature of phosphor bronze. Similar results were obtained by other researchers also. Yang et al. (2017) mentioned that during USMW of copper sheets at different energy levels, the temperature increased very quickly due to the influence of weld energy. He recorded the interfacial temperature of about 400℃ using a K-type thermocouple of 0.15 mm in diameter. Elangovan et al. (2009), simulated the Cu/Al interface temperature using finite element analysis and found that the maximum interfacial reached up to 336℃. Thus, there is a direct relationship between weld energy and the interfacial temperature. The most important observation made during this work was that the maximum temperature obtained by the interface was well below the melting temperature of phosphor bronze, copper, or aluminium; hence, no melting occurred during bond formation.

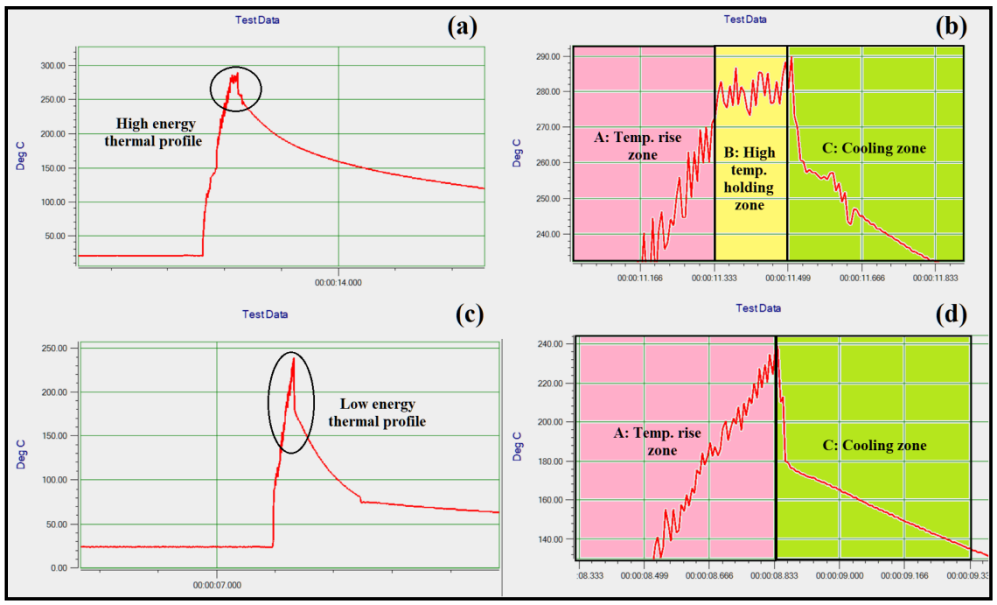

Figure 6.4: Weld thermal profiles: (a) and (c) showing high and low energy profiles respectively, (b) and (d) showing enlarged view of encircled portion of high and low energy profiles

It is generally observed during welding that initially, the temperature increases rapidly, and afterwards, the heat generation and the heat loss achieve a steady state. As more energy is utilized by the joint, the weld interface attains a higher value of temperature, resulting in stronger joints. Further analysis of the thermal profiles of the weld coupons prepared at high and low energy levels during welding, depicted in Figure 6.4 supported this concept. The enlarged views of the peaks of the thermal profiles drawn at high and low energy levels are shown in Figure 6.4. The peak of high temperature profile shown in Figure 6.4(b) was divided into three distinct zones: (A) the temperature rise zone, (B) the high temperature holding zone, and (C) the cooling zone. Such demarcations were not visible in the low energy profile depicted in

Figure 6.4(d), which is an enlarged view of the low temperature profile encircled in Figure 6.4(c). In the 'temperature rise zone', the temperature of the interface increased at a very high rate of 230°C/s, which was the result of tremendous heat generation in a very short time period. As explained earlier, the simultaneous action of deformation of metal and friction between the mating sheets produces such a high temperature instantaneously. During this period, most of the weld energy was consumed to soften the metal to enable it for deformation. The second zone was the 'high temperature holding zone'. During this short span, the temperature neither increased nor decreased, and a thermal equilibrium was established between heat generation and heat loss. However, this period was very small but, very essential for a strong joint, as the bonding reactions took place during this period. In the third zone, the 'cooling zone', the supply of acoustic power to the sonotrode was cut-off and the temperature started falling back to the room temperature, but at a much slower rate (almost one-fifth) as compared to the rate of temperature rise in zone 'A'. The given explanation justified the lower values of tensile-shear loads at lower energy levels, causing weaker joints. The above observation was consistent with the results of Zhang et al. (2014) during the ultrasonic welding of Al and Ti alloys.

6.3 Effect of Weld Energy on Weld Strength

The variation of the tensile-shear load with respect to the varying weld energy, keeping the values of clamping force and vibration amplitude fixed, is shown in Figure 6.5, Figure 6.7, and Figure 6.8 respectively for PB-PB, PB-Cu, and PB-Al joints. The gradual change in the fractured surface of PB-PB joints with increasing weld energy is shown in Figure 6.6. In the case of PB-PB joints, the weld joint started carrying a minimum load at a welding energy of 0.4 kJ. Before that, the joint was not able to sustain any load.

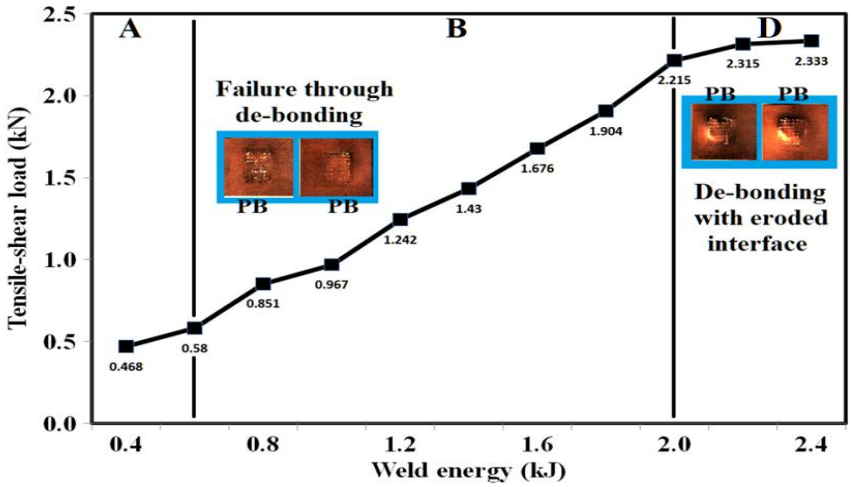

Figure 6.5: Tensile-shear load versus weld energy curve showing different stages for PB-PB similar joints (A: Beginning stage, B: Escalation stage and D: Stable stage)

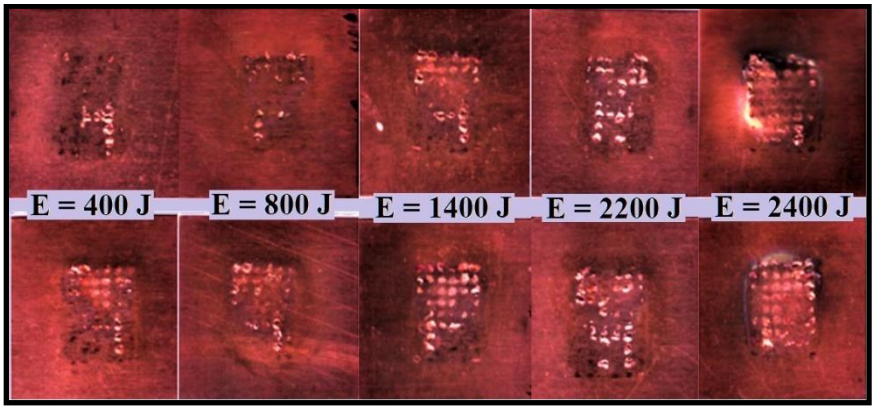

Figure 6.6: PB-PB fractured specimens in the tensile-shear strength test showing increasing weld area with increasing weld energy. Upper and bottom sheets are shown in upper and lower rows respectively

It was observed that the load curves of these metal combinations are composed of the following distinct stages; A: the beginning stage, B: the escalation stage, C: the fall stage, and D: the stable stage. In the case of PB-PB and PB-Al joints, A, B, and D stages were observed. But in the case of PB-Cu joints, a fourth stage was also involved, as shown in Figure 6.7. This stage existed between the escalation and the stable stage. After reaching a certain peak load, there is a sudden drop in the failure load. The weld coupons got fractured at the edge of the joint from the copper sheet due to lower strength of the copper compared to the phosphor bronze.

There was no significant increment in the value of tensile-shear load with increasing weld energy in the 'beginning stage', but a sharp and continuous rise was observed in the values of tensile-shear load with the increase in weld energy later in the 'escalation stage'. The 'stable stage' was almost flat, showing practically no change in the load values, and the peak load was achieved at around 2.4 kJ, 2.9 kJ and 1.9 kJ of weld energy for PB-PB, PB-Cu, and PB-Al joints. The clamping force brings the faying surfaces of the weld coupons into close contact with each other during the beginning stage. The ultrasonic vibrations produced by the sonotrode are transferred to the weld surfaces and a parallel relative motion starts between them. This action leads to progressive deformation and shearing of the surface asperities along with the weld metal under the sonotrode tip. During this process, the contaminants and the oxide layer also get scattered, and the virgin metallic surfaces come into close proximity, which results in the formation of tiny micro-bonds. In the 'beginning stage', the number of micro-bonds is less as the lower energy dissipates a smaller amount of heat, which ultimately leads to a small weld area and a low value of peak loads. With the increase in the weld energy, the temperature at the interface increases and the number as well as the size of the micro-bonds starts to grow at a faster rate. This is the onset of the 'escalation stage'. Now, the growth and coalescence of these micro-bonds results in a larger weld area in the overlapped portion of the weld coupons. The

increasing value of weld energy finally saturates the joint and the weld area obtains its maximum value, which may expand up to the size of the sonotrode tip depending upon the penetration of its serrations. The saturated weld joints have almost the same values of joint strength, which is clear from the 'stable stage' where the load curve becomes asymptotic and reaches an ultimate value of tensile-shear load, as shown in Figure 6.5 and Figure 6.8. Similar results were also obtained by Yang et al. (2017) during the ultrasonic welding of copper sheets. They observed that increasing weld energy resulted in the increased lap-shear strength of the weld coupons, which finally converged to their peak values.

The fractured surfaces for PB-PB similar joints shown in Figure 6.6 revealed the fact that the weld area increased with an increase in welding energy and reached its maximum value during welding. The mode of failure at lower values of energy was de-bonding of the interface, but it was accompanied by the erosion of the interface at the bottom of the weld nugget in the end. The energy level above the saturated value resulted in the burnt and cracked sheets near the joint, and hence, posed a limit for going beyond this level, as shown in Figure 6.7.

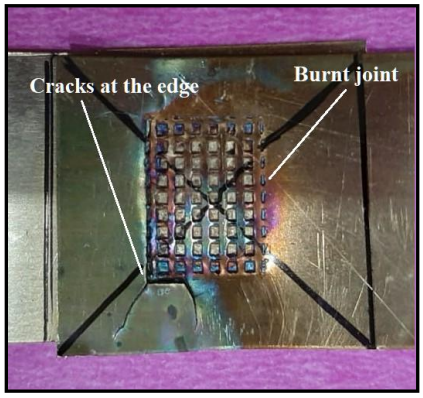

Figure 6.7: Cracked and burnt edges of the joint at a very high energy level

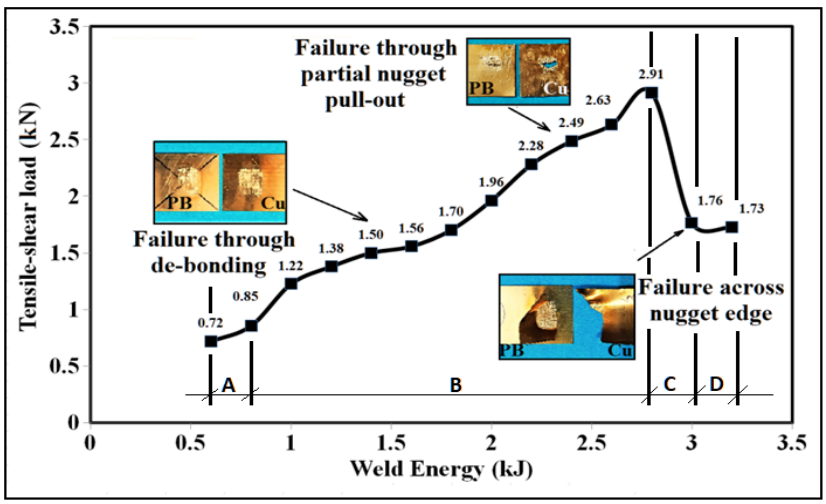

Figure 6.8: Tensile-shear load versus weld energy curve PB-Cu joints (A: Beginning stage, B: Escalation stage, C: Fall stage and D: Stable stage)

In the case of the PB-Cu dissimilar joint, the curve between the weld energy and the tensile-shear load continuously increased to obtain the peak value of 2913 N at 2800 J of weld energy. It was the last point of the 'escalation stage'. The failure mode changed from de-bonding at the interface at the lower value of weld energy to the partial nugget pull-out mode at higher values, i.e., above 2200 J up to 2800 J. Afterwards, the load value dropped suddenly, and the failure mode changed from 'partial nugget pull-out' to 'failure across nugget edge' at the copper sheet. It is evident from Figure 6.8.

It has been established that at lower weld energies, the interface temperature is not high enough to support the interface activities and there is hardly any diffusion at the interface. At lower weld energy, the interface is loosely bound. However, at the higher energy level, there is sufficient diffusion due to temperature rise and higher strain rate to make a sound joint (Haddadi and Abu-Farha, 2016). But after the peak load is achieved, there is a sharp fall in the value of the tensile-shear load. However, the weld energy is increased. It was observed that the joint cracked at the circumference around the nugget at the softer copper side, and ultimately the copper sheet had broken. It showed that the joint was stronger than the strength of the parent metal. Similar results were also observed by Mirza et al. (2016) and Kong et al. (2005).

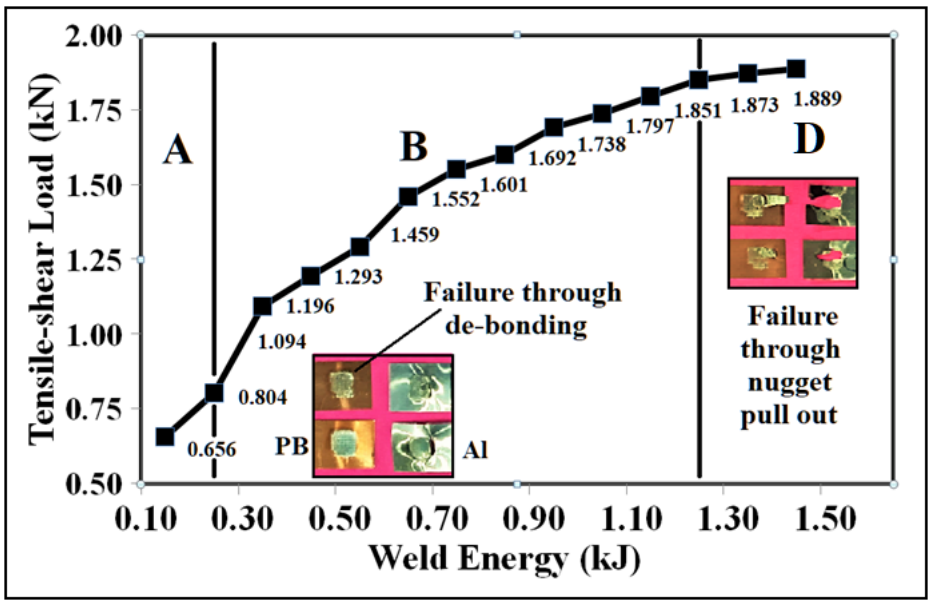

Figure 6.9: Tensile-shear load versus weld energy curve showing different stages for PB-Al dissimilar joints (A: Beginning stage, B: Escalation stage, and D: Stable stage)

The variation of the tensile-shear load with the weld energy was shown in Figure 6.9 for PB-Al dissimilar joints. The joining started at around 150 J where weak joints were obtained. The tensile-shear load increased continuously with the increasing weld energy till the peak value of

the joints (=1889 N) was achieved at 1450 J. However, the tensile-shear load appeared to get saturated after 1250 J of weld energy. The curve shown in Figure 6.9 was also divided into three regions, similar to the case of PB-PB joints. The failure mode transformed from interfacial de-bonding mode to nugget pull-out mode at higher energy. The microstructural studies conducted and explained later in the chapter verified this change over.

The conversion of fracture mode from the interfacial to the volumetric in the form of nugget pull-out was observed by other researchers also during USMW at higher values of energy. For example, Fujii et al. (2016) during an investigation of the ultrasonic weldability of aluminium alloy to stainless steel found similar results. Further investigation of the microstructures of the weld coupons explained the increased strength at higher energy levels as described below.

6.4 Metallurgical and SEM Analysis

The microstructural evolution was examined by optical microscopy and supported by the SEM images for further exploration.

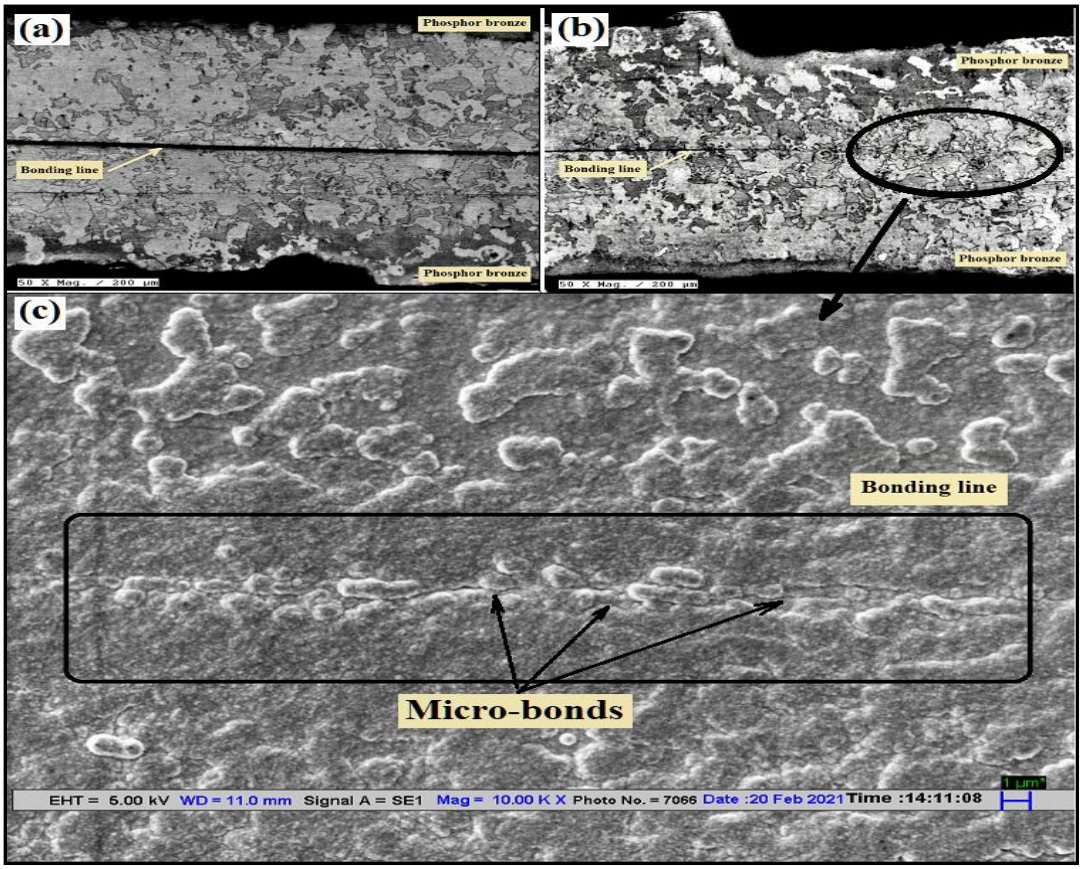

Figure 6.10: Microstructure of cross-section of weld interface for PB-PB joints (a) bonding line at low energy value (b) micrograph showing bonding at high weld energy at low resolution (c) SEM image of perfectly joined bonding line at high weld energy

Figure 6.10 (a) shows the cross-section of the PB-PB joint at low energy level where a clearly visible parting line was seen throughout the bonded area. The distribution of the grains was uniform on both sides of the joining line. Figure 6.10 (b) is the micrograph of the cross-section of the joint at high energy level taken at low resolution where it was seen that the parting line started from one end of the weld coupon and vanished afterward when the joining started.

Figure 6.10 (c) is an enlarged view of the joint area enclosed by the circle shown in Figure 6.10 (b). It shows that the grains of both the upper and lower strips of phosphor bronze merged with each other and were uniformly distributed in the bonded region. The disappearance of the parting line in the bonded region implies that the bonding was successful. The bonding region was composed of both the micro-bonds as indicated in Figure 6.10 (c) and the unbounded region at some places as shown in Figure 6.11.

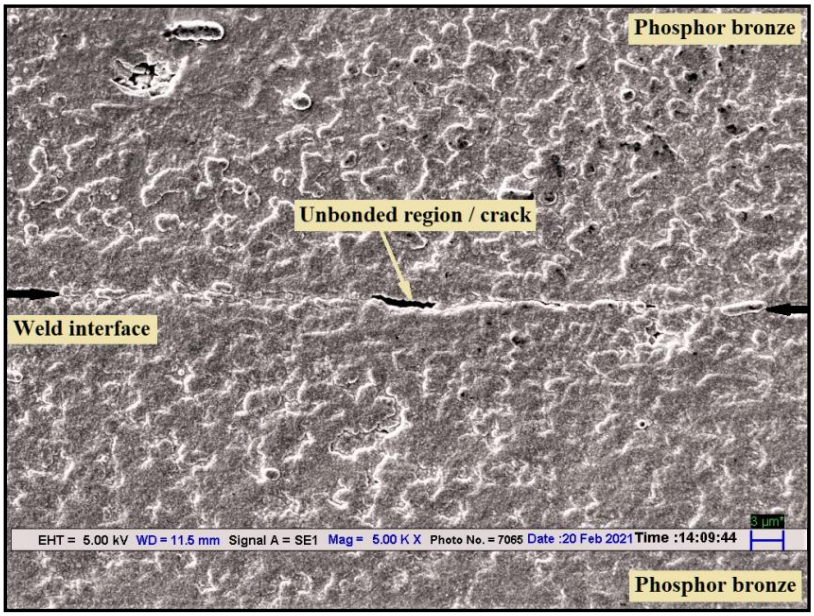

Figure 6.11: Unbonded region/cracks appeared at some of the places at the weld interface

The grain size, which is an indicator of the mechanical properties of the metal, remained unaffected in the present case. Metals typically exhibit grain growth when the temperature exceeds the recrystallization temperature. But, in the present case, the possibility of grain growth is very low due to the high heat conductivity of the weld metal and, secondly, due to an extremely low weld time of the order of 1 second. The shape of the bonded region was seen slightly curvy, which shows the flow of the metal with weld energy. The increased bond strength was due to the interlocking at the interface visible in Figure 6.12 (a) due to the swirling motion of the weld metal along the interface. There were some regions, as shown in Figure 6.12 (b) where some gaps were visible and metal and/or oxide particles were found entrapped in between.

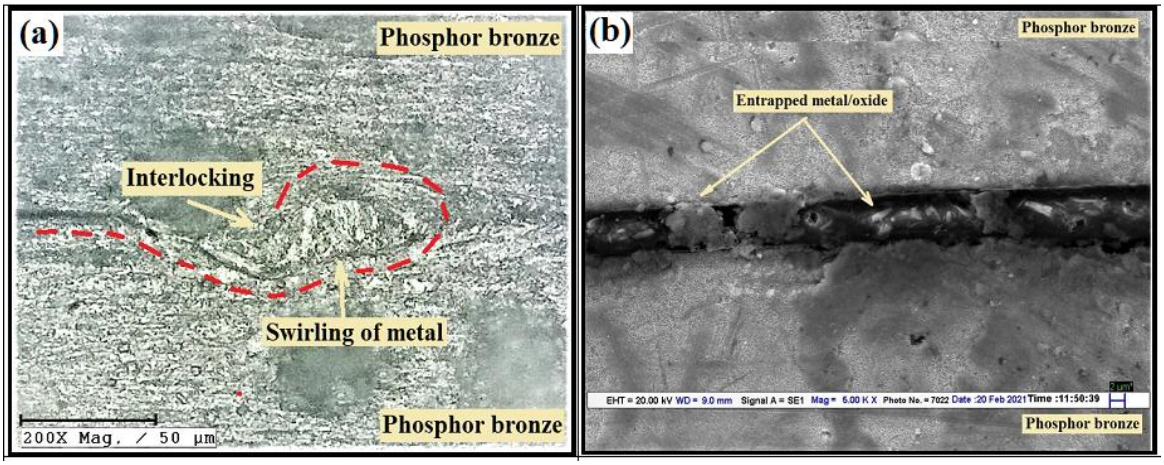

Figure 6.12: (a) Swirling of metal around the bonding line resulting in interlocking (b) SEM image of entrapped metal/oxide at the weld interface

A similar pattern was observed in the case of PB-Cu and PB-Al joints as shown in Figure 6.13 and Figure 6.14. Figure 6.13 (a) shows the weld interface between phosphor bronze and copper sheets at a low value of weld energy. The bonding line was clearly seperated, resulting in a low value of tensile-shear load. But at a higher value of the weld energy, as shown in Figure 6.13 (b), the bonding line was clear and without any gap. The SEM image of the joint made at a high weld energy shown in Figure 6.13 (c) clearly shows that a strong and sound joint was formed along the bonding line. There was a smooth mixing of the particles. There were no gaps or unbonded regions. It was also evident that the weld interface was the result of the microbonds as well as mechanical interlocks.

The microscopic and SEM images of PB-Al joints shown in Figure 6.14 (a) and (b) also indicated that the joining line was loosely formed along the interface at low weld energy level, which transformed into a uniform and firm bonding line at higher energy level. Similar to the weld joints of PB-PB and PB-Cu, the weld joint at the PB-Al interface was also composed of microbonds and mechanical interlocks. It is evident from Figure 6.14 (c).

The higher weld energy promoted the formation and spread of the microbonds along the weld interface. The weld metal at the interface softened and squeezed into the other side due to higher temperatures and clamping force. As the weld metal gets soft, the sonotrode teeth penetrate deeper into it, thereby, pushing the metals at the interface to move in a wave-like pattern (Mirza et al., 2016).

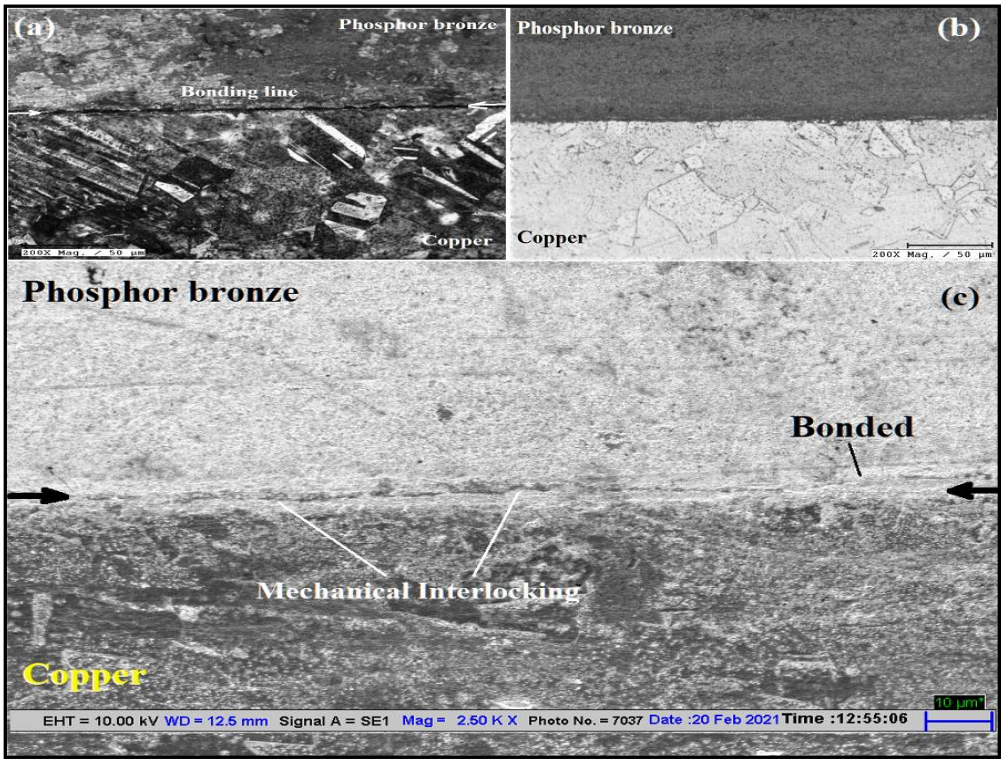

Figure 6.13: Microstructure of cross-section of weld interface for PB-Cu joints (a) bonding line at low energy value (b) micrograph showing bonding at high weld energy at low resolution (c) SEM image of perfectly joined bonding line at high weld energy

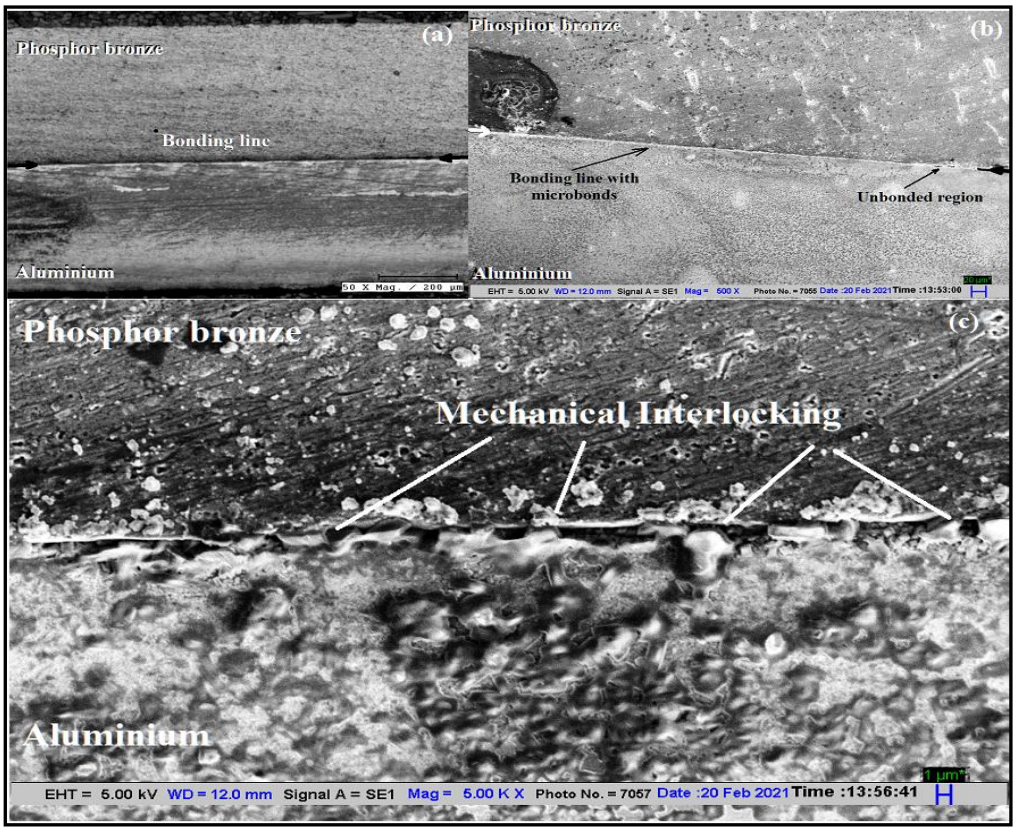

Figure 6.14: Microstructure of cross-section of weld interface for PB-Al joints (a) bonding line at low energy value (b) SEM image showing bonding at high weld energy (c) SEM image of weld interface having mechanical interlocks at high weld energy

6.5 Bonding Mechanism

Ultrasonic spot metal welding is a complex process. Several theories have been put forward by scientists in respect of bond formation, such as inter-atomic diffusion across the weld interface (Haddadi and Abu-Farha, 2015; Patel et al., 2011; Pragnell et al., 2011), micro-bonding due to significant heat generation and plastic deformation at the interface (Mirza et al., 2016; Yang et al., 2009), mechanical interlocking (Fujii et al., 2016; H. P. C. Daniels, 1965) and even localized melting at the interface (Balle and Magin, 2015; Hazlette and Ambekar, 1970). Out of these theories, the possibility of bulk inter-atomic diffusion and localized melting as the mode of joining is very low in the present case. This is because the joining process took a very short time and the temperature rise at the interface was far below the melting temperature of the weld metal.

It has been reported by Gunduz et al. (2005) that the diffusivity under ultrasonic welding conditions can increase to a great extent due to accelerated dislocation assimilation and enhanced vacancy concentration in the bond region. A strain rate as high as 1000 s^{-1} was observed during USW of Al and Zn. The concept of enhanced diffusion comes into the picture in USMW. But, in the case of PB-PB similar metal joints, the bulk diffusion at the interface is hardly observable by optical microscopic examination due to similar metal joining. However, the SEM images show a uniform microstructure at the weld interface. This is possible only if the enhanced diffusion occurred at the weld interface in the small period of weld time.

Another mode of joint formation, localized melting, is related to the temperature rise at the weld interface. The heat generation at the weld interface is the outcome of the dynamic frictional forces and the deformation of the metal under the sonotrode tip. Different approaches to interfacial temperature measurement were employed by different researchers, but in all the cases, the measured interface temperature was found to be quite below the melting temperature of the metal. However, it could not be ascertained that the temperature at some of the points at the interface could reach up to or above the melting point, as in most of the cases, the temperature measured was the average temperature of a certain volume of metal. The possibility of local melting was supported by H. Kreye (1977) during the USW of Al and Cu, where some indications of short time melting followed by rapid cooling were observed. Similarly, Gunduz et al. (2005) also observed local melting at Al-Zn solid solution. Thus, to a large extent, except for a few cases, it can be concluded that most ultrasonic metal welding is a solid-state joining process. Secondly, if some joining method involves melting at the joining region, then associated grain-growth due to heating is also observed (T. Shintomi, 2003). It is clear from

Figures 6.10, 6.13, and 6.14 that there was no enlargement of the size of the grains in the bonding region as compared to that located at some distance. As the grain size was the same, it indicated no melting or re-crystallization in the bonded region. In the present case, no corroboration of the localized melting was observed along the weld interface and the peak temperature observed was well below the melting temperature of the base metal.

The micro-bonding at the nascent metal surface points takes place due to inter-atomic forces. But it occurs only when the mating surfaces are clean at atomic level and there is an intimate contact between them. While the intimate contact may be obstructed by the oxide layer which exists on the metallic surfaces, it is very necessary to remove the oxide layer between the mating surfaces to obtain true metal-to-metal contact during USMW. The frictional forces produced by ultrasonic vibrations finely disperse the oxides away from the weld interface, allowing the nascent metal points to come into close contact. Sometimes, interface debris in the form of entrapped metal or oxide flakes was also seen within the weld, as shown in Figure 6.12 (b). In the current study, the oxide layer was found to have vanished in most of the bonded regions. Smooth and uniformly mixed grains were visible. There were some areas where gaps were seen due to the oxide layer which could not be removed completely; therefore, pure metal spots did not come into close contact. The micro-bonds at the weld interface were the primary cause for the joint formation, but as the weld energy increased, the metal started flowing across the weld interface due to the swirling motion of material. Then, the convoluted metal created mechanical interlocks in the bonding region (Z. Zhang, 2017). The combined effect of diffusion and mechanical interlocks further increased the strength of the joint in the present case.

Thus, micro-bonding through metallurgical adhesion, diffusion, and mechanical interlocking appeared to be dominant modes of joint formation at the weld interface in this study. The formation of the weld joint at the interface has been identified with three stages in the same cross-section of the weld coupon: (i) micro-bond formation (ii) twisting of the joining line due to material whirling across the interface (iii) final wave-like bonding line. It is evident from SEM images that initially micro-bonding started randomly, but with the ongoing shear oscillations around these micro-bonds, the metal started swirling and rolling across the interface in a wave-like shape. Finally, the bonding line took the form of a curvy, convoluted interfacial wave. This explanation was in agreement with the findings of Bakavos and Prangnell (2010). Hence, it can be concluded that joint strength in USMW was the combined result of the formation of micro-bonds and mechanical interlocking due to the swirling of metal at the interface.

6.6 Summary

In this chapter, a relation among peak interface temperature, weld energy, and tensile-shear strength of the joint has been developed. It is found that weld energy directly affects the joint strength and the peak interface temperature. The fracture modes of the weld specimens at different energy levels were analysed. There is a gradual shift from detachment to nugget pull-out mode as weld energy increases. The microstructural evolution was also observed at different energy levels. The observed run-time interfacial temperature provided necessary information to understand the joining mechanism by estimation and comparison of the microstructural results. It was established from the microstructural analysis that the joint was formed due to micro-bonding along with mechanical interlocking.

CHAPTER-7

CONCLUSIONS AND FUTURE WORK

7.1 Introduction

One of the major solid-state joining methods gaining popularity in recent years is ultrasonic spot metal welding (USMW). This process involves the application of ultrasonic shear vibrations accompanied by moderate pressure between the sheet metal work pieces. This action is capable of scattering the oxide layer and other contaminants that existed between the sheets to bring the pure metallic surfaces into close contact. Among numerous assorted applications that range from the automobile sector to aerospace, USMW is involved in the joining of both similar and dissimilar metal and non-metal joints. But the biggest challenge faced by the industry is to precisely control the process parameters to obtain a desired quality level for each application. Therefore, the current work was carried out to investigate the mechanical, thermal, and metallurgical properties of the similar and dissimilar joints among phosphor bronze, copper, and aluminium to propose some improvements in the prevailing manufacturing practices. The following conclusions were drawn from different studies of the current work:

7.2 Conclusions

i. Similar and dissimilar joints of phosphor bronze, copper and aluminium under different combinations of weld time, weld pressure and vibration amplitude were made using USMW. Sound joints were obtained within the defined ranges of these process parameters with no visual defects. The maximum tensile-shear load obtained experimentally, which represented the weld strength, was 2353.33 N, 2129.67 N and 1810 N for PB-PB, PB-Cu, and PB-Al joints, respectively. The estimated results of tensile-shear load using a simulated annealing optimization algorithm were found to be better than the experimental results. Weld time and weld pressure were found to be the most influential parameters for all the three combinations. Vibration amplitude has no significant effect on the weld strength. However, it has a significant effect when combined with weld pressure for PB-PB and weld time for PB-Cu and PB-Al. Effects of individual parameters were greater than those of their interactions. Hence, weld time and weld pressure play an important role in deciding the mode of joint formation. It reflects that different combinations of PB, Cu, and Al give very good responses to the ultrasonic

spot metal welding in the given ranges of the parameters. This joining technique can be effectively used for the fabrication of thin components made of these metals.

ii. The developed thermal model of USMW effectively forecasts the interface temperature under various welding conditions. The peak temperature observed at the weld interface through simulation was well below the melting point of weld metals, supporting USMW as a solid-state joining technique. Clamping force and bonding ratio directly influenced the interface temperature. There was an apparent presence of TMAZ and HAZ at the weld interface. However, the size of the HAZ was quite small as compared to that in the case of fusion welding techniques due to the involvement of a lower amount of heat. But TMAZ was spread over a comparatively larger area. The thermal model was validated with a small error between the observed and predicted temperature for all three combinations. Hence, the boundary conditions presumed in this model may be considered justified. A correlation coefficient of more than 0.9 was found between the simulated temperature result and the weld strength in all the cases. Thus, it can be concluded that the interface temperature has a strong linear relationship with joint strength and is a major deciding factor for achieving strong joints. The interface temperatures predicted by FEA were found to be fairly similar to the experimentally measured temperatures.

iii. Weld interface temperature, weld energy and tensile-shear load were found to be inter-connected. Interface temperature and tensile-shear load increased with increased weld energy. There was a minimum energy value which was required to initiate the bonding, but weaker joints were obtained. On the other hand, a limit was posed by weld energy on the higher side, beyond which the sound joints could not be obtained. The fracture mode shifted from sheet detached mode to nugget pull-out mode at higher energy values in the case of PB-PB and PB-Al joints. But there was a sudden drop in the tensile-shear load in PB-Cu joints after a certain value of weld energy was achieved. The failure mode changed to tearing at the edge of the joint on the copper sheet at a higher energy level due to the lesser strength of the copper sheet in comparison to phosphor bronze sheets.

iv. Microstructural evolution observed at a higher energy level showed small uniform grains at the bond area. The joint formation at the low energy level was random, heterogeneous, and the bonding line was clearly visible. Higher energy expanded the plastically deformed zone. The bonding line disappeared and material started flowing in a convoluted, wavy fashion in the bonding region, giving support to enhanced diffusion,

forming micro-bonds. No observable change in the grain size throughout the weld metal was noticed. Therefore, the possibility of recrystallization and local melting was ruled out. Hence, it can be concluded that joint strength in USMW was the combined result of the formation of micro-bonds and mechanical interlocking due to the swirling of metal at the interface.

7.3 Thesis Contribution and Novelty

In the light of the observations and conclusions above, the main contribution of the current work can be summed up as follows:

The role of USMW in joining dissimilar metals becomes more significant in the current scenario. Despite the fact that many metal combinations have been investigated, there are still many that haven't been looked at and need attention for their ultrasonic weldability. One of these alloys with numerous uses is phosphor bronze. The joining of small components consisting of copper, aluminum, and phosphor bronze is a process that is engaged in the fabrication of BEVs, solar panels, and other electrical devices, among other industries. The intuitive approach adopted by many industries can be replaced by the methodological approach as discussed in the current work. To better understand the process factors including weld time, weld pressure, and vibration amplitude, the influence of parameters and their relationships were thoroughly studied. The method of simulated annealing optimization utilized to determine the optimal parameters values worked extremely well and delivered the accurate results. The assessment of HAZ and TMAZ with the help of FEM and simulation recommended a better understanding of the effects of weld energy at the microstructural level. Further, analysis regarding bonding mechanism has substantiated the previous theories and added more useful information to it. Overall, the current research opens up new possibilities for ultrasonic metal welding to combine thin metal sheets made of different metals, such as copper, aluminum, and phosphor bronze.

7.4 Scope for Future Work

The work carried out through this research will definitely motivate other researchers to explore the USMW process in more detail. The following suggestions can be imparted for future research:

- USMW is applicable to thin sheets only presently. This limitation can be addressed by doing research in the area of enhancing ultrasonic power.

- A lot of materials combinations (both metallic and non-metallic) are still unexplored as far as USMW is concerned. Their ultrasonic weldability can be investigated.
- Research related to ultrasonic welding in cryogenic and under water environments may also be carried out.
- There is a scope for the measurement of hardness profile along the weld joint in the current work.

APPENDIX A-1

CODING FOR SIMULATED ANNEALING ALGORITHM

A 1.1 Coding for PB-PB joint

Code 1:

```
function Output = objective_function_pbpb(Input)

Wt = Input (1);
Wp = Input (2);
Va = Input (3);

Output = -1*(-6735.23 -3805.71 * (Wt) + 484.65 * (Wp) + 446.58 * (Va) +
        282.44 * (Wt) * (Wp)+ 142.04 * (Wt) * (Va) + 97.5 * (Wp) * (Va) –
        243.41 * (Wt)^2 -565.08 * (Wp)^2 -12.25 * (Va)^2);
end;
```

Code 2:

```
fun_call = @ objective_function_pbpb;

lower_bound = [0.5, 0.2, 28];

upper_bound = [1.2, 0.36, 35];

mid_value = mean([lower_bound; upper_bound]);

[x,fval] = simulannealbnd(fun_call, mid_value, lower_bound, upper_bound)

options = optimoptions(@simulannealbnd, ...

        'PlotFcn',{@saplotbestf,@saplottemperature,@saplotf,@saplotstopping});

simulannealbnd(fun_call, mid_value, lower_bound, upper_bound, options);

end;
```

A 1.2 Coding for PB-Cu joints

Code 1:

```
function Output = objective_function_pbcu(Input)

Wt = Input (1);
```

```
Wp = Input (2);
Va = Input (3);

Output = -1 * (-7251.01 + 7376.62 * (Wt) + 636.87 * (Wp) + 265.18 * (Va) +
        8750 * (Wt) * (Wp) – 0.36 * (Wt) * (Va) + 13.39 * (Wp) * (Va) –
        4491.25 * (Wt)^2 – 9945.31 * (Wp)^2 – 3.83 * (Va)^2);
end;
```

Code 2:

```
fun_call = @ objective_function_pbcu;

lower_bound = [0.6, 0.14, 28];

upper_bound = [1.0, 0.30, 35];

mid_value = mean([lower_bound; upper_bound]);

[x,fval] = simulannealbnd(fun_call, mid_value, lower_bound, upper_bound)

options = optimoptions(@simulannealbnd, ...

            'PlotFcn',{@saplotbestf,@saplottemperature,@saplotf,@saplotstopping});

simulannealbnd(fun_call, mid_value, lower_bound, upper_bound, options);

end;
```

A 1.3 Coding for PB-Al joints

Code 1:

```
function Output = objective_function_pbal(Input)

Wt = Input (1);
Wp = Input (2);
Va = Input (3);

Output = -1 * (-2739.62 + 7878.73 * (Wt) – 7045.20 * (Wp) + 193.25 * (Va) -
        4642.86 * (Wt) * (Wp) - 110 * (Wt) * (Va) + 84.69 * (Wp) * (Va) –
        3052.40 * (Wt)^2 + 17596.94 * (Wp)^2 – 2.8 * (Va)^2);
end;
```

Code:

```
fun_call = @ objective_function_pbal;

lower_bound = [0.2, 0.2, 24.5];
```

```
upper_bound = [0.7, 3.4, 31.5];
mid_value = mean([lower_bound; upper_bound]);
[x,fval] = simulannealbnd(fun_call, mid_value, lower_bound, upper_bound)
options = optimoptions(@simulannealbnd, ...
                'PlotFcn',{@saplotbestf,@saplottemperature,@saplotf,@saplotstopping});
simulannealbnd(fun_call, mid_value, lower_bound, upper_bound, options);
end;
```

APPENDIX A-2

HEAT FLUX CALCULATIONS

The thermal modelling and simulation of the weld interface during ultrasonic welding is based on the heat generated at the weld interface. Actually, the power dissipated in the deformation zone produces heat flux at the interface, which is a function of the average sonotrode velocity and the weld force (E. DeVries, 2004). The basic model for the calculation of heat flux is based upon the fact that the joint is formed as a result of heat produced due to:

i. The shear deformation of the weld metal below the sonotrode tip and
ii. The friction between the contacting surfaces of the weld metal.

The shear deformation of the weld metal is subjected to (i) the normal compressive stresses due to clamping force and (ii) the shear stresses due to ultrasonic vibrations. The combined effect of these two stresses brings the material under plastic deformation, resulting in the generation of excessive heat, which raises the temperature of the material instantly. As the deformation takes place under one normal and one shear stress, the failure of the material may be considered to follow the Tresca's failure criterion, which states that failure occurs when the maximum shear stress reaches its critical value, which is the yield stress in a normal tensile test. Using this concept, the value of shear stress, which is responsible for the deformation, may be calculated as:

$$f_{max} = \frac{\sigma_1 - \sigma_2}{2} = \sqrt{\left(\frac{\sigma_N}{2}\right)^2 + (f_s)^2}$$

Where f_{max} is the maximum shear stress, σ_1 and σ_2 are principal stresses, σ_N is the normal stress due to pressure, and f_s is the shear stress responsible for deformation. So, according to Tresca's condition, if 'Y' is the yield stress of the material during a normal tensile test, Equation (a2.1) can be written as:

$$\frac{Y}{2} = \sqrt{\left(\frac{\sigma_N}{2}\right)^2 + (f_s)^2} \qquad \text{(a2.1)}$$

So, value of shear stress, $f_s = \sqrt{\left(\frac{Y}{2}\right)^2 - \left(\frac{\sigma_N}{2}\right)^2}$ (Tresca's failure stress)

Or

$$f_s = \sqrt{\left(\frac{Y_t}{2}\right)^2 - \left(\frac{F_c / A_d}{2}\right)^2} \qquad \text{(a2.2)}$$

Where Y_t is the temperature-dependent yield stress, F_c is clamping force and A_d is the area of the deformation zone. The clamping force F_c was measured by a force sensor installed with the USMW experimental set-up. The display on the machine gives the values of the clamping force corresponding to the weld pressure in set-up mode. Based on that data, the Clamping Force Vs Weld Pressure graph is shown in Figure A2.1.

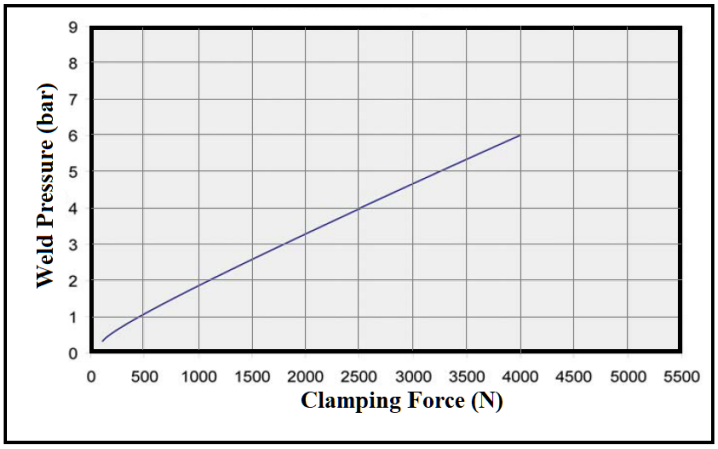

Figure A2.1: Clamping Force V/s Weld Pressure graph for the USMW experimental set-up

The power dissipated (P) in the deformation zone produces heat flux at the interface, which is a function of the average sonotrode velocity (V_{avg}) and the weld force (F_w). Therefore, the heat flux due to deformation (H_d) in W/m^2 can be shown as Equation (a2.3):

$$H_d = \frac{P}{A_d} = \frac{F_w \times V_{avg}}{A_d} \qquad \text{(a2.3)}$$

Ideally, for thin sheets and flat sonotrode tip, the area of deformation (A_d) can be considered equal to the area of the sonotrode tip (A_s) since the entire area beneath the sonotrode tip gets deformed. But, in the case of serrated sonotrode tips, the deformed area depends upon the extent of penetration of the teeth into the weld metals. Now, equation (a2.3) in terms of weld area (W_a), which has been calculated separately, can be written as:

$$H_d = \frac{f_s \times W_a \times V_{avg}}{A_s}$$

$$H_d = (W_a/A_s) \times V_{avg} \times f_s \qquad \text{(a2.4)}$$

Substituting the shear stress, f_s in Equation (a2.4) from Equation (a2.2), we can write Equation (a2.6) as

$$H_d = (W_a/A_s) \times V_{avg} \times \sqrt{\left(\frac{Y_t}{2}\right)^2 - \left(\frac{F_c/A_s}{2}\right)^2} \qquad \text{(a2.5)}$$

$$H_d = \left(\frac{\beta}{2}\right) \times V_{avg} \times \sqrt{(Y_t)^2 - (F_c/A_s)^2} \qquad \text{(a2.6)}$$

The average velocity of the sonotrode in Equation (a2.6) can be calculated by $V_{avg} = 4 \times V_a \times V_f$ where V_a and V_f are the amplitude and frequency of the ultrasonic vibrations. 'β' is the bonding

ratio, which signifies the extent of the area under the sonotrode tip that is transformed into a weld zone. Its value is an indicator of the effectiveness of the process, which itself is the resultant of many factors, one of which is the heat generated at the interface. The ideal value of 'β' should be 1 when the whole of the area under the sonotrode tip is engrossed with the micro-welds, but due to the presence of oxide, asperities, and other contaminants, some portion remains unbounded.

The temperature-dependent yield strength (Y_t) of phosphor bronze is assumed to be equal to its yield strength in normal conditions. Some alloys such as phosphor bronze do not lose an appreciable amount of their strength at higher temperatures until 350℃ (Bhargava et al., 2017), and it was observed during experimentation that the maximum average temperature did not exceed 354.74℃.

The heat flux due to friction (H_f) between the mating surfaces of workpieces depends upon the dynamic coefficient of friction between the surfaces (μ_k), the clamping force (F_c) and the average sonotrode velocity (V_{avg}). Heat flux due to friction may be calculated using Equation (a2.7).

$$H_f = \frac{\mu_k \times F_c \times V_{avg}}{A_s} \qquad \text{(a2.7)}$$

The value of limiting friction for each combination was calculated experimentally. The experimental setup as shown in Figure A2.2 included the weights and the measuring electronic scale. The lower sheet of each pair of metals was fixed on the table and the measuring scale was attached to the upper sheet, i.e. PB. A weight was placed on the upper sheet, which was increased continuously by 50 gm. The values of the limiting coefficient of friction for each combination are given in Table A2.1.

Figure A2.2: Experimental set-up for measuring limiting coefficient of friction

Table A2.1: Dynamic coefficient of friction of PB-PB, PB-Cu and PB-Al metal combinations

S. No.	Metal combination	μ_k
1	PB-PB	0.276
2	PB-Cu	0.286
3	PB-Al	0.332

The total heat flux H is the sum of heat flux due to deformation (H_d) and heat flux due to friction (H_f):

$$H = H_d + H_f \quad \text{(a2.8)}$$

The calculated heat flux is given as input to the CAD model along with other conditions for simulation.

REFERENCES

1. Abedini R., Abdullah A. & Alizadeh Y. (2017). Ultrasonic hot powder compaction of Ti-6Al-4V, Ultrasonics Sonochemistry, 37, pp 640-647
2. Adalarasan R., Santhanakumar M. & Rajmohan M. (2015). Application of grey taguchi-based response surface methodology (GT-RSM) for optimization the plasma arc cutting parameters of 304L stainless steel, Internal Journal of Advance Manufacturing Technology, Vol. 78, No. 5-8, pp. 1161-1170
3. Allameh S. M., Mercer C., Popoola D. & Soboyejo W. O. (2005). Microstructural Characterization of Ultrasonically Welded Aluminum, Journal of Engineering Materials and Technology, Vol. 127, pp. 65-74
4. Al-Sarraf Z. and Lucas M. (2012). A study of weld quality in ultrasonic spot welding of similar and dissimilar metals, Modern Practice in Stress and Vibration Analysis, Journal of Physics: Conference Series, 382, pp. 1-6
5. Anand K., Elangovan S. & Rathinasuriyan C. (2017). Modeling and prediction of weld strength in ultrasonic spot metal welding process using artificial neural network and multiple regression method, Material Science & Engineering International Journal, Vol. 1, Issue 2, pp. 39-46
6. Anand K. and Elangovan S. (2017). Optimizing the ultrasonic inserting parameters to achieve maximum pull–out strength using response surface methodology and genetic algorithm integration technique, Measurement, 99, pp 145–154.
7. Annoni M. and Carboni M. (2011). Ultrasonic metal welding of AA 6022-T4 lap joints: Part I–Technological characterisation and static mechanical behaviour, Science and Technology of Welding and Joining, Vol. 16, No. 2, pp. 107–115
8. ASTM International codes D1002-05 (2005). Standard test method for apparent shear strength of single lap joint adhesively bonded metal specimens by tension loading (metal to metal)
9. Baboi M. and Grewell D. (2010). Evaluation of Amplitude Stepping in Ultrasonic Welding, Welding Journal, pp. 161-s to 165-s
10. Bakavos D. and Prangnell P. B. (2010). Mechanisms of joint and microstructure formation in high power ultrasonic spot welding 6111 aluminium automotive sheet, Materials Science and Engineering A, 527(23), pp. 6320–6334
11. Balasundaram R., Patel V. K., Bhole S. D. & Chen D. L. (2014). Effect of Zinc interlayer on ultrasonic spot welded aluminium to copper joints, Material Science and Engineering A, 607, pp. 277-286

12. Balle F. and Eifler D. (2012). Statistical test planning for ultrasonic welding of dissimilar materials using the example of aluminum-carbon fiber reinforced polymers (CFRP) joints, Wiley Online Library, Material Science and Engineering Technology, Vol. 43, No. 4, pp. 286-292
13. Balle F. and Magin J. (2015). Ultrasonic spot and torsion welding of aluminium to titanium alloy: Process, properties and interfacial microstructure, Physics Procedia, 70, pp. 846-849
14. Bergmann Jean Pierre, Regensburg Anna, Schurer Rene, Petzoldt Franziska & Herb Alexander (2017). Effect of the interface characteristics on the joint properties and diffusion mechanisms during ultrasonic metal welding of Al/Cu, Weld World, Online, pages 1-8
15. Beytolamani M., Kolahan F. & Moghaddam M. A. (2018). Using design of experiment approach and simulated annealing algorithm for modeling and optimization of EDM process parameters, Journal of Advanced Materials and Processing, Vol 6, No. 3, pp. 45-56
16. Bhargava A. K. and Banerjee M. K. (2017). Chapter 09196 - 2.14 Heat-Treating Copper and Nickel Alloys, Vol. 2. Elsevier Ltd., pp. 398-419
17. Bjelic M. B., Kovanda K., Kolarik L., Vukicevic M. N. & Radicevic B. S. (2016). Numerical modeling of two dimensional heat transfer and temperature based calibration using simulated annealing optimization method: Application to gas metal arc welding, Thermal Science, Vol. 20, No. 2, pp. 655-665
18. Bloss M. C. (2008). Ultrasonic Metal Welding: The Weldability of Stainless Steel, Titanium and Nickel-based Superalloys, M. S. Thesis, The Ohio State University
19. Born Christoph, Kuckert Hagen, Wagner Guntram & Eifler Dietmar (2003). Ultrasonic Torsion Welding of Sheet Metals to Cellular Metallic Meterials, Advanced Engineering Materials, 5, 11, pp 779-786
20. Bournias-Varotsis A., Friel R. J. Harris, R. A. & Engstrom D. S. (2018). Ultrasonic Additive Manufacturing as a form-then-bond process for embedding electronic circuitry into a metal matrix, Journal of Manufacturing Processes, 32, June, pp. 664-675
21. Box G. E. P. and Behnken D. W. (1960). Some New Three Level Designs for the Study of Quantitative Variables, Technometrics, 2:4, pp. 455-475
22. Box, G. E. P. and Draper, N. R. (1987). Empirical Model Building and Response Surfaces, John Wiley & Sons, New York

23. Brown A. M. (2001). A step-by-step guide to non-linear regression analysis of experimental data using a microsoft excel spreadsheet, Computer Methods and Programs in Biomedicine, Vol. 65, No. 3, pp. 191–200
24. Carboni M. and Annoni M. (2011). Ultrasonic metal welding of AA 6022-T4 lap joints: part II – Fatigue behaviour, failure analysis and modelling, Science and Technology of Welding and Joining, Vol. 16, No. 2, pp. 116-125
25. Chang U. I. and Frisch J (1974). On optimization of some parameters in ultrasonic metal welding, Welding Journal, 53, 1, pp. 23s-36s
26. Chaskalovic J. (2008). Finite Element Methods for Engineering Sciences: Theoretical Approach and Problem Solving Techniques, Springer
27. Chen K. K. and Zhang Y. S. (2015). Numerical analysis of temperature distribution during ultrasonic welding process for dissimilar automotive alloys, Sci. Technol. Weld. Join., Vol. 20, No. 6, pp. 522–531
28. Chen Kunkun and Zhang Yensong (2014). Thermal-mechanical analysis of ultrasonic spot welding considering acoustic softening effect, Procedia Engineering, 81, pp. 2117-2122
29. Chen Y.C. (2012). HAZ development and accelerated post-weld natural ageing in ultrasonic welding aluminium 6111-T4 automotive sheet, Acta Materialia, Vol. 60, pp. 2816–2828
30. Consiglio S., Fleschutz T., Seliger G. & Seutemann J. (2006). Development of a Duothermal Soldering Process, CIRP Annals, Vol. 55, No. 1, pp. 1–4
31. Conway P. P., Fu E.K.Y. & Williams D. J. (2002). Precision high temperature lead-free solder interconnections by means of high-energy droplet deposition techniques, CIRP Annals, Vol. 51, Issue 1, pp. 177–180
32. Czitrom Veronica (1999). One-Factor-at-a-Time Versus Designed Experiments, The American Statisticians, Vol. 53, No. 2, pp. 126-131
33. Damongeot A. and Andre G. (1988). Noise from Ultrasonic Welding Machines: Risks and Prevention, Applied Acoustics, 25, pp. 49-66
34. Daniels H.P.C. (1965). Ultrasonic Welding, Ultrasonics, October-December, pp. 190-196
35. Das A., Li Dezhi, Williams David and Greenwood David (2018). Joining Technologies for Automotive Battery Systems Manufacturing, World Electric Vehicle Journal, 9, pp. 1-22
36. Das Abhishek, Masters Iain & Williams David (2018). Process robustness and strength analysis of multi-layered dissimilar joints using ultrasonic metal welding. International Journal of Advanced Manufacturing Technology, 101, pp. 881-900

37. Davis J. R. and Davis & Associates (2001). ASM Specialty Handbook- Copper and copper alloys, 2001Edition, ASM International, Materials Park, OH 44073-0002
38. Debnath Kishore, Singh Inderdeep, Dvivedi Akshay (2014). Rotary mode ultrasonic drilling of glass fiber-reinforced epoxy laminates, Journal of Composite Materials, 49, 8, pp. 949-963
39. Dehoff R. R. and Babu S. S. (2010). Characterization of interfacial microstructures in 3003 aluminum alloy blocks fabricated by ultrasonic additive manufacturing, Acta Materilia, Vol. 58, No. 13, pp. 4305–4315
40. Delgarm Navid, Sajadi Behrang, Azarbad Khadijeh & Delgarm Saeed (2018). Sensitivity analysis of building energy performance: A simulation-based approach using OFAT and variance-based sensitivity analysis methods, Journal of Building Engineering, 15, pp. 181–193
41. Devine Janet (1993). Ultrasonic Welding, ASM Handbook, Vol. 6, ASM International
42. Demirel Muhammet and Kayan Berkant (2012). Application of response surface methodology and central composite design for the optimization of textile dye degradation by wet air oxidation, International Journal of Industrial Chemistry, 3:24, Online, pages 1-10
43. Devine Janet and Walsh Joe, Ultrasonic welding of aluminum sheet, http://www.ultrasonics.org/aws/UIA/asset_manager/get_file/Devine_2006_UIA.pdf?ver=1 1098 (Accessed on 20 October 2020)
44. Ding Yong and Kim Jang-Kyo (2008). Numerical analysis of ultrasonic wire bonding: Part 2. Effects of bonding parameters on temperature rise, Microelectronics Reliability, 48, pp. 148-157
45. Duck Francis and Leighton Timothy (2018). Frequency bands for ultrasound, suitable for consideration of its health effects, The Journal of the Acoustical Society of America, 144, pp. 2490-2500
46. Egorova O., Savchenko M., Hagivara I. & Savchenko V (2007). Modeling of Quality Parameters for Improving Meshes, Japan J. Indust. Appl. Math., 24, pp. 181-195
47. Elangovan S., Anand K. & Prakasan K. (2012). Parametric optimization of ultrasonic metal welding using response surface methodology and genetic algorithm, International Journal of Advance Manufacturing Technology, 63, pp. 561-572
48. Elangovan S., Semeer S., & Prakasan K. (2009). Temperature and stress distribution in ultrasonic metal welding-An FEA-based study, Journal of Materials Processing Technology, Vol. 209, No. 3, pp. 1143–1150

49. Fentahun Mekonnen Asmare, Mahmut Prof & Savaş Ahsen (2018). Materials Used in Automotive Manufacture and Material Selection Using Ashby Charts, International Journal of Materials Engineering, 8, 3, pp. 40-54
50. Ferreira S.L.C., Bruns R.E., Ferreira H.S., Matos G.D., David J.M., Brandão G.C., Da Silva E.G.P., Portugal L.A., Reis P.S. Dos, Souza A.S. & Dos Santos W.N.L. (2007). Box-Behnken design: An alternative for the optimization of analytical methods., 597(2), pp. 179–186
51. Fletcher L. S. (1988). Recent Developments in Contact Conductance Heat Transfer, Journal of Heat Trarnsfer, Vol. 110 (4b), pp. 1059-1070
52. Froes F. H. (1994). Advanced metals for aerospace and automotive use, Materials Science and Engineering A, 184, 2, pp. 119-133
53. Fujii Hiromichi T., Goto Y., Sato Y. S. & Kokawa H. (2014). Microstructural evolution in dissimilar joint of Al alloy and Cu during ultrasonic welding, Materials Science Forum, 783, pp. 2747-2752
54. Fujii Hiromichi T., Goto Y., Sato Y. S. & Kokawa H. (2016). Microstructure and lap shear strength of the weld interface in ultrasonic welding of Al alloy to stainless steel, Scripta Materialia, 116, pp. 135-138
55. Fujii Hiromichi T., Sriraman M. R. & Babu S. S. (2011). Quantitative evaluation of bulk and interface microstructures in Al-3003 alloy builds made by very high power ultrasonic additive manufacturing, Metallurgical and Materials Transactions A: Physical Metallurgy and Materials Science, 42, 13, pp. 4045-4055
56. Gallego-Juárez J.A. (2015). Power Ultrasonics, Introduction to power ultrasonics, Woodhead Publishing series in electronic and optical Materials, Online, pp. 1-6
57. Gary F. Benedict (1987). Ultrasonic Welding: Nontraditional Manufacturing Processes, Marcel Dekker, New York
58. Goldsmith Mike (2015). Sound: A Very Short Introduction, Oxford Unviersity Press; DOI: 10.1093/actrade/9780198708445.001.0001, pp 82-94
59. Gonda Neddermeijer H., Van Oortmarssen G. J., Piersma N. (2000). A framework for Response Surface Methodology for simulation optimization, Winter Simulation Conference Proceeding, 1, pp. 129–136
60. Graff K. (1999). Introduction to High Power Ultrasonics, Columbus: Edison Welding Institute, Ohio, US
61. Graff K. (2005). New Developments in Advanced Welding. Ultrasonic Metal Welding, Woodhead, Cambridge

62. Graff Karl & Bloss Matt (2008). Understanding ultrasonic welding, https://www.thefabricator.com/thewelder/article/arcwelding/understanding-ultrasonic-welding (Accessed on 25 August 2020)
63. Guillon D., Morin P., Guillemin R., Hartmann S., Trussel D., Fischer F., Beyer H. & Rahimo M. (2018). Particle prevention during ultrasonic welding process, PICM, Nuremberg, Germany, pp. 1468-1474
64. Gunaraj V. and Murugan N. (1999). Application of response surface methodology for predicting weld bead quality in submerged arc welding of pipes, Journal of Materials Processing Technology, 88(1-3), pp. 266–275
65. Gunaraj V. and Murugan N. (1999). Prediction and comparison of the area of the heat-affected zone for the bead-on-plate and bead-on-joint in submerged arc welding of pipes, Journal of Materials Processing Technology, 95, pp. 246-261
66. Gunduz Ibrahim E., Ando T., Shattuck E., Wong P. Y. & Doumanidis C. C. (2005). Enhanced diffusion and phase transformations during ultrasonic welding of zinc and aluminum, Scripta Materialia, 52, pp. 939-943
67. Gupta M. K., Sood P. K. & Sharma V. S. (2015). Machining parameters optimization of titenium alloy using response surface methodology and particle swarm optimization under minimum quantity lubrication environment, Material and Manufacturing Processes, Vol. 31, No. 13, pp. 1671-1682
68. Haddadi F. and Abu-Farha F. (2015). Microstructural and mechanical performance of aluminum to steel high power ultrasound spot welding, Journal of Materials Processing Technology, 225, pp. 262-274
69. Haddadi Farid and Abu-Farha Fadi (2016). The effect of interface reaction on vibration evolution and performance of aluminium to steel high power ultrasonic spot joints, Materials and Design, 89, pp. 50-57
70. Haddadi F., Strong D. & Prangnell P. B. (2012). Effect of Zinc Coatings on Joint Properties and Interfacial Reactions in Aluminum to Steel Ultrasonic Spot Welding, JOM, 64, 3, pp. 407-413
71. Haddadi F. and Tsivoulas D. (2016). Grain structure, texture and mechanical property evolution of automotive aluminium sheet during high power ultrasonic welding, Materials Characterization, 118, pp. 340-351
72. Harman George G. and Albers John (1977). The Ultrasonic Welding Mechanism as Applied to Aluminium and Gold-Wire Bonding in Microelectronics, IEEE Transactions on Parts, Hybrids and Packages, Vol. PHP-13, No. 4, pp. 406-412

73. Harvey Gerald Gachagan, Anthony Mutasa & Tapiwa (2014). Review of high-power ultrasound-industrial applications and measurement methods; IEEE Transactions on Ultrasonics, Ferroelectrics, and Frequency Control, 61, 3, pp. 481-495
74. Hasan S. H., Srivastava P. & Talat M. (2009). Biosorption of Pb (II) from water using biomass of Aeromonas hydrophila: Central composite design for optimization of process variables, Journal of Hazardous Materials, 168, pp. 1155-1162
75. Hazlett T.H. and Ambekar S. M. (1970). Additional Studies on Interface Temperatures and Bonding Mechanisms of Ultrasonic Welds, America Welding Society, May, pp. 196s-200s
76. He Tao, Ye Xin Quan & Zhao Yang **(**2015**)**. Optimization design for ultrasonic horn with large amplitude based on genetic algorithm, Journal of Vibroengineering, 17, 3, pp. 1157-1168
77. Hu T., Zhalehpour S., Gouldstone A., Muftu S. & Ando T. (2014). A method for the estimation of the interface temperature in ultrasonic joining, Metallurgical and Materials Transactions A: Physical Metallurgy and Materials Science, 45(5), pp. 2545–2552
78. Imai Hisashi & Matsuoka Sin-ichi (2006). Direct Welding of Metals and Ceramics by Ultrasonic Vibration, SME International Journal Series A, 49, 3, pp. 444-450
79. Ingber Lester (2012). Chapter 4: Adaptive simulated annealing (ASA), Stochastic Global Optimization and its Applications with Fuzzy Adaptive Simulated Annealing, Springer, pp. 33-62
80. Introduction to Design of Expeirments (DOE), Reliability Hotwire (2008). E-magazine for the Reliability Professional, Weibull.com, https://www.weibull.com/hotwire/issue85/relbasics85.htm (accessed on 27 June, 2020)
81. Jahn R., Cooper R. & Wilkosz D. (2007). The Effect of Anvil Geometry and Welding Energy on Microstructures in Ultrasonic Spot Welds of AA6111-T4, Metallurgical and Materials Transactions A., 38(A), pp. 570-583
82. Janaki Ram G. D., Robinson C., Yang Y. & Stucker B. E. (2007). Use of Ultrasonic consolidation for fabrication of multi-material structure, Journal of Rapid Prototype, 13, pp. 226-235
83. Jedrasiak P. and Shercliff H. R. (2018). Finite element analysis of heat generation in dissimilar alloy ultrasonic welding, Materials Design, Vol. 158, pp. 184–197
84. Jedrasiak P., Shercliff H. R., Chen Y. C., Wang L., Prangnell P. & Robson J. (2015). Modelling of the Thermal Field in Dissimilar Alloy Ultrasonic Welding, Journal of Materials Engineering and Performance, Vol. 24, No. 2, pp. 799–807

85. Jedrasiak P., Shercliff H. R., Reilly A., McShane G. J., Chen Y. C., Wang L., & Prangnell P. (2016). Thermal Modelling of Al-Al and Al-Steel Friction Stir Spot Welding, Journal of Materials Engineering and Performance, 25, pp. 4089-4098
86. Jeyaraj P. (2018), Effect of temperature distribution in ultrasonically welded joints of copper wire and sheet used for electrical contacts, Materials, 11, 6, pp. 1-13
87. Jhang C. and Li L. (2009). A Coupled Thermal-Mechanical Analysis of Ultrasonic Bonding Mechanism, Metallurgical and Materials Transactions B, 40(B), pp. 196-207
88. Kang Bongsu, Cai Wayne & Tan Chin-An (2014). Vibrational energy loss analysis in battery tab ultrasonic welding, Journal of Manufacturing Process, 16, pp. 218-232
89. Khan Urfi, Khan Noor Zaman & Gulati Jasdeep (2017). Ultrasonic Welding of Bi-Metals: Optimizing Process Parameters for Maximum Tensile-shear Strength and Plasticity of Welds, Procedia Engineering, Implast 2016, 173, pp 1447-1454
90. Kido K., Momose F., Nishimura Y. & Goto T. (2010). Development of copper-copper bonding by ultrasonic welding for IGBT modules, Proceedings of the IEEE/CPMT International Electronics Manufacturing Technology (IEMT) Symposium
91. Kim Mi Ae, Im Chang Seo & Park Dong Sam (2019). Tip-replaceable Horn with Full Wavelength for Ultrasonic Welding, MATEC Web of Conferences
92. Kim W., Argento A., Grima A., Scholl D. & Ward S. (2011). Thermo-mechanical analysis of frictional heating in ultrasonic spot welding of aluminium plates, Proceedings of the Institution of Mechanical Engineers, Part B: J. Engineering Manufacture, Vol. 225, pp. 1093-1103
93. Kim, T. H., Yum, J., Hu, S. J., Spicer, J. P., & Abell, J. A. (2011). Process robustness of single lap ultrasonic welding of thin, dissimilar materials, CIRP Annals - Manufacturing Technology, 60(1), pp. 17–22
94. Kirkpatrick S., Gelatt G. D. and Vecchi M. P. (1983). Optimization by simulated annealing", Science, Vol. 220, No. 4598, pp. 671-680
95. Kong C. V., Soar R. C. & Dickens P. M. (2004). Optimum process parameters for ultrasonic consolidation of 3003 aluminium, Journal of Materials Processing Technology, 146, pp 181-187
96. Kong C. V., Soar R. C. & Dickens P. M. (2005). A model for weld strength in ultrasonically consolidated components, Proceedings of the Institution of Mechanical Engineers, Part C: J. Mechanical Engineering Science, Vol. 219, pp 83-91

97. Kong C. Y., Soar R. C. & Dickens P. M. (2003). Characterization of aluminium alloy 6061 for the ultrasonic consolidation process, Materials Science and Engineering A, 363, pp. 99-106
98. Kremer D., Saleh S. M., Ghabrial S. R. Moisan A. (1981). The State of the Art of Ultrasonic Machining, CIRP Annals, Vol. 30, Issue 1, pp. 107-110
99. Kreye H. (1977). Melting Phenomena in Solid State Welding Processes, America Welding Society, May, pp. 154-s to 158-s
100. Kuczmann M. (2015). Overview of the finite element method, Acta Technica Jaurinensis, Vol. 8, No. 4, pp. 347-383
101. Kumar S., Wu C. S., Padhy G. K. & Ding W. (2017). Application of ultrasonic vibrations in welding and metal processing : A status review, Journal of Manufacturing Processes, 26, pp. 295-322
102. Kuo K. & Tsao C. (2012). Rotary ultrasonic-assisted milling of brittle materials, Transactions of Nonferrous Metals Society of China, 22, Suppl 3, pp. s793-s800
103. Langenecker B. (1966). Effects of ultrasound on deformation characteristics of metals, IEEE Transactions on Sonics and Ultrasonics, Vol. 13, pp. 1-8
104. Li H. & Cao B. (2019). Effects of welding pressure on high-power ultrasonic spot welding of Cu / Al dissimilar metals, Journal of Manufacturing Processes, 46, pp. 194-203
105. Li S., Wu Y., Nomura M., & Fujii T. (2018). Fundamental Machining Characteristics of Ultrasonic-Assisted Electrochemical Grinding of Ti–6Al–4V, Journal of Manufacturing Science and Engineering, Transactions of the ASME, 140, 7, pp. 1-9
106. Macwan A. and Chen D.L. (2015). Microstructure and mechanical properties of ultrasonic spot welded copper-to-magnesium alloy joints, Materials and Design, 84, pp. 261-269
107. Magin J. and Balle F. (2014). Solid state joining of aluminum, titanium and their hybrids by ultrasonic torsion welding, Mat.-wiss. u. Werkstofftech, 45, 12, pp. 1072-1083
108. Malaki M., & Ding H. (2015). A review of ultrasonic peening treatment; Materials and Design, Vol. 87, pp. 1072-1086.
109. Martin Julia, Adana David Daffos RuizDe & Asuero Agustin G. (2017). Chapter 7: Fitting Models to Data: Residual Analysis, A Primer, IntechOpen, pp. 134-173
110. Martinsen K., Hu S. J. & Carlson B. E. (2015). Joining of dissimilar materials, CIRP Annals - Manufacturing Technology, 64, 2, pp. 679-699
111. Matheny M. and Graff K., Ultrasonic Welding of Metals (2014), Power Ultrasonics: Applications of High-Intensity Ultrasound; pp. 259-293

112. Matsuoka Shin-ichi and Imai H. (2009). Direct welding of different metals used ultrasonic vibration, Journal of Material Processing Technology, 209, pp. 954-960
113. Mirza F. A., Macwan A., Bhole S. D., Chen D. L. & Chen X. G. (2016). Effect of welding energy on microstructure and strength of ultrasonic spot welded dissimilar joints of aluminium to steel sheets, Materials Science and Engineering A, 668, pp. 73–85
114. Mo B., Guo Z., Li Y., Huang Z. & Wang G. (2011). Mechanism of resistance microwelding of insulated copper wire to phosphor bronze sheet, Materials Transactions, Vol. 52, No. 6, pp. 1252–1258
115. Moghaddam M. A., Hamid D., Farhad K. & Sharifi S. M. R. (2019). Modeling and optimization of ultimate tensile strength in TIG welding process using simulated annealing algorithm- A case study for Shirvan combined cycle power plant, Proceedings 1st National Congress on Adv. In Mech. And Aero. Engg., Tehran, Iran
116. Mohan Raj N., Kumaraswamidhas L. A. & Arungalai Vendan S. (2016). Experimental studies and finite element simulation of ultrasonic welding of Cu alloy, Bulletin of Polish Academy of Sciences Technical Sciences, Vol. 64, No. 3, pp. 535–546
117. Montgomery Douglas C (2001). Design and Analysis of Experiments, Fifth Edition, John Wiley and Sons, Inc, New York, USA
118. Myers R. H. and Montgomery D. C. (1995). Response Surface Methodology: Process and Product Optimization Using Designed Experiments, John Wiley & Sons, New York
119. Nasma A., Aishath N., Azilah A. & Sulaiman A. Z. (2018). Optimization of vitexin and isovitexin compounds extracted from dried Mas Cotek leaves using one-factor-at-a-time (OFAT) approach in aqueous extraction, International Food Research Journal, 25(6), pp. 2562-2573
120. Ni Zenglei, Zhao Hongjian, Mi Pengbo & Ye Fuxing (2016). Microstructure and mechanical performances of ultrasonic spot welded Al/Cu joints with Al 2219 alloy particle interlayer, Materials & Design, 92, pp. 779–786
121. O'Brien R. L. (1997). Ultrasonic Welding, American Welding Society Handbook, Vol. 2, 8th Edition, Miami, FL
122. O'Brien R. L. (2007). Welding Handbook, Welding Processes Part 2, Vol. 3, 9th Edition, American Welding Society, Miami, FL
123. Okada Minoru, Shin Shigeo, Miyagi Masakazu & Matsuda Hiromi (1962). Joint mechanism of ultrasonic welding, Journal of Japan Institute of Metals, 4(26), pp. 250-256

124. Onwubolu Godfrey C. and Kumar Shivendra (2006). Response surface methodology-based approach to CNC drilling operations, Journal of Materials Processing Technology, 171, pp. 41–47
125. Pannerselvam R. (2012). Design and Analysis of Experiments, PHI Learning Pvt. Ltd., New Delhi, India
126. Panteli A., Robson J. D. & Pragnell P. B. (2012). The effect of high strain rate deformation on intermetallic reaction during ultrasonic welding aluminum and magnesium, Materials Science & Engineering A, 556, pp. 31-42
127. Park D. S., Jang Ho Su & Park W. Y. (2013). Tensile Strength of Cu Sheets Welded by Ultrasonic Metal Welding, Advanced Materials Research, Vol. 658, pp. 202-208
128. Patel V. K., Bhole S. D. & Chen D. L. (2011). Influence of ultrasonic spot welding on microstructure in a magnesium alloy, Scripta Materialia, 65, pp. 911-914
129. Patel V. K., Bhole S. D. & Chen D. L. (2012). Improving weld strength of Magnesium to Aluminium dissimilar joints via Tin interlayer during ultrasonic spot welding, Science and Technology of Welding and Joining, 17(5), pp. 342-347
130. Patel V. K., Bhole S. D. & Chen D. L. (2013). Formation of zinc interlayer texture during dissimilar ultrasonic spot welding of magnesium and high strength low alloy steel, Materials and Design, 45, pp. 236-240
131. Paul Kah (2017). Overview of techniques for joining dissimilar materials, https://www.thefabricator.com/thefabricator/article/assembly/overview-of-techniques-for-joining-dissimilar-materials (Accessed on 22 August, 2020)
132. Pragnell P., Haddadi F. & Chen Y. C. (2011). Ultrasonic spot welding of aluminum to steel for automotive applications-microstructure and optimization, Materials Science and Technology, 27(3), pp. 617-624
133. Puertas Arbizu I. and Luis Pérez C.J. (2003). Surface roughness prediction by factorial design of experiments in turning processes, Journal of Materials Processing Technology, 143-144, pp. 390–396
134. Pye J.D. and Langbauer W.R. (1998). Ultrasound and Infrasound, Animal Acoustic Communication. Springer, Berlin, Heidelberg. https://doi.org/10.1007/978-3-642-76220-8_7
135. Pytel Andrew and Kiusalaas Jaan (2010). Mechanics of Materials, IInd Edition, Cengage Learning, USA
136. Rao J. S. and Kumar B. (2012). 3D Blade root shape optimization, 10th International Conference on Vibrations in Rotating Machinery, IMechE, London, pp. 173-188

137. Roopa Rani M., Prakasan K. & Rudramoorthy R. (2015). Studies on thermo-elastic heating of horns used in ultrasonic plastic welding, Journal of Materials Processing Technology, 186, 1-3, pp. 138-146
138. Rozenberg L. and Mitskevich A. (1973). Ultrasonic welding of metals, Vol. 1, Plenum Press, Moscow
139. Sabdin S. D., Hussein N. I. S., Sued M. K., Ayob M. S., Rahim M. A. S. A. & Fadzil M. (2019). Effects of ColdArc welding parameters on the tensile strengths of high strength plates investigated using the Taguchi approach, Journal of Mechanical Engineering and Sciences, Vol. 13, Issue 2, pp. 4846-4856
140. Sanga Bharat, Wattal Reeta and Nagesh D. S. (2018). Mechanism of Joint Formation and Characteristics of Interface in Ultrasonic welding: Literature Review, Periodicals of Engineering and Natural Sciences, Vol. 6, No. 1, pp. 107-119
141. Sarabia L. A. and Ortiz M. C. (2009). Response Surface Methodology, Comprehensive Chemometric: Chemical and Biochemical Data Analysis, Vol. 1, pp. 345-390
142. Sathiya P., Aravindan S., Noorul Haq A. & Panneerselvam K. (2006). Optimization of friction welding parameters using simulated annealing, Indian Journal of Engineering and Materials Sciences, Vol. 13, pp. 37-44
143. Satpathy Mantra Prasad, Mohapatra Kasinath Das & Sahoo Susanta Kumar (2018). Ultrasonic spot welding of Al-Cu dissimilar metals: a study on parametric influence and thermo-mechanical simulation, Vol. 38, pp. 83-95
144. Satpathy Mantra Prasad, Mohapatra Kasinath Das, Sahoo Anand Kumar & Sahoo Sushant Kumar (2018). Parametric Investigation on Microstructure and Mechanical Properties of Ultrasonic Spot Welded Aluminium to Copper Sheets, IOP Conference Series: Materials Science and Engineering, 338, 012024
145. Satpathy Mantra Prasad, Moharana Bikash Ranjan, Dewangan Shailesh & Sahoo Sushanta Kumar (2015). Modeling and optimization of ultrasonic metal welding on dissimilar sheets using fuzzy based genetic algorithm approach. Engineering Science and Technology, an International Journal, Vol. 18, Issue 4, pp. 634-647
146. Satpathy Mantra Prasad, Sahoo Sushant Kumar & Datta Saurav (2014). Optimization of tensile strength during ultrasonic lap welding of dissimilar metals using Taguchi's philosophy, Applied Mechanics and Materials, Vols. 592-594, pp. 652-657
147. Seo Jeong Seok, Jang Ho Su & Park Dong Sam (2015). Ultrasonic Welding of Ni and Cu Sheets, Materials and Manufacturing Processes, Vol. 30, Issue 9, pp. 1069-1073

148. Shakil M., Tariq N. H., Ahmad M., Choudhary M. A., Akhter J. I. & Babu S. S. (2014). Effect of ultrasonic welding parameters on microstructure and mechanical properties of dissimilar joints, Materials and Design, 55, pp. 263-273
149. Shin, H. S., and De Leon, M. (2015). Parametric study in similar ultrasonic spot welding of A5052-H32 alloy sheets, Journal of Materials Processing Technology, Vol. 224, pp. 222–232
150. Shintomi T., Chikushi I., Hashimoto Y., Ohata M., Mochizuki M. & Toyoda M. (2003). Effect of Weld HAZ Softening on Tensile Strength, Journal of the Japan Welding Society, 21(3), pp. 397–403
151. Simplifying Acoustics, Acoustic Bulletin, 21 March 2017. https://www.acousticbulletin.com/simplifying-acoustics (Accessed on 11 July 2019)
152. Soffar Hoba (2016). Ultrasonic welding process uses, advantage and disadvantages, https://www.online-sciences.com/industries/ultrasonic-welding-process-uses-advantages-and-disadvantages/ (Accessed on 22 August, 2020)
153. Sooriyamoorthy Elangovan, Henry Shenton Ponnayya John & Kalakkath Prakasan (2011). Experimental studies on optimization of process parameters and finite element analysis of temperature and stress distribution on joining of Al-Al and Al-Al_2O_3 using ultrasonic welding, International Journal of Advanced Manufacturing Technology, 55, pp. 631-640
154. Sprawls Perry (1995), The Physical Principles of Medical Imaging, 2nd Edition, Medical Physics Pub Corp, USA
155. Srivastava S. and Garg R. K. (2017), Process parameter optimization of gas metal arc welding on IS 2062 mild steel using response surface methodology, Journal of Manufacturing Processes, Vol. 25, pp. 296-305
156. Summers Patrick T, Chen Yanyun, Rippe Christian M., Allen Ben, Mouritz Adrian P., Case Scott W. & Lattimer Brian Y. (2015). Overview of aluminum alloy mechanical properties during and after fires, Fire Science Reviews, 4(1), Pages 1-36
157. Suresh K. S., Rani M. R., Prakasan K. & Rudramoorthy R. (2007), Modelling of temperature distribution in ultrasonic welding of thermoplastics for various joint designs, Journal of Materials Processing Technology, Vol. 186, No. 1–3, pp. 138–146
158. Thermal Contact Conductance Metal Surface Air, https://www.engineersedge.com/heat_transfer/thermal_contact_conductance_13849.htm (accessed on 23 April 2020)
159. Torabi A. and Kolahan F. (2018). Optimizing pulsed Nd:YAG laser beam welding process parameters to attain maximum ultimate tensile strength for thin AISI316L sheet using

response surface methodology and simulated annealing algorithm, Optics & Laser Technology, Vol. 103, pp. 300–310

160. Tsujino J., Ueoka T., Asada Y., Taniguchi S. & Iwamura Y. (1998). Measurement of the temperature rise at the welding surface of different metal specimens joined by a 15 kHz ultrasonic butt welding system, Japanese Journal of Applied Physics, Part 1, 37(5), pp. 2996–3000
161. Vries, E. de (2004) Mechanics and Mechanisms of Ultrasonic Metal Welding. Ph.D. Thesis, The Ohio State University, USA
162. Vural M. (2014). Welding Processes and Technologies, Comprehensive Materials Processing, Vol. 6, pp. 3–48
163. Waber Austin (2003). The Economics of Ultrasonics, Assembly http://www.assemblymag.com/articles/83104-the-economics-of-ultrasonics (Accessed on 20 October 2020)
164. K. Wang, Shriver D., Banu M., Jack Hu S., Arinez J. & Fan Hua-Tzu (2017). Performance prediction for ultrasonic spot welds of short carbon fiber-reinforced composites under shear loading, Journal of Manufacturing Science and Engineering, 139 (11): 111001 (10 pages)
165. Wang S. Q., Patel V. K., Bhole S. D., Wen G. D. & Chen D. L. (2015). Microstructure and mechanical properties of ultrasonic spot welded Al/Ti alloy joints, Materials and Design, 78, pp. 33-41
166. Watanabe T., Sakuyama H. & Yanagisawa A. (2009). Ultrasonic welding between mild steel sheet and Al-Mg alloy sheet, Journal of Materials Processing Technology, 209, pp. 5475-5480
167. Watanabe T., Yanagisawa A. & S. Sunaga (2003). Auger Electron Spectroscopy Analysis at the Ultrasonically Welded Interface between Alumina and Aluminum, Metallurgical and Materials Transactions A, 34(A), pp. 1107-1111
168. Weigl M., Schmidt M., Govekar E. and Jeric A. (2009). CIRP Annals - Manufacturing Technology Laser droplet generation : Application to droplet joining, Vol. 58, pp. 205–208
169. Wiens Stefan and Nilsson Mats E. (2017). Performing Contrast Analysis in Factorial Designs: From NHST to Confidence Intervals and Beyond, Educational and Psychological Measurement, Vol. 77(4), pp. 690-715
170. Winter M. (2013). Benchmark and Validation of open source CFD codes with focus on compressible and rotating capabilities for integration on the SimScale platform, Master's Thesis, Chalmers University of Technology, Sweden

171. Wu Xin, Liu Tang & Cai Wayne (2015). Microstructure, welding mechanism and failure of Al/Cu ultrasonic welds, Journal of Manufacturing Processes, Vol. 20, pp. 321-331
172. Yang J. and Cao B. (2015). Investigation of resistance heat assisted ultrasonic welding of 6061 aluminum alloys to pure copper, Materials Design, Vol. 74, pp. 19–24
173. Yang J., Cao B. & Lu Q. (2017). The effect of welding energy on the microstructural and mechanical properties of ultrasonic-welded copper joints, Materials, 10(193), page 1-13
174. Yang Y., Janaki Ram G. D. & Stucker B. E. (2009). Bond formation and fiber embedment during ultrasonic consolidation, Journal of Materials Processing Technology, 209(10), pp. 4915–4924
175. Youssef A. Youssef, Beauchamp Yves & Thomas Marc (1994). Comparison of a full factorial experiment to fractional and taguchi designs in a lathe dry turning operation, 27(1-4), pp. 59–62
176. Zhang C. Q., Robson J. D. & Pregnell P. B. (2016). Dissimilar ultrasonic spot welding of aerospace aluminum alloy AA2139 to titanium alloy TiAl6V4, Journal of Materials Processing Technology, 231, pp. 382-388
177. Zhang C. Q., Robson J. D., Ciuca O. & Pregnell P. B. (2014). Microstructural characterization and mechanical properties of high power ultrasonic spot welded aluminum alloy AA6111-TiAl6V4 dissimilar joints, Materials Characterization, 97, pp. 83-91
178. Zhang C. Y., Chen D. L. & Luo A. A. (2014). Joining 5754 Automotive Aluminium Alloy 2-mm-Thick Sheets Using Ultrasonic Spot Welding, Welding Journal, Vol. 93, pp 131-s to 138s
179. Zhang Z., Wang K., Li J., Yu Q. & Cai W. (2017). Investigation of Interfacial Layer for Ultrasonic Spot Welded Aluminium to Copper Joints, Scientific Reports, 7(1), page 1–6
180. Zhao D., Ren D., Zhao K., Pan S. & Guo X. (2017). Effect of welding parameters on tensile strength of ultrasonic spot welded joints of aluminum to steel – By experimentation and artificial neural network, Journal of Manufacturing Processes, Vol. 30, pp. 63–74
181. Zhao D., Ren D., Zhao K., Pan S. & Guo X. (2017). Ultrasonic welding of magnesium–titanium dissimilar metals: A study on influences of welding parameters on mechanical property by experimentation and artificial neural network, Journal of Manufacturing Science and Engineering, Vol. 139, No. 3, pp. 031019 1-9
182. Zhao Y. Y., Li D., & Zhang Y. S. (2013). Effect of welding energy at interface zone of Al-Cu ultrasonic welded joint, Science and Technology of Welding and Joining, 18 (4), pp. 354-360

183. Zhong X., Feng J. & Yao S. (2019). Temperature field modelling and experimental study on ultrasonic consolidation for Al-Ti foil , Vol. 33, No. 6, pp. 2833–2840
184. Zhu A., Lee K. Y. & Wang X. (2012). Ultrasonic welding of dissimilar metals, AA6061 and Ti6Al4V, International Journal of Advance Manufacturing Technology, 59, pp. 569-574
185. Zhu Congcong, Sun Liqiang, Gao Wenli, Li Guangyao & Cui Junjia (2019). The effect of temperature on microstructure and mechanical properties of Al/Mg lap joints manufactured by magnetic pulse welding, Journal of Materials Research and Technology, JMRTEC-710

LIST OF PUBLICATIONS

1. Bharat Sanga, Reeta Wattal and D. S. Nagesh, "Mechanism of Joint Formation and Characteristics of Interface in Ultrasonic welding: Literature Review", Periodicals of Engineering and Natural Sciences, Vol. 6, No. 1, pp: 107-119, May 2018, (SCOPUS Indexed, ISSN 2303-4521, Cite Score: 1.7 - 2020)
   (Link: http://pen.ius.edu.ba/index.php/pen/article/view/158/185)

2. Bharat Sanga, Reeta Wattal and D. S. Nagesh, "Experimental Analysis and Parametric Optimization in Ultrasonic Welding of Phosphor Bronze sheets", International Journal of Mechanical and Production Engineering Research and Development (Transstellar), Vol. 10, Issue 6, pp: 449-460, December, 2020, (SCOPUS Indexed, ISSN: 2249-8001, Impact Score: 0.74 - 2020)
   (link: http://www.tjprc.org/publishpapers/2-67-1609746753-IJMPERDDEC202050.pdf)

3. Bharat Sanga, Reeta Wattal and D. S. Nagesh, "An FEA based study of thermal behaviour of ultrasonically welded phorphor bronze sheets", Journal of Mechanical Engineering and Sciences (JMES), Vol. 15, Issue 2, pp 8057-8071, June, 2021, (ESCI Indexed, ISSN: 2289-4659, Cite Score: 2.2 – 2019, Impact Score: 1.49 – 2020).
   DOI: doi.org/10.15282/jmes.15.2.2021.10.0635
   (Link: https://journal.ump.edu.my/jmes/article/view/4928/1342)

4. Bharat Sanga, Reeta Wattal and D. S. Nagesh, "Weld joint characterization in ultrasonic welding of phosphor bronze sheets", Engineering Science and Technology, an International Journal (JESTECH), Volume 30, June 2022, 101040, (SCIE Indexed, Elsevier, ISSN: 2215-0986, Cite Score: 9.0, Impact Factor: 4.36)
   DOI: https://doi.org/10.1016/j.jestch.2021.07.003
   (Link: https://doi.org/10.1016/j.jestch.2021.07.003)

5. Bharat Sanga, Reeta Wattal and D. S. Nagesh, "Ultrasonic Metal Welding: A novel joining technique for phosphor bronze sheets", Ist International conference on Energy, Material Sciences & Mechanical Engineering (EMSME) - 2020, National Institute of Technology, Delhi, India, Published in Advances in Mechanical and Materials Technology, Lecture Notes in Mechanical Engineering, Springer, Singapore, January 2022, pp 735-747

6. Bharat Sanga, Reeta Wattal and D. S. Nagesh, “Optimization of Ultrasonic Spot Metal Welding Parameters in Dissimilar Metal Joints”, International conference on Simulation Automation and Smart Manufacturing (SASM 2021), GLA University, Mathura, India.